ABSTRACT

Title of dissertation: SUPERCONDUCTING ARTIFICIAL MATERIALS WITH A NEGATIVE PERMITTIVITY, A NEGATIVE PERMEABILITY, OR A NEGATIVE INDEX OF REFRACTION

Michael Christopher Ricci
Doctor of Philosophy, 2007

Dissertation directed by: Professor Steven M. Anlage
Department of Physics

Artificial materials are media made of inclusions such that the sizes and spacing of the inclusions is much smaller than the incident electromagnetic radiation. This allows a medium to act as an effective bulk medium to electromagnetic radiation. Artificial materials can be tailored to produce desired values of the permittivity, permeability, and index of refraction at specific frequencies. The applications of this tailoring include electromagnetic cloaking, and, theoretically, subwavelength imaging resolution. However, the success of these applications depends on their sensitivity to loss.

This research uses superconducting niobium (Nb) metals to create arrays of wires, split-ring resonators, and a combination of wires and split-ring resonators, with very low loss. These arrays are used to investigate properties of a medium with an index of refraction that contains a bandwidth of frequency where the real part is negative. The Nb wire arrays produce a frequency bandwidth with a negative real part of the permittivity, while the Nb split-ring resonators produce a frequency

bandwidth with a negative real part of the permeability. The combination of Nb wires and Nb split-ring resonators creates an artificial medium with a negative real part of the index of refraction.

The electromagnetic transmission of the wires, split-ring resonators, and combination medium is measured in a waveguide as a function of frequency, and models of the permittivity and permeability are used to fit this data. For a single Nb split-ring resonator, the change in the resonant frequency and quality factor with temperature is measured and fit with a two-fluid model of superconductivity. The change in the resonant frequency and quality factor with an applied dc H field and applied power is also measured and compared to, respectively, magneto-optical imaging and laser scanning photoresponse measurements. Bianisotropy and perturbations in the resonant frequency are investigated, and simulated with commercial electromagnetic modeling software. The electromagnetic transmission of a single Nb split-ring resonator is compared to resonators made of $YBa_2Cu_3O_{7-\delta}$, Copper, and a Nb closed-ring resonator. Similar measurements are made with the single resonators embedded in a metallic wire array.

SUPERCONDUCTING ARTIFICIAL MATERIALS WITH A NEGATIVE PERMITTIVITY, A NEGATIVE PERMEABILITY, OR A NEGATIVE INDEX OF REFRACTION

by

Michael Christopher Ricci

Dissertation submitted to the Faculty of the Graduate School of the
University of Maryland, College Park in partial fulfillment
of the requirements for the degree of
Doctor of Philosophy
2007

Advisory Committee:
Professor Steven M. Anlage, Chair/Advisor
Professor Thomas M. Antonsen
Professor Victor L. Granatstein
Professor Christopher J. Lobb
Assistant Professor Min Ouyang

© Copyright by
Michael Christopher Ricci
2007

Dedication

Dedicated to you.

Acknowledgments

I first would like to thank the taxpaying citizens of the United States of America, and the State of Maryland. This work was funded by the National Science Foundation grant number NSF/ECS-0322844, and various material needs were purchased with the state purchasing account.

I would like to thank my advisor, Steven Anlage, for giving me the research project and supporting me on the project. I would like to thank my committee members, Thomas M. Antonsen, Victor L. Granatstein, Christopher J. Lobb, and Min Ouyang, for agreeing to be on the defense committee. I also thank all the professors I have learned from throughout my schooling.

I would like to thank Russ Frizzell, Gus Vlahacos, Peter Kneisel and Larry Turlington for their help in the fabrication process; Berkeley mask facilities; Brian Straughn and Doug Bensen; J. Hamilton for his assistance in parts of this project; Dragos Mircea, Sameer Hemmady, Hua Xu, Nate Orloff, Atif Imtiaz, John Lee, Sudeep Dutta, Josh Higgins for their help along the way.

I would like to thank my family, especially my parents, sister, brother-in-law, and my new niece...I promise not to scare you with an orange.

Other people who have made this enjoyable: Diana Aljets, Joseph 'TF' Crenshaw, Nick Cummings and Sara, Beth and Dan Dakin, Scott Fletcher, Chad Galley, Jimmy 'The Hague' Hague, $M\alpha\nu\acute{\omega}\lambda\eta\varsigma$ $X\omega\upsilon\rho\delta\acute{\alpha}\kappa\eta\varsigma$, Patrick Hughes, Neil 'The Enforcer' Jonas, Jonathan and Joanna King, Ryan 'Fishhook' McCabe, Timmah 'Limmah' McCaskey, Willie Merrell, Chad Mitchell, John Palastro, Jon Sappington, Keith 'FB' Thomas, Brian Tighe, W. Andy Tillotson, Randy 'Florentine Pogen'

Watson; Old roomies Steve, Keary, and Scott. The chantey-men and women at the Royal Mile.

Thanks to all the countless musicians I've met along the way, especially Brooks and Helm (JennX), and the ones who I have no chance of meeting, and especially Frank Zappa, who once said,

> "There are plenty of yuppies out there with absolutely nothing upstairs. Graduate airheads with Ph.D.s and everything, but they don't know anything. And what do they listen to? Certainly not *my* records."

Contents

List of Tables

List of Figures

Chapter 1

Introduction

1.1 Overview

This chapter details the work that preceded the experiments presented in this dissertation. While every attempt is made to document relevant work, many articles are not referenced here, especially for earlier works. Hopefully, a fuller account of the history of the topic of negative index of refraction can be gathered by cross referencing all the references in the cited articles. Due to space and time considerations, this cannot be done in this dissertation. When a physical reference has been found, quotations from said reference will be displayed in order to clarify the reference's importance to this history. However, not all references cited were found, and so an overview based on the article citing the original will be given, and both the original and citing article are cited.

It is also noted that a large amount of material was published in the former Soviet Union in the CE mid-1900s. While some translations do exist, there are some articles where a translation is unknown. Thus, when possible both the translated and original article in Russian are cited, and in order to be as precise as possible, the transliterated journal name is cited, with the original Russian name as a note.

1.2 Early work

The subject of electromagnetics begins at least with the ancient Greeks, who knew of the electrostatic and magnetostatic properties of amber and lodestones, or at least their effects [1]. A full survey of the entire scope of electrodynamics is not given here, and the reader is directed to Reference [2]. Rather, the story presented in this dissertation begins at the beginning of the twentieth century*. The research presented in this dissertation is concerned with materials with a negative real part of the permittivity, negative real part of the permeability, and, ultimately, a negative real part of the index of refraction. Most naturally occurring materials have each of those quantities greater than zero. Figure (1.1) shows an incoming ray of electromagnetic radiation in a medium with relative permittivity, relative permeability, and index of refraction of, respectively, $\epsilon_1,\ \mu_1,\ n_1$, incident on a boundary with a second medium with relative permittivity, relative permeability, and index of refraction of, respectively, $\epsilon_2,\ \mu_2,\ n_2$. The reflected ray is not shown, but two possibilities of refraction are shown: a positive angle of refraction, labeled $\theta_{T,p}$, and a negative angle of refraction, labeled $\theta_{T,n}$. Note that the red lines are the propagation of energy, or Poynting vector, while the blue lines are the phase velocity vectors.

In Reference [4], Lamb wrote "[a] question of some interest arises, as to whether it is possible for the group-velocity, in any real case, to be negative...That is, to have opposite sign to the wave-velocity." Lamb also imagined a mechanical device

*Many of the earlier references presented here were obtained from Reference [3].

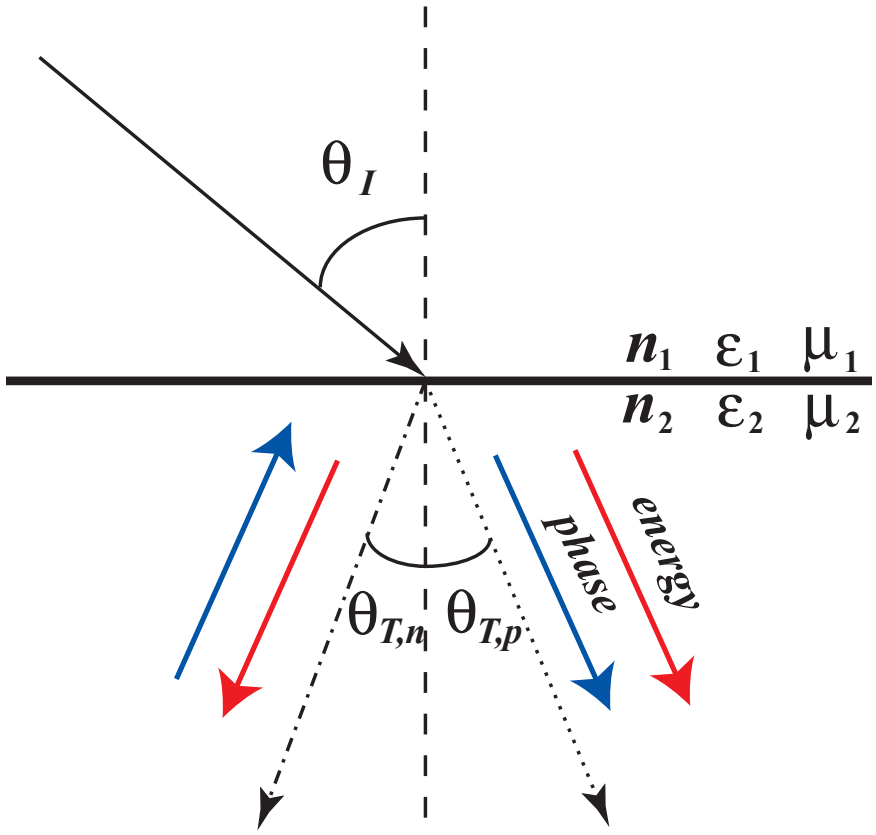

Figure 1.1: A plot of the refraction of an electromagnetic ray for two semi-infinite media. Each medium has a relative permittivity, ϵ_i, relative permeability, μ_i, and index of refraction, n_i, where i is either 1 or 2 and refers to the medium. The thick black horizontal line is the interface between the two media, and the dashed line orthogonal to the thick horizontal black line is the normal to the interface. The incoming electromagnetic ray is the solid black line, making an angle θ_I with the normal. Two refracted rays are shown, a positively refracted ray, shown dotted with angle $\theta_{T,p}$ to the normal, and a negatively refracted ray, shown dotted with angle $\theta_{T,n}$ to the normal. The blue lines are the phase velocity, and the red lines are the energy flow.

where the group velocity was negative, and opposite to the phase velocity. He states [4] "when a local disturbance is produced...groups of waves will be propagated outwards, whilst the individual waves composing a group will be found to be moving inwards." Lamb states at the end of the article that [4] "[i]t is hardly to be expected that the notion of a negative group-velocity will have any very important physical application... ." Lamb also stated in Reference [5, p. 383] that "a disturbance might be propagated outwards from a centre in the form of a group, whilst the individual waves composing the group were themselves travelling backwards, coming into existence at the front, and dying out as they approach the rear."

Lamb states Schuster as proposing the idea of a negative group-velocity. In his book, Reference [6], Schuster states [6, p. 330],

> "If there is a convection of energy forward, the waves must therefore move backwards. In all optical media where the direction of the dispersion is reversed, there is a very powerful absorption, so that only thicknesses of the absorbing medium can be used which are smaller than a wave-length of light. Under these circumstances it is doubtful how far the...results have any application."

Schuster also considers negative refraction [6, p. 330], "the deviation of the wave on entering such a medium is greater than the angle of incidence, so that the wave normal is bent over to the other side of the normal..."

In CE 1945, L. I. Mandelshtam showed[†] that a medium with a negative index of refraction would have a ray exactly as that in Figure (1.1), where the ray refracts

[†]Supposedly, there is an earlier reference by Mandelshtam, Reference [7], where he shows this

at an angle $\theta_{n,T}$, and the phase velocity points towards the boundary, rather than away [8]. In CE 1951, G. D. Malyuzhinets made a similar claim to the phase velocity as Mandelshtam, and an example of a backward-wave transmission line was also presented [9, 10]. In CE 1957, D. V. Sivukhin extended the idea of a backward-wave medium to one in which the permittivity, and permeability, were both negative [11], but apparently stopped at that realization [10].

1.3 Veselago's Work

In CE 1959 V. E. Pafomov published an article concerning Cerenkov radiation [12, 13]. In this article, the case of a medium where both the permittivity and permeability are negative was considered. It was stated that [12, 13],

> "Undamped electromagnetic waves can exist for $\epsilon > 0,\ \mu > 0$ as well as for $\epsilon < 0,\ \mu < 0$ since the index of refraction $n = \sqrt{\epsilon\mu}$ is a real quantity in both of these cases...In the frequency region in which the group velocity is negative the solution is given by advanced potentials, with phases which do not move away from the radiator but approach it."

Note that the statement about the group velocity was in reference to the case of $\epsilon < 0,\ \mu < 0$. Another interesting point presented in this article, concerned the "inverse" Doppler effect [12, 13]: "It is apparent from Eq. (14) that in the frequency region in which the projections of the wave vector and the group velocity on the direction of

effect. The citation in the main text is a peer-reviewed journal reference.

motion have different signs[,] lower frequencies are radiated in the forward direction ("inverse" Doppler effect)." There are citations in Reference [12, 13] with regard to this "inverse" Doppler effect, and with regard to the negative group velocity.

Beginning in CE 1967, V. G. Veselago began to accumulate all the preceding knowledge on media with a negative index of refraction. In Reference [14, 15], Veselago discussed some basic properties of materials with simultaneously negative permittivity and permeability. He mentioned the inverse Doppler effect, and reversed Cerenkov radiation, and the properties of transmission through a thin slab where $n < 0$. There is another very interesting statement that will become useful in later sections. Suppose that the permittivity and permeability have some amount of loss. Then for the values where the real parts of the permittivity and permeability are negative, the imaginary part of the wave number, $k = \omega\sqrt{\epsilon\mu}$ where ω is the frequency of the electromagnetic wave, will be negative. Veselago states that [14, 15] "even in this case the material will also absorb, and not radiate, energy, [sic] since it follows from Eq. (4) that the wave grows in the direction of the phase velocity and not the group velocity." It was suggested that the better way to observe dissipation properties of the medium is through the complex frequency, $\omega = \omega_r + i\gamma$, assuming that the wave number is real [14, 15, Eqs. (5) and (6)].

In Reference [16, 17], Veselago considered a gaseous sphere of electric and magnetic monopoles, and it was shown that for "a light beam falling radially on the sphere...from all sides, [the sphere] will experience a compression from all sides." Radiation tension was also considered, and references to previous articles by Veselago were cited. Perhaps most interesting is the citation of studies of conducting

ferromagnets as media where the permittivity and permeability are negative. It is stated, in fact, that [16, 17] "experimental observations have been reported on the transmission of coupled plasma and spin waves through such conducting ferromagnets."

The final CE 1967 article by Veselago to be discussed here is the seminal article, Reference [18, 19], where the basic properties of a material with simultaneously negative values of ϵ and μ were summarized. This article demonstrated, theoretically, the effects of a medium with a negative index of refraction. In addition to those already stated, the properties of convergent and divergent lenses are reversed, and in fact a flat slab, that is, a slab with parallel sides, may focus an image, as shown in Figure (1.2). There are two focal points, one inside the slab, and one outside the slab [18, 19, Fig. (4)]. It was also shown in Equation (23) in Reference [18, 19] that given considerations on the energy of the electromagnetic fields, there can only be negative permittivity and negative permeability when there is frequency dispersion.

It is noted that this article, Reference [18, 19], is the typical article cited as the origin to the field of metamaterials with simultaneously negative permittivity and permeability. However, due to a lack of materials with a negative index of refraction, the work was considered a theoretical curiosity, and most work on the subject was postponed until the CE 2000s.

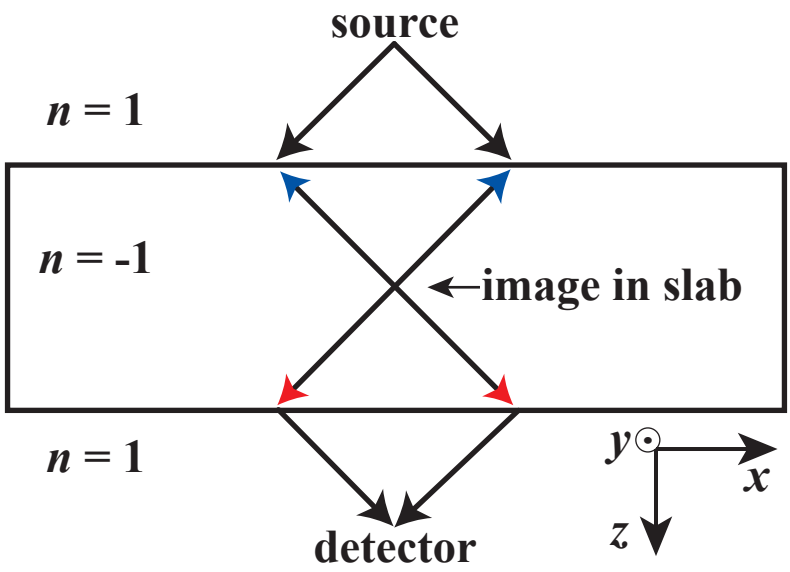

Figure 1.2: Ray transmission through a flat slab, denoted as the rectangle, with a negative index of refraction with no loss. The slab is two dimensional, and extends to infinity in the $\pm$ x directions. The slab has an index of refraction of $n = -1$, and is embedded in vacuum with $n = 1$. There is an image inside the slab, as well as outside the slab, at the detector. The black arrowheads indicate direction of propagation of energy and phase, the blue arrowheads indicate direction of phase, and red arrowheads indicate direction of energy.

1.4 Early experimental work

1.4.1 Wire arrays

Artificial materials, composed of dielectrics and metal inclusions much smaller than the wavelength of the incident electromagnetic radiation, were introduced in the mid-1900s. J. Brown has a summary of the history of this field, and states that the need for artificial materials were a result of radar studies in the second World War [20, p. 195], although groundwork was laid out by Mossotti [21, p. 199] and Rayleigh [22, 23]. The desire was to reduce the weight of a microwave lens, which, due to the incident wavelength of the radiation, could be very large [20, p. 195], with "apertures up to ten feet." Brown cites Rust [24] and Kock [25] as independently suggesting the use of artificial materials. In Reference [25], Kock created a lens made of conducting plates parallel to the incident electric field polarization vector, which "constitutes a refraction medium with index of refraction less than unity." Kock later wrote a widely cited article [26] that [20, p. 195] "suggested that a lattice of conducting elements would act as a dielectric at microwave frequencies."

In CE 1953, J. Brown published an article describing an artificial dielectric with an index of refraction less than one [27]. The artificial dielectric was composed of an array of infinitely long metallic wires with their lengths parallel to the y-axis, and an infinite number of such wires in the $x - z$ plane, with a lattice parameter of a, such that $a \ll \lambda$, where λ is the incident radiation wavelength. Thus, it could be thought of that the incident electromagnetic wave "sees" a homogenous medium. It was shown that the cutoff wavelength of the wire array is the smallest root of [27,

Eq. (9)],

$$\theta \tan\left(\frac{\theta}{2}\right) = A, \tag{1.1}$$

where $\theta = 2\pi a/\lambda_c$, where λ_c is the cutoff wavelength, and [27, Eq. (6)],

$$A = \frac{\pi}{\ln[a/(2\pi r)]}, \tag{1.2}$$

where r is the wire radius. A plot of the roots of Equation (1.1) is shown in Figure (4) of Reference [27]. Brown also considered anisotropic lattice parameters, oblique incidence of the applied electromagnetic field, and reflections at the surface of the metallic wire medium.

In CE 1962, W. Rotman published a article where it was shown that parallel-plate and artificial dielectrics made of parallel metallic wires could simulate a plasma, in the absence of a dc magnetic field [28]. A three-dimensional infinite array of metallic wires, with their lengths parallel to the three Cartesian axes, was considered, and although Rotman was not the first to consider such a setup*, it appears he may have been the first to publish on the subject of plasma simulation with dielectrics. Rotman showed that the characteristic impedance of the wire array, and the characteristic propagation constant, match similar parameters for a plasma, in the absence of a dc magnetic field, stating [28] "[r]odded artificial dielectrics and parallel-plate structures tend to maintain the characteristics of plasma media, such as the relation between the characteristic impedance...and the propagation constant." A distinction between the plasma frequency of a plasma and the cutoff frequency of the wire array was made, which seems to imply that a different mechanism was believed to

*See references in Reference [28].

be responsible for each.

In CE 1965, K. E. Golden published a article continuing the study of simulating a plasma in the absence of a dc magnetic field with a wire array [29]. The experiment was to observe the radiation pattern of a horn antenna with a wire array, acting as a "plasma sheath," placed at the aperture. There are several very interesting statements made. Golden states that [29] "the permittivity of a homogeneous plasma can be simulated by a rodded medium," because "[c]urrents induced in the rods tend to simulate the oscillating inductive currents in a plasma." The explicit cutoff frequency was written for the wire array, similar to the work of Brown, and a small lattice parameter approximation was given as [29, Eq. (7)],

$$\lambda_p^2 = 2\pi d^2 \ln\left(\frac{d}{2\pi r}\right), \tag{1.3}$$

where d is the lattice parameter of the wire array, r is the radius of the wires, and λ_p is the wavelength of the radiation at the cutoff frequency. Equation (1.3) was derived for the condition that $\lambda \gg d$, where λ is the incident wavelength of radiation. In terms of the frequency, ω, Equation (1.3) can be rewritten as,

$$\omega_p^2 = \frac{2\pi c^2}{d^2 \ln(d/2\pi r)}, \tag{1.4}$$

where c is the speed of light in vacuum.

1.4.2 Arrays of split-ring resonators

The diamagnetic properties of metallic loops has been known since at least H. Lenz. In CE 1952, Schelkunoff and Friis wrote a method of exploiting Lenz's law

for a microwave antenna. The motivation was a method of increasing the permeability, and their method involved a single loop of metallic wire with a gap along the circumference [30, p. 584]. Assume that metal plates are coupled to the wire ends of the gap, as a way to increase the capacitive area, then for a loop with radius R, the magnetic susceptibility for a medium with N such loops per unit volume is given by [30, p. 584, Eq. (54)],

$$\chi_m = \frac{N(\omega/c)^2(\pi R^2)^2 C/\epsilon_0}{1-(\omega/\omega_0)^2}, \tag{1.5}$$

where ω_0 is the resonant frequency of the loop, c is the speed of light in vacuum, and C is the capacitance. If the area of the aforementioned plates is A, and they are separated by a distance d, then,

$$\chi_m = \frac{F\omega^2}{\omega_0^2-\omega^2}, \tag{1.6}$$

and the relative permeability is given by [30, p. 577, Eq. (15)],

$$\mu = 1 - \frac{F\omega^2}{\omega^2-\omega_0^2}, \tag{1.7}$$

where,

$$F \stackrel{def}{=} N\pi R^2 \frac{A}{d}\left(\frac{\pi R^2\omega_0}{c}\right)^2. \tag{1.8}$$

In practice, metallic cylinders with a gap in the circumference running the length of the cylinder have been suggested for nuclear magnetic resonance imaging since at least the CE 1970s, as found in References [31, 32]. In fact, in Reference [32], the term "split-ring resonator" was used to describe the resonating cylinder. The use of a cylinder was presented as a high frequency, tunable, low-weight alternative to bulky cavities and solenoids. Most other research up to CE 1999 involved

measurements of chiral media, using loop-wire and omega-particle devices. See, for instance, Reference [33], and references therein.

1.5 Pendry's arrays of wires and split-ring resonators

In the CE 1990s, J. B. Pendry and his group published articles that built upon the aforementioned earlier work, with the motivation of producing a medium with a negative index of refraction as discussed by Veselago. In the first set of articles, the Pendry group wrote down the cutoff frequency for a three-dimensional infinite array of metallic wires, similar to [29], however with a different motivation. In another set of articles, the Pendry group wrote down the permeability of an array of split-ring resonators, as a way to achieve negative permeability over a limited frequency bandwidth, using non-magnetic metals.

1.5.1 The wire array

In CE 1996, J. B. Pendry, A. J. Holden, W. J. Stewart, I. Youngs published a article on a method of reducing the plasma frequency of bulk metal to microwave frequencies [34]. In that article, they considered a three-dimensional infinite array of metallic wires with their lengths parallel to the Cartesian axes. The group then equated the magnetic vector potential, $\mathbf{A}$, with the effective mass of the electrons, and as a result of [34] "confining electrons to thin wires we have enhanced their mass by 4 orders of magnitude so that they are now as heavy as nitrogen atoms." The effective density of the electrons is also reduced, compared to the bulk metal.

They continue by stating that the cutoff frequency of the wires is due to a plasmonic resonance, and that [34] "[o]ur new reduced plasma oscillation is every bit the quantum phenomenon as its high frequency brother." This plasma frequency is written as [34, Eq. (14)],

$$\omega_p^2 = \frac{2\pi c^2}{a^2 \ln(a/r)}, \tag{1.9}$$

where a is the lattice parameter of the wire array, r is the radius of a wire, and c is the speed of light in vacuum. Note that Equation (1.9) is an approximation in the limit of $r \ll a$ [35], and, except for a factor of 2π, is exactly the same result as Equation (1.3). The idea of a plasmon responsible for the reduction of the plasma frequency was a novel idea, not discussed in the earlier articles. A plasmon is defined as a [36, p. 278] "quantum of plasma oscillation." typically, plasmons are excited by scattering an electron off of the plasma, and measuring the energy lost by the electron [36, p. 278]. This plasmon model of the metallic wire array will give rise to some controversy, and this discussion is postponed for now.

1.5.2 The split-ring resonator array

In CE 1999, J. B. Pendry, A. J. Holden, D. J. Robbins, W. J. Stewart published an article on how to create a highly resonant response to the magnetic field of an incident electromagnetic wave with non-magnetic metals [37]. In that article, they note that an infinite array of infinitely-long metallic cylinders with their axes aligned with the applied magnetic field, will have a diamagnetic response to the applied magnetic field. In order to create a resonant response to the applied mag-

netic field, another metallic cylinder is inserted concentrically to the first metallic cylinder, and a gap is created along the circumference of each metallic cylinder. This gap [37] "prevents current from flowing around any one ring. However there is considerable capacitance between the two rings which enables current to flow." The relative permeability is shown to be, using global parameters rather than specific variables [37, Eq. (17)],

$$\mu = 1 - \frac{f\omega^2}{\omega^2 - \omega_0^2 + i\Gamma\omega}, \tag{1.10}$$

where ω_0 is the resonant frequency, Γ is a loss parameter, and f is the filling, or volume, fraction of a single array element. Note the similarity between Equation (1.10) and Equation (1.7), where the main difference lies in the form of the filling fractions. The group finally states that the system of the infinite cylinders is highly anisotropic, and that using two-dimensional slices orthogonal to the cylinder axes, called split-ring resonators, an isotropic medium can be created, with the same frequency response given in Equation (1.10).

1.6 Media with simultaneously negative permittivity and permeability

Perhaps the most striking article written about media with simultaneously negative permittivity and permeability was by J. B. Pendry in CE 2000 where it was shown that a slab with $\epsilon = \mu = -1$ would amplify evanescent waves [38]. While conventional lenses have a resolution limit of roughly $\lambda/2$, the slab with $\epsilon = \mu = -1$ would allow perfect imaging with no resolution limitation as a result of the amplified

evanescent waves. The slab was shown in Figure (1.2), and shows that there are two images: one inside the slab and another outside the slab. There also is no optical axis. Pendry used the typical expressions for the transmission and reflection Fresnel coefficients for a dielectric medium in his calculations, and a limit of the permittivity and permeability taking on a value of -1 showed no reflection, and evanescent growth of the transmission. As another example, he showed that in the electrostatic limit, that is, where the dimensions of the system are much smaller than the incident radiation, the electric and magnetic fields decouple, and the only consideration needed would be either $\epsilon = -1$ or $\mu = -1$ [38].

In CE 2001, D. R. Smith, W. J. Padilla, D. C. Vier, S. C. Nemat-Nasser, and S. Schultz introduced a medium based on the arrays of metallic wires, and the split-ring resonators [39], in which both the wires and split-ring resonators were printed on circuit board materials, with the wire array on one side of the circuit board, and the split-ring resonators on the other side of the circuit board. In Reference [39], the experiment was essentially a one-dimensional microwave transmission experiment, and the electromagnetic transmission data presented showed a dip in electromagnetic transmission for the split-ring resonator–only setup, and a peak in electromagnetic transmission for the split-ring resonator and wire combination. This data was presented again, along with a transfer matrix model of the experiment, in Reference [40], where it was shown that the transfer matrix model gave qualitative results that agreed with the experimental data.

This combination medium showed actual negative refraction in Reference [41], where the composite medium had an angle of refraction of approximately $-60°$,

versus a teflon prism, which had an angle of refraction of approximately 30°, both measured at 10.5 GHz. This work was extended in Reference [42], where the electric field amplitude was measured as a function of position. This spatial mapping showed a beam of radiation refracting with a negative angle of refraction for the composite material prism, and a positive angle of refraction for a teflon prism. In Reference [43], negative refraction was again shown, however, the radiation was measured in the far-field, approximately 14 to 28 times the free-space wavelength of the microwave radiation used, which was 12.6 GHz.

Note however that these are not the first experiments to show negative refraction, for instance, see Figure (10) in Reference [44]. The difference is the cause of the negative refraction, as in the case of Reference [44], the negative index of refraction was due to,

> "two Floquet-Bloch waves corresponding to the upper and lower branches of the dispersion contour in the [wave-vector diagram]...excited simultaneously in the vicinity of the Bragg-reflection regime, resulting generally in two rays propagating in different directions."

There has been a trend recently to push the frequency limits of these materials to higher frequencies. This limit of frequency is due to two reasons: the first is losses. At higher frequencies, the metallic wires and split-ring resonators must be made smaller in order to be in the limit of an effective medium, since the wavelength of the incident radiation is decreasing. However, for a wire, and for a split-ring resonator with loops approximated as being composed of wires, the resistance, R,

scales as [45] $R \sim 1/r^2$, where r is the radius of the wire making up the wire or split-ring resonator. Thus, for wires and split-ring resonators made up of wires with $r \ll 1$, the resistance will increase like $1/r^2$. With decreasing wire radius, the resistance can be very large, especially at nano-scale lengths.

Another supposed limitation was mentioned by Landau and Lifshitz. In Reference [46], an estimate is given relating the size of the body upon which a magnetic field is incident, to the body's susceptibility. They write [46, p. 269, Eq. (79.4)],

$$l^2 \ll \frac{\chi c^2}{\omega^2}, \tag{1.11}$$

where l is the size of the body, χ is the magnetic susceptibility, and c is the speed of light in vacuum. They continue to state that for atomic dimensions, a, it must hold that $l \gg a$ for any magnetic susceptibility concept to be meaningful, however at high frequencies, $\chi \sim v^2/c^2$ and $\omega \sim v/a$, where v is the velocity of the electron in the atom, which means $l^2 \sim a^2$, and thus [46, p. 269] "there is no meaning in using the magnetic susceptibility from optical frequencies onward..." However they do claim that this approximation was for isotropic media [46, p. 269, footnote].

Many experiments have been performed at terahertz and higher frequencies. In CE 2004, T. J. Yen, W. J. Padilla, N. Fang, D. C. Vier, D. R. Smith, J. B. Pendry, D. N. Basov and X. Zhang published work where copper split-ring resonators were fabricated on quartz substrates [47]. The size of the split-ring resonators was roughly 30 μm, and the resonant frequency was roughly 1.0 THz. While the values were extracted from simulations and not the data, the permeability was shown to be negative for some frequency bandwidth. This frequency bandwidth was extended

to 100 THz by S. Linden, C. Enkrich, M. Wegener, J. Zhou, T. Koschny, C. M. Soukoulis [48], and finally to the optical regime by A. N. Grigorenko, A. K. Geim, H. F. Gleeson, Y. Zhang, A. A. Firsov, I. Y. Khrushchev, and J. Petrovic [49]. While it was noted that a negative index of refraction was not achieved in Reference [49], free-space impedence matching was shown. While this list of references is by no means exhaustive, cross referencing may provide a more thorough history of the field.

1.7 Controversy

There has been much controversy surrounding artificial materials with a negative permittivity and permeability. Two subjects that have received the most objections are the experimental results of negative refraction and the concept of perfect imaging. They will be discussed in that order.

1.7.1 Wire arrays and negative index of refraction

There has been some controversy surrounding the wire arrays of the Pendry group [34]. In Reference [50], Mikhailov argues that the quantum interpretation of a plasmon oscillation in the wires is erroneous, and that the expression for the plasma frequency "was derived from the classical Faraday law and does not contain the Planck constant." Mikhailov continues by stating that the observed reduction of the plasma frequency is a purely classical result, and predicts a plasma frequency in the long-wavelength limit to be $\omega_p \sim c/a$ where c is the speed of light in vacuum,

and a is the wire array lattice parameter [50, Eq. (5)]. This expression was also written for a photonic crystal of metallic wires in Equation (2) of Reference [51].

The main response by the Pendry group [52] to this comment was to argue the plasma frequency that Mikhailov wrote [50, Eq. (4)] was wrong. They state that the difference between their equation for the plasma frequency [52, Eq. (1)] and Mikhailov's equation [50, Eq. (4)] is due to the self-inductance of the wire. They then claim that agreement of numerical simulations to within 5%, and also experimental results, although no actual agreement value was given, implies that their equation [52, Eq. (1)] is correct.

Another argument to the plasmon model was given by R. M. Walser, A. P. Valanju, and P. M. Valanju [53]. They base their arguments on two points. The first is that the microwave plasmons cannot exist due to very short electron collision times, and the second is that the effective mass was derived using the magnetic vector potential, $\mathbf{A}$, which is written as [54, p. 234, Eq. (5.59)],

$$\mathbf{B} = \nabla \times \mathbf{A}, \tag{1.12}$$

where $\mathbf{B}$ is the magnetic field. Since the magnetic vector potential is gauge dependent, an "arbitrary constant vector" may be added to the magnetic vector potential without changing $\mathbf{B}$ in Equation (1.12) [54, p. 238], and since $\mathbf{B}$ is the observable quantity, R. M. Walser, A. P. Valanju, and P. M. Valanju argue that [53] "[o]ne can obtain any m_{eff} from [the magnetic vector potential] by adding a gauge term $v_{\text{drift}} = \bar{\nabla} f(x,\ y,\ z)$ to [$\mathbf{A}$] without changing the fields." They then cite some of the earlier works on wire arrays cited in this dissertation, and state that while the

permittivity can be given as Equation (2) in Reference [34], the cutoff frequency is not a plasma frequency, but rather an LC resonance of the wire lattice. Note that as of 1 May 2007, the Pendry group has not responded to this comment.

A final comment to the plasmon model was from Pokrovsky and Efros [55]. In that article, they reject the plasmon argument of the Pendry group in [34], and base their work on [55] "conventional electrodynamics." Although the expressions are very cumbersome, a dispersion relation, that is, $\omega(\mathbf{k})$, is derived in Equation (6) of Reference [55], as well as a cutoff frequency, Equation (8) of Reference [55], and permittivity, Equation (14) of Reference [55], that shows negative real values for frequencies less than the cutoff frequency. They conclude by arguing that inserting this wire array into a homogenous medium with $\mu < 0$ will not produce any propagating electromagnetic waves, and therefore the result of Reference [41] should be reinterpreted.

Marqués and Smith commented on Reference [55] in Reference [56]. Their main argument was not on the criticized plasmon modes of the wires, but on the claim of the wires embedded in the $\mu < 0$ medium. Marqués and Smith state that there in fact is no homogenous medium of $\mu < 0$ as assumed in Reference [55], and the vacuum between the wires and split-ring resonators is significant and to first order, the metallic wires and split-ring resonators do not effect the currents of each other. Pokrovsky and Efros reply in Reference [57] by stating that they "admit that the idea of spatial separation of fields created by both subsystems might be a good guess for a solution of the microscopic equations[, h]owever, the macroscopic permittivity and permeability should be far from those of the subsystems." This is

due to the magnetic field of a wire diminishing as [54, p. 221, Eq. (5.41)] $1/\rho$, where ρ is the distance from the wire. Note that the magnetic field boundary conditions in Reference [34] forced the magnetic field to diminish faster than $1/\rho$, and perhaps staying within the limits suggested by Marqués and Smith in Reference [56].

Perhaps the longest comment on the experimental results of Reference [41] was presented by P. M. Valanju, R. M. Walser, A. P. Valanju in Reference [58]. They considered not a single, monochromatic incident radiation on a slab of a negative index of refraction medium, but rather two waves with slightly different frequencies. The main concern was the following: that while they agree that the phase velocity will refract negatively, the group velocity always has a positive angle of refraction. They argue that the group velocity is orthogonal to the "group velocity front" of a wave and that due to this, the group velocity fronts would have to travel some finite distance in zero time, and [58] "[s]ince this is nonphysical, no physical signal or energy front can travel forward and negatively refract in the NIM fashion... ." They also argue against the perfect imaging slab [38], such that one can only get focusing with a slab where $n(\omega) = -1$, which is not physical, and that because of this [58], "the perfect lens of Ref. [5] has large spherical as well as chromatic aberrations even for phase rays," and is no longer a perfect lens. Finally, they comment on the experimental results of Reference [41] where they state [58] "[w]e interpret the angular intensity profile observed at the short distance of 15 cm $\approx 5\lambda$ as near-field effects."

A response to this article was written by Pendry and Smith [59]. The only topic they discuss is on the issue of the direction of the group velocity. They argue that

while the interference fronts of the two waves considered in Reference [58] do refract with a positive angle of refraction, the Valanju group is [59] "wrong to interpret the normal to the interference front as the direction of the group velocity. The discrepancy can be resolved by noting that propagation of the front is crabwise, and antiparallel to the phase velocity... ." There is also a convincing plot of a spherical pulse as it enters a medium with a negative index of refraction [59, Fig. (3)]. The pulse elongates into an ellipse, and while the orthogonal to the major axis appears to refract with a positive angle of refraction, the pulse moves with a group velocity that has a negative index of refraction, and that explains the elongation. These arguments were later written more explicitly in Reference [60].

The Valanju group's response essentially agreed with the elongated pulses, see for instance Figure (1) of Reference [61], however they state that "[c]ausality implies that, after refraction, v_g differs from v_p and energy velocity v_E, causing anomalously rapid, dispersive wave decay[,]" and that Reference [59] is incorrect to say that the group velocity is antiparallel to the phase velocity because this neglects dispersion effects [61].

Note that there were no responses to the interpretation of the Valanju group with respect to the actual negative angle of refraction experiment in Reference [41]. However, since the Valanju group believed that far-field measurements would disprove the negative refraction, Reference [43] dealt with this topic.

1.7.2 The perfect lens

While no argument was made against the Valanju group's claims against the perfect lens [58], there are several articles that do discuss the limitations of a perfect lens [38]. Discussion of one comment, made by J. Williams [62], is not discussed here. In Reference [63], G. W. t'Hooft made several comments against the idea of a perfect lens with an index of refraction, $n = -1$. The main concerns can be summarized as follows: first, the wave vector orthogonal to the slab interface should change signs as suggested by Veselago, but not written by Pendry; second, the Fresnel coefficient of transmission is exponentially increasing across the slab, while the electric field amplitude is exponentially decreasing across the slab; third, the summation used by Pendry does not converge because there are infinities encountered inside the slab when $\epsilon = \mu = -1$. This third comment will not be discussed, and is shown in Appendix A that through algebraic manipulation, these divergences disappear. The response given by Pendry [64] states, for the most part, that the equations written in Reference [38] followed conventional scattering theory, and that the amplification follows from multiple reflections inside the slab.

An article by N. Garcia, and M. Nieto-Vesperinas discusses the multiple reflections further [65]. They state that the Fresnel coefficient of reflection is not infinite, as suggested by t'Hooft [63], but rather it is identically zero, and so there cannot be any amplification due to multiple reflections inside the slab because there are no reflections inside the slab. The second comment they make is that any real system with real losses will destroy the perfect lens idea. While Pendry does not explicitly

discuss the multiple reflection in his comment [66], he does question some equations in Reference [65], although these were actually misprints [67] and did not effect the results of Reference [65]. Pendry does concede that losses will limit the resolution, however he states that [66] "by making absorption sufficiently small the resolution can be increased to be as large as desired without causing any divergences in the wave field." Garcia and Nieto-Vesperinas point out that Pendry's main objection was a missprint, and state that the summation involving the multiple reflections for the silver slab example in Reference [38] is over all wave vectors, however the geometry of the problem limits the wave vectors amplified, and therefore the summation should not have been used [68].

As a final note, there have been several articles that have dealt with losses in the negative index of refraction slab, and three important ones are given as References [69, 70, 71]

1.8 Applications

There have been many proposed applications of artificial materials and negative index media. As stated earlier, the subwavelength resolution is an important breakthrough in optics. In Reference [72], subwavelength resolution was shown for a pattern made in chromium (Cr). This pattern had a line width of 40 nm. Ultra-violet light, $\lambda = 365$ nm, irradiated the Cr, and the image was "burned" into photoresist. The width of the lines in the photoresist were measured after an exposure time of approximately 30 to 60 seconds [72]. The measurement was performed with and

without a slab of silver in front of the photoresist, which acted as a superlens. The results were line-widths of 89 nm with the lens, and 321 nm without the lens, and while both results were sub-wavelength, the silver slab experiment gave the best results, as predicted.

Two applications involving antennas can be found in Reference [73], and references therein, where an electrically small antenna was shown to have an increase in radiative power when surrounded by an isotropic material with a negative permittivity, and also in Reference [74], where it was shown that a slab of wires can create a highly directional antenna, similar to the work in Reference [29]. Perhaps the most impressive application so far has been cloaking at microwave frequencies, found in Reference [75].

1.9 Motivation for the experiments presented in this dissertation

The main motivation behind the research presented in this dissertation are ohmic and dielectric substrate losses. Copper was the metal of choice for many of the experiments discussed earlier in this chapter, and despite copper being a very good conductor with low loss, superconducting metals have even lower losses, as long as the temperature is below the critical temperature of the superconductor. While electromagnetic transmission experiments may allow for copper to be used without seeing much passband insertion loss compared to the noise floor, a sensitive experiment such as perfect imaging requires losses to be as small as possible. In fact, in Reference [69], an upper bound to the losses for a near-field imaging

technique is given in terms of the imaginary part of the relative permittivity as $\Im[\epsilon] \ll \exp(-2k_x d)$, where d is the thickness of the slab, k_x is the lateral wave number. The finest details are imaged by very small wavelengths, which correspond to very large values of k_x, and therefore, in order to meet the requirement on $\Im[\epsilon]$, the losses must be as small as possible. In addition to metallic losses, the substrates of the materials are lossy too. Most experiments used G10 as the substrate for copper, however, it is seen that the research presented in this dissertation used quartz substrates, which have a lower loss tangent than G10. Many of the articles cited state that loss is a reason against the observation of negative refraction, for instance Reference [58].

Another motivation is the tunability of superconducting metals. Given the large kinetic inductance near the critical temperature of a superconductor, and that the resonant frequencies of the split-ring resonators, and to a lesser extent the wires, is essentially the same as an LC resonator, the frequency bandwidth of negative permeability should be tunable with temperature.

1.10 Outline of dissertation

This dissertation is written in a style that treats all subject matters separately. First, the early work, background, and motivation for pursuing the research are presented. Next, the mathematical foundations as they relate to the experiments are presented. The third chapter details the experimental materials, and setup. The next three chapters cover experiments performed on metallic wire arrays, split-ring

resonator arrays, and arrays made of a combination of the metallic wires and split-ring resonators. The final main chapter contains conclusions and future work. Two appendices are given: the first derives some important equations, and the second contains comparisons of fit parameters of various data.

Chapter 2

Background Theory for the experiment

2.1 Overview

This chapter details the theories that are relevant to the experiments in this dissertation. The first section is an introduction to electromagnetic theory that starts with Maxwell's equations, and covers topics such as linear media, refraction, and waveguides. The next section details the mathematical theory of a homogeneous medium with a negative index of refraction, followed by a discussion of an artificial material composed entirely of metallic wires. In this case, the metallic wires are treated as creating a cold plasma composed of the conducting electrons. A plasma frequency is derived as a function of the metallic wire lattice parameter and radius. In the fourth section, a discussion of an artificial material composed entirely of metallic split-cylinders shows how a non-magnetic metal can be engineered to have a magnetic permeability that is highly frequency dependent about a resonance frequency. The next section discusses how the mathematical theory of a medium with a negative index of refraction is physically obtained, and observed in a waveguide. Finally, bianisotropy, and superconductivity are discussed in relation to the artificial materials used in this dissertation.

2.2 Introductory electromagnetic theory

2.2.1 Electromagnetic plane waves in linear media

A classical electromagnetic plane wave is composed of electric and magnetic fields, $\mathbf{E}$ and $\mathbf{B}$, respectively. The way that these fields propagate through space and media is fully described by Maxwell's equations. In SI units, Maxwell's equations are [1, p. 238, Eq. (6.6)],

$$\nabla \cdot \mathbf{D} = \rho_f, \tag{2.1}$$

$$\nabla \times \mathbf{E} = -\frac{\partial \mathbf{B}}{\partial t}, \tag{2.2}$$

$$\nabla \cdot \mathbf{B} = 0, \tag{2.3}$$

$$\nabla \times \mathbf{H} = \mathbf{J}_f + \frac{\partial \mathbf{D}}{\partial t}, \tag{2.4}$$

with electric displacement, $\mathbf{D}$, H field, $\mathbf{H}$, sometimes referred to as the magnetic field*, and ρ_f and $\mathbf{J}_f$ are the free charge and free current densities, respectively. The operator $\partial/\partial t$ is the derivative with respect to time, and $\nabla \stackrel{def}{=} \hat{\mathbf{x}}\partial/\partial x + \hat{\mathbf{y}}\partial/\partial y + \hat{\mathbf{z}}\partial/\partial z$, for Cartesian coordinates, is called the vector derivative [54, p. 16, Eq. (1.39)], or "del." Assuming a linear and isotropic infinite media, $\mathbf{D}$ and $\mathbf{H}$ can be rewritten as [1, p. 14],

$$\mathbf{D} = \tilde{\epsilon}\mathbf{E}, \tag{2.5}$$

$$\mathbf{B} = \tilde{\mu}\mathbf{H}. \tag{2.6}$$

where $\tilde{\epsilon}$ and $\tilde{\mu}$ are the permittivity and permeability, respectively. The constitutive relations in Equations (2.5) and (2.6) also assume that the electromagnetic fields are

*See Reference [54, p. 271].

not too large to cause nonlinear effects. Compare Equation (2.5) to Reference [1, p. 255, Eq. (6.92)], and Equation (2.6) to Reference [1, p. 256, Eq. (6.99)] for a more complete description.

Assuming a medium with no sources, Equations (2.1–2.4), together with Equations (2.5) and (2.6), form the Helmholtz equations [1, p. 296, Eq. (7.3)],

$$(\nabla^2 + \tilde{\mu}\tilde{\epsilon}\omega^2)\mathbf{E} = 0, \tag{2.7}$$

$$(\nabla^2 + \tilde{\mu}\tilde{\epsilon}\omega^2)\mathbf{B} = 0. \tag{2.8}$$

A solution can be written as [1, p. 296, Eq. (7.8)],

$$\mathbf{E}(\mathbf{x}, t) = \mathbf{A}_1 e^{i(\mathbf{k}\cdot\mathbf{x} - \omega t)}, \tag{2.9}$$

$$\mathbf{B}(\mathbf{x}, t) = \mathbf{A}_2 e^{i(\mathbf{k}\cdot\mathbf{x} - \omega t),} \tag{2.10}$$

where $\mathbf{A}_i$ is a constant amplitude vector, $\mathbf{k}$ is the wave vector, $\mathbf{x}$ is the position vector, ω is the angular frequency, and t is the time. Inserting Equation (2.9) into Equation (2.7), or Equation (2.10) into Equation (2.8), a condition on the wave number is found to be [1, p. 296, Eq. (7.4)],

$$k^2 = \tilde{\mu}\tilde{\epsilon}\omega^2, \tag{2.11}$$

where $k = |\mathbf{k}|$. While Equation (2.11) holds true for a linear media with no sources, such an equation is generally referred to as a dispersion relation.

The velocity of a line of constant phase, also called the phase velocity, v_p, of an electromagnetic plane wave is given by [1, p. 296, Eq. (7.5)],

$$v_p = \frac{\omega}{k}. \tag{2.12}$$

Using Equation (2.11), the phase velocity in terms of the permittivity and permeability is written as [1, p. 296, Eq. (7.5)],

$$v_p = \frac{1}{\sqrt{\tilde{\mu}\tilde{\epsilon}}} = \frac{c}{n}, \tag{2.13}$$

where n is the index of refraction, and $c = 1/\sqrt{\mu_0\epsilon_0}$, where the zero-subscript refers to the values of free space. It follows that the index of refraction can be written in terms of a relative permittivity and relative permeability,

$$n = \sqrt{\mu\epsilon}, \tag{2.14}$$

where,

$$\epsilon = \tilde{\epsilon}/\epsilon_0, \tag{2.15}$$

$$\mu = \tilde{\mu}/\mu_0. \tag{2.16}$$

In terms of actual values, the permeability of free space is $\mu_0 \stackrel{def}{=} 4\pi \times 10^{-7}$ henrys per meter, and the permittivity of free space is $\epsilon_0 = 10^7/(4\pi c^2)$ farads per meter, where $c \stackrel{def}{=} 1/\sqrt{\epsilon_0\mu_0} = 299\ 792\ 458$ meters per second, exactly. These values, along with an interesting discussion of electromagnetic units, are found in Reference [1, p. 780]. The group velocity, v_g, is, for most media, the speed of the propagation of information, or the speed of the actual wave packet, and is given by [54, p. 399, Eq. (9.150)],

$$v_g = \frac{d\omega}{dk}. \tag{2.17}$$

Assume for the moment a medium with zero loss, that is, no dissipation of energy. Then k in Equation (2.11) is purely real, and the electromagnetic waves

are propagating waves. However, suppose that k in Equation (2.11) is purely imaginary, which could arise from either $\tilde{\mu}$ or $\tilde{\epsilon}$ possessing a negative real part. In this case, where k in Equation (2.11) is purely imaginary, the electromagnetic waves are non-propagating, or evanescent, waves. Take, for instance, a one dimensional electromagnetic wave traveling along the $+z$-axis. Rewriting Equation (2.11) as,

$$k_z = \frac{\omega\sqrt{\mu\epsilon}}{c}, \tag{2.18}$$

let $\epsilon = -1$, and $\mu = 1$. Then it follows that $k_z = i\omega/c$, and from Equation (2.9), for instance, with $\mathbf{A}_1 = \hat{z}$,

$$\mathbf{E}(z,t) = \hat{z}e^{i(k_z z - \omega t)} = \hat{z}e^{i(i\omega/c)z - i\omega t} = \hat{z}e^{-\omega z/c}e^{-i\omega t}. \tag{2.19}$$

Thus, the wave is spatially decaying along the $+z$-axis.

2.2.2 The permittivity and permeability of linear media

Most media can be described as either a conductor or a dielectric. For a conductor, the valence electrons of the atoms making up the conductor are free, while in a dielectric, the electrons are typically confined to a single atom or molecule. The electrons interact with the electric and magnetic fields of an incident electromagnetic field, and in the case of the electric field, this interaction can be described by the permittivity, discussed earlier. A general form of the permittivity for a dielectric can be written as [1, p. 310, Eq. (7.51)],

$$\frac{\tilde{\epsilon}(\omega)}{\epsilon_0} = 1 + \frac{Ne^2}{\epsilon_0 m}\sum_j F_j(\omega_j^2 - \omega^2 - i\omega\gamma_j)^{-1}, \tag{2.20}$$

where the sum is performed over the number of electrons. Here, N is the molecule, or atom, density of the dielectric, e is the charge of an electron, m is the mass of an electron, ω_j is the binding frequency of the j^{th} electron, and γ_j is the damping constant of the j^{th} electron. The term F_j is called the oscillator strength, and is constrained to follow [1, p. 310, Eq. (7.52)],

$$\sum_j F_j = Z, \tag{2.21}$$

where Z is the number of electrons per molecule.

Equation (2.20) can also apply to a metal, as long as the proper assumptions are made. For instance, there is no binding energy associated with a free electron in a metal, at least in the limit of perfect conductivity, and so $\omega_j = 0$ for all values of j [76, p. $32-10$]. If a further assumption is made that all damping is independent of the electrons due to taking an average of the applied field [76, p. $32-10$], then Equation (2.20) can be rewritten as [34, Eq. (2)],

$$\epsilon(\omega) = 1 - \frac{\omega_p^2}{\omega^2 + i\omega\gamma}, \tag{2.22}$$

where [1, p. 313, Eq. (7.60)],

$$\omega_p^2 \stackrel{def}{=} \frac{NZe^2}{\epsilon_0 m} = \frac{ne^2}{\epsilon_0 m}, \tag{2.23}$$

is the square of the plasma frequency, and n is the number density of electrons. In terms of real and imaginary parts, Equation (2.22) is,

$$\epsilon(\omega) = \epsilon_r(\omega) + i\epsilon_i(\omega) = 1 - \frac{\omega_p^2\omega^2}{\omega^4 + (\omega\gamma)^2} + i\frac{\omega_p^2\omega\gamma}{\omega^4 + (\omega\gamma)^2}, \tag{2.24}$$

where $\epsilon_r \stackrel{def}{=} \Re[\epsilon]$, and $\epsilon_i \stackrel{def}{=} \Im[\epsilon]$. A plot of the real and imaginary parts of Equation (2.24) is shown in Figure (2.1), where the plasma frequency is $\omega_p = 2\pi \times 10$

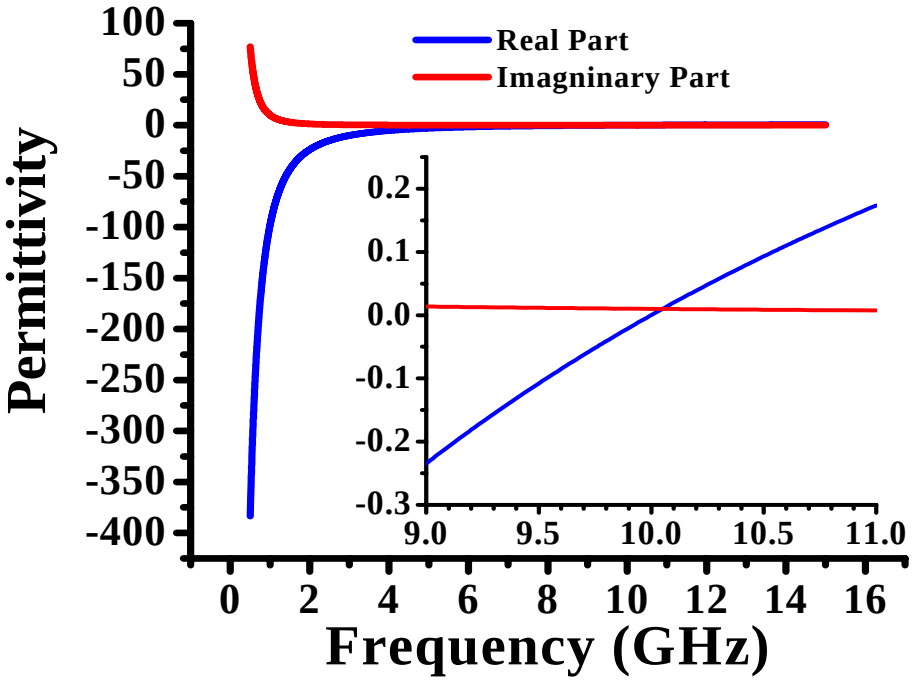

Figure 2.1: A plot of the permittivity of a plasma with a plasma frequency of $\omega_p = 2\pi \times 10$ GHz and loss parameter of $\gamma = 2\pi \times 0.1$ GHz. The blue curve is the real part of the permittivity, and the red curve is the imaginary part of the permittivity. The inset shows a close-up of the larger plot in the vicinity of the plasma frequency, ω_p.

GHz, and the damping constant, or loss parameter, is $\gamma = 2\pi \times 0.1$ GHz. Since the imaginary part of the plot is related to the losses in the material [1, p. 310], at low frequencies the losses are very large. Thus, if an interest lies in obtaining a negative permittivity with low loss, it is necessary to remain near the plasma frequency, where $\Re[\epsilon(\omega_p)] \approx 0$, in order to reduce losses. For a typical bulk metal, the plasma frequency is in the ultraviolet frequency range [1, p. 314].

When an applied electric field is incident on a finite slab of a dielectric and leaves the dielectric with a slightly positive charge on one end, and a slightly negative

charge on the other, the dielectric is said to be polarized. Some media, such as water molecules, are already polarized, at least on a microscopic scale, without the need of an applied electric field. The electric dipole moment, $\mathbf{p}$, is related to the electric field through the polarization tensor, $\underline{\underline{\alpha}}$, by [54, p. 162, Eq. (4.3)],

$$\mathbf{p} = \underline{\underline{\alpha}} \cdot \mathbf{E}. \tag{2.25}$$

The polarization, $\mathbf{P}$, is given by [54, p. 166],

$$\mathbf{P} = \frac{\mathbf{p}}{V}, \tag{2.26}$$

where V is the volume of the medium, and is related to the electric field in a linear dielectric medium through [54, p. 184, Eq. (4.38)],

$$\mathbf{P} = \epsilon_0 \underline{\underline{\chi_e}} \cdot \mathbf{E}, \tag{2.27}$$

where $\underline{\underline{\chi_e}}$ is the electric susceptibility tensor. The electric displacement is then written as, for linear media [54, p. 180, Eq. (4.31)],

$$\mathbf{D} = \epsilon_0 \mathbf{E} + \mathbf{P} = \epsilon_0 \underline{\underline{I}} \cdot \mathbf{E} + \epsilon_0 \underline{\underline{\chi_e}} \cdot \mathbf{E} = \epsilon_0 (\underline{\underline{I}} + \underline{\underline{\chi_e}}) \cdot \mathbf{E}, \tag{2.28}$$

where [54, p. 180, Eq. (4.32)],

$$\underline{\underline{\epsilon}} = \underline{\underline{I}} + \underline{\underline{\chi_e}}, \tag{2.29}$$

and $\underline{\underline{I}}$ is the identity matrix [77, p. 473, Eq. (25)].

While a general form of the permeability is not written in a similar fashion to Equation (2.20), magnetic materials may have a magnetic dipole moment, $\mathbf{m}$, as well as a magnetization, $\mathbf{M}$, equal to the magnetic dipole moment per unit volume [54,

p. 262, Eq. (6.9)]. In the case of linear media [54, p. 274, Eq. (6.29)],

$$\mathbf{M} = \underline{\underline{\chi_m}} \cdot \mathbf{H}, \tag{2.30}$$

where $\underline{\underline{\chi_m}}$ is the magnetic susceptibility tensor. The H field in Equation (2.6) is actually defined through [54, p. 269, Eq. (6.18)],

$$\mathbf{H} = \frac{1}{\mu_0}\mathbf{B} - \mathbf{M}, \tag{2.31}$$

and together, Equation (2.30) and Equation (2.31) give, for linear media [54, p. 275, Eqs. (6.30) and (6.31)],

$$\mathbf{B} = \mu_0(\mathbf{H} + \mathbf{M}) = \mu_0(\underline{\underline{I}} \cdot \mathbf{H} + \underline{\underline{\chi_m}} \cdot \mathbf{H}) = \mu_0(\underline{\underline{I}} + \underline{\underline{\chi_m}}) \cdot \mathbf{H}, \tag{2.32}$$

where [54, p. 275, Eq. (6.32)],

$$\underline{\underline{\mu}} = \underline{\underline{I}} + \underline{\underline{\chi_m}}. \tag{2.33}$$

2.2.3 Refraction of an electromagnetic plane wave

When an applied electric field is incident on a boundary between two media with different indices of refraction, and possibly different wave impedances, there will generally be a reflected wave and a transmitted wave. The amount of transmission and reflection, as well as the direction of the transmitted electromagnetic wave, will depend on the index of refraction and wave impedance. Consider Figure (2.2) where there are two media, each with their own index of refraction, n_j, and frequency dependent wave number, $k_j(\omega)$, describing the dispersion of the medium. The subscript j refers to the particular medium, and has a value of either 1 or 2. The thick black horizontal line is the interface of the two media, and the dashed

line orthogonal to the thick black horizontal line is the normal of the interface. The incoming wave, approaching the interface from the top left, is shown in two orientations. The red orientation is for P-polarization, and the green orientation is for S-orientation. The orientations refer to the electric and magnetic field orientations with respect to the plane of incidence*. The plane of incidence is defined as the plane in which the incident ($\mathbf{k}_I$), reflected ($\mathbf{k}_R$), and transmitted ($\mathbf{k}_T$) wave vectors lie.

In Figure (2.2), the ray traces of the electromagnetic waves are shown as dotted, dot–dot–dashed, and dot–dashed for the incoming, reflected, and transmitted waves, respectively. Each ray makes an angle with respect to the normal of the interface, and these angles are labeled θ_I, θ_R, and θ_T for the incoming, reflected, and transmitted waves, respectively. As shown in Appendix A, the incoming and reflected wave angles are equal [1, p. 304, Eq. (7.35)],

$$\theta_I = \theta_R, \tag{2.34}$$

while the incoming and transmitted wave angles obey Snell's law [1, p. 304, Eq. (7.36)],

$$\frac{\sin\theta_I}{\sin\theta_R} = \frac{n_2}{n_1}. \tag{2.35}$$

The ratio of the incident electric field to the reflected electric field, r, is called the Fresnel coefficient of reflection, and the ratio of the incident electric field to the reflected electric field, t, is called the Fresnel coefficient of transmission. These are

*See Footnote (15) of Reference [78, p. 34].

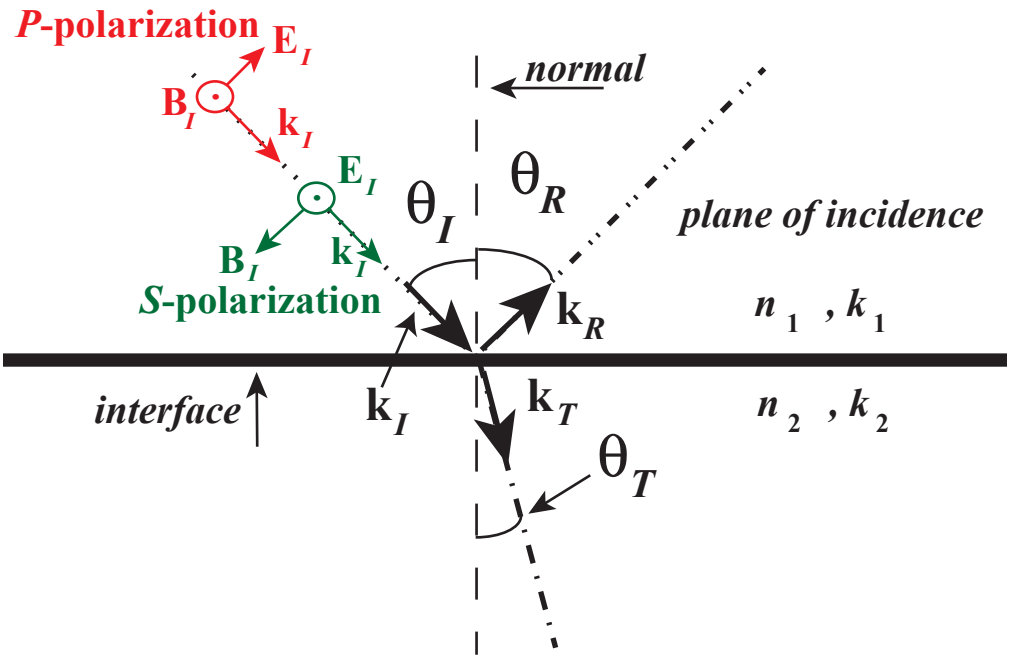

Figure 2.2: An electromagnetic plane wave incident on a boundary separating two media. The media have indices of refraction, n_j, and frequency dependent wave numbers, $k_j(\omega)$, where j refers to medium 1 or 2. The thick black horizontal line is the interface, and the dashed line orthogonal to the interface is the normal. The incoming wave makes an angle θ_I, the reflected wave makes an angle θ_R, and the transmitted wave makes an angle θ_T, all with respect to the normal. All wave vectors lie in the same plane, called the plane of incidence. Two orientations of an incoming wave are shown. The red orientation is a P-polarized wave, and the green orientation is an S-polarized wave.

derived in Appendix A for S-polarization and normal incidence as [38, Eq. (18)],

$$t = \frac{2\mu_2 k_1}{\mu_2 k_1 + \mu_1 k_2}, \tag{2.36}$$

$$r = \frac{\mu_2 k_1 - \mu_1 k_2}{\mu_2 k_1 + \mu_1 k_2}, \tag{2.37}$$

and for P-polarization as [38, Eqs. (22) and (23)],

$$t = \frac{2\epsilon_1 k_1}{\epsilon_1 k_1 + \epsilon_2 k_2}, \tag{2.38}$$

$$r = \frac{\epsilon_1 k_1 - \epsilon_2 k_2}{\epsilon_1 k_1 + \epsilon_2 k_2}. \tag{2.39}$$

See Equations (A.129–A.130), and Equations (A.150–A.151) for derivations. The Fresnel coefficients for the two layer medium can be used to derive the coefficients of reflection and transmission for a three-layer medium, for instance the film of a soap bubble in air. This is presented in Appendix A, and is used in the section on evanescent wave amplification.

2.2.4 Waveguides

All experiments were performed inside of a waveguide, and the electromagnetic field equations are different inside of a waveguide compared to free space. For instance, in free space, there is no longitudinal component to the electric or magnetic fields [54, p. 379]; however in a waveguide, the boundary conditions require that such a component exists. For the rectangular waveguides used in this experiment, it is convenient to reduce the equations for the electromagnetic fields into longitudinal

and transverse field components, for example, $\mathbf{E} = \mathbf{E}_T + \mathbf{E}_Z$, where $\mathbf{E}_T$ is the applied transverse electric field and $\mathbf{E}_Z$ is the applied longitudinal electric field. The equation for the magnetic field is similar, $\mathbf{B} = \mathbf{B}_T + \mathbf{B}_Z$. For the $\mathbf{E}$ and $\mathbf{B}$ examples just given, the z-axis is aligned with the waveguide axis, that is, the longitudinal component. The $x-y$ plane is considered to be the cross-section of the waveguide, and is referred to in this dissertation as the transverse plane. The type of wave admitted in the waveguide is determined by the longitudinal component. For instance, for the experiments presented in this dissertation, the lowest order waveguide mode is a transverse electric (TE) mode, where $\mathbf{E}_Z = 0$ [1, p. 359].

If a normal to the interface of a conducting wall of the waveguide, and the dielectric filling the waveguide, vacuum or otherwise, is a unit vector labeled $\hat{\mathbf{n}}$ pointing from the conductor into the dielectric, as in Figure (2.3), then the relevant boundary conditions are [1, p. 353, Eq. (8.3)],

$$\hat{\mathbf{n}} \times \mathbf{E} = 0, \tag{2.40}$$

$$\hat{\mathbf{n}} \cdot \mathbf{B} = 0. \tag{2.41}$$

Thus, normal components of $\mathbf{B}$ and tangential components of $\mathbf{E}$ must be continuous as the boundary is traversed, and for a perfect conductor, these components must be zero at the boundary. This assumes that there was no magnetic field to begin with, as the magnetic field inside a perfect conductor is constant, and not necessarily zero, and inside of a perfect conductor, $\mathbf{E} = 0$ [54, p. 405, Eq. (9.175)]. The normal component of $\mathbf{D}$ and the tangential components of $\mathbf{H}$ at the interface are not necessarily zero. These values differ from zero by the free surface charge of the

conductor, Σ_f, and the free surface current, $\mathbf{K}_f$, such that [1, p. 352, Eq. (8.1) and p. 353, Eq. (8.2)],

$$\hat{\mathbf{n}} \cdot \mathbf{D} = \Sigma_f, \tag{2.42}$$

$$\hat{\mathbf{n}} \times \mathbf{H} = \mathbf{K}_f. \tag{2.43}$$

For the transverse electric mode of a waveguide, the condition that $E_z = 0$ holds everywhere, while for the transverse magnetic mode, $B_z = 0$ everywhere [1, p. 359]. For $E_z = 0$ and $B_z = 0$, the mode is said to be transverse electromagnetic [1, p. 358]. To solve for the fields inside of a waveguide, the transverse components are written in terms of the longitudinal components, B_z and E_z, as done in Appendix A. The solution is then reduced to solving the Helmholtz equations, Equations (2.7) or (2.8), depending on the type of mode admitted. For this dissertation, the transverse electric mode is used, $E_z = 0$, and so the fields inside the waveguide are found from [1, p. 361, Eq. (8.41)],

$$\left(\frac{\partial^2}{\partial x^2} + \frac{\partial^2}{\partial y^2} + \left(\frac{\omega \sqrt{\epsilon \mu}}{c} \right)^2 - k^2 \right) B_z = 0. \tag{2.44}$$

The solution to Equation (2.44), found by the separation of variables method, is [1, p. 361, Eq. (8.42)],

$$B_{mn,z} = B_{mn,0} \cos\left(\frac{m\pi x}{a} \right) \cos\left(\frac{n\pi y}{b} \right) e^{i(k_{mn} z - \omega t)}, \quad m, n = 0, 1, 2, ..., \tag{2.45}$$

where the positive integers m and n refer to the mode of the electromagnetic wave, and k is understood to be k_z, where the z subscript was dropped for future clarity. These transverse electric modes are called TE_{mn} modes. The wave number is shown

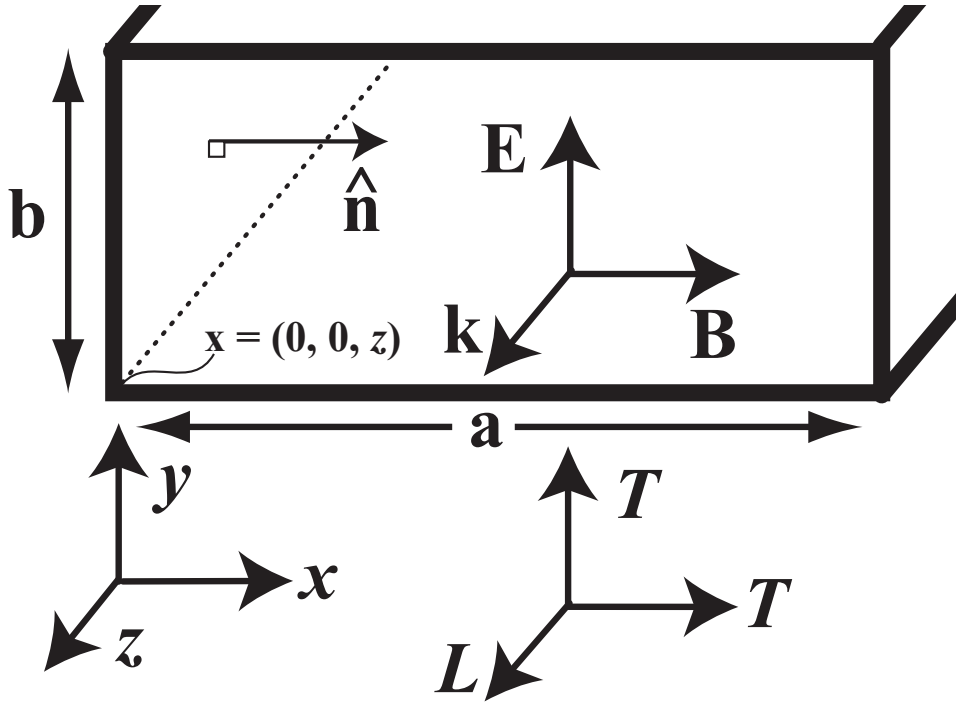

Figure 2.3: Geometry of a slice of the transverse plane of a metallic waveguide that extends to $\pm\infty$ along the z-direction. The dimension b is the length of the narrow-side walls, while a is the length of the broad-side walls. The unit vector $\hat{\mathbf{n}}$ points from the conductor into the waveguide for each wall. The TE_{10} mode is shown with the wave vector pointing along the z-direction. The waveguide axes are shown at the bottom left, and at the bottom right are the labels of transverse (T) and longitudinal (L) with respect to the waveguide axes. The position of the inside edge at some arbitrary location along the longitudinal length of the waveguide is labeled as $\mathbf{x} = (0,\ 0,\ z)$.

Table 2.1: Cutoff frequencies for a vacuum-filled X-band waveguide for the first five TE modes.

Mode	TE_{10}	TE_{20}	TE_{01}	TE_{11}	TE_{30}
$\omega_{c,mn}/2\pi$ (GHz)	6.562	13.123	14.764	16.156	19.685

in Appendix A to be [1, p. 360, Eq. (8.37) with Eq. (8.43)],

$$k_{mn}^2 = \left(\frac{\omega\sqrt{\mu\epsilon}}{c}\right)^2 - \left(\frac{m\pi}{a}\right)^2 - \left(\frac{n\pi}{b}\right)^2. \tag{2.46}$$

Immediately from Equation (2.46), it is noticed that values of ω for which [1, p. 362, Eq. (8.44)],

$$\omega_{mn} \leq \frac{c\pi}{\sqrt{\mu\epsilon}}\sqrt{\left(\frac{m}{a}\right)^2 + \left(\frac{n}{b}\right)^2}, \tag{2.47}$$

will make the right side of Equation (2.46) less than zero, and thus k will be imaginary. These values of ω_{mn} correspond to evanescent modes, and the frequency for which the equality holds in Equation (2.47) is called the cutoff frequency [1, p. 362]. Table (2.1) lists the cutoff frequencies of a vacuum-filled X-band waveguide, with $a = 22.86$ mm and $b = 10.16$ mm, for the first five TE modes.

Note that the dispersion relation for a waveguide, rewritten as [1, p. 360, Eq. (8.39)],

$$(kc)^2 = \omega^2 - \omega_{c,mn}^2, \tag{2.48}$$

looks very similar to the plasma frequency of a lossless plasma [1, p. 313, Eq. (7.61)],

$$(kc)^2 = \omega^2 - \omega_p^2. \tag{2.49}$$

Thus, an empty waveguide below the lowest cutoff frequency can be thought of as a plasma with a negative permittivity [79]. This is investigated in Chapter 4. It is also worth noting that from Equation (2.46), the wave number inside a waveguide is modified compared to a wave number in free space. This is also true of the wavelength, and inside of the waveguide, the wavelength of an electromagnetic wave is referred to as the guide wavelength. Take the TE_{10} mode, for instance, with the longitudinal axis of the vacuum-filled waveguide aligned the with z-axis, as in Figure (2.3). Then, from Equation (2.46), the wave number is,

$$k_z^2 = \left(\frac{\omega}{c}\right)^2 - \left(\frac{\pi}{a}\right)^2. \tag{2.50}$$

The guide wavelength, λ_g is equal to [76, p. $24-5$],

$$\lambda_g = \frac{2\pi}{k_z} \tag{2.51}$$

$$= \frac{2\pi}{\sqrt{(\omega/c)^2 - (\pi/a)^2}} \tag{2.52}$$

$$= \frac{2\pi c/\omega}{\sqrt{1-(\pi c/a\omega)^2}}. \tag{2.53}$$

If the free-space wavelength, λ_0, is defined as [76, p. $24-5$],

$$\lambda_0 \stackrel{def}{=} \frac{2\pi c}{\omega}, \tag{2.54}$$

then Equation (2.53) becomes [76, p. $24-5$, Eq. (24.19)],

$$\lambda_g = \frac{\lambda_0}{\sqrt{1-(\lambda_0/2a)^2}}. \tag{2.55}$$

The guide wavelength in Equation (2.53) approaches infinity as the frequency approaches the cutoff frequency of the waveguide, and this implies that the wave number approaches zero since $\lambda = 2\pi/k$. For imaginary values of the guide wavelength, there will be an associated imaginary value for the wave number. Thus, for frequencies less than the cutoff frequency, the wave number is imaginary, and the waveguide mode is evanescent, while for frequencies greater than the cutoff frequency, the waveguide mode is propagating. This was already implied in Equation (2.46).

Rewriting Equation (2.46) as [80, p. 182, Eq. (37a)],

$$k^2 = \frac{\mu\epsilon\omega^2}{c^2} - k_{c,mn}^2, \tag{2.56}$$

where,

$$k_{c,mn}^2 = \left(\frac{m\pi}{a}\right)^2 + \left(\frac{n\pi}{b}\right)^2, \tag{2.57}$$

then if the waveguide is filled with vacuum so that $\epsilon = \mu = 1$, then the frequency, ω_o, for which $k(\omega_o) = 0$ is,

$$\omega_o^2 = k_{c,mn}^2 c^2, \tag{2.58}$$

where ω_o in this case is equal to the cutoff frequency, $\omega_{c,mn}$. However, if a dielectric now fills the waveguide, with $\mu = 1$, Equation (2.58) becomes,

$$\omega_o^2 = \frac{k_{c,mn}^2 c^2}{\epsilon} = \frac{\omega_{c,mn}^2}{\epsilon}. \tag{2.59}$$

Thus, the observed cutoff frequency for a dielectric filled waveguide is less than the cutoff frequency for the mode, $\omega_{c,mn}$, assuming $\epsilon > 1$.

Suppose now that the dielectric medium filling the waveguide is a plasma with $\gamma = 0$ in Equation (2.22), and with $\mu = 1$, then plugging Equation (2.22) into Equation (2.59) yields,

$$\omega_o^2 = \frac{k_{c,mn}^2 c^2}{\epsilon(\omega_o)} \tag{2.60}$$

$$= \omega_{c,mn}^2 \frac{\omega_o^2}{\omega_o^2 - \omega_p^2}, \tag{2.61}$$

which can be solved for the observed cutoff frequency, ω_o,

$$\omega_o = \sqrt{\omega_p^2 + \omega_{c,mn}^2}. \tag{2.62}$$

Thus, the observed cutoff frequency, ω_o, will be equal the the plasma frequency of the plasma filling the waveguide, ω_p, and the cutoff frequency of the mode, $\omega_{c,mn}$, added in quadrature.

In order to determine the transverse electric and magnetic fields inside the waveguide in Figure (2.3), the transverse electric and magnetic field components are written in terms of the longitudinal electric and magnetic field components, as done in Equations (A.21), (A.23), (A.24), and (A.25) in Appendix A. For the TE_{10} mode, the longitudinal electric field is zero everywhere, and the longitudinal magnetic field is given by Equation (2.45), with $m = 1$ and $n = 0$. The transverse fields are then found by plugging Equation (2.45), with $m = 1$ and $n = 0$ into Equations (A.21), (A.23), (A.24), and (A.25) in Appendix A, and are found to

be [1, p. 362, Eq. (8.46)],

$$B_z = B_0 \cos\left(\frac{\pi x}{a}\right) e^{i(k_{10}z-\omega t)}, \tag{2.63}$$

$$B_x = -\frac{k_{10}ai}{\pi} B_0 \sin\left(\frac{\pi x}{a}\right) e^{i(k_{10}z-\omega t)}, \tag{2.64}$$

$$E_y = \frac{\omega ai}{\pi} B_0 \sin\left(\frac{\pi x}{a}\right) e^{i(k_{10}z-\omega t)}. \tag{2.65}$$

These equations show that the longitudinal magnetic field is maximum at the walls of the waveguide, and zero in the center, while the opposite is true of the transverse magnetic field, and the transverse electric field. These field structures will be exploited when the bianisotropic nature of the split-ring resonators is investigated in Chapter 5, and a plot of these field structures is given in Figure (A.1), in Appendix A.

2.3 Negative index of refraction

Refraction was discussed in Section 2.2.3, and while no explicit values were used, the angle of refraction is generally positive, due to a positive index of refraction. This was shown pictorially as the dotted line in Figure (1.1) in Chapter 1. However, suppose that the index of refraction is negative. This case was shown as the dash–dot line in Figure (1.1) in Chapter 1, along with many consequences, such as flat slab focusing, in Figure (1.2).

The next three sections of this chapter are concerned with a medium that possesses a negative index of refraction. First, the general mathematics of obtaining a negative index of refraction from a medium possessing a negative permittivity and a negative permeability is presented. The next two sections present methods

of obtaining a negative permittivity from an array of metallic wires, and a negative permeability from an array of split-ring resonators. A discussion follows on the experimental realization of a negative index of refraction from a medium made of arrays of split-ring resonators inserted between rows of an array of metallic wires.

2.3.1 Mathematics of negative index of refraction

Suppose that in Figure (1.1), $n_2 = -1$, and $n_1 = 1$, and the angle of incidence is $\theta_I = \pi/6$. Since sine is an odd function [81, p. 43, Eq. (12.28)], that is, $\sin(-x) = -\sin(x)$, it follows from Equation (2.35) that $\theta_T = -\pi/6 < 0$. This is interpreted as an angle measured from the same side of the normal as the angle of incidence, as is shown in Figure (1.1). In that figure, the positively-refracted wave makes an angle $\theta_{T,p}$ with respect to the normal of the interface, while the negatively-refracted wave makes an angle $\theta_{T,n}$ with respect to the normal of the interface.

One method of obtaining a value of the index of refraction less than zero is by manipulating the permittivity and permeability of an artificial medium. The permittivity and permeability can be written as complex quantities,

$$\epsilon = |\epsilon| e^{i\alpha}, \tag{2.66}$$

$$\mu = |\mu| e^{i\beta}. \tag{2.67}$$

Here, the imaginary part is related to the losses, and for a passive material, the permittivity and permeability are restricted to the upper-half complex plane [1, p. 310]. When multiplying the permittivity and permeability, the angles add, giving,

$$n^2 = |\epsilon||\mu| e^{i(\alpha+\beta)}. \tag{2.68}$$

When taking the square root, a branch cut must be defined, due to the multi-valued nature of the solutions of the complex square root function. It is typically defined to be the negative real axis, in the complex plane. Thus, angles are measured as positive in the upper-half complex plane, and negative in the lower-half complex plane. The original angles were in the upper-half complex plane by definition, however, upon adding the two angles, it is possible that the new angle, that is, $\alpha + \beta$, is larger than π, and therefore crossed the branch. This is not a problem, but must be considered after taking the square root.

The square root of a complex number takes the square root of the magnitude, and divides the angle in half. The direction of dividing the angle in half is always towards an angle of zero, such that the branch is not crossed. In other words, the division is clockwise in the upper-half complex plane, and counter-clockwise in the lower-half complex plane. For any complex number written as, for unit length, $z = \exp i\theta$, the square root must be written as [82, p. 29, Eq. (1.4–12)],

$$z^{1/2} = \exp i(\theta/2 + j\pi), \quad j \in \mathbb{Z}. \tag{2.69}$$

The reason for the addition of $j\pi$ is that squaring the solution of the square root, that is, Equation (2.69), yields the same solution for $j = 0$ and $j = 1$. In other words, for $j = 0$,

$$\begin{aligned} \left(z^{1/2}\right)^2 &= \left(e^{i(\theta/2+0\pi)}\right)^2 && (2.70) \\ &= e^{i\theta}, && (2.71) \end{aligned}$$

while for $j = 1$,

$$\left(z^{1/2}\right)^2 = \left(e^{i(\theta/2+1\pi)}\right)^2 \tag{2.72}$$

$$= e^{i(\theta+2\pi)} \tag{2.73}$$

$$= e^{i\theta}. \tag{2.74}$$

Only $j = 0$ and $j = 1$ are used in Equation (2.69), since any other integer is a 2π addition. In other words, suppose that $j = n$, where n is even. Then $n = 2m$, where m can be even or odd. Equation (2.69) then becomes,

$$e^{i(\theta/2+2m\pi)} = e^{i(\theta/2+0\pi+2m\pi)} \tag{2.75}$$

$$= e^{i(\theta/2+0\pi)}\left(e^{i2\pi m}\right) \tag{2.76}$$

$$= e^{i(\theta/2+0\pi)}. \tag{2.77}$$

Similarly, for j odd, $j = n+1$, where n is defined the same as for Equations (2.75)–(2.77), and,

$$e^{i(\theta/2+1\pi+2m\pi)} = e^{i(\theta/2+1\pi)}\left(e^{i2\pi m}\right) \tag{2.78}$$

$$= e^{i(\theta/2+1\pi)}. \tag{2.79}$$

Thus, when taking the square root of a complex function, only the integers $j = 0$, 1 are considered, since any other integer is a redundant solution. Note that in this case, $\exp ij\pi = \pm 1$, where the positive sign is taken for $j = 0$, and the negative sign taken for $j = 1$. The solution to Equation (2.68) is then,

$$n = \sqrt{|\epsilon||\mu|}e^{i[(\alpha+\beta)/2+j\pi]} = \pm\sqrt{|\epsilon||\mu|}e^{i(\alpha+\beta)/2} \tag{2.80}$$

Since we are restricted to the upper-half complex plane, the value of j that places the final answer, n, into upper-half complex plane is chosen.

In order to calculate the index of refraction for a purely real and negative permittivity and permeability, a small amount of loss is introduced and the limit of zero loss is taken at the end of the calculation. Let,

$$\epsilon = \mu = e^{i(\pi-\delta)}, \tag{2.81}$$

where $0 < \delta \ll 1$. Upon taking,

$$n^2 = \epsilon\mu = e^{i2(\pi-\delta)} = e^{-i2\delta}, \tag{2.82}$$

the angle, -2δ, is in the lower-half complex plane. The square root cuts this angle in half, and in order to place the solution in the proper half of the complex plane due to the physics of a dissipative medium [1, p. 310], the solution for $j = 1$ is taken, so that, $n = \exp i(\pi - \delta)$. In the limit that there are no losses, that is, $\delta \to 0$, the solution for the index of refraction for a medium with purely real, negative, and loss-less permittivity and permeability is $n = \exp i\pi = -1$.

The physical problem now becomes how to construct such a medium. Since the permittivity and permeability are frequency dependent, it may be possible to artificially construct two media such that the permittivity of one medium is negative, while the permeability of the other is negative, over similar frequency ranges. While many prescriptions exist for creating a frequency range, or frequency bandwidth, of negative permittivity and negative permeability, this dissertation follows previous experiments in using an array of metallic wires to create a large frequency

bandwidth of negative permittivity, and split-ring resonators to create a more narrow frequency bandwidth of negative permeability. These two methods are now discussed, beginning with the array of metallic wires.

2.3.2 Theory of a metamaterial metallic wire array

Metallic wire arrays were used as artificial materials in experiments since at least the CE 1940s, as discussed in Chapter 1. At that time, they were used to simulate a plasma in the absence of a magnetic field, for the purpose of aerospace engineering applications [28]. In CE 1996, J. B. Pendry, A. J. Holden, W. J. Stewart, and I. Youngs, exploited the plasmalike properties in order to reduce the plasma frequency of a metal from the ultraviolet frequency range, to the gigahertz frequency range [34, 35]. The group describes taking a solid piece of metal, for example, aluminum, and carving out chunks of the metal until a three dimensional array of thin metallic wires remains. If the wavelength of the incident electromagnetic radiation is larger than the associated spacing, called the lattice parameter, and diameter of the metallic wires, then the metallic wire mesh may behave like a homogeneous medium. Effective medium parameters, such as an effective permittivity, can then describe the metallic wire medium.

The Pendry group begins the calculation by considering an array of metallic wires, with radius r, aligned with the z-axis, spaced at regular intervals of a in the $x-y$ plane, as in Figure (2.4). They then proceed to create a mesh of squares in the $x-y$ plane, such that each square is centered on a metallic wire, and the length of an

edge is equal to the lattice parameter, a. These squares are the individual domains of their respective metallic wires, however, since the magnetic field of a metallic wire with current flowing through it will be azimuthal, it would be more convenient for the domains to also be circular. The Pendry group reforms the domains to contain the same area as the squares, but to be in the shape of a circle with radius $R_c = a/\sqrt{\pi}$. They state that [35] "[a]t any given point in the $x - y$ plane the magnetic field only has contributions from the circle inside whose circumference it lies." However, there is no mention of the overlap of the circles, which is clear in Figure (2.4).

The calculation considers a longitudinal plasmonic excitation traveling along the length of the metallic wires. This is written as [35, Eq. (16)],

$$\mathbf{D} = \mathbf{D}_0 e^{i(kz-\omega t)}, \tag{2.83}$$

where $\mathbf{D}_0$ is a constant amplitude vector pointing along the z-axis. Equation (2.83) has the constraint that the wavelength is much larger than the lattice parameter. This plasmonic excitation presumably has arisen due to an external electric field excitation, for example, an electromagnetic wave traveling along the x-axis, and polarized along the z-axis. This excitation creates a current density, j, in the wires that gives rise to a magnetic field. It is at this point where the Pendry group uses the boundaries for each metallic wire, stated earlier. In each circle domain, a magnetic field is present due only to the metallic wire that lies within the circumference of

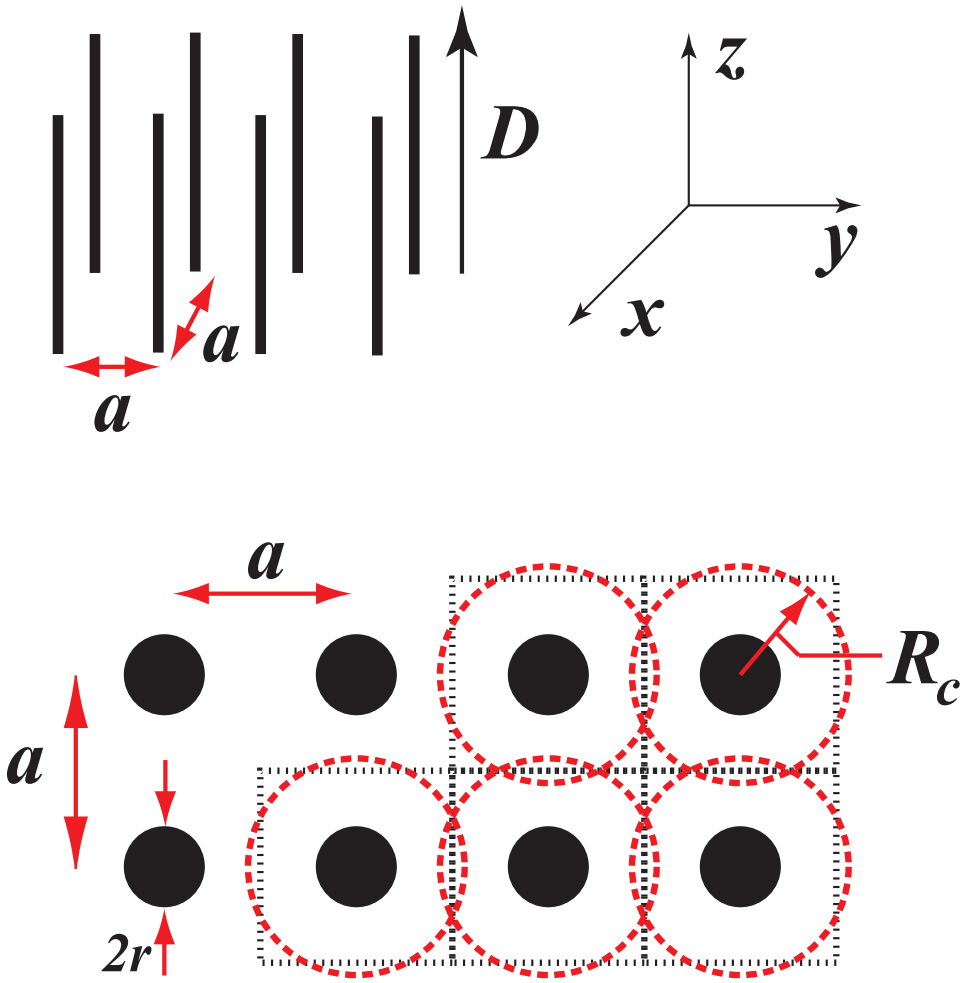

Figure 2.4: Setup for the derivation of Pendry's metallic wire array. *Top*: The geometry of the problem. The metallic wires extend to infinity in the $\pm z$-direction, and there are an infinite number of metallic wires orthogonal to the $x-y$ plane, with a lattice parameter of a in both the $\pm x$ and $\pm y$-directions. The electric displacement of the plasmonic excitation is shown. *Bottom*: A slice of the $x-y$ plane of the top figure. The radius of the metallic wires is shown, and equal to r. The dashed squares with edge length a are the original domain mesh, while the dashed circles are the perturbed boundary, with a radius $R_c = a/\sqrt{\pi}$.

the circle domain. This field is written in terms of the H field as [35, Eq. (20)],

$$H_c(\rho) = \begin{cases} \frac{j}{2\pi\rho} - \frac{j\rho^2}{2\pi\rho R_c^2} & \text{for } 0 < \rho < R_c \\ 0 & \text{for } \rho > R_c \end{cases}, \tag{2.84}$$

where ρ is the distance from the (assumed infinitely thin) metallic wire to a point in the $x-y$ plane. Equation (2.84) differs from the typical equation for the magnetic field due to a current carrying metallic wire in order to have the field vanish at the boundary of the circle within which the metallic wire lies.

Exploiting the use of a magnetic vector potential, the Pendry group states that in [35] "classical mechanics, electrons in a magnetic field have an additional contribution to their momentum, $e\mathbf{A}$..." However, this deserves more attention, as a distinction between mechanical and canonical momentum must be made. For a particle in the absence of a velocity dependent force, the mechanical and canonical momentum are equal. However, since the force from a magnetic field is velocity dependent, the mechanical and canonical momentum are not equal for a charged particle, and the difference between the mechanical and canonical momentum is equal to $e\mathbf{A}$ [83, p. 335, footnote]. Suppose a single, charged particle is traveling in the presence of static magnetic and electric fields, pointing in arbitrary directions. The Lagrangian, $\mathcal{L}$, is written as [83, p. 55],

$$\mathcal{L} = \sum_i \left(\frac{1}{2} m x_i^2 - q\phi(x_i) + q\mathbf{A}(x_i) \cdot \dot{\mathbf{x}}_i \right), \tag{2.85}$$

where m is the mass, x is the position, $\dot{x}$ is the velocity, q is the charge, ϕ is the electric potential, $\mathbf{A}$ is the magnetic vector potential, and the subscript i is summed over each axis. The generalized momentum conjugate to a particular coordinate, x_i,

which is also known as the canonical momentum, is given by the partial derivative with respect to the coordinate velocity [83, p. 55, Eq. (2.45)],

$$p_{x_i} \overset{def}{=} \frac{\partial L}{\partial \dot{x}_i} = m\dot{x}_i + qA_{x_i}. \tag{2.86}$$

Here, $m\dot{x}_i$ is the mechanical momentum, and qA_{x_i} is the additional contribution to the canonical momentum. The Pendry group associates $q\mathbf{A}$ with an effective mass times velocity in order to obtain a large mass for the plasmons in the metallic wire array.

Before writing down this effective mass, the magnetic vector potential is found by using [1, p. 180, Eq. (5.27)],

$$\mathbf{B} = \nabla \times \mathbf{A}, \tag{2.87}$$

and Equation (2.6) with $\mu = \mu_0$, which leads to [35, Eq. (21)],

$$A_c(\rho) \;=\; \begin{cases} \frac{\mu_0 j}{2\pi}\left[\ln(\frac{\rho}{R_c}) - \frac{\rho^2 - R_c^2}{2R_c^2}\right] & \text{for } 0 < \rho < R_c \\ 0 & \text{for } \rho > R_c \end{cases}. \tag{2.88}$$

Note that the magnetic vector potential, $\mathbf{A}$, points parallel to the metallic wire, along the $+z$-axis. Exploiting the definition of R_c in terms of the lattice parameter [35, Eq. (19)], the vector potential at the surface of a metallic wire is given by [35, Eq. (22)],

$$A_c(\rho = r) = \frac{\mu_0 j}{2\pi}\left[\ln\left(\frac{r\sqrt{\pi}}{a}\right) - \frac{\pi r^2}{2a^2} + \frac{1}{2}\right]. \tag{2.89}$$

In order to use this equation to derive the new mass of the electrons, the Pendry group rewrites the current density as* $\pi r^2 nve$, and substitutes this into Equa-

*Note that this is dimensionally a current, *not* a current density. It is the belief of the author of

tion (2.89) [35, Eq. (7)],

$$A_c(r) = \frac{\mu_0 \pi r^2 nve}{2\pi} \left[\ln\left(\frac{r\sqrt{\pi}}{a}\right) - \frac{\pi r^2}{2a^2} + \frac{1}{2} \right], \tag{2.90}$$

where v is the mean electron velocity in the metallic wire, n is the number density of electrons, r is the metallic wire radius, and e is the charge of an electron. The "momentum" per unit length at the metallic wire radius is written as [35, Eq. (8)],

$$e\pi r^2 n A(r) = \frac{\mu_0 e^2 v (\pi r^2 n)^2}{2\pi} \left[\ln\left(\frac{r\sqrt{\pi}}{a}\right) - \frac{\pi r^2}{2a^2} + \frac{1}{2} \right] = m_{\text{eff}} v n \pi r^2, \tag{2.91}$$

where the effective mass of the electrons, m_{eff}, is written as [35, Eq. (9)],

$$m_{\text{eff}} = \frac{\mu_0 e^2 \pi r^2 n}{2\pi} \left[\ln\left(\frac{r\sqrt{\pi}}{a}\right) - \frac{\pi r^2}{2a^2} + \frac{1}{2} \right]. \tag{2.92}$$

The effective electron density is rewritten to account for the lattice parameter as [35, Eq. (4)],

$$n_{\text{eff}} = n\frac{\pi r^2}{a^2} = nf, \tag{2.93}$$

where n is the actual electron density in the metallic wires, and,

$$f \stackrel{def}{=} \pi r^2 / a^2, \tag{2.94}$$

is the filling fraction, or volume fraction, of the metallic wires. The plasma frequency is derived to be [35, Eq. (12)],

$$\omega_p^2 = \frac{n_{\text{eff}} e^2}{\epsilon_0 m_{\text{eff}}} = \frac{2\pi c^2}{a^2 [\ln(\frac{r\sqrt{\pi}}{a}) - \frac{\pi r^2}{2a^2} + \frac{1}{2}]}, \tag{2.95}$$

this dissertation that throughout the Pendry group's derivation of the magnetic vector potential, **A**, the current, and not the current density, was meant by j.

where $c^2 = 1/\mu_0\epsilon_0$. Although the expression for the magnetic vector potential was derived for an essentially one-dimensional case, the result is applied to a three-dimensional array of metallic wires, which implies that for oblique incidence, only the metallic wires that are parallel to components of the applied electric field will couple to the applied electric field.

There are some issues of the Pendry group's derivation that arise, including the appropriate use of the magnetic vector potential. These issues were raised by R. M. Walser, A. P. Valanju, and P. M. Valanju in Reference [53], and were discussed in Chapter 1. There is more discussion of their objections, as well as a correction to a missing minus sign in Equation (2.90), in Appendix A.

2.3.3 Negative permeability with metallic split-cylinders

The preceding section dealt with experimentally obtaining a negative permittivity with an artificial material made of metallic wires. In that case, the electric field coupled to the metallic wires, and the structure of the metallic wire array appeared as a cold plasma to the applied electric field. In order to create an artificial material with a negative permeability, the magnetic field must couple to the structure. A large diamagnetic response is necessary in order to create a large and negative magnetic susceptibility, defined in Equation (2.30). While an array of metallic wires may be used to generate magnetic plasmons [84], Lenz's law will be exploited to generate a negative permeability.

In CE 1999, Pendry, Holden, Robbins, and Stewart, showed that an infinite

array of infinitely long metallic cylinders with their axes parallel to an applied ac H field will decrease the effective permeability by the filling fraction, f, assuming no losses [37, Eq. (13)],

$$\mu(\omega) = 1 - f, \tag{2.96}$$

with f defined in a similar manner as in the case of the metallic wire arrays, Equation (2.94), where r is the radius of the metallic cylinders, and a is the lattice parameter of the metallic cylinder array. The solution shows that an artificial material that couples to an applied magnetic field has a diamagnetic response, also stated in Reference [80, p. 510]. In order to introduce a resonant response to the applied H field, a gap is introduced in the circumference of the metallic cylinder [37]. Another metallic cylinder is inserted inside the original metallic cylinder, in order to increase the inductance and capacitance of the array element, which can decrease the resonant frequency of the array element into the gigahertz frequency range. The metallic cylinders are concentric, and both metallic cylinders have gaps in the circumference, however these gaps are aligned 180 degrees apart, as shown in Figure (2.5).

The solution to the metallic split-cylinder problem is detailed in Appendix A. While the specific relations of the parameters to the details of the problem are very complicated, the frequency response of the metallic split-cylinder array in Figure (2.5) is written as [37, Eq. (20)],

$$\mu(\omega) = 1 - \frac{f\omega^2}{\omega^2 - \omega_0^2 + i\Gamma\omega}, \tag{2.97}$$

where ω_0 is the resonant frequency of the metallic split-cylinders, and Γ is the loss parameter. The functional form of Equation (2.97) is shown in Figure (2.6) for $f =$

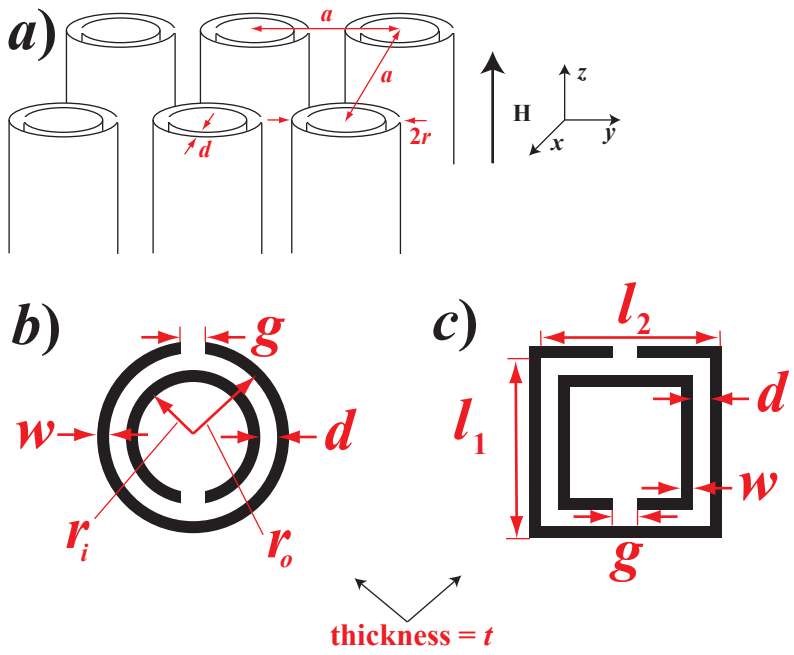

Figure 2.5: Setup for the derivation of the Pendry group's metallic cylinder array. a): The geometry of the problem. The metallic cylinders extend to infinity in the $\pm z$-direction, and there are an infinite number of metallic cylinders orthogonal to the $x-y$ plane, with a lattice parameter of a in both the $\pm x$ and $\pm y$-directions. The separation of concentric metallic cylinders is d, and each metallic cylinder has a gap in the circumference. The H field is shown. b): A slice of a single element of part (a) in the $x-y$ plane, called a split-ring resonator. The inner and outer average radii are r_i and r_o, respectively. The thickness of each metallic sheet making up the cylinder wall is w, while the thickness of the slice is t. The gap width is g. c): The actual split-ring resonator geometry used in this dissertation.

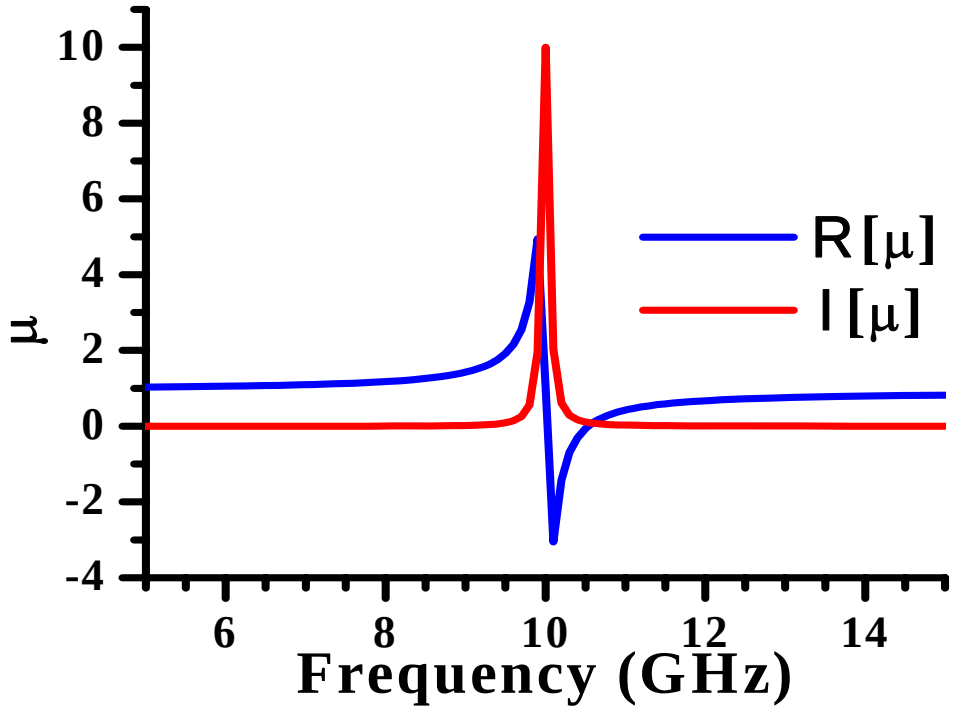

Figure 2.6: A plot of the real part of the permeability, $\Re[\mu]$, shown in blue, and the imaginary part of the permeability, $\Im[\mu]$, shown in red, versus frequency. The values used to generate this plot were $f = 0.1$, $\omega_0 = 2\pi \times 10$ GHz, and $\Gamma = 2\pi \times 0.1$ GHz, in Equation (2.97).

0.1, $\omega_0 = 2\pi \times 10$ GHz, and $\Gamma = 2\pi \times 0.1$ GHz. The imaginary part remains positive for all frequencies, but has a large increase at the resonant frequency. The real part, however, is positive for frequencies immediately below the resonant frequency, but negative at frequencies immediately above the resonant frequency. The second zero-crossing of μ is called the magnetic plasma frequency, ω_{mp}, and in fact, the frequency region of negative permeability is sometimes modeled like a plasma with $\mu \sim 1 - (\omega_{\text{mp}}/\omega)^2$ [38, Eq. (25)].

Figure (2.6) shows that there is a limited bandwidth of frequencies for which the real part of the permeability is less than zero. Thus, an applied electromagnetic

field incident on an array of metallic cylinders described earlier will be propagating up to the resonant frequency. For frequencies between the resonant frequency and magnetic plasma frequency, the electromagnetic waves will be non-propagating. Finally, for frequencies above the magnetic plasma frequency, the electromagnetic waves are once again propagating.

2.3.4 Physical realization of a medium with a negative index of refraction

Specific details of the experimental setup will be given in Chapter 3, but a discussion now follows on how the theories of metallic wires and metallic split-cylinders are used. The plasma frequency in Equation (2.95) was derived for an array of metallic wires with their lengths parallel to the polarization of the electric field of an applied electromagnetic field. This is simple to construct, as ordinary metallic wires made of Cu can be inserted into a styrofoam matrix for support, for instance. For the metallic split-cylinder theory, however, infinite metallic cylinders were used, and these may be difficult to implement, especially along with an array of metallic wires. However, two-dimensional slices of the metallic cylinders, such that the slice is performed orthogonal to the cylindrical axis as in Figure (2.5.b), may be used and still produce the same frequency response as Equation (2.97). These slices are referred to as split-ring resonators, and were used in this dissertation.

In order to create an artificial material with a negative real part of the index of refraction, arrays of split-ring resonators are inserted between the rows of the

metallic wire arrays. In fact, the original experiments utilized printed circuit boards with metallic wires on one side, and split-ring resonators on the other side [41]. This orientation allows complete coupling to a transverse electromagnetic mode, as long as the wave vector lies in the plane of the split-ring resonator. Since there is a limited frequency bandwidth where the real part of the permeability is less than zero with the split-ring resonator array, as opposed to the metallic wire array with a larger frequency bandwidth where the real part of the permittivity is less than zero, the frequency bandwidth where the real part of the index of refraction is less than zero is largely dictated by the split-ring resonators. Any interaction between the split-ring resonators and the metallic wires will shift the frequency bandwidth where the real part of the index of refraction is less than zero [85]. In other words, for a split-ring resonator resonant frequency occurring less than, but not near, the metallic wire array plasma frequency, the electromagnetic transmission spectra should reveal a frequency bandwidth of little electromagnetic transmission from the negative real part of the permittivity of the metallic wire array but a positive real part of the permeability of the split-ring resonator array, followed by a peak in electromagnetic transmission due to the frequency bandwidth where the real parts of the permeability and permittivity are both negative, followed by another frequency bandwidth of little electromagnetic transmission due to the negative real part of the permittivity but positive real part of the permeability, and finally, the plasma frequency of the metallic wire array where the real parts of the permeability and permittivity are both positive. When the split-ring resonator resonant frequency is near, or even on, the plasma edge of a metallic wire array, the electromagnetic transmission is

slightly more complicated, and there is actually a sharp dip in electromagnetic transmission followed by a sharp peak in electromagnetic transmission, due to the split-ring resonator array. This is reserved for Chapter 6.

2.4 Modeling the Transmission and Reflection of a Waveguide

A question that arises in the preceding sections is how do we know what the electromagnetic transmission spectrum for a medium inside of a waveguide where either the real parts of the permittivity or permeability (or both) are less than zero? Since a waveguide limits the problem to essentially one dimension, a refraction experiment is out of the question. One feature of media with either a negative real part of the permittivity or a negative real part of the permeability is the presence of evanescent waves in the frequency bandwidth for which the real part of the permittivity or permeability is negative. In the case that the real part of both the permittivity and permeability are negative, there will be propagating waves.

In order to fit and model the experiment, a transfer matrix model is used with appropriate values of the permittivity and permeability, assuming a waveguide is present with its ends extending to infinity. Suppose that there are three layers of media inside the waveguide, each layer having its own permittivity and permeability, as in Figure (2.7). While only three layers are shown in Figure (2.7), more layers can be imagined, and the equations for arbitrary layers will be given later. For now, the three-layer model will be discussed. Define the following two matrices [86, Eqs.

(4) and (5)],

$$\underline{\underline{\mathbf{Z}}}_{i,j} = \frac{1}{2Z_j}\begin{pmatrix} Z_j + Z_i & Z_j - Z_i \\ Z_j - Z_i & Z_j + Z_i \end{pmatrix}, \tag{2.98}$$

$$\underline{\underline{\mathbf{T}}}_{i} = \begin{pmatrix} e^{k_i d_i} & 0 \\ 0 & e^{-k_i d_i} \end{pmatrix}, \tag{2.99}$$

where $Z_i \stackrel{def}{=} \sqrt{\mu_i/\epsilon_i}$, d_i is the thickness of the layer, and the subscript, i, refers to a layer. With those definitions, the three-layer transfer matrix of an electromagnetic wave is the solution to the following equation [86],

$$\begin{pmatrix} 1 \\ S_{11} \end{pmatrix} = \underline{\underline{\mathbf{Z}}}_{1,2} \cdot \underline{\underline{\mathbf{T}}}_{2} \cdot \underline{\underline{\mathbf{Z}}}_{2,3} \cdot \begin{pmatrix} S_{21} \\ 0 \end{pmatrix}, \tag{2.100}$$

The solution to this equation, assuming that layers 1 and 3 are vacuum and therefore $\epsilon = \mu = 1$, is given by [87, Eqs. (3) and (4)],

$$S_{21} = \frac{(1-\Xi^2)\xi}{1-\Xi^2\xi^2}, \tag{2.101}$$

$$S_{11} = \frac{(1-\xi^2)\Xi}{1-\Xi^2\xi^2}, \tag{2.102}$$

where,

$$\xi = \exp(ik_2 d_2), \tag{2.103}$$

is a transmission coefficient, and Ξ is the reflection coefficient, given by,

$$\Xi \stackrel{def}{=} \frac{\sqrt{\mu_2/\epsilon_2} - 1}{\sqrt{\mu_2/\epsilon_2} + 1}. \tag{2.104}$$

Note that an extension of Equation (2.100) can be made for an arbitrary number of

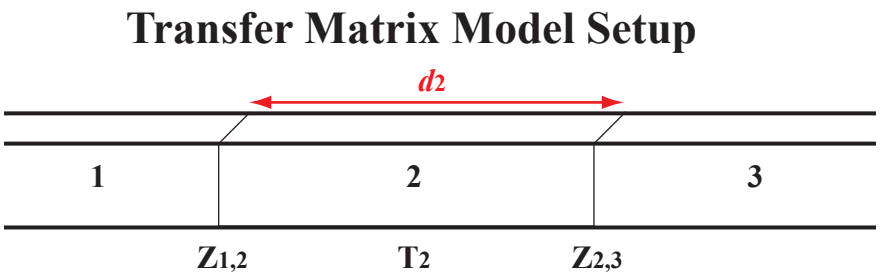

Figure 2.7: Setup of the three-layer transfer matrix model inside a waveguide. The layers are labeled 1, 2, 3, with the associated impedance matrix, Z_{ij}, and transmission matrix, T_k, where $i,\ j,\ k$ refer to a specific layer. Layers 1 and 3 extend to infinity, while layer 2 has thickness d_2.

N layers by [86, Eqs. (4) and (5)],

$$\begin{pmatrix} 1 \\ \\ S_{11} \end{pmatrix} = \underline{\underline{\mathbf{Z}}}_{1,2} \cdot \underline{\underline{\mathbf{T}}}_{2} \cdot \underline{\underline{\mathbf{Z}}}_{2,3} \cdot \underline{\underline{\mathbf{T}}}_{3} \cdot \ldots \cdot \underline{\underline{\mathbf{Z}}}_{m-1,m} \cdot \underline{\underline{\mathbf{T}}}_{m} \cdot \ldots \cdot \underline{\underline{\mathbf{Z}}}_{N-1,N} \cdot \begin{pmatrix} S_{21} \\ \\ 0 \end{pmatrix}, \tag{2.105}$$

where $m < N$ is an integer.

The wave number in Equation (2.103) was already written for a waveguide geometry in Equation (2.99), however a slight modification was made. The new wave vector used in the transfer matrix model is given by, for X-band dimensions with the width of the waveguide, given as $a = 0.02286$ m in Figure (2.3), and for the TE_{10} mode [86, Eq. (12)],

$$k_i = \sqrt{\omega^2 \tilde{\epsilon}_i \tilde{\mu}_i - \left(\frac{\pi}{0.02286}\right)^2 \mu_i}, \tag{2.106}$$

and the impedance is defined as [86],

$$Z_i = \frac{\omega \tilde{\mu}_i}{k_i}, \tag{2.107}$$

where, again, the subscript i denotes the i^{th} layer. Note that plugging Equations (2.106) and (2.107) into Equation (2.100) yield the same result as plugging

the relative permittivity, relative permeability, and wave number directly into Equations (2.101) and (2.102).

The first step is to check that Equation (2.100) accurately replicates the theoretical electromagnetic transmission is to test an empty waveguide setup. This is shown as a blue curve in Figure (2.8). Full electromagnetic transmission, that is, $|S_{21}| = 0$ dB, is observed at approximately 6.5 GHz, which is approximately the cutoff frequency of an X-band waveguide. The electromagnetic transmission values below cutoff appears larger than expected, as will be experimentally shown in Chapter 4, however, the three-layer transfer matrix model appears to accurately model an empty waveguide.

Figure (2.8) also plots, as a green curve, the electromagnetic transmission of the three-layer transfer matrix model with the middle layer filled with a medium with a permittivity given by Equation (2.22), with $\omega_p = 2\pi \times 16$ GHz, and $\gamma = 2\pi \times 0.1$ GHz. Note that there is a large frequency bandwidth of very low electromagnetic transmission between approximately 2 GHz and approximately 15 GHz, as a result of a negative real part of the permittivity within this frequency bandwidth. Also, the frequency of full electromagnetic transmission, that is, $|S_{21}| = 0$ dB, is not at the plasma frequency, $\omega_p = 2\pi \times 16$ GHz. This is due to the imaginary part to the permittivity, and shows that the plasma frequency is not defined as the frequency where $\Re[\epsilon] = 0$, but is rather defined by Equation (2.23). It is expected that an array of metallic wires will produce a similar electromagnetic transmission spectrum, under the constraints stated earlier.

Figure (2.9) shows the electromagnetic transmission of a three-layer transfer

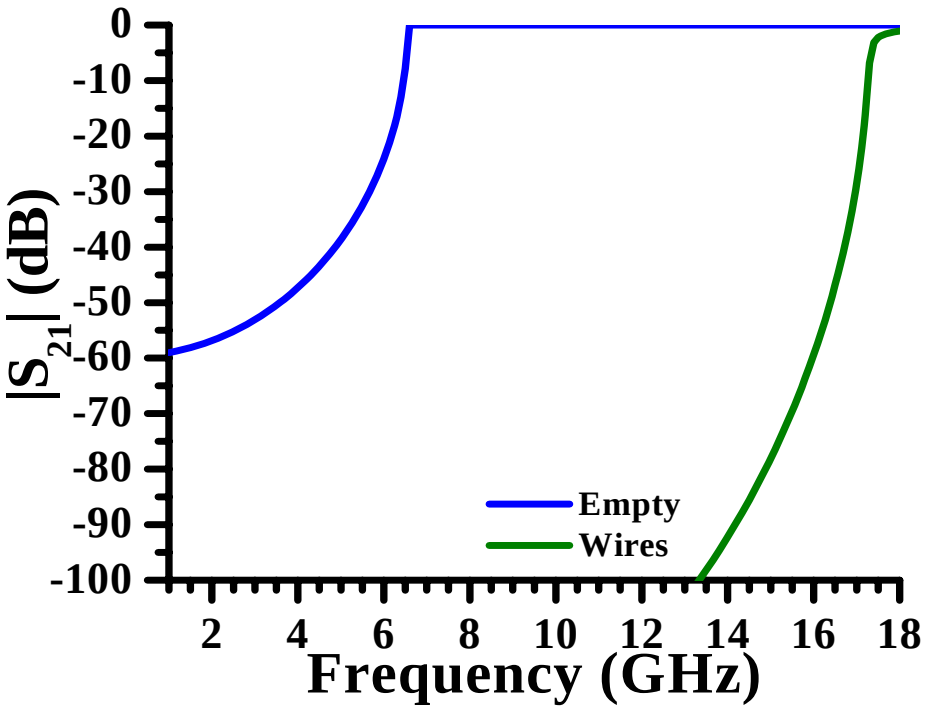

Figure 2.8: Plot of the electromagnetic transmission of the three-layer transfer matrix model for an empty waveguide, shown in blue, and one filled with a material with a permittivity given by Equation (2.22), shown in green, with $\omega_p = 2\pi \times 16$ GHz, and $\gamma = 2\pi \times 0.1$ GHz. The length of the middle layer in the three-layer transfer matrix model was $l = 1$ m.

matrix model loaded with an array of split-ring resonators, shown as the blue curve, with metallic wires, shown as the black curve, and a combination of metallic wires and split-ring resonators, shown as the green curve. The black curve is exactly the same as the green curve in Figure (2.8), and discussed earlier. The blue curve in Figure (2.9) uses a permeability given by Equation (2.97) with $\omega_0 = 2\pi \times 10$ GHz, $f = 0.01$, and $\Gamma = 2\pi \times 0.1$ GHz. Note the sharp dip in electromagnetic transmission centered at 10 GHz. This dip is due to the large increase in the real part of the permeability, and thus a large impedance mismatch, immediately below 10 GHz, while immediately above 10 GHz, the real part of the permeability is less than zero. At approximately 10.5 GHz, the second zero-crossing of the real part of the permeability occurs, and beyond 11 GHz is full electromagnetic transmission, that is, $|S_{21}| = 0$ dB. Also note that up to this resonance, the electromagnetic transmission spectrum is the same as an empty waveguide. These are the expected electromagnetic transmission results of an X-band waveguide loaded with an array of split-ring resonators.

The green curve in Figure (2.9) is the expected electromagnetic transmission results of an X-band waveguide loaded with a medium consisting of both an array of metallic wires, and an array of split-ring resonators. The permittivity used was Equation (2.22), and the permeability used was Equation (2.97), and the parameters in these equations were the same as those given for the green curve in Figure (2.8) and the blue curve in Figure (2.9). Note that the green curve in Figure (2.9) largely follows the same curve as the metallic wire-loaded X-band waveguide, shown as a black curve, except for the frequency bandwidth of 8 GHz to 12 GHz. Within

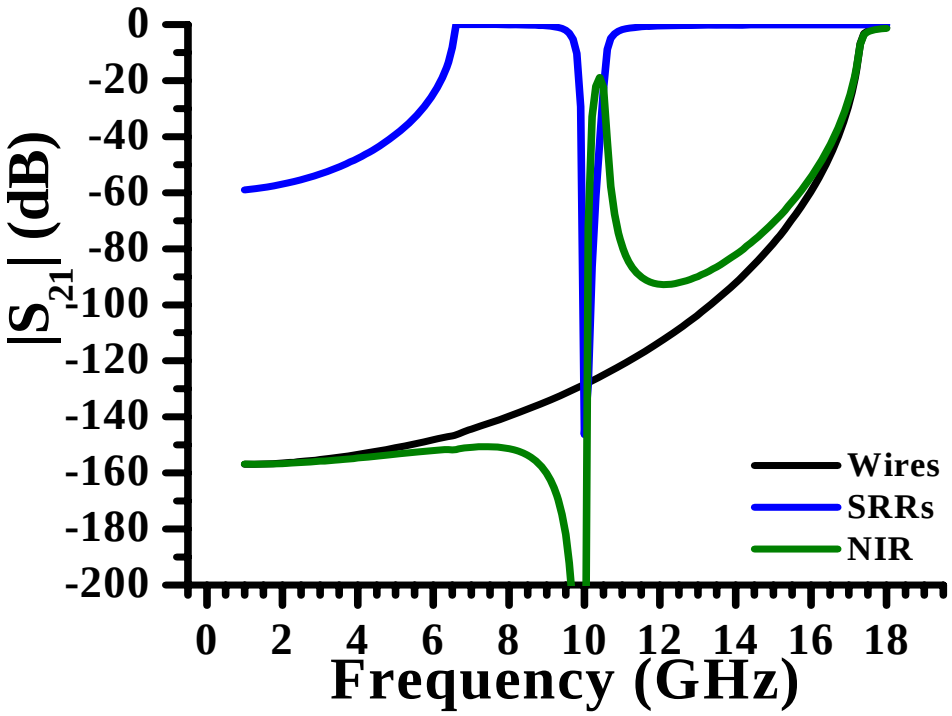

Figure 2.9: Plot of the electromagnetic transmission of the three-layer transfer matrix model for a split-ring resonator loaded X-band waveguide, labeled SRRs, with a permeability given by Equation (2.97) with $\omega_0 = 2\pi \times 10$ GHz, $f = 0.01$, and $\Gamma = 2\pi \times 0.1$ GHz, shown in blue, a metallic wire-loaded X-band waveguide with a permittivity given by Equation (2.22), shown in black, with $\omega_p = 2\pi \times 16$ GHz, and $\gamma = 2\pi \times 0.1$ GHz, and an X-band waveguide with a medium with a negative index of refraction, labeled as NIR, using the aforementioned parameters, shown in green. The length of the middle layer in the three-layer transfer matrix model was $l = 1$ m.

this frequency bandwidth, there is a sharp dip in electromagnetic transmission, followed by a sharp peak in electromagnetic transmission. By the same argument given for the results of the blue curve in Figure (2.9), the sharp dip is due to the large increase in the real part of the permeability, and thus the wave number has a large increase in the imaginary part as well. Since the real part of the permittivity is still less than zero, the electromagnetic transmission must decrease in magnitude. Once the split-ring resonator resonant frequency is crossed, however, the real parts of the permeability and permittivity are both negative, and transmission is possible, and therefore a sharp peak in electromagnetic transmission occurs. The height of this peak in electromagnetic transmission is largely determined by two properties. The first is the values of the permittivity and permeability, and the second is the loss of the system. For zero loss, and $\epsilon = \mu = -1$, the peak should reach $|S_{21}| = 0$ dB. The results of the three-layer transfer matrix model in Figures (2.8) and (2.9) will be tested in each of the experimental chapters, and the three-layer transfer matrix model will be used to fit these experimental results.

2.4.1 Extraction of the permittivity and permeability from the S-parameters

Given the S-parameters, S_{11} and S_{21}, the relative permittivity and permeability may be extracted. Early papers that investigated this include References [87] and [88]. Defining [87, Eq. (5)],

$$X \stackrel{def}{=} \frac{S_{11}^2 - S_{21}^2 + 1}{2S_{11}}, \tag{2.108}$$

the reflection coefficient, Equation(2.104), is given by [87, Eq. (6)],

$$\Xi = X \pm \sqrt{X^2 - 1}, \tag{2.109}$$

where the plus or minus sign is chosen such that $|\Xi| \leq 1$, due to conservation of energy. The transmission factor, Equation (2.103), is given by [87, Eq. (7)],

$$\xi = \frac{S_{11} + S_{21} - \Xi}{1 - (S_{11} + S_{21})\Xi}. \tag{2.110}$$

The extraction proceeds as follows. Defining [87, Eqs. (8) and (9)],

$$h_1 \stackrel{def}{=} \left(\frac{1 + \Xi}{1 - \Xi}\right)^2, \tag{2.111}$$

$$h_2 \stackrel{def}{=} -\left[\frac{c}{\omega d} \ln\left(\frac{1}{\xi}\right)\right]^2, \tag{2.112}$$

where d is the thickness of the medium. The relative permittivity and permeability are then calculated from [87, Eq. (10)],

$$\mu = \sqrt{h_1 h_2}, \tag{2.113}$$

$$\epsilon = \sqrt{\frac{h_2}{h_1}}. \tag{2.114}$$

Since all of the quantities in Equations (2.108) – (2.114) are complex, the branch cuts must be considered. For the square roots in Equations (2.113) and (2.114), the solution to the branch cut is similar to that for the index of refraction discussed earlier. If the imaginary part of either the permittivity or permeability in Equations (2.113) and (2.114) is less than zero, then the permittivity or permeability in Equations (2.113) and (2.114) is multiplied by -1 in order to have a

positive imaginary part, due to loss considerations of a passive medium. However, the logarithm in Equation (2.112) also needs to be considered. The logarithm of a complex number, $z = |z| \exp i\phi$, is written as [82, p. 105],

$$\ln z = \ln |z| + i\phi + i2\pi n, \quad n \in \mathbb{Z} \tag{2.115}$$

and n must be determined.

One method of determining n is through the group delay [88]. If $S_{21} = |S_{21}| \exp i\phi$, then the group delay, τ_g, is defined as [88, Eq. (11)],

$$\tau_g \stackrel{def}{=} -\frac{d\phi}{d\omega}. \tag{2.116}$$

Once the permittivity and permeability are extracted by Equations (2.113) and (2.114), the S-parameters can be recalculated through Equations (2.103) and (2.104), giving a recalculated $S_{21,c} = |S_{21,c}| \exp i\phi_c$. This can then be used to recalculate the group delay, $\tau_{g,c} = -d\phi_c/d\omega$. Since the group delay is an independent quantity, it must be the same for the data as for the recalculated quantities. Thus, the value of n chosen in Equation (2.115) is the one such that,

$$\tau_{g,c} - \tau_g = 0. \tag{2.117}$$

This is discussed further in Chapter 7.

2.5 Bianisotropy

The split-ring resonators used in the experiments, shown in Figure (2.5.c), are very complicated in terms of their coupling to an electromagnetic field. In fact,

the constitutive relations given by Equations (2.5) and (2.6) are an approximation, due to the bianisotropic nature of the split-ring resonators that occurs due to the split-ring resonator geometry. Bianisotropy gives rise to a resonance due to the applied transverse electric field at the same frequency as the resonance from the applied transverse magnetic field, or the applied longitudinal magnetic field if the split-ring resonators are oriented in such a way as to couple to that component of the applied electromagnetic field. Ideally, the split-ring resonator should resonate due to only the applied transverse magnetic field, and so the bianisotropic nature of the split-ring resonator makes it difficult to determine if certain behaviors are due to an electric or magnetic response to the applied electromagnetic field.

While Equations (2.5) and (2.6) hold for linear media, they can be generalized for anisotropic media. Let $\underline{\underline{\epsilon}}$ be the relative permittivity tensor, and $\underline{\underline{\mu}}$ be the relative permeability tensor. Then [89, p. 4, Eqs. (7a) and (7b)],

$$\mathbf{D} = \underline{\underline{\epsilon}} \cdot \mathbf{E}, \tag{2.118}$$

$$\mathbf{B} = \underline{\underline{\mu}} \cdot \mathbf{H}. \tag{2.119}$$

For instance, suppose that a medium is electrically isotropic. In this case, $\underline{\underline{\epsilon}} = \epsilon \underline{\underline{I}}$, where $\underline{\underline{I}}$ is the identity matrix. This is equivalent to Equation (2.5). An anisotropic medium can have a different value of the permittivity or permeability along each orthogonal axis, as well as off-diagonal terms. An example of a material with off-diagonal terms is a ferrite in an applied dc H field [90, p. 458, Eq. (6.98)].

Equations (2.118) and (2.119) hold for anisotropic materials such that their electric and magnetic properties are mutually exclusive. However, suppose that an

applied electric field generates a magnetic response within the material. In this case, the medium is said to be bianisotropic. Bianisotropy introduces additional tensor quantities to relate the H field and electric displacement, and the electric and magnetic fields. The constitutive relations in Equations (2.118) and (2.119) can be written for a bianisotropic medium as [89, p. 5, Eqs. (10a) and (10b)],

$$\mathbf{D} = \underline{\underline{\epsilon}} \cdot \mathbf{E} + \underline{\underline{\eta}} \cdot \mathbf{H}, \tag{2.120}$$

$$\mathbf{B} = \underline{\underline{\tau}} \cdot \mathbf{E} + \underline{\underline{\mu}} \cdot \mathbf{H}. \tag{2.121}$$

The application of bianisotropy to the split-ring resonators starts with the orientation of the split-ring resonator with respect to the applied electromagnetic field. Figure (2.10) shows the different orientations within a waveguide for which the lowest-order mode, that is, the TE_{10} mode, will interact with the split-ring resonator. Only the outer ring is shown. The applied electromagnetic field is shown at the bottom of the figure, and each split-ring resonator orientation is shown with its respected axes. Note that these axes change with the orientation of the split-ring resonators so that when referring to a specific applied field, the orientation of the field with respect to the split-ring resonator will be recognized from the subscript. Starting from the top left and moving clockwise in Figure (2.10), the orientations are referred to in this dissertation as plane-parallel gap-parallel, plane-parallel gap-orthogonal, plane-orthogonal gap-parallel, and plane-orthogonal gap-orthogonal. The first part of these definitions is in reference to the orientation of the plane of the split-ring resonator, assuming zero thickness, with respect to the wave vector, $\mathbf{k}$, and the second part of these definitions is in reference to an

imaginary line closing the gap of the split-ring resonator with respect to the applied transverse electric field. This is shown in the top of Figure (2.10). For example, the plane-parallel gap-parallel orientation has the plane of the split-ring resonator, assuming zero thickness, parallel to the applied wave vector, and the gap of the split-ring resonator parallel to the applied transverse electric field, inasmuch as it is imagined that a line were to close this gap.

The Marqués group has written the expressions relating the dipole moments and magnetic moments of the split-ring resonator to the applied electromagnetic field. If the axes are taken to be those in Figure (2.10), then these moments are [91, Eqs. $(1a)$–$(1c)$],

$$p_x = \alpha_{xx}^{ee} E_x + \alpha_{xy}^{ee} E_y + \alpha_{xz}^{em} B_z, \tag{2.122}$$

$$p_y = \alpha_{xy}^{ee} E_x + \alpha_{yy}^{ee} E_y + \alpha_{yz}^{em} B_z, \tag{2.123}$$

$$m_z = -\alpha_{xz}^{em} E_x - \alpha_{yz}^{em} E_y + \alpha_{zz}^{mm} B_z, \tag{2.124}$$

where p_z is ignored because the assumption made is that the split-ring resonators are planar structures, and m_x and m_y are zero because no magnetic dipole can be excited along the x and y axes in the TE_{10} mode. According to Reference [91], $\alpha_{xy}^{ee} = \alpha_{xz}^{em} = 0$ due to the symmetries of the $x - z$ plane and the $x - y$ plane of the split-ring resonator. Equations (2.122)–(2.124) simplify depending on the orientation of the split-ring resonator with respect to the applied electromagnetic

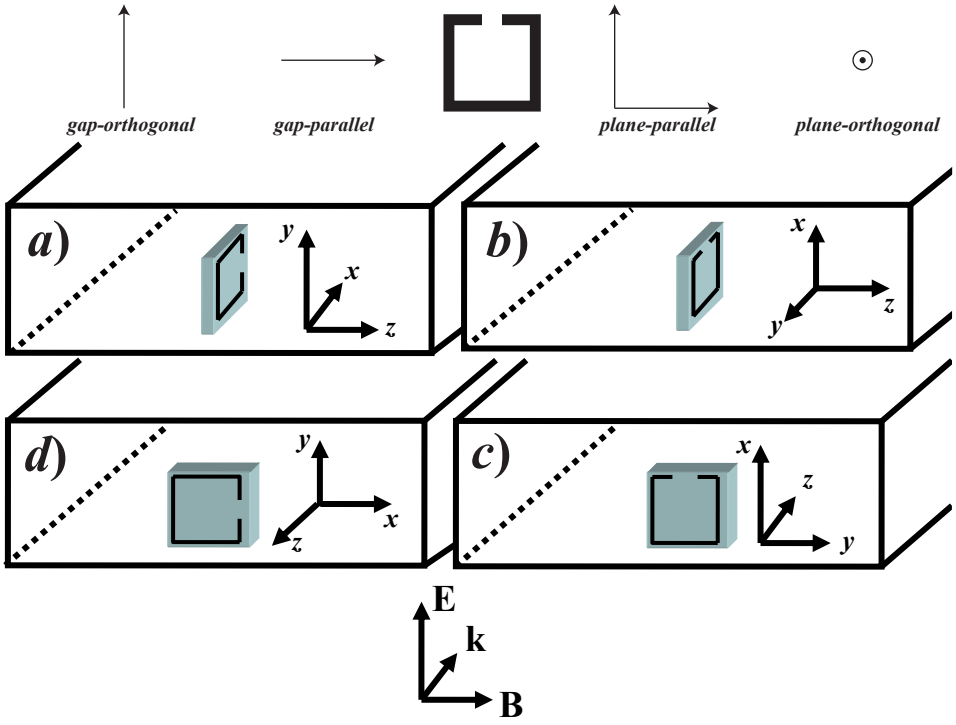

Figure 2.10: *Top*: Definitions of the orientations of orthogonal axes with respect to the split-ring resonators. *Middle*: Orientations of the bianisotropic split-ring resonator with respect to the applied electromagnetic field shown at the bottom of the figure. The first part of the orientation definition is with respect to the wave vector, **k**, and the second part of the orientation definition is with respect to the applied transverse electric field. Note that the axes to the right of each split-ring resonator changes with each split-ring resonator orientation inside the waveguide, but not with the split-ring resonator itself. Each orientation is labeled: (*a*): plane-parallel gap-parallel; (*b*): plane-parallel gap-orthogonal; (*c*): plane-orthogonal gap-orthogonal; (*d*): plane-orthogonal gap-parallel. *Bottom*: The applied electromagnetic field for the TE_{10} mode.

field. For the plane-parallel gap-parallel orientation, $E_x = 0$, and so [91],

$$p_x = 0, \tag{2.125}$$

$$p_y = \alpha_{yy}^{ee} E_y + \alpha_{yz}^{em} B_z, \tag{2.126}$$

$$m_z = -\alpha_{yz}^{em} E_y + \alpha_{zz}^{mm} B_z; \tag{2.127}$$

for the plane-parallel gap-orthogonal orientation, $E_y = 0$, and [91],

$$p_x = \alpha_{xx}^{ee} E_x, \tag{2.128}$$

$$p_y = \alpha_{yz}^{em} B_z, \tag{2.129}$$

$$m_z = \alpha_{zz}^{mm} B_z. \tag{2.130}$$

Note that the electric and magnetic fields are functions of position. However, for the plane-parallel gap-parallel and plane-parallel gap-orthogonal orientations, the electric and magnetic fields have the same functional form, and diminish as the split-ring resonator is placed close to the narrow-side wall of the waveguide. In other words, with the split-ring resonator placed against the narrow-side wall of the waveguide, and assuming it does not short with the wall, the applied transverse electric and magnetic fields vanish, while the applied longitudinal magnetic field does not couple to the split-ring resonator.

For the plane-orthogonal gap-parallel orientation, $E_x = 0$, and B_z is a function of the position of the split-ring resonator, since $B_z(u = a/2) = 0$, where u is the same as the x used in Figure (2.3), and is used here to avoid confusion with the axes of the split-ring resonators. The applied transverse electric field vanishes at the narrow-side wall, and is maximum in the center of the waveguide, while at a

narrow-side wall $B_z(u=0,a) \neq 0$, and so [91],

$$p_x = 0, \tag{2.131}$$

$$p_y = \alpha_{yy}^{ee} E_y(u) + \alpha_{yz}^{em} B_z(u), \tag{2.132}$$

$$m_z = -\alpha_{yz}^{em} E_y(u) + \alpha_{zz}^{mm} B_z(u). \tag{2.133}$$

Finally, for the plane-orthogonal gap-orthogonal orientation, $E_y = 0$, and B_z still depends on how far from the narrow-side wall the split-ring resonator is located, and so [91],

$$p_x = \alpha_{xx}^{ee} E_x(u), \tag{2.134}$$

$$p_y = \alpha_{yz}^{em} B_z(u), \tag{2.135}$$

$$m_z = \alpha_{zz}^{mm} B_z(u). \tag{2.136}$$

The electromagnetic transmission of the four positions of Figure (2.10) are shown in Chapter 5 and Chapter 6, while the dependence of u in Equations (2.131)–(2.136) is simulated in Chapter 5.

2.6 Superconductivity

Principles of superconductivity were not the focus of the research presented in this dissertation, but were exploited with the artificial materials. Some properties of superconductors need to be addressed. While there exists a resistance to an alternating current in a superconductor, this resistance must approach zero as the frequency of the alternating current approaches zero. This is also referred to as zero direct current resistance, or perfect conductivity [92, p. 2]. Another property is

the screening of magnetic fields, or perfect diamagnetism, at least beyond a specific distance away from the surface and into the superconductor, called the penetration depth [92, p. 2]. Perfect diamagnetism differs from a perfect conductor in that for a perfect conductor the magnetic field inside the metal is constant, while for the superconductor the magnetic field inside the metal is spontaneously excluded as the temperature is decreased through the critical temperature.

For this dissertation, the description of electromagnetic fields interacting with a superconductor is through the London Equations. This model of superconductivity imagines two fluids of electrons. One fluid is made of normal-conducting electrons, and the other is the superfluid electrons, or Cooper pairs. While this model is only an approximation, and more elegant theories exist, such as BCS theory and Ginzaberg-Landau theory, the London Equations will suffice for the discussion here. The equations are, in SI units [93, p. 29, Eqs. (I) and (II)],

$$\mathbf{e} = \frac{\partial}{\partial t}\left(\frac{m}{n_s e^2}\mathbf{j}_s\right), \tag{2.137}$$

$$\mathbf{b} = -\nabla \times \left(\frac{m}{n_s e^2}\mathbf{j}_s\right), \tag{2.138}$$

where n_s the number density of Cooper pairs of electrons, m the mass of the Cooper pairs, and e the electron charge. The lower-case letters are used for the fields and current density since the theory is a microscopic theory, rather than the macroscopic theory so far developed in this chapter. Maxwell's equations, Equations (2.1)–(2.4) are still true in the microscopic limit, however the electric displacement and the H field are replaced by $\mathbf{e}$ and $\mathbf{b}$, respectively, since the charges are absorbed into the microscopic charge density and microscopic current density [1, p. 248]. The

penetration depth is the distance a magnetic field will penetrate the superconductor, and has the approximate form of [93, p. 61],

$$\lambda = \sqrt{\frac{m}{n_s e^2}} \approx \frac{\lambda(0)}{\sqrt{1-(T/T_c)^2}}, \tag{2.139}$$

where T is the temperature, and T_c is the critical temperature of the superconductor. Note that the exponent factor of 2 in Equation (2.139) was used in this dissertation, rather than the typical factor of 4 in Reference [93, p. 61].

The split-ring resonators used in this dissertation were made of Niobium (Nb), which is a superconductor below a bulk critical temperature, T_c, of 9.25 K [94, inside back cover]. The resonant frequency, $\omega_0 = 2\pi f_0$, of a split-ring resonator may be approximated to be the same as an LC resonator [95, Eq. (1)],

$$\omega_0 = \frac{1}{\sqrt{LC}} \tag{2.140}$$

where L is the inductance, and C is the capacitance [90, p. 482, Eq. (7.2)]. In the experimental chapters of this dissertation, Equation (2.140) will suffice in fitting data. However, a question arises as to which expressions are used for the inductance and capacitance in Equation (2.140).

All conductors have a geometric inductance, determined by the geometry of the conductor, and a kinetic inductance, determined by the inertial mass of the electrons that determine the current flowing through the conductor. The kinetic inductance can be written as [96, Eq. (1)],

$$L_k = \frac{2}{I^2}\int \frac{1}{2} m v^2 n d^3x, \tag{2.141}$$

where I is the current, n the number density of electrons, m the mass of an elec-

tron, and v the mean drift velocity. The integral is performed over the volume of the conductor. In a normal conductor, that is, a conductor that is not in the superconductive state, the kinetic inductance is small compared to the geometric inductance. Even in a superconductor well below the critical temperature, the kinetic inductance can be a small contribution to the total inductance [96]. However, as will be shown, near the critical temperature, the kinetic inductance of a superconductor will dominate the total inductance, and if the split-ring resonators are thought to have a resonant frequency similar to an LC resonator, there will be a noticeable change in the resonant frequency near the critical temperature, due to the kinetic inductance of the superconductor.

For the superconducting split-ring resonators, the calculation of the kinetic inductance begins by determining the current flowing through the rings. Two approximations are made at this point. The first assumption is that the rings that make up a split-ring resonator in Figure (2.5.c) are closed, so that there is no longer a capacitive gap. The second assumption is that there is only one ring, rather than two concentric rings. These two assumptions oversimplify the problem, nevertheless, the result of this calculation was able to fit the experimental data with few parameters.

The setup for the problem is shown in Figure (2.11), for a superconducting ring with thickness, d, inner radius, r_i, and outer radius, r_o. The current density is assumed to flow in the azimuthal direction, and the current density is assumed to only vary with thickness [97], that is, $\mathbf{j} = j_\phi(z)\hat{\phi}$. Several equations of the current density in a superconductor are derived in Appendix A, and are the solution to,

assuming $\nabla \cdot \mathbf{j} = 0$, under quasistationary conditions [93, p. 32, Eq. (3″)],

$$\nabla^2 \mathbf{j} = \frac{1}{\lambda^2}\mathbf{j}, \tag{2.142}$$

where $\mathbf{j} \stackrel{def}{=} \mathbf{j}_s + \mathbf{j}_n$, and $\mathbf{j}_n$ is the normal-fluid current density. For the dissertation, however, the kinetic inductance was taken from Reference [98, Eq. (7)], where the geometry consisted of a linear microstrip, referred to by the authors as a "stripline insulated from a ground plane," although no stripline geometry was actually used. The kinetic inductance used in this dissertation was* [98, Eq. (7)],

$$L_k = \frac{2\pi\mu_0 R}{w}\lambda(T)\coth\left[\frac{t}{\lambda(T)}\right], \tag{2.143}$$

where $R = (1/2)(r_i + r_o)$ is the average radius, $w = (r_o - r_i)$ is the width of the ring, and t is the thicknes of the ring.

The geometric inductance of a ring has the following proportionality [1, p. 233, Problem 5.32c],

$$L_g \propto \mu_0 R, \tag{2.144}$$

where R is the radius. Since the split-ring resonators used in this dissertation were square and contain a gap, as shown in Figure (2.5.c), the constant of proportionality in Equation (2.144) is found in References [99, p. 102, Eq. (10)] and [100, p. 53,

*Note that in Reference [98, Eq. (7)], $\mathrm{t}_0 = 0$, and the $\lambda_{\mathrm{gp}}\coth(\mathrm{d}_{\mathrm{gp}}/\lambda_{\mathrm{gp}})$ term was ignored. Also, use $\mathrm{L} = 2\pi R$, where $R = (1/2)(r_i + r_o)$, with r_i, r_o as defined in Figure (2.11).

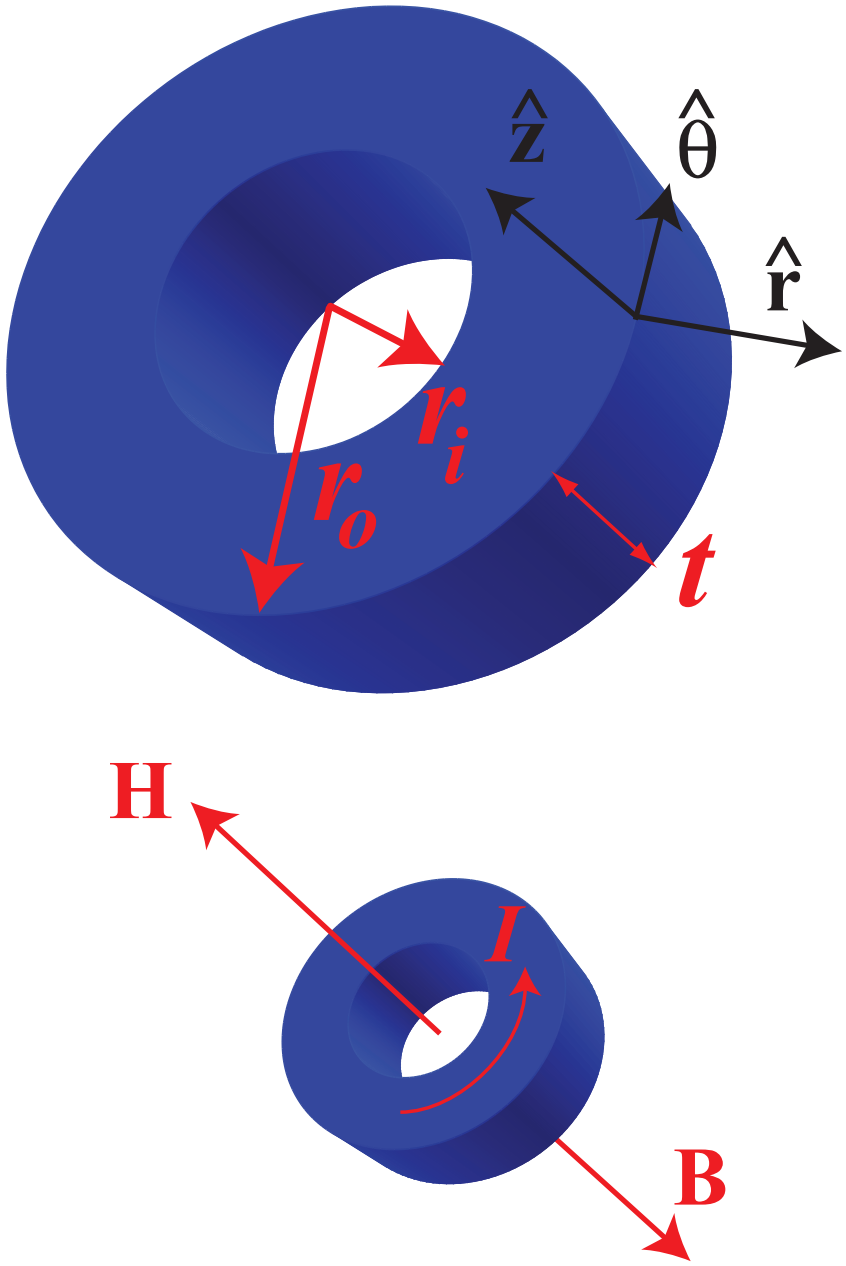

Figure 2.11: *Top*: A closed ring with inner radius r_i, outer radius r_o, and thickness t. The black axes show the cylindrical coordinate axes. *Bottom*: A closed ring with an applied magnetic field, $\mathbf{B}$, inducing a current, I, that generates an H field, $\mathbf{H}$.

Eq. (34)],

$$\begin{aligned}\kappa &= \frac{2}{\pi}\left[\log\left(\frac{2l_1l_2}{(l_1+\sqrt{l_1^2+l_2^2})(w+t)}\right)\right. \\ &+ \frac{l_2}{l_1}\log\left(\frac{2l_1l_2}{(l_2+\sqrt{l_1^2+l_2^2})(w+t)}\right) \\ &- \left.\frac{l_1+l_2}{2l_1}+\frac{2\sqrt{l_1^2+l_2^2}}{l_1}+0.447\frac{w+t}{l_1}\right], \end{aligned} \tag{2.145}$$

and so using $l_1 = l_2 = 2.36 - 0.154$ mm $= 2.206$ mm, $t = 200$ nm, and $w = 0.154$ mm, the geometric inductance of a split-ring resonator with only one ring is approximately,

$$L_g = \kappa\mu_0 R \approx 4.332\mu_0 R. \tag{2.146}$$

Note that Equation (2.145) is valid for a gap separation, denoted as g in Figure (2.5), of $g \approx 0$ [99, p. 102, Fig. (3)], which is not true in the case of the split-ring resonators used in this dissertation. However, this approximation should be within an order of magnitude, and fits the data presented in Chapter 5.

The total inductance, L_T, of the split-ring resonator is the geometric inductance, L_g, plus the kinetic inductance, L_k,

$$L_T = L_g + L_k. \tag{2.147}$$

This total inductance is inserted into Equation (2.140), along with the approximate

form of the kinetic inductance, Equation (2.143) [45],

$$\omega_0 = \frac{1}{\sqrt{L_T C}} = \frac{1}{\sqrt{(L_g + L_k)C}} = \frac{1}{\sqrt{L_g C}} \frac{1}{\sqrt{1 + L_k/L_g}} \tag{2.148}$$

$$= \frac{\omega_{0,g}}{\sqrt{1 + 2\pi\mu_0 R\lambda \coth(t/\lambda)(\mu_0 R w\kappa)^{-1}}} \tag{2.149}$$

$$= \frac{\omega_{0,g}}{\sqrt{1 + 2\pi\lambda(0) \coth[t\sqrt{1-(T/T_c)^2}/\lambda(0)]/[w\kappa\sqrt{1-(T/T_c)^2}]}} \tag{2.150}$$

$$= \frac{\omega_{0,g}}{\sqrt{1 + \beta\Upsilon^{-1} \coth(\chi\Upsilon)}}, \tag{2.151}$$

where $\lambda(T) = \lambda(0)/\sqrt{1-(T/T_c)^2} = \lambda(0)/\Upsilon$, $\beta = 2\pi\lambda(0)/(\kappa w)$, $\chi = t/\lambda(0)$, and $\omega_{0,g} = (L_g C)^{-1/2}$ is the resonant frequency due to the geometrical inductance and capacitance alone.

The quality factor, Q, of a superconducting resonator will also be temperature dependent since it can be written as [101, Eq. (4)]*,

$$\frac{1}{Q_T} = \frac{1}{Q_b} + \frac{R_{\text{eff}}}{\omega L_T}, \tag{2.152}$$

where Q_T is the total quality factor, Q_b is the background quality factor, ω is the frequency of operation, L_T was defined earlier as the total inductance, and R_{eff} is the effective resistance [101, Eq. (A6)]†,

$$R_{\text{eff}} = R_s(T)\left[\coth\left(\frac{t}{\lambda}\right) + \left(\frac{t}{\lambda}\right)\frac{1}{\sinh^2(t/\lambda)}\right]. \tag{2.153}$$

*In Reference [101], Equation (4), let $\tan\delta = 0$, and $\beta s = 0$.

†Ignore the second term in Equation (A6) of Reference [101].

The term $R_s(T)$ is written in terms of the two-fluid model of superconductivity [94, p. 129, Eq. (6)],

$$R_s = (\omega\mu_0)^2\lambda^3\sigma\frac{n_n}{2n}, \tag{2.154}$$

where σ is the normal-state conductivity, n_n is the number density of normal-fluid electrons, and n is the number density sum of normal and super-fluid electrons. The term $n_n/2n$ is rewritten in terms of the temperature [94, p. 131, Eq. (8)],

$$\frac{n_n}{2n} \approx \left(\frac{T}{T_c}\right)^2. \tag{2.155}$$

Again, an exponent factor of 2 was used rather than an exponent factor of 4, in Equation (2.155).

Combining Equations (2.152)–(2.155), together with the total inductance, given by Equation (2.147) with Equations (2.143) and (2.146), the total quality factor is written as,

$$\begin{aligned}\frac{1}{Q_T} &= \frac{1}{Q_b} + \frac{1}{2}(\omega\mu_0)^2\lambda^3\sigma(T/T_c)^2\left[\coth\left(\frac{t}{\lambda}\right) + \left(\frac{t}{\lambda}\right)\frac{1}{\sinh^2(t/\lambda)}\right] \\ &+ \frac{1}{\omega\{\mu_0 R\kappa + [2\pi\mu_0 R\lambda\coth(t/\lambda)]/w\}}.\end{aligned} \tag{2.156}$$

Using the following [81, p. 54, Eq. (14.24)],

$$\coth(x) + x/\sinh^2(x) = \cosh(x)/\sinh(x) + x/\sinh^2(x) \tag{2.157}$$

$$= [\cosh(x)\sinh(x) + x]/\sinh(x) \tag{2.158}$$

$$= [1/2\sinh(2x) + x]/\sinh(x), \tag{2.159}$$

Equation (2.156) can be simplified to [45],

$$\begin{aligned}\frac{1}{Q_T} &= \frac{1}{Q_b} + \frac{1}{2}(\omega\mu_0)^2\lambda^3\sigma(T/T_c)^2\frac{\sinh(2d/\lambda)/2 + t/\lambda}{\sinh(t/\lambda)} \\ &+ \frac{1}{\omega\{\mu_0 R\kappa + [2\pi\mu_0 R\lambda\coth(t/\lambda)]/w\}} \qquad (2.160)\end{aligned}$$

$$= \frac{1}{Q_b} + \frac{\zeta(T/T_c)^2[\sinh(2\chi\Upsilon) + 2\chi\Upsilon]}{\Upsilon^2[\Upsilon\sinh^2(\chi\Upsilon) + \beta\sinh(2\chi\Upsilon)]}, \qquad (2.161)$$

where χ, β, and Υ where defined in Equation (2.151), and,

$$\zeta \stackrel{def}{=} \frac{[\lambda(0)]^3\omega_0\sigma\mu_0 G}{2R\kappa}, \qquad (2.162)$$

and G is a geometric factor, determined by the actual current density profile in the Nb loops that make up the Nb split-ring resonator [102, Chp. 2]. Without knowledge of this geometric factor, an estimate of ζ cannot be given, however, a comparison between a single Nb split-ring resonator in an otherwise empty waveguide and a single Nb split-ring resonator in an array of metallic wires should give approximately the same value of ζ since there are no terms that depend on the wire array, except for maybe a slight correction to G due to a wire-Nb split-ring resonator interaction.

2.7 Summary

Basic principles of electromagnetic theory were written. The basic ideas of linear media, and in particular the permittivity and permeability of media, were shown. These ideas were used as a basis for more complicated theories involving negative values of the permittivity and permeability, along with non-linear, bian-isotropic media. Since the experiments in this dissertation were performed inside

a waveguide, the basic theories of waveguides were written, and showed how field structures may be exploited by the geometry of the split-ring resonators. The theory of refraction was also shown, and this was used, along with the waveguide theories, to derive a transfer matrix model in order to model the experiments in this dissertation. Basic principles of superconductivity were shown, and a temperature dependent resonant frequency and quality factor of the split-ring resonators was derived using the London model.

The chapter also discussed the theory of obtaining a negative real part of the permittivity, a negative real part of the permeability, and a negative real part of the index of refraction, at microwave frequencies. First, an infinite array of metallic wires, with their infinite lengths parallel to the polarization of an applied electromagnetic field, were shown to act as a solid slab of metal for incident radiation with a wavelength much larger than the lattice parameter and metallic wire thickness. A plasma frequency was derived as a function of the lattice parameter and metallic wire radius, and for frequencies below this plasma frequency, the real part of the permittivity was shown to be negative. Next, an infinite array of metallic split-cylinders, with the cylindrical axes aligned with an applied ac H field, were shown to have a resonant response to the applied ac H field. This resonant response produced a large diamagnetic response, and produced a frequency bandwidth where the real part of the permeability was negative. Finally, the physical implementation of these theories was discussed, where two-dimensional slices of the infinite metallic split-cylinders, called split-ring resonators, were inserted between rows of metallic wires, and an applied electromagnetic field was incident such that the applied transverse

electric field coupled to the metallic wires, while the applied transverse magnetic field coupled to the split-ring resonators. The result was a medium with a frequency bandwidth where the real part of the index of refraction was negative, located near the frequency overlap where the permittivity and permeability were both negative.

Chapter 3

Fabrication of materials and experimental setup

3.1 Overview

This chapter details the construction and properties of the wires, split-ring resonators, and waveguides, and details the setup of the two experimental probes. Niobium (Nb) wires and Nb split-ring resonators were used in most of the experiments, however $YBa_2Cu_3O_{7-\delta}$ and an alloy of copper (Cu), nickel (Ni), and gold (Au) were also used to construct some split-ring resonators. A Nb X-band (WR–90) waveguide was used for most of the experiments, however the applied dc H field experiment utilized a brass X-band waveguide, with the inside walls coated with silver (Ag), due to the Meißner screening of the Nb X-band waveguide that would have prevented the applied dc H field from reaching the inside of the Nb waveguide [92, p. 2]. The power dependence experiment also used the brass X-band waveguide. The waveguide-to-coaxial cable couplers of a Ka-band (WR–28) waveguide were used for some experiments.

Most experiments were performed between 4 and 12 K. This required the use of liquid Helium, and a Dewar that could contain the liquid. Since liquid Helium is a dielectric, electromagmetic transmission features, such as the waveguide cutoff frequency, were shifted down in frequency when the fluid was present. To remove this effect, one experimental probe allowed for the evacuation of a cavity, within

which the waveguides were placed. This allowed for an experiment to be performed almost entirely in vacuum, and allowed for the use of a temperature controller. The other experimental probe immersed the waveguide and sample directly into the liquid Helium, which allowed for quick, proof-of-principle experiments. For both probes, Cu coaxial cables were inserted into the Dewars, and connected to a vector network analyzer on one end, and to a waveguide on the other end. The measurements were mostly controlled by a computer. Each aspect of the experiment is now discussed.

3.2 Wires

The wires used in this experiment were made of either Nb or Cu, and all wires had a diameter of 0.25 mm. There were two different brands of Nb wire used in the experiments. The first brand was from a company called Alpha Aesar, however a switch was made to a company called Advent Research Materials LTD, due to concerns about the T_c of the Nb wire from Alpha Aesar, as it was believed that there was "rust" on the Nb wire after experiments. The Nb wire from Advent Research Materials LTD was temper annealed by the company, and had a purity of 99.9% according to the shipping documentation. A spool of Nb wire is shown in Figure (3.1), along with Nb wire removed from a waveguide after an experiment. The company that provided the Cu wire is unknown.

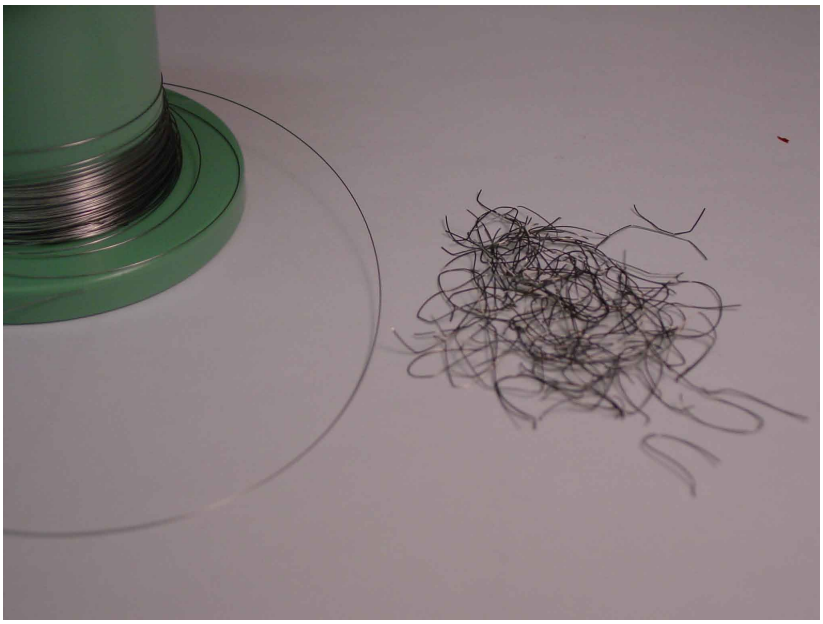

Figure 3.1: *Left:* A spool of the Nb wire. *Right:* Spent Nb wire after removal from a waveguide.

3.3 Nb split-ring and closed-ring resonators

The Nb split-ring resonators, as well as the Nb closed-ring resonators, were made in a process that involved three main steps: sputtering, lithography, and etching. Each process is described below.

3.3.1 rf sputtering the Nb film

The process of sputtering allows a material, such as Nb, to be deposited onto a substrate in the form of a thin film. The sputtering system consisted of a main chamber connected to a cryogenic vacuum pump, a loadlock chamber, a sputtering gun, a substrate holder, and a quartz oscillator to determine the thickness of the film that was being deposited onto the substrate. The substrates used for the Nb split-

ring resonators and closed-ring resonators were quartz single crystal wafers, with a diameter of 76.5 mm, and a thickness of 350 μm, purchased from University Wafer. The main chamber was initially evacuated to a base pressure of $\sim 2 \times 10^{-7}$ torr. The substrate was first placed inside the loadlock. The loadlock was then evacuated to $\sim 5 \times 10^{-4}$ torr, whereupon the valve separating the main chamber from the loadloack was opened, and the substrate was loaded into the main chamber. The valve separating the main chamber and the loadloack was then closed, and the main chamber was evacuated to $\sim 2 \times 10^{-7}$ torr*. The valve to the cryogenic vacuum pump was then closed, and then partially reopened, and inert Argon (Ar) gas was introduced into the chamber at a pressure of approximately 5 mtorr.

In rf sputtering, the The device used to sputter the metal is called the sputtering gun, while the metal itself is called the target. The sputtering gun creates a local magnetic field, and electrons follow the magnetic field lines and collide with, in this case, an Ar atom. This collision knocks an electron off of the Ar atom, and the atom now has a positive charge. The sputtering gun has a negative dc bias voltage, and so the Ar^+ atoms are attracted to the gun, and collide with the target, in this case Nb, and this knocks a Nb atom, or several Nb atoms, off of the target. This neutral Nb atom travels to the substrate and deposits on the substrate [103, p. 185]. The process is more complicated than stated, since the Ar^+ collisions do not always free a Nb atom, nor do the Nb atoms simply deposit on the substrate. For instance, in the former case, an Ar^+ atom could reflect off of the Nb surface [103,

*The pressure of the main chamber increases slightly when the valve separating the main chamber from the loadlock is opened.

p. 184], while in the latter case a Nb atom may deposit on the substrate, and then re-evaporate [103, p. 201]. However, for this experiment, the Nb can be considered to sputter immediately from the target to the substrate.

Before sputtering the Nb, the chamber was gettered, or presputtered, with Nb. Presputtering cleans the target by removing the top few layers of Nb, which may have adsorbed impurities such as oxygen. Presputtering the chamber also removes any water vapor and oxygen that may still be in the chamber [103, p. 197]. A shutter was used to protect the substrate during the presputtering, however, since the vacuum was degraded by introducing Ar gas to the chamber, some Nb likely traveled around the shutter and deposited onto the substrate. This effect was considered to be minimal for the experiment. The chamber was presputtered at a forward sputtering gun rf generator power of 600 W, for a time of 180 s.

After presputtering, the shutter protecting the substrate was opened, and Nb was deposited onto the substrate to a thickness of 200 nm. The thickness was monitored with a quartz oscillator that detects a change in its mechanical resonant frequency, and attributes this change with a thickness of the film on the substrate. Thus, the proper parameters must be programmed into the thickness monitor to account for the orientation of the quartz oscillator relative to the sputtering gun. In this case, the parameters were preprogrammed*. The thickness was later measured independently with a Dektak IIA system at two locations on a single Nb split-ring resonator. The two measurements were in agreement with the expected thickness;

*The sputtering gun was at an angle relative to the plane of the substrate, and approximately 31 cm below the substrate.

one measurement yielded a thickness of 231 nm, and the other measurement was 265 nm.

Once the desired thickness was reached, the sputtering gun was shut off, the Ar gas was shut off, and the valve to the cryogenic vacuum pump was opened to remove the excess Ar gas. The substrate and film were then inserted into the loadlock, and the loadlock was vented to atmospheric pressure.

3.3.2 Lithography of the Nb film

After sputtering Nb onto the quartz wafer, the split-ring resonator shape was patterned on the entire surface of the Nb film using standard lithographic procedures. First, the Nb film was cleaned with acetone and methanol. After drying the Nb film with nitrogen gas, AZ 5214-E photoresist was spin-coated onto the film, which was spinning at a rate of 4700 rpm, for a time of 60 s. The photoresist was then baked on a hotplate at a temperature of 90° C, for 180 s.

The next step in the lithography was the patterning of the photoresist. A CIFF file containing the design of the split-ring resonator array was created using the ICED computer program. Each square split-ring resonator had the following dimensions, shown in Figure (3.2.b): an outer loop side length of 2.360 mm, an inner loop side length of 1.448 mm, ring (capacitive) gap widths of 0.300 mm, and the gap between the inner and outer rings was 0.302 mm. All line widths were 0.154 mm. The entire array had center-to-center split-ring resonator separation lengths of 5.008 mm and 3.090 mm horizontally and vertically, respectively, as shown in

Figure (3.2.d). The CIFF file was sent to the Microfabrication Lab at the University of California, Berkeley, and a photomask was constructed, made of glass and chromium (Cr) film, with metallic split-ring resonators embedded in the glass. The closed-ring resonators were exactly the same as the split-ring resonators described above, however there was no capacitive gap, as shown in Figure (3.2.e).

The split-ring resonator photomask covered most of the film, and was exposed to 365 nm (UV) light for 10 s. The exposure made the regions of photoresist on the film that were not covered by the mask split-ring resonator features soluble in developer solution. This was due to the fact that AZ 5214 photoresist is a positive resist. After exposure to the ultra-violet light, the wafer was immersed in CD-30 developer solution for 15 s, which dissolved the unwanted resist. The wafer was then placed on a 120° C hotplate for 30 min. This allowed the remaining regions of photoresist, which were in the shape of the split-ring resonators, to harden and become more resistant to chemicals during the etching process.

3.3.3 Etching of the Nb film and dicing of the substrate

Once the Nb film was patterned, the Nb that was not covered by the photoresist after development was etched. Several wet etch solutions were tried, however none were able to etch the Nb. The likely cause for this was the creation of a passivation layer. When an etchant solution reacts with the topmost layer of a film, there is the possibility of the etchant forming a non-reacting layer, thus inhibiting any further etching of the film. In order to etch the Nb, the wet etch techniques

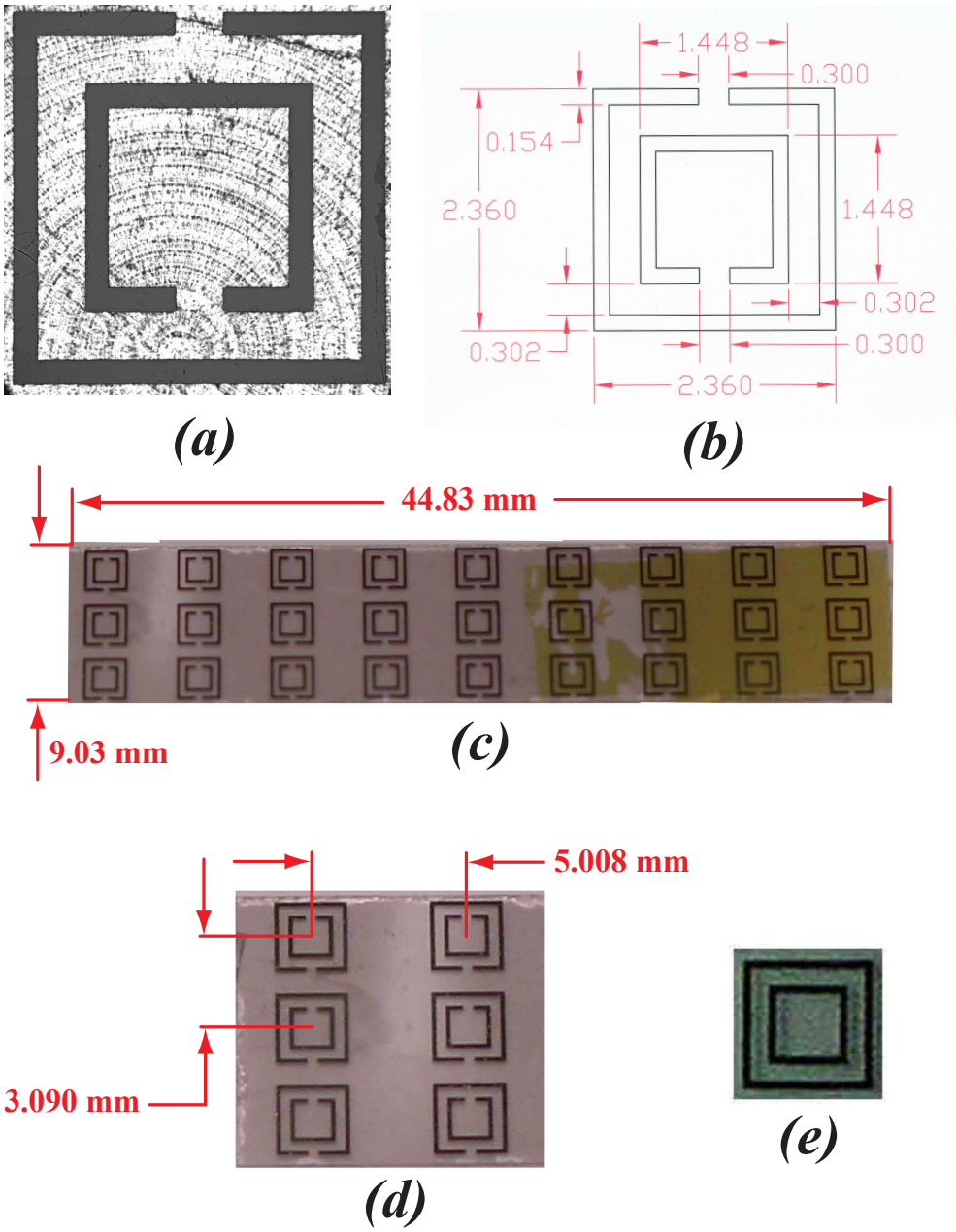

Figure 3.2: (a) A single Nb split-ring resonator. (b) An Auto-CAD drawing of a single split-ring resonator with dimensions, all in mm. (c) A split-ring resonator "chip," containing an array of three-by-nine Nb split-ring resonators. The yellow tape on the back right of the chip was used to connect two chips lengthwise in order to create a longer split-ring resonator array. (d) A close-up of the chip, with dimensions. (e) A Nb closed-ring resonator with the same dimensions as (b).

were abandoned and plasma etching was used.

Plasma etching is similar to sputtering. A gas is injected into a cavity, and a plasma is formed to ionize the gas. These ions react with the surface of the film, and the new compounds evaporate from the surface, and are removed from the cavity by a vacuum pump [103, p. 298]. In this experiment, the reacting gas was sulfur hexafluoride, SF_6, although for more recent etches, this gas failed to etch the Nb. For more recent teches, CF_4 was used as the etching gas, along with oxygen.

First, the etching chamber was evacuated to ~ 75 mtorr and cleaned, a process called "ashing," with oxygen gas (O_2) for 5 min, at an rf generator power of 300 W. Ashing is typically used to remove photoresist, however it can also serve to clean the chamber. The oxygen will react with any organic material in the cavity and form an ash, which is removed by the vacuum pump [103, p. 297]. After ashing, the quartz wafer with the patterned Nb film was place inside the chamber, and the chamber was evacuated to ~ 50 mtorr. The SF_6 was then introduced at a pressure of 300 mtorr, and a plasma was formed at an rf generator power of 300 W. The film was etched for 15 min. After etching, the surface was cleaned with acetone and methonal to remove any photoresist, and the remaining features on the quartz wafer were Nb split-ring resonators. For more recent etches, a mixture of CF_4 and O_2 were used to etch the Nb. There appeared to be an optimal ratio of pressure of each gas, with a minimum of $1:1$ CF_4 to O_2, although a ratio of slightly more CF_4 pressure than O_2 pressure was preferred. The etching time for this mixture of gasses was approximately 6 min for a quartz chip with a single Nb split-ring resonator and Nb strip.

Once the Nb features were etched, the quartz wafers were diced, that is, they were cut into strips of quartz with an array of three-by-nine Nb split-ring resonators on the quartz, called "chips," as shown in Figure (3.2.c). The dicing was performed at The Laboratory for Physical Sciences in College Park, MD, by Russ Frizell. The procedure used tape applied to the back of the wafer to prevent fractures, and a thin dicing blade to cut the wafer into the aforementioned strips. The tape was then carefully peeled from the strips. Each chip had dimensions of 9.03×44.83 mm^2 for an array of three-by-nine Nb split-ring resonators. In order to create a larger array of Nb split-ring resonators, two chips were taped lengthwise for a Nb split-ring resonator array of three-by-eighteen. Several single Nb split-ring resonators were harvested from surplus chips. The Nb closed-ring resonator wafers were not diced, since only a single Nb closed-ring resonator was needed for the experiments, and individual Nb closed-ring resonators were harvested from the larger wafers as needed.

3.4 $YBa_2Cu_3O_{7-\delta}$ split-ring resonators

The $YBa_2Cu_3O_{7-\delta}$ split-ring resonator had the same dimensions as the Nb split-ring resonators, since the same mask was used for the $YBa_2Cu_3O_{7-\delta}$ lithography. The $YBa_2Cu_3O_{7-\delta}$ was deposited on a substrate of $NdGaO_3$ by pulsed laser deposition, by Hua Xu. The process is summarized in Reference [104, p. 17].

3.5 Cu-Ni-Au split-ring resonators

The Cu-Ni-Au split-ring resonators were produced by an outside company. They consisted of three layers of metal, one of Cu, one of Ni, and one of Au. The thickness of each layer, respectively, was 35 μm, 30 μm, and 2 μm. The dimensions of the Cu-Ni-Au split-ring resonators were slightly larger than the dimensions of the other ring resonators. The Cu-Ni-Au split-ring resonator dimensions were the following: an outer loop side length of 2.6 mm, and inner loop side length of 1.6 mm, ring gap widths of 0.3 mm, and the gap between the loops was 0.3 mm. All line widths were 0.2 mm. The arrays had a center-to-center spacing of 5.0 mm horizontally, and 3.0 mm vertically. The Cu-Ni-Au split-ring resonators were printed on G-10 circuit board, which had a thickness of 0.80 mm.

3.6 Critical temperature measurement of the Nb wires and Nb split-ring resonators

The critical temperature of the Nb wires and Nb split-ring resonators was measured by ac magnetic susceptibility. Samples were placed between two metallic wire loops, and cooled in liquid Helium. Since the cooling was done by lowering the probe manually into the liquid Helium, the accuracy of the results depended on how slowly the probe was moved in order to achieve temperature steps of one-tenth of a Kelvin, which was the minimum step size recordable. The plots are shown in Figure (3.3). The metallic wire loops generate and measure a magnetic field, and the magnetic susceptibility, χ_m, is calculated and plotted versus temperature.

Above the critical temperature of the superconducting Nb, the applied magnetic field penetrates the film. However, below the critical temperature of the Nb, the flux of magnetic field penetrating the film is reduced. At the critical temperature of the Nb, the real part of the ac magnetic susceptibility has a sharp, step-functionlike decrease in its value, while the imaginary part of the ac magnetic susceptibility has a sharp peak. This peak determines the critical temperature of the film [104, p. 27], although the step in the real part of the ac magnetic susceptibility is a reasonable estimate of the critical temperature, especially for situations where the superconducting metal does not cover the entire loops of the measurement probe.

The top of Figure (3.3) are the results for a single Nb split-ring resonator, and the Nb wire results are in the bottom of the figure. The Nb wire critical temperature is reported as 9.4 K, which is roughly equal to the bulk value for Nb, between 9.25 K [94, inside back cover] and 9.50 K [36, p. 336, Tbl. (1)]. The Nb split-ring resonator T_c appears to be at 8.65 K. A four-point probe measurement was also performed on a single split-ring resonator to compare to the ac magnetic susceptibility measurement. In this case, at the critical temperature of the film, the resistance should change in a step-functionlike manner between 0 Ω, and some value greater than 0 Ω. The results are shown in Figure (3.4), and agree with the ac magnetic susceptibility measurement, with a T_c of 8.65 K.

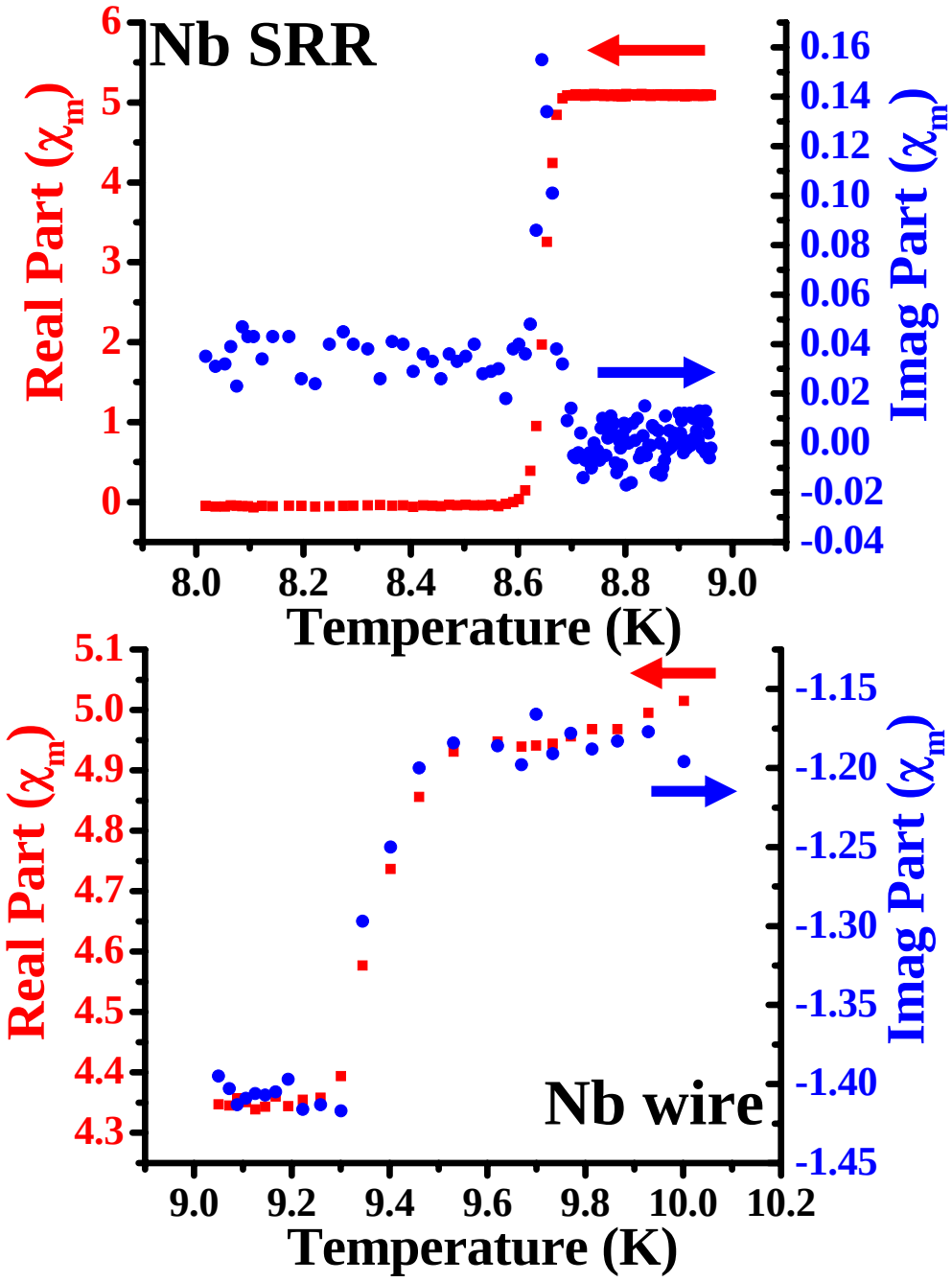

Figure 3.3: *Top:* The ac magnetic susceptibility, χ_m, versus temperature of a single Nb split-ring resonator, labeled SRR. *Bottom:* The ac magnetic susceptibility, χ_m, versus temperature of the Nb wire. The critical temperature is measured at the peak in the imaginary part, if present, otherwise, the step-functionlike change in values of the real part is a reasonable approximation. The red squares denote the real part of the ac magnetic susceptibility, while the blue circles denote the imaginary part.

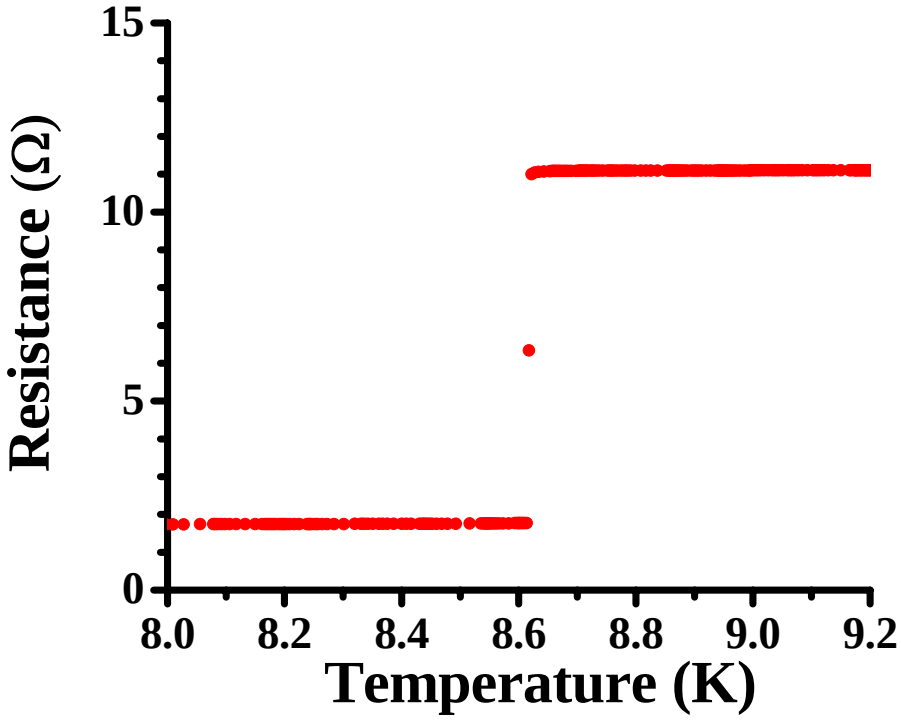

Figure 3.4: A four-point probe resistance measurement of a single Nb split-ring resonator. The critical temperature is at the step-functionlike change in values, at approximately 8.65 K. Due to residual resistance, the resistance does not drop to 0 Ω.

3.7 Waveguides

Two X-band waveguides were used in this experiment, one made entirely of Nb, and the other made of brass (Cu and Zn) with the inner walls coated in Ag, as shown in Figure (3.5). A brass Ka-band waveguide was also used for some experiments. The following sections detail each waveguide.

3.7.1 Ag-plated brass X-band waveguide

The Ag-plated brass X-band waveguide had inner cavity dimensions of 22.86 mm wide by 10.16 mm tall, as shown in Figure (3.5), which are standard X-band (WR-90) dimensions, and had a total length, not including the waveguide-to-coaxial cable couplers, of 12.28 cm. The broadsides of the Ag-plated brass X-band waveguide were perforated with 0.51 mm diameter holes to allow a metallic wire array to be woven into the waveguide. The holes formed an array of twenty-one holes along the length, and five holes transverse to the length, and ended before the waveguide flange joints. In both directions, that is, the transverse and longitudinal directions, the hole spacing was 5.08 mm, and the holes next to the wall were spaced 1.27 mm from the narrowside wall. The waveguide-to-coaxial cable couplers for the Ag-plated brass X-band waveguide were purchased from Penn Engineering Components, and were made of Cu, with the same inner cavity dimensions of width and height. The total depth of a Cu waveguide-to-coaxial cable coupler was 36.30 mm, with the antenna located in the center transversely, at a depth of 29.50 mm from the flange. The antenna was pre-built into the waveguide-to-coaxial cable coupler,

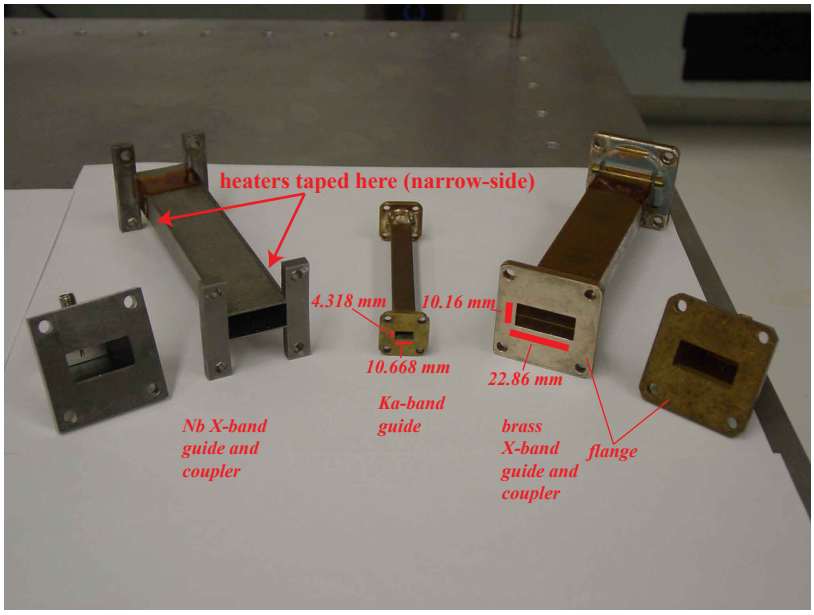

Figure 3.5: Waveguides used in the experiments, with inner dimensions specified. From left to right: X-band Nb waveguide-to-coaxial cable coupler; X-band Nb waveguide; Ka-band waveguide; Ag-plated brass X-band waveguide; X-band brass waveguide-to-coaxial cable coupler.

and consisted of a small diameter wire extension of the coaxial center conductor with a larger diameter cylinder soldered on the end. The antenna extended approximately halfway down, 5.08 mm, into the cavity. There was a small set screw in the waveguide-to-coaxial cable coupler located in the center transversely, and at a depth of 23.16 mm from the flange plane. This screw served to adjust the quality factor of the waveguide, and change standing wave patterns, however it was left at its factory setting.

3.7.2 Nb X-band waveguide

In order to reduce the waveguide losses at low temperatures, an X-band waveguide was fabricated entirely out of Nb. The Nb metal was obtained through Peter Kneisel, and the machining of the Nb into the waveguide shape was performed by Larry Turlington at the Thomas Jefferson National Accelerator Facility in the city Newport News, in the Commonwealth of Virginia. This included the waveguide-to-coaxial cable couplers, but did not include the antennas, which are discussed below. The critical temperature of the waveguide was found by measuring the ac magnetic susceptibility of shavings from part of the flange of the Nb waveguide that was removed, and appears to be 8.5 K, as seen from the ac magnetic susceptibility plot in Figure (3.6), although this measurement may not be very accurate since the device under test was not a solid piece of Nb. The inner dimensions of the Nb X-band waveguide were the same as the Ag-plated brass X-band waveguide, and the length of the Nb X-band waveguide was 12.2 cm. The waveguide-to-coaxial cable couplers had the same inner dimensions as the Nb X-band waveguide, and the depth of each waveguide-to-coaxial coupler was 33 mm, with the antenna located in the middle transversely, at a depth of 26 mm from the flange. The Nb X-band waveguide also had a 0.51 mm diameter hole array drilled into its broadsides. This array, however, extended the length of the waveguide, such that the flange was cut out to accommodate the hole array. There were a total of twenty-seven holes along the length, and five holes transverse. The holes were spaced by 4.57 mm in the longitudinal and transverse directions, and the holes along the wall were spaced 2.29

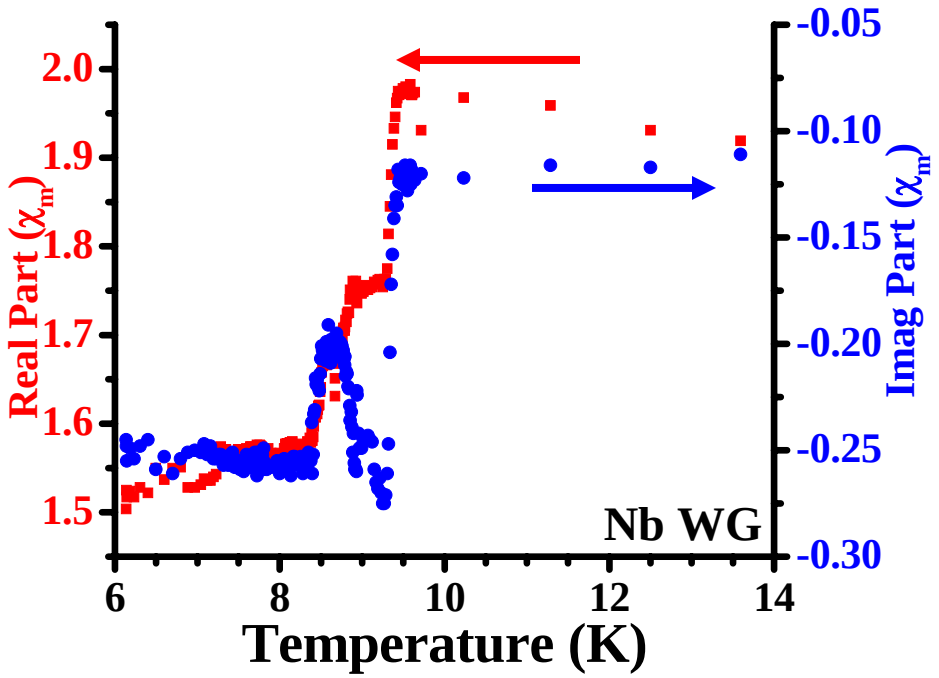

Figure 3.6: The ac magnetic susceptibility, , χ_m, versus temperature, of the Nb X-band waveguide, labeled Nb WG. The red squares denote the real part of the ac magnetic susceptibility, while the blue circles denote the imaginary part of the ac magnetic susceptibility.

mm from the wall.

3.7.3 Brass Ka-band waveguide

A brass Ka-band waveguide was used for some experiments. In this case, the waveguide cutoff frequency is well above the lowest-order resonant frequency of all of the split-ring resonators used in the experiments. For frequencies below this cutoff frequency, the waveguide can be considered to have a permittivity with a real part less than zero, and wires are not necessary to create a medium with the real part of the permittivity less than zero over some frequency bandwidth [86]. The inner

dimensions of the waveguide were 4.32×10.67 mm^2. Since the electromagnetic waves at the frequency of 10 GHz are evanescent for a Ka-band waveguide, only the waveguide-to-coaxial cable couplers were used.

3.8 Antennas

The antennas for the Nb X-band waveguide and the brass Ka-band waveguide were stock SMA antennas, purchased from M/A-COM, Inc. The antennas were flange mount jack receptacles, made of gold-plated beryllium copper, with a polytetrafluoroethylene (PTFE) dielectric surrounding the antenna [105, p. 70]. The total original length of a single antenna from the antenna tip to the flange was 27.4 mm, which was greater than the height of any waveguide used in this experiment. Thus, the antenna lengths had to be truncated for the Nb X-band waveguide and the brass Ka-band waveguide, and so several antenna lengths were tested to find the optimal length for each waveguide. For the brass Ka-band waveguide, the best electromagnetic transmission results came from an antenna that was almost the entire height of the cavity. For the Nb X-band waveguide, the electromagnetic transmission results are shown in Figure (3.7) for a total length of 14.22 mm, which corresponds to a length of ~ 6.80 mm within the waveguide, measured from the top inside of the waveguide-to-coaxial cable coupler, to the bottom of the anenna*. The data in Figure (3.7) was collected at room temperature with the Nb X-band waveguide and Nb couplers. Two antennas were cut to various lengths, at 0.25 mm increments, and

*The distance from the bottom of the antenna to the bottom of the waveguide was thus 3.36 mm.

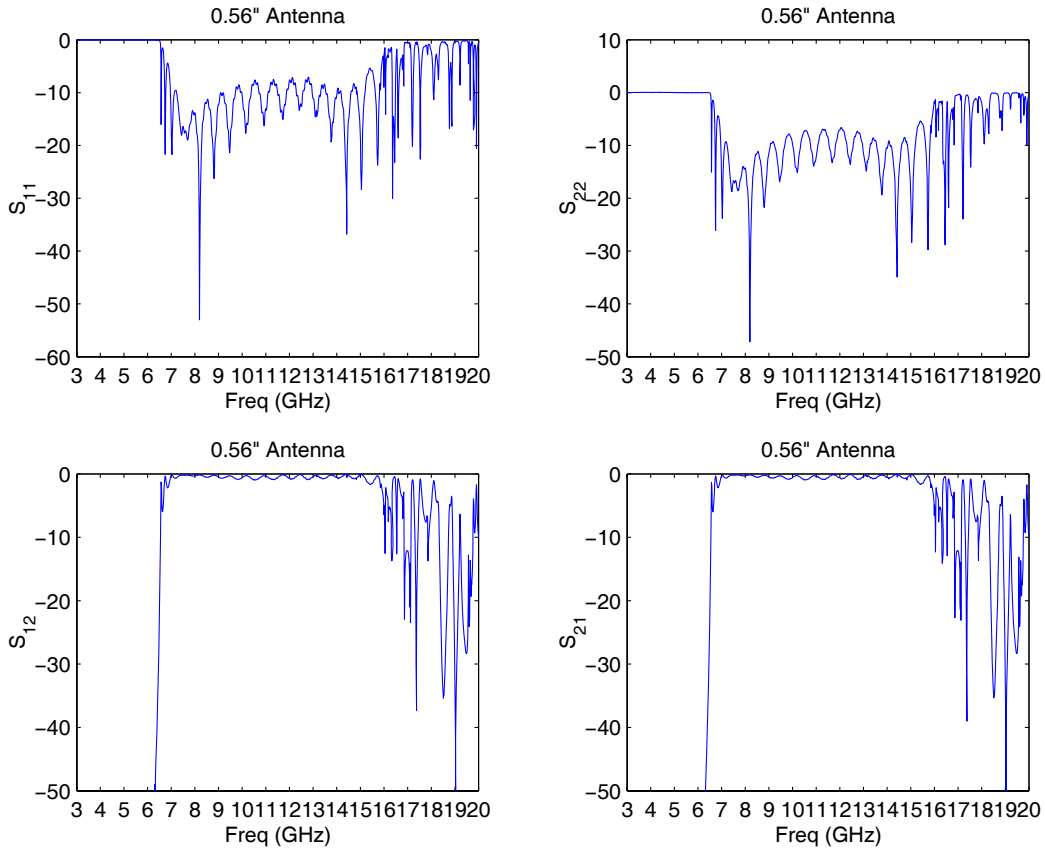

Figure 3.7: S-parameter plots of the all-Nb X-band waveguide at room temperature for the antenna length used in the experiment.

the S-parameters were compared for each length. The chosen length shown in Figure (3.7) had an electromagnetic transmission spectrum with the smallest amount of electromagnetic transmission ripple between 7 and 12 GHz, as well as the smallest amount of cutoff noise at 6.5 GHz.

3.9 Experimental orientation of the wires and split-ring resonators

3.9.1 Wires

The wires were "woven" into the waveguide, through the holes in the broadsides, as shown in Figures (3.8.a) and (3.8.b). Generally, two or more sets of wires were needed. In other words, using a single strand of wire for the entire waveguide was too difficult without the wire breaking, except for short arrays of wires, for example, seven rows deep. When more than one strand of wire was used, the ends sticking out of the waveguide were twisted together in order to couple the strands. The wire orientation coupled to the electric field in the TE_{10} mode of the waveguide. Since the Nb X-band waveguide had a shorter lattice parameter than the Ag-plated brass X-band waveguide, it was difficult to weave the Nb wire array into the Nb X-band waveguide such that the Nb wires were parallel to the applied transverse electric field. The result is shown pictorially in Figure (3.9), and data results are shown in Figure (4.8) in Chapter 4. To overcome the issue of curvy wires, adjacent holes in the Nb X-band waveguide were skipped, and the wire was pulled tight through each hole, as shown in Figure (3.8.b).

3.9.2 The split-ring resonators and Rohacell® HF foam

The split-ring resonators were oriented to couple to the transverse magnetic field of the TE_{10} mode of the waveguide. In order to remain in such an orientation, Rohacell® HF foam was used to stabalize the split-ring resonator arrays. Rohacell® HF is a polymethacrylimide–based foam that is available in three types,

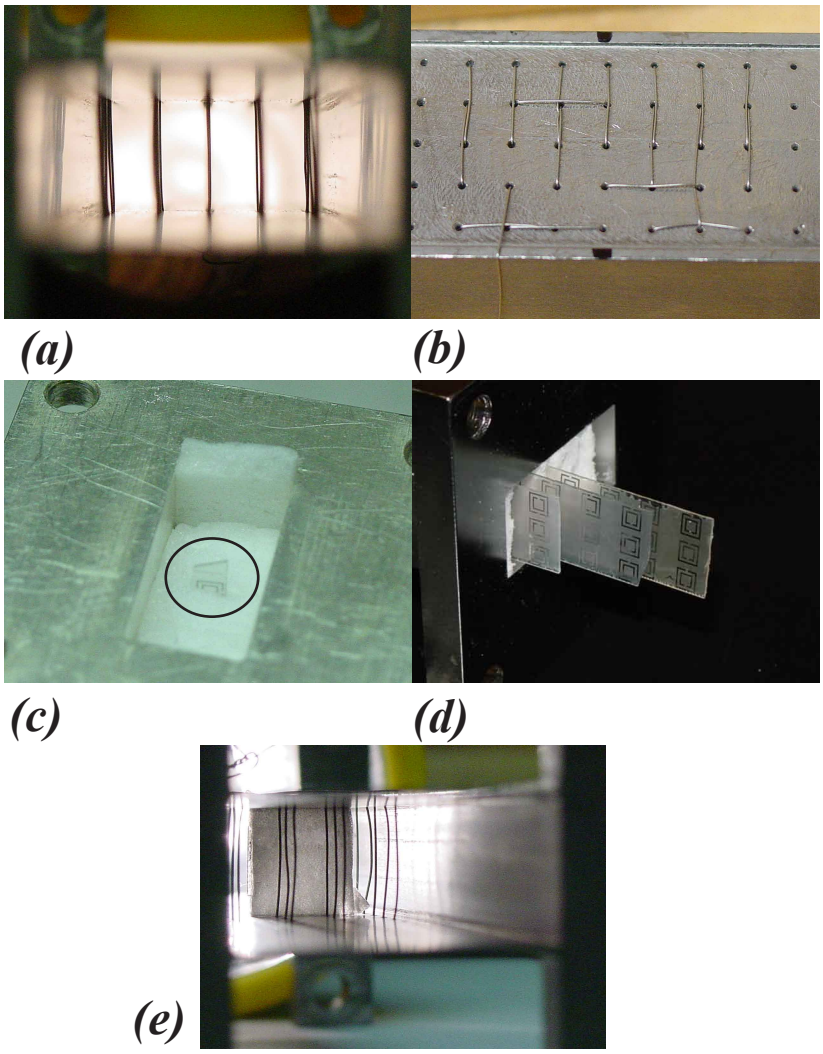

Figure 3.8: (a) Nb wire array in the Nb X-band waveguide looking in the longitudinal direction of the waveguide; (b) Nb wire array looking at the broadside face of the waveguide from outside the Nb X-band waveguide; (c) Single Nb split-ring resonator, circled, in a slab of Rohacell® HF in the Ag-plated brass X-band waveguide; (d) Nb split-ring resonator array with Rohacell® HF spacers in a non-perforated Nb X-band waveguide; (e) single Nb split-ring resonator in a slab of Rohacell® HF in a Nb wire array in the Nb X-band waveguide.

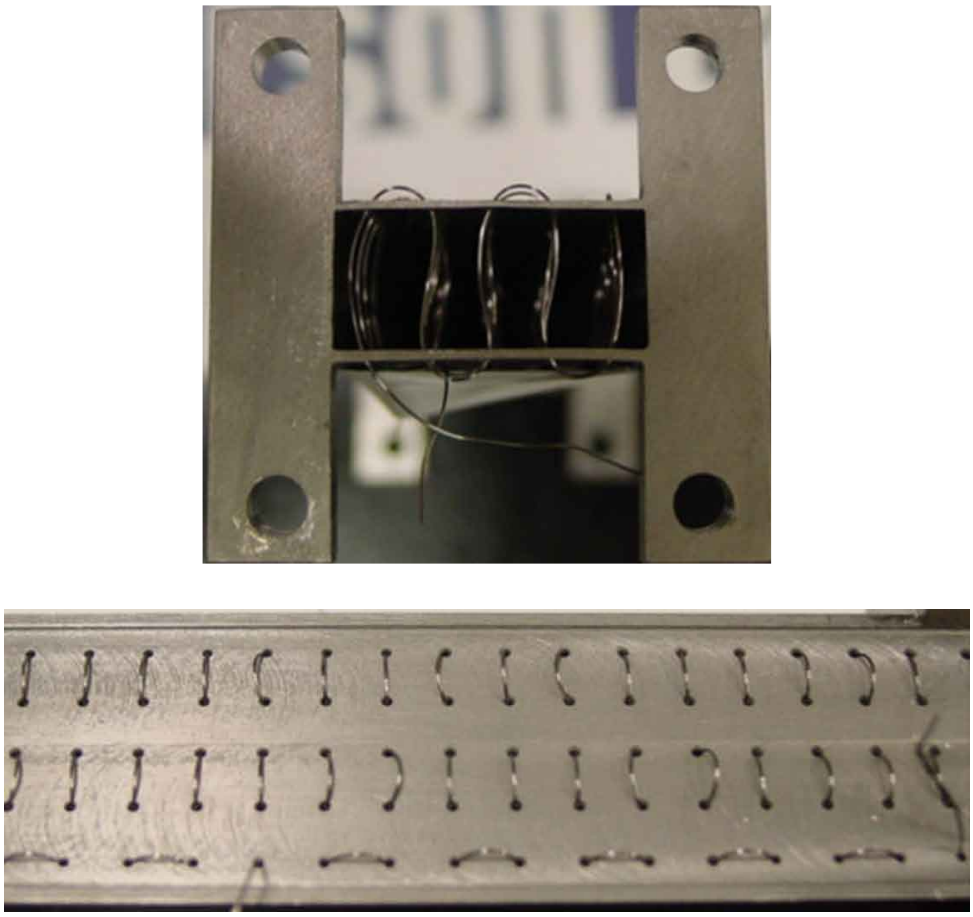

Figure 3.9: A Nb wire array in the Nb X-band waveguide, with a lattice parameter of $a = 4.57$ mm. The short lattice parameter prevented the wires from being pulled straight, and forced the wires inside the Nb X-band waveguide to be curved, as shown in the top of the figure. The bottom of the figure shows a view of the broadside of the Nb X-band waveguide from the outside.

named 31, 51, and 71 by the company, although only types 31 and 51 were used in the experiments. One difference between each type of foam is the density, with a more dense material as the product number increases. All types of Rohacell® HF have a low real part of the relative permittivity and loss tangent at microwave frequencies. For instance, at 10 GHz, the real part of the relative permittivity ranges between 1.046 and 1.093, while the loss tangent ranges between 0.0017 and 0.0038, with increasing values for increasing density [106]. When a single ring resonator was used, a slab of Rohacell® HF was used for stability, with a small incision inside of which the single split-ring resonator was placed, as shown in Figure (3.8.c). For long chips with split-ring resonators, slabs of Rohacell® HF were used to keep the chips in the proper orientation, as shown in Figure (3.8.d).

3.9.3 Combination of wires and split-ring resonators

When a combination of split-ring resonators and wires was formed, the split-ring resonators were placed in between the long rows of wires, except for the space between the wires and the walls of the waveguide, with a preferable distance of exactly midway between rows of wires. Thus, there were five rows of wires and four rows of split-ring resonator arrays. In the case of a single ring-resonator in an array of wires, the orientation with respect to the wires was changed depending on the desired orientation with respect to the incoming electromagnetic field, for instance Figure (3.8.e). A view along the y–axis in Figure (2.3) is shown in Figure (3.10). The black circles are the wires, and the black rectangles are the split-

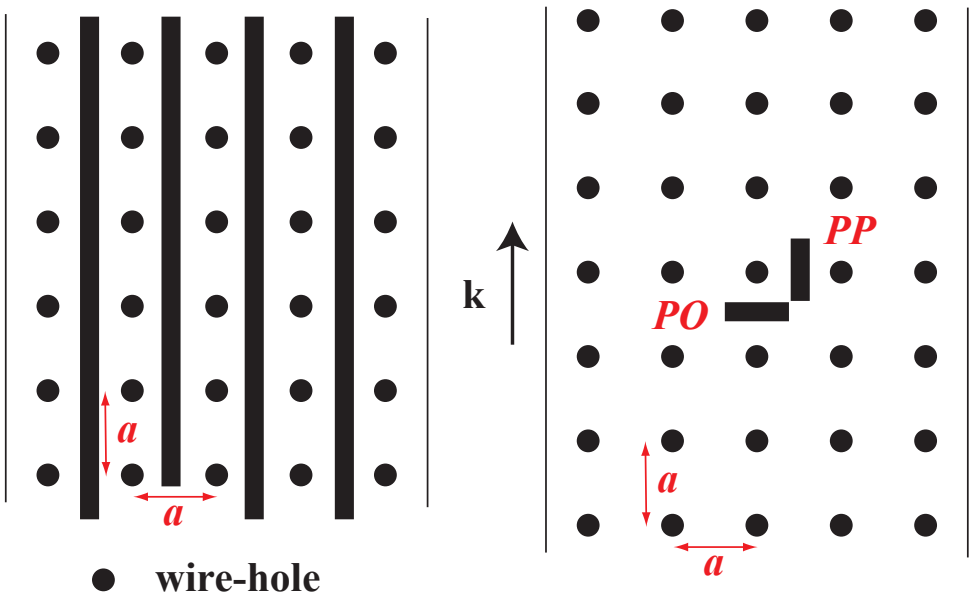

Figure 3.10: A metallic wire array, shown as black circles with lattice parameter, a, and an array of split-ring resonators, shown as the black rectangles. The view is along the y–axis in Figure (2.3). *Left*: Long arrays of split-ring resonators and wires. *Right*: A single split-ring resonator in the wire array. The positions are labeled PP for plane-parallel, and PO for plane-orthogonal. The orientation is in reference to the wave vector, shown in the middle of the figure.

ring resonators. The left figure shows that there were only four rows of the long split-ring resonator arrays, oriented roughly midway between the rows of metallic wires for each lattice parameter of metallic wires used. The right figure shows the orientations of a single split-ring resonator. The positions are labeled PP, meaning plane-parallel, and PO, meaning plane-orthogonal, and that definition is in reference to the applied wave vector, shown in the middle of the figure. The location of the single split-ring resonator was midway between the wires in each orientation.

3.10 Dewars

All experiments, except where indicated, were performed inside of Dewars specifically designed to hold liquid helium. Two Dewars were used, and they differed mostly in their dimensions. Both Dewars consisted of an inner core chamber where the liquid Helium and experimental probe were contained, and a jacket, which was an empty chamber between the inner core and the outermost wall of the Dewar. This jacket was evacuated with a Drytel pump for three days, and served as a thermal buffer between the liquid Helium core and room temperature, in order to prolong the lifetime of the liquid Helium. The jacket did not need regular evacuations as long as the Dewar was cooled regularly.

The smaller Dewar contained the simplest probe for the experiment, as shown in Figure (3.11.a). In this case, there were four fittings at the top of the Dewar; two fittings were for the coaxial cables that connected to the waveguide, one fitting was used for the temperature monitor, and the last fitting was for the solenoid wires for the applied dc H field experiment. Since the coaxial cables would not have been able to hold the weight of the waveguide, a hollow steel rod was screwed into the top of the Dewar, and into an Aluminum (Al) block at the bottom of the Dewar. This Al block was coupled to the flange of the waveguide, and provided structural stability for the experiment. The waveguides in this geometry were immersed in liquid Helium.

The larger Dewar contained a probe that was used in a previous experiment not related to this experiment, and already had the coaxial cables and thermom-

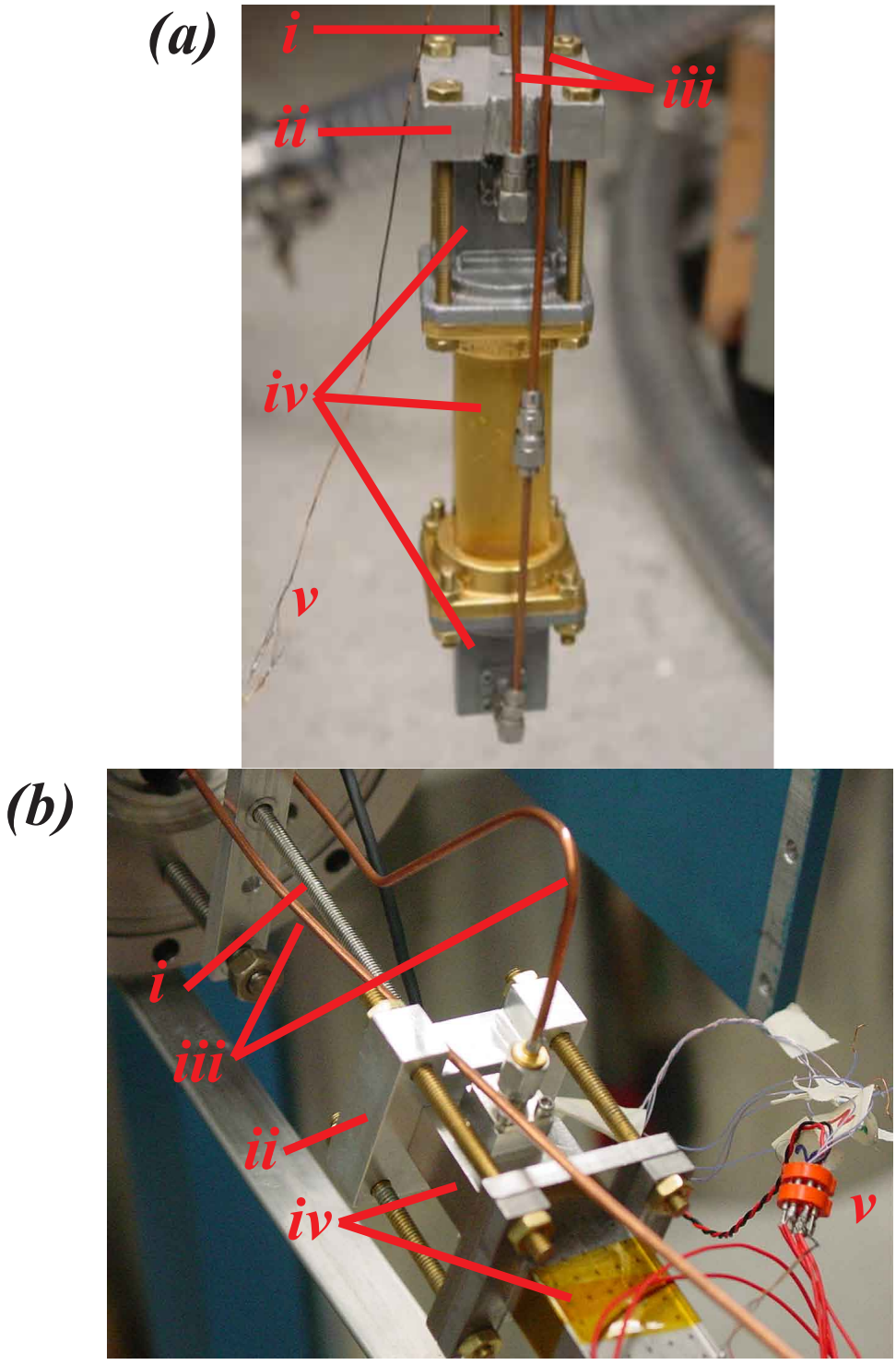

Figure 3.11: The experimental probes. (a) Small Dewar probe. (b) Large Dewar probe. Both figures contain numbers that refer to the same features: (i) support rod; (ii) Al block; (iii) coaxial cables; (iv) waveguide and couplers; (v) thermometer (and heater for (b)).

etry built-in, although some re-wiring was necessary. The probe is shown in Figure (3.11.b). The advantage of the larger Dewar was its vacuum capabilities. Attached at the bottom of the probe for the larger Dewar was a steel can that could be evacuated with the use of a Drytel pump. A new can was constructed since the original can was not long enough for the waveguides to fit inside, and this also necessitated making a collar that went on the top of the Dewar to compensate for the extra length of the larger vacuum can. The Dewar probe sat on top of the collar. The vacuum can used an Indium (In) O-ring, and the typical time to evacuate the vacuum can was 24 h. This vacuum can was immersed in liquid Helium, and in order to provide a thermal coupling to the waveguide, approximately 6 cm^3 at STP of Helium gas was injected into the vacuum can after the evacuation of air in the can, and after immersion into liquid Helium.

3.11 Temperature control

A Lakeshore 340 Temperature Controller was used for the temperature control in all the experiments. This included temperature monitoring through the use of a diode thermometer in both Dewar probes, and heaters for the larger Dewar probe in order to control the temperature to within ± 5 mK. The heaters were taped, with a silicon adhesive Kapton® tape, to the narrowside walls of the waveguide, on the outside of the waveguide. Heaters were not used in the smaller Dewar probe since the liquid Helium was in contact with the waveguide.

3.12 Coaxial cables

Two types of coaxial cables were used for the experiments. The first type were rigid UT-40 coaxial cables with the outer and inner conductors made of Cu, and a dielectric of polytetrafluoroethylene (PTFE) between the two conductors. These coaxial cables were approximately 1.5 m in length, and were inserted into the Dewars through Ultra–Torr fittings. Sub-Miniature A (SMA) female jacks and male plugs were soldered to each end of the coaxial cables in order to connect one end to the waveguide antennas, and the other to the vector network analyzer.

The other type of coaxial cables used were phase-maintaining coaxial cables. These cables had the ability be reoriented after a calibration without changing the phase of the signal; they were purchased from Megaphase, LLC, and the model numbers were VN26–2031–30 and VN26–2032–30 for the male and female-type connectors, respectively. Each phase-maintaining cable was approximately 0.75 m in length, and they coupled the vector network analyzer to the rigid coaxial cables. On one end of each phase-maintaining cable was a 2.4 mm connector that connected to the vector network analyzer, and on the other end was a 3.5 mm connector that connected to a "safety" connector. The role of a safety connector is to protect a more expensive connector, for instance the ones on the ends of the phase-maintaining coaxial cable, by using a less expensive connector for repeated attach-detach applications. Since the end of the safety connector that is connected to the more expensive connector is rarely used, the less expensive connector may be discarded after heavy use without having to replace the more expensive connector, or the entire

cable. Safety connectors were also used to connect the vector network analyzer to the phase-maintaining coaxial cables.

3.13 Solenoid

A solenoid was constructed for the applied dc H field experiments, as shown in Figure (3.12). This solenoid was constructed by wrapping superconducting wire, made of a Nb-Ti allow from Supercon, Inc., around a cylindrical core of Bakelite, with length of 6.20 cm, and a diameter of 20.83 mm. There was a notch in the middle of the core with a width of 24.89 mm, and the Ag-plated brass X-band waveguide was placed into this notch. This aligned the cylidrical axis of the core with the midway point of the height of the Ag-plated brass X-band waveguide. The core was also turned down near both ends of the length in order to wrap the superconducting wire around the core. Copper wire was soldered to the ends of the superconducting wire, and inserted through a fitting in the smaller probe at the top of the Dewar. While the solenoid was immersed in liquid Helium, the resistance was measured to be 0.5 Ω.

The solenoid was powered by an HP E3612A dc power supply, which had a current range of 0.0 to 0.5 A, and a voltage range of 0 to 60 V. Two multimeters were used. One multimeter was connected in series, and another multimeter was connected in parallel, with the power supply in order to obtain more accurate current and voltage readings than what was read off of the E3612A display. The current was increased by hand since there were no automation capabilities.

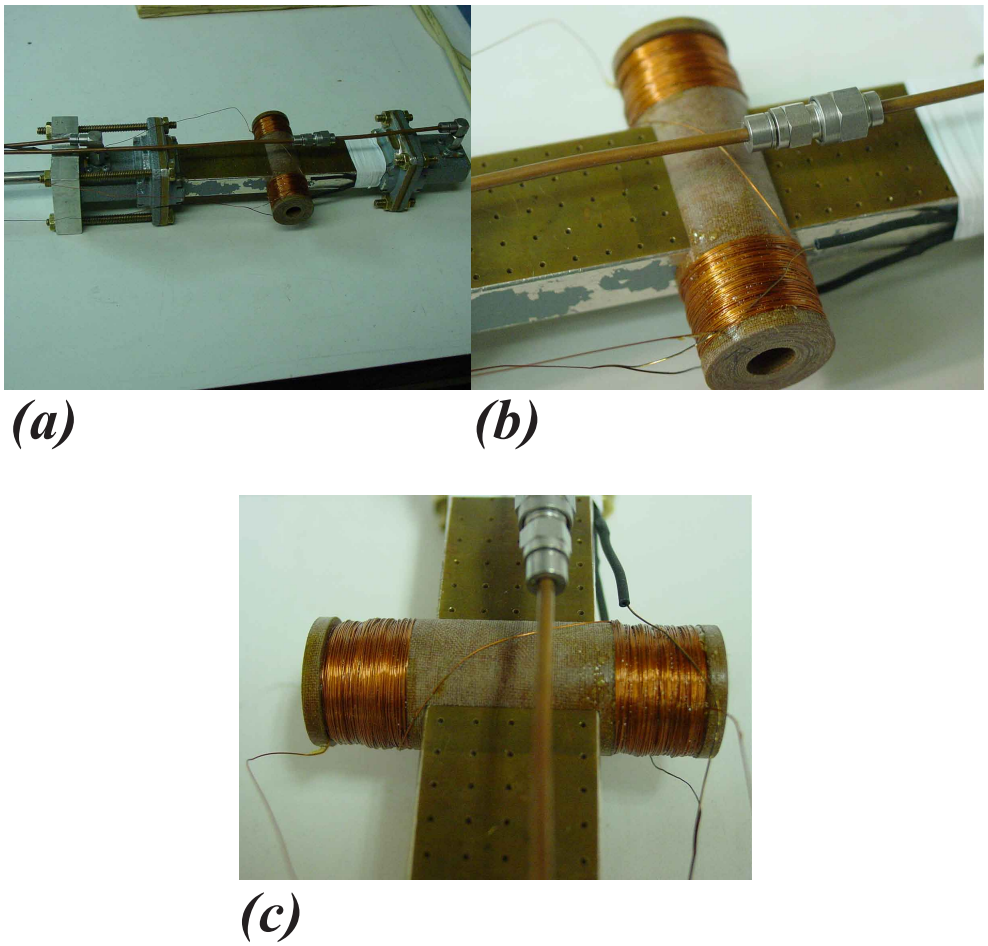

Figure 3.12: The superconducting solenoid used in the applied dc H field experiments, installed on the Ag-plated brass X-band waveguide. (a) The entire Ag-plated brass X-band waveguide with the solenoid. (b) and (c) Closeups of the solenoid on the Ag-plated brass X-band waveguide.

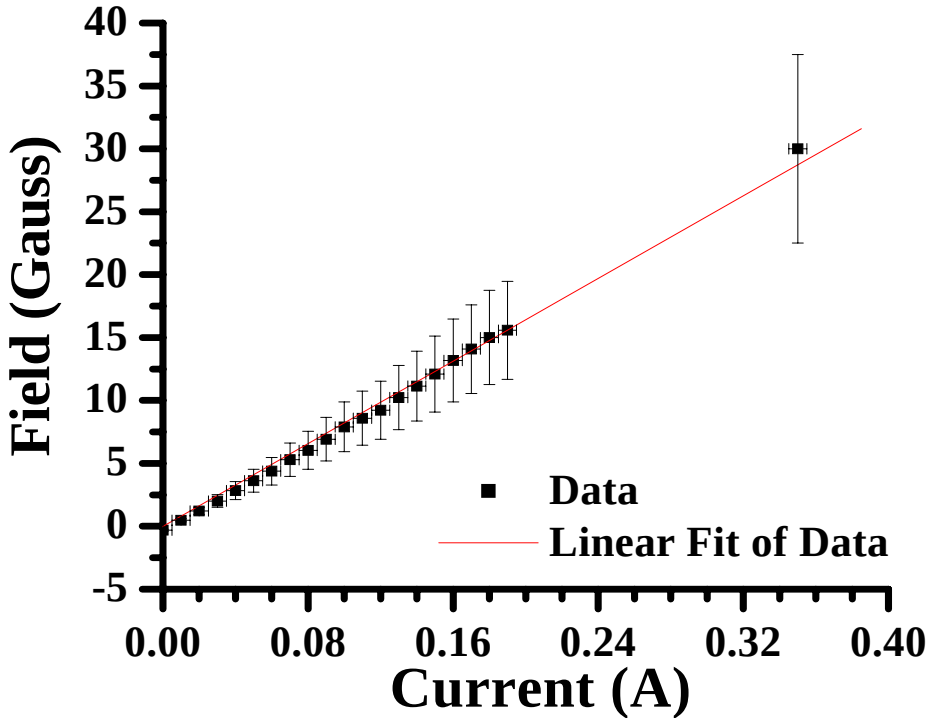

Figure 3.13: The magnetic field data and fit for the superconducting solenoid used in the applied dc H field experiments. The black squares are the data and the red line is the fit.

In order to calibrate the solenoid, the dc magnetic field along the axis of the solenoid was measured. This was performed at room temperature with the aforementioned power supply, and measured with an F. W. Bell Gaussmeter, model 9200. The results are shown in Figure (3.13). These results were fit to a line with a forced y-intercept at $y = 0$, after the measured magnetic field was plotted versus the measured current. The linear fit was calculated as,

$$B(I) = 82.084 * I, \tag{3.1}$$

where B is the magnetic field, and I is the current flowing through the solenoid.

3.14 Microwave amplifier

The effects of increasing microwave power applied to a Nb split-ring resonator were measured. For this experiment, an HP 8349B Microwave Amplifier was coupled to Port 1 of the vector network analyzer, and the output of the amplifier was coupled directly to the waveguide through the coaxial cable described earlier. This is shown in Figure (3.14). The amplifier was able to amplify the microwave signal by approximately +20 dBm. For some output powers of the vector network analyzer, this would be too much amplification for Port 2 to handle without being damaged. Thus, a −20 dB attenuator was placed directly before Port 2 of the vector network analyzer.

3.15 Vector network analyzer

A Hewlett-Packard vector network analyzer model 8722Du was used to inject the electromagnetic signal into the waveguide, and to measure the complex scattering S-parameters as a function of frequency. All experiments used the same main parameters, except for the power dependence experiment. The input power of the electromagnetic signal was −5 dBm, and the number of frequency points for all frequency ranges was 1601 frequency points. Averaging was used in order to improve the signal-to-noise ratio, and the averaging number was set at 16. Decreasing the intermediate frequency bandwidth, or IF bandwidth, also increased the signal-to-noise ratio by reducing the bandwidth of the receiver in the vector network analyzer. The IF bandwidth for the experiments was 1 kHz. A side effect of a lower IF bandwidth

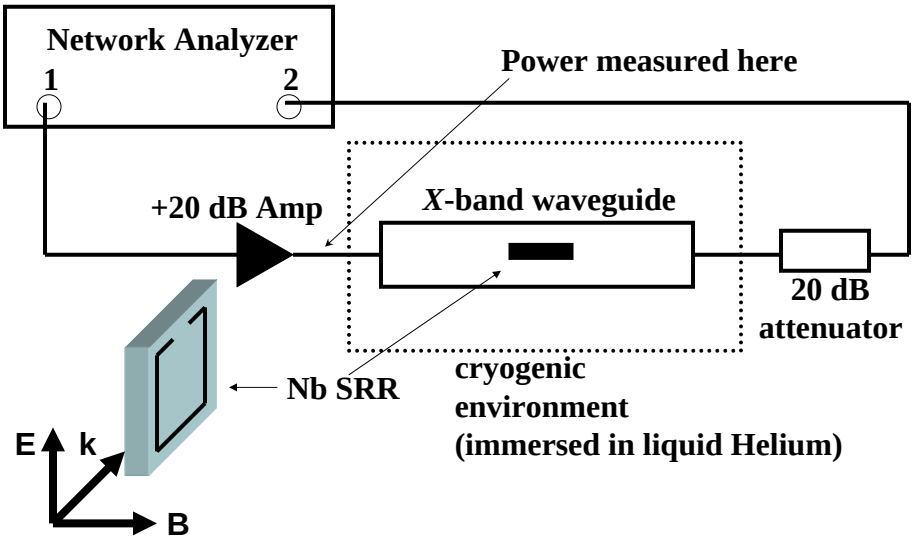

Figure 3.14: The experimental setup for the rf power experiment. A +20 dB amplifier is coupled to Port 1 of the vector network analyzer. The amplified signal is measured after the amplifier but before the waveguide. A 20 dB attenuator is used to reduce the amplified signal in order not to destroy the vector network analyzer. The bottom left figure shows the split-ring resonator orientation with respect to the applied electromagnetic field.

is that the frequency sweep takes a longer time to complete. With the averaging and IF bandwidth set as described, the total sweep time was approximatley 60 s.

3.15.1 Calibration

In order to remove any effects of the cables, the plane of calibration was moved to the very ends of the safety connectors on the phase maintaining coaxial cables. The plane of calibration was not set at the waveguide, which would have been ideal, due to the difficulties of calibrating a waveguide at low temperatures. An Agilent N4691A 3.5 mm electronic calibration kit was used to calibrate the vector network analyzer. This calibration kit was coupled to the HP 8722Du vector network analyzer with an Agilent 85097B vector network analyzer interface kit. The electronic calibration kit allowed for a calibrated frequency range of 0.5 to 26.5 GHz, however, once the range of 0.5 to 26.5 GHz was calibrated, any frequency range within this larger range was also calibrated by frequency interpolation of the error coefficients. This was useful for S-parameter features that changed with temperature, as the feature could be re-centered without losing the calibration.

An X-band calibration kit was also attempted in order to obtain a calibration to the waveguide flanges. This was a manual calibration, and used the calibration kit X7005 by Maury Microwave Corporation. This calibration was very difficult, and often resulted in peaks and dips in electromagnetic transmission with very large quality factor, and so this calibration technique was not used.

3.16 Magneto-optical imaging

The magneto-optical imaging was performed at the Ames Laboratory at Iowa State University. The setup is shown in Figure (3.15). Incident light is incident on a sample that is placed under a magneto-optical material. An applied dc H field is orthogonal to the sample. When the incident light strikes the magneto-optical material, a Faraday rotation occurs, shown in the right side of the figure. The Faraday rotated light then travels to a charge-coupled device camera, and imaged. Depending on how much the applied dc H field penetrates the superconducting film under test determines the amount of Faraday rotation of the incident light.

3.17 Computer hardware and software

The experiment was mostly controlled by a Windows-based computer. Connections between the computer and devices were made with General Purpose Interface Bus, or GPIB, cables. The software that ran the code to collect data was Matlab version 6.0.0.88 Release 12. This program was also used to analyze some of the data. Mathematica, version 5.1.1.0 was used to fit various data, and the fit of the combination of wires and a single Nb split-ring resonator was performed on a computer whose hard drive was lost, although the data was already published by this point. Microwave Studio CST version 2006B was used to simulate many experiments, however due to licensing, only limited amounts of data can be presented in this dissertation.

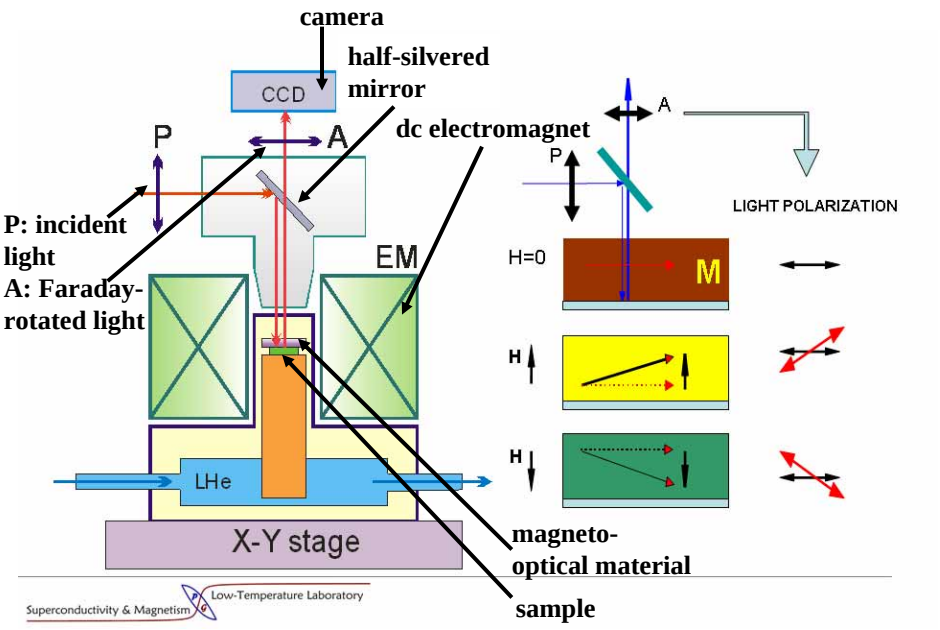

Figure 3.15: The experimental setup for the magneto-optical experiment. Incident light is directed to a sample with a half-silvered mirror. The sample is underneath a magneto-optical material, and an applied dc H field is orthogonal to the sample. The incident light experiences a Faraday rotation, shown in the right side of the figure. The Faraday rotated light travels to a charge-coupled device camera, and imaged.

3.18 Summary

The Nb wires were aquired from Advent Research Materials LTD, and the manufacture of the Cu-Ni-Au split-ring resonators was also outsourced. All Nb split-ring resonators were made in-house by rf sputtering Nb film, performing lithography, and plasma etching excess Nb. The wire and split-ring resonator properties were measured inside $X-$ and Ka-band waveguides made of either Nb or brass. These waveguides were used with two probes. One probe was immersed in liquid Helium, while the other was in vacuum, which itself was immersed in liquid Helium. A Lakeshore 340 was used to control any heaters and monitor the temperature, while an HP 8722Du vector network analyzer measured the S-parameters of the experiment. A dc solenoid was used for the applied dc H field experiment, and a magneto-optical experiment setup was also shown. A Windows-based PC controlled the entire experiment through Matlab. All analysis was performed with Matlab and Mathematica, and simulations were performed with Microwave Studio CST.

Chapter 4

Experiments on empty waveguides and on arrays of metallic wires in X-band waveguides

4.1 Overview

This chapter is concerned with methods of obtaining a negative real part of the permittivity at microwave frequencies, while minimizing losses. As stated in Chapter 2, negative real part of the permittivity is achieved through the use of an array of metallic wires [28, 34]. An empty waveguide at frequencies below the lowest cutoff frequency may also act as if the waveguide possessed an effective negative real part of the permittivity [86].

This chapter begins with electromagnetic transmission results for empty X-band and Ka-band waveguides. Comparisons of the electromagnetic transmission spectra, $|S_{21}|$, between Ag-plated brass and all-Nb X-band waveguides are also made. Next, electromagnetic transmission results for the Nb wire arrays in the Ag-plated brass X-band waveguide and the Nb X-band waveguide are shown, along with fits to these data using the three-layer transfer matrix model. The permittivity is extracted in order to estimate the loss in the Nb wire array. A comparison of the electromagnetic transmission of a Nb wire array to a Cu wire array is then presented. Finally, the chapter ends with electromagnetic transmission results for a

longitudinally-shortened Nb wire array in the Ag-plated brass X-band waveguide.

4.2 Empty X-band and Ka-band waveguides

An X-band waveguide has been described as having little or no transmission for frequencies less than the cutoff frequency, approximately 6.56 GHz, and full transmission for frequencies greater than 6.56 GHz. Experimentally, there is a lower limit to the transmission amplitude of the signal being measured, such that for values less than this limit the measuring device measures noise. In this case, the measuring device is an HP 8722Du vector network analyzer, and the noise floor is approximately -90 dB. The electromagnetic transmission, $|S_{21}|$, versus frequency is shown in Figure (4.1) for the empty Ag-plated brass X-band waveguide, denoted by the blue curve. Figure (4.1) shows several common features, such as evanescent tunneling features at approximately 4 GHz and 5.25 GHz, ringing at the cutoff frequency, and propagation of higher order modes beginning at approximately 13.1 GHz and degrading the smooth passband at about 14.7 GHz.

The red curve in Figure (4.1) is the data for the electromagnetic transmission through the Ag-plated brass X-band waveguide, with a $22.86 \times 10.16 \times 69$ mm^3 slab of Rohacell® HF centered in the waveguide. As stated in Chapter 3, Rohacell® HF has a real part of the relative permittivity almost equal to unity, and a low loss tangent, at microwave frequencies, and Figure (4.1) shows that the effects of a Rohacell® HF slab on the electromagnetic transmission are minimal, although the dip in $|S_{21}|$ at 13.1 GHz appears to have been removed.

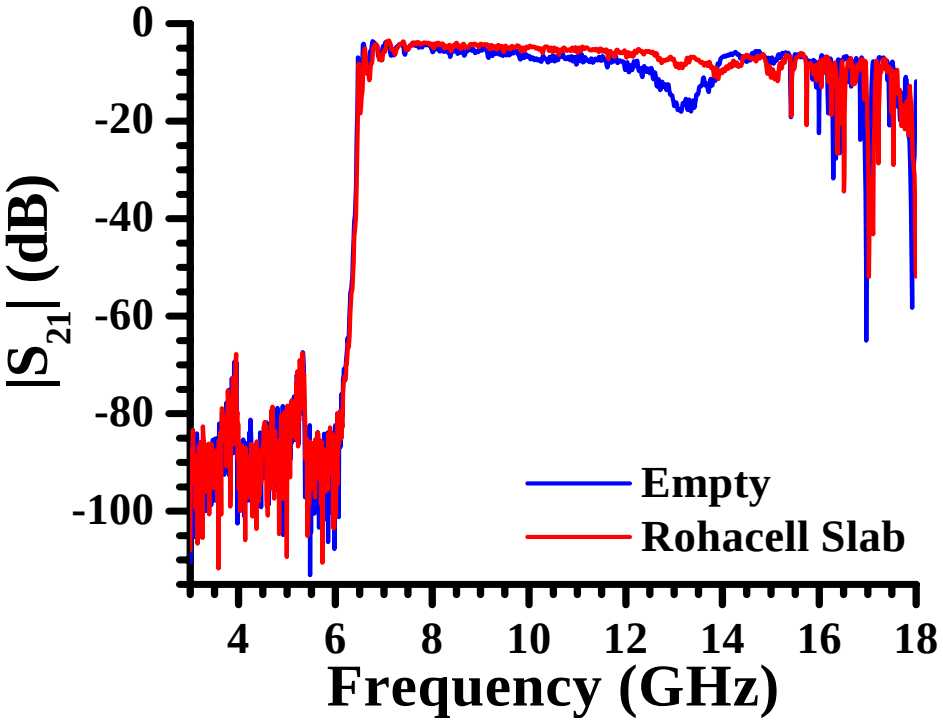

Figure 4.1: A plot of the electromagnetic transmission, $|S_{21}|$, versus frequency for an empty Ag-plated brass X-band waveguide (blue curve), and a Ag-plated brass X-band waveguide with a $22.86 \times 10.16 \times 69$ mm^3 slab of Rohacell® HF inside (red curve). Both sets of data were taken while the Ag-plated brass X-band waveguide was immersed in liquid Helium.

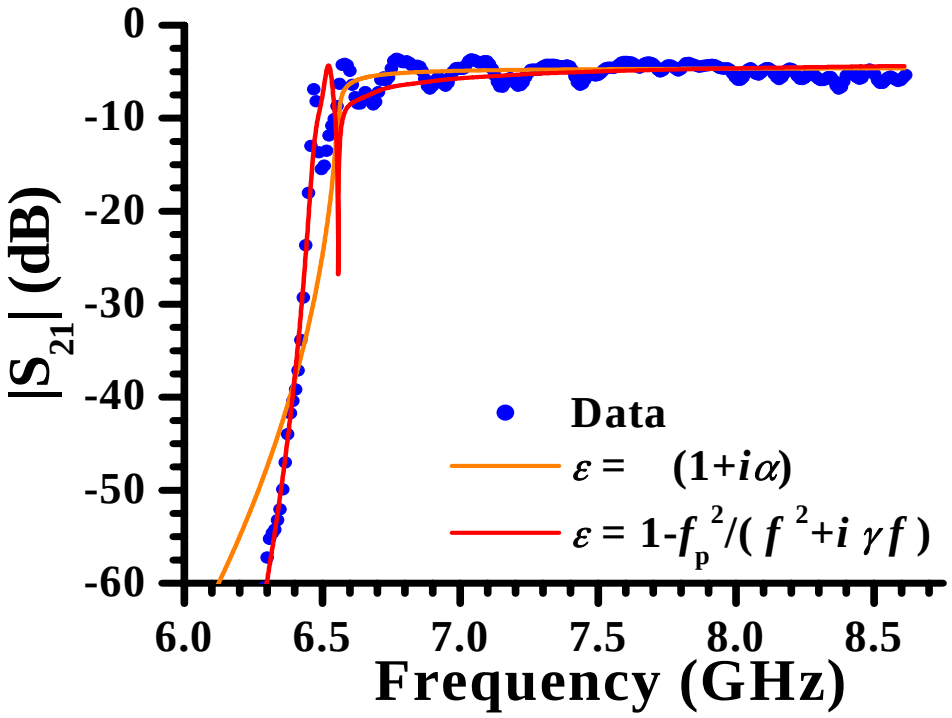

Figure 4.2: A plot of the electromagnetic transmission, $|S_{21}|$, versus frequency for an empty Ag-plated brass X-band waveguide immersed in liquid Helium, denoted by the blue circles, and two fits using the transfer matrix model. The red curve used a plasma-like permittivity, and the orange curve used a constant complex permittivity. Both used a relative permeability of $\mu = 1$.

Figure (4.2) contains the electromagnetic transmission data for the empty Ag-plated brass X-band waveguide from Figure (4.1), along with two three-layer transfer matrix model fits, shown as solid curves*. Two permittivities were used; first, a constant complex permittivity was used†,

$$\epsilon = 1 + i\alpha, \tag{4.1}$$

where α was a fit parameter. This is shown as an orange curve in Figure (4.2). Another fit was performed using the plasmalike permittivity, given in Equation (2.22). This is shown as a red curve in Figure (4.2). In both cases, the permeability was set to $\mu = 1$. The other free parameters, in the case of the plasmalike permittivity, were length, l, an overall fit constant, C, to adjust the insertion loss, and a cutoff frequency, $\omega_c = 2\pi \times f_c$. The results of both fits are tabulated in Table (4.1). Note that the cutoff frequency is not a parameter in the constant complex permittivity model, but rather determined entirely through k of Equation (2.56). The values in parentheses for α and γ in Table (4.1) were calculated using Equation (2.22), along with either the fit parameters determined by the transfer matrix model, or the theoretical values. The two methods agree with each other, and with the expected results of a cutoff frequency at approximately 6.5 GHz, a length of approximately 18.3 cm, and low losses. This implies that a waveguide can be thought of as a one-dimensional plasma, where the cutoff frequency acts as the plasma frequency [86].

*There is a sharp dip at the cutoff frequency for the transfer matrix model curves in Figure (4.2), and this comes at the frequency where $k = 0$, or $\lambda_g \to \infty$.

†Note that the permittivity and permeability used throughout this chapter are understood to be the relative permittivity and permeability, defined in Equations (2.15) and (2.16).

Table 4.1: Fit parameter results for the empty Ag-plated brass X-band waveguide.

Parameter	$\epsilon = 1 + i\alpha$	$\epsilon = 1 - \frac{\omega_p^2}{\omega^2 + i\gamma\omega}$
α	3.26×10^{-3}	$(7.58 \times 10^{-3})^a$
γ	$(2\pi \times 21.4 \text{ MHz})^b$	$2\pi \times 48.9$ MHz
l	0.131 m	0.219 m
C	-4.1 dB	-3.6 dB
ω_p	$(2\pi \times 6.56 \text{ GHz})^c$	$2\pi \times 6.45$ GHz

[a]This value was calculated using Equation (2.22).

[b]Same as previous footnote, however the other root in the solution was $\gamma = 2\pi \times 2.01$ THz.

[c]This is the theoretical cutoff frequency, ω_c.

While Ag is a very good conductor, a Nb X-band waveguide was used for most of the experiments presented in this dissertation. The comparison of the empty Nb X-band waveguide to the empty Ag-plated brass X-band waveguide is shown in Figure (4.3). Both sets of data were taken at room temperature. The electromagnetic transmission data for both waveguides are very similar, although the Nb X-band waveguide appears to have less cutoff noise, while the Ag-plated brass X-band waveguide has less transmission ripple above the cutoff frequency.

While X-band waveguides are useful for looking at split-ring resonators with a resonant frequency above the waveguide cutoff frequency, as will be shown in Chapter 5, it is also useful to observe the behavior of split-ring resonators in a waveguide with a cutoff frequency above the resonant frequency of the split-ring resonators, since a waveguide acts as a plasma along the axial direction [79]. Another type

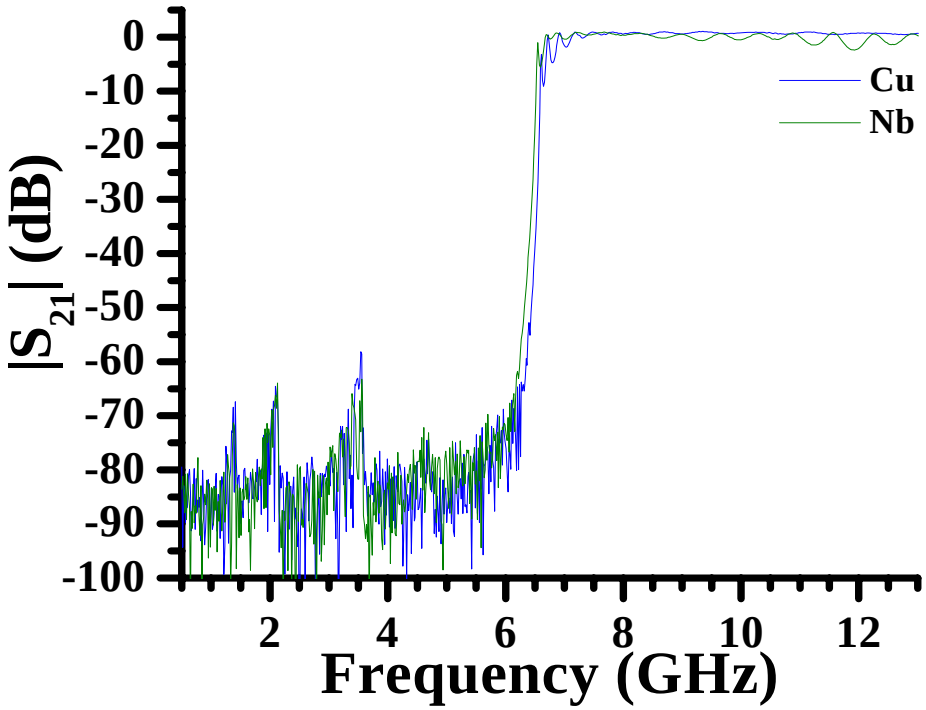

Figure 4.3: A plot of the electromagnetic transmission, $|S_{21}|$, versus frequency for an empty Ag-plated brass X-band waveguide, shown as a blue curve, and an empty Nb X-band waveguide, shown as a green curve. The data were taken at room temperature.

of waveguide used in experiments presented in this dissertation was a Ka-band waveguide, with a cutoff frequency of approximately 21 GHz. A plot of the electromagnetic transmission, $|S_{21}|$, versus frequency for an empty Ka-band waveguide at room temperature is shown as a red curve in Figure (4.4). The length of the waveguide is unknown, but it was at least 25 mm, and at most 100 mm. The data show a noise floor of approximately -90 dB from 0.5 GHz, to approximately 21 GHz. Due to standing waves inside the waveguide arising from an impedance mismatch between the waveguide and the antennas, the electromagnetic transmission at frequencies greater than 21 GHz had very narrow peaks of almost full transmission, followed by dips of approximately -20 dB.

One motivation for using the Ka-band waveguide is the evanescent modes below cutoff. Since the split-ring resonators investigated in Chapter 5 possess a resonant frequency of approximately 10 GHz, and the cutoff frequency of the Ka-band waveguide is approximately 21 GHz, the evanescent modes below the cutoff frequency of the Ka-band waveguide at the split-ring resonator resonant frequency decay rapidly with distance, as discussed in Chapter 2. This means that very little electromagnetic transmission is observed for long waveguides. However, if only the Ka-band waveguide-to-coaxial cable couplers are used, the length of the waveguide is minimized to twice the depth of the antennas from the waveguide flange. Data for two coupled Ka-band waveguide-to-coaxial cable couplers at room temperature are shown as the blue curve in Figure (4.4). Note how the edge of the cutoff frequency for the coupled waveguide-to-coaxial cable couplers is not as steep as the edge of the cutoff frequency for the case of the waveguide-to-coaxial cable couplers plus

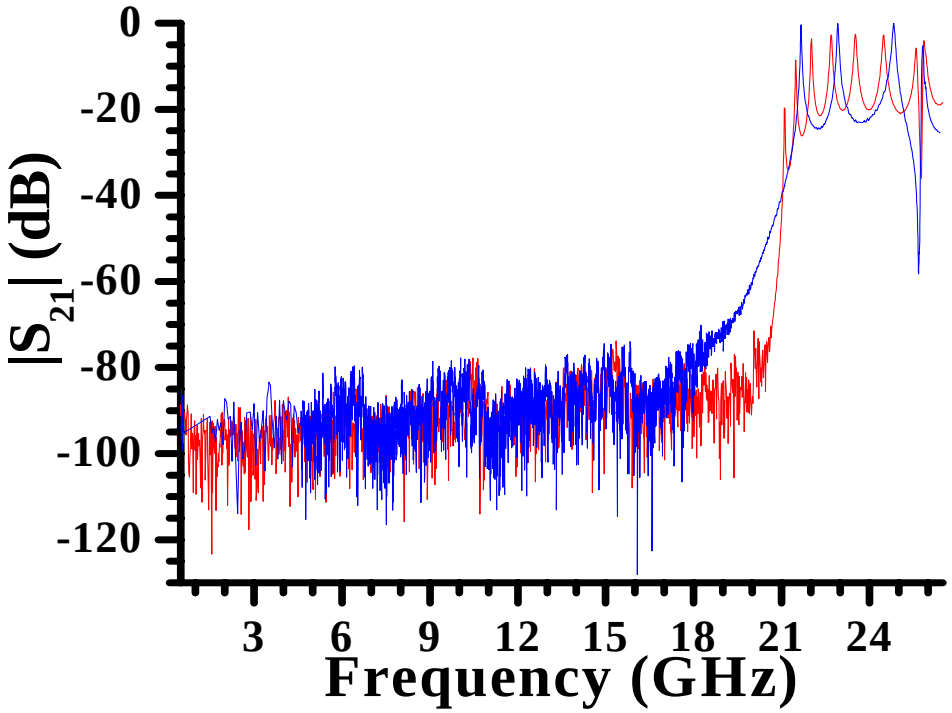

Figure 4.4: A plot of the electromagnetic transmission, $|S_{21}|$, versus frequency for an empty Ka-band waveguide. The red curve is data taken from the waveguide-to-coaxial cable couplers plus a waveguide that was at least 25 mm in length and at most 100 mm in length, while the blue curve is data taken for the case where the waveguide-to-coaxial cable couplers are directly coupled. The data for both curves were taken at room temperature.

waveguide. This is a sign of electromagnetic tunneling. The length between the antennas of the coupled waveguide-to-coaxial cable couplers is short enough to allow some evanescent modes to couple the two antennas. This produces an electromagnetic transmission spectrum with regions of transmission much greater than the waveguide-to-coaxial cable coupler plus waveguide counterpart at the same frequencies near the waveguide cutoff frequency. Once the cutoff frequency is crossed, both setups have, in principle, equal electromagnetic transmission spectra, although in practice they will have different standing wave patterns due to an impedance mismatch between the waveguide and the antennas. This is observed above 21 GHz in Figure (4.4), where the narrow peaks for each case do not align.

4.3 Nb wire arrays in X-band waveguides – long arrays

Long arrays, that is, more than twenty rows deep, of Nb wires with various lattice parameters were tested in two X-band waveguides. The first waveguide used was the Ag-plated brass X-band waveguide, where the electromagnetic transmission, $|S_{21}|$, for lattice parameters of $a = 5.08$ mm and $a = 7.19$ mm was measured at 7 K and at room temperature. The electromagnetic transmission through a Nb wire array was also measured for the Nb X-band waveguide for lattice parameters of $a = 4.57$ mm and $a = 6.47$ mm.

4.3.1 Ag-plated brass X-band waveguide

The Ag-plated brass X-band waveguide had an array of holes drilled through the broadsides with a lattice parameter of $a = 5.08$ mm in both the transverse and longitudinal directions. This allowed for an array of Nb wires to be "woven" into the waveguide, with various lattice parameters. The electromagnetic transmission, $|S_{21}|$, for the $a = 5.08$ mm and $a = 7.19$ mm lattice parameters was measured. While the $a = 5.08$ mm lattice parameter had a Nb wire in every hole drilled into the Ag-plated brass X-band waveguide broadsides, the $a = 7.19$ mm lattice parameter skipped every other hole. This is shown in Figure (4.5). This section shows the results of the electromagnetic transmission through the $a = 5.08$ mm and $a = 7.19$ mm lattice parameters at 7 K, and room temperature. A discussion on two theories, and their predictions for the plasma frequency, defined below, follows the sections on the data.

4.3.1.1 Cryogenic measurements

An electromagnetic transmission experiment was performed on the Ag-plated brass X-band waveguide with an array of Nb wires inside the waveguide. The setup for the two lattice parameters is shown in Figure (4.5), and the data are shown in Figure (4.6). The circles in Figure (4.6) are the data for the $a = 5.08$ mm lattice parameter, and the triangles are the data for the $a = 7.19$ mm lattice parameter. Since the Ag-plated brass X-band waveguide was initially immersed in liquid Helium, the data was taken when the temperature reached 7 K, when it

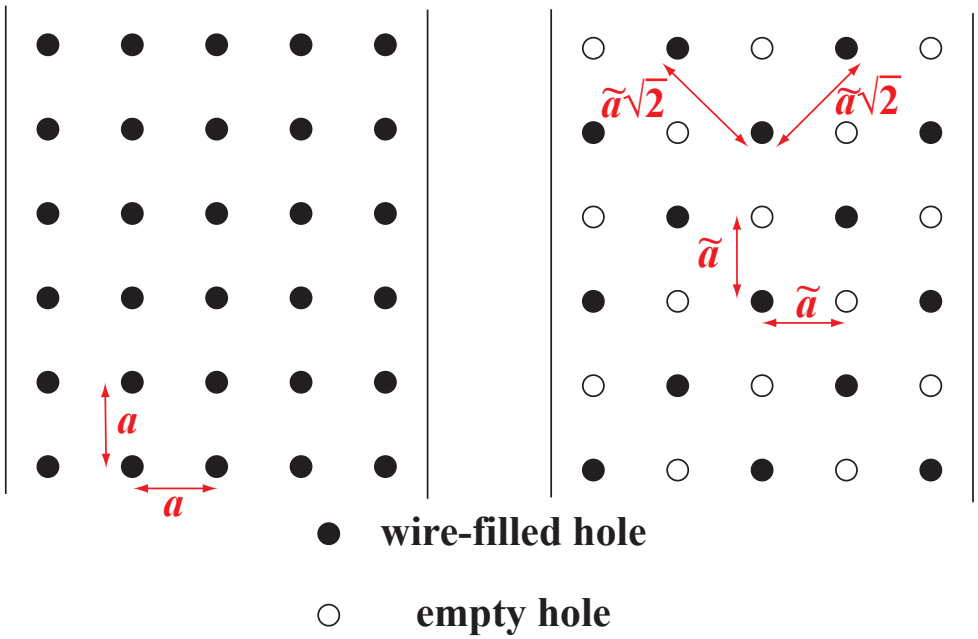

Figure 4.5: A diagram of the setup of the Nb wire arrays inside the X-band waveguides, looking along the y-axis in Figure (2.3). The left diagram is the $a = 5.08$ mm lattice parameter, and the right diagram is the $a = 7.19$ mm lattice parameter. The solid circles are holes in the X-band waveguide with a wire passing through the hole, while the empty circles are holes with no wire passing through the hole. The vertical lines are the walls of the X-band waveguide. Note that a in the left figure is equal to $\tilde{a}$ in the right figure. This diagram is not to scale.

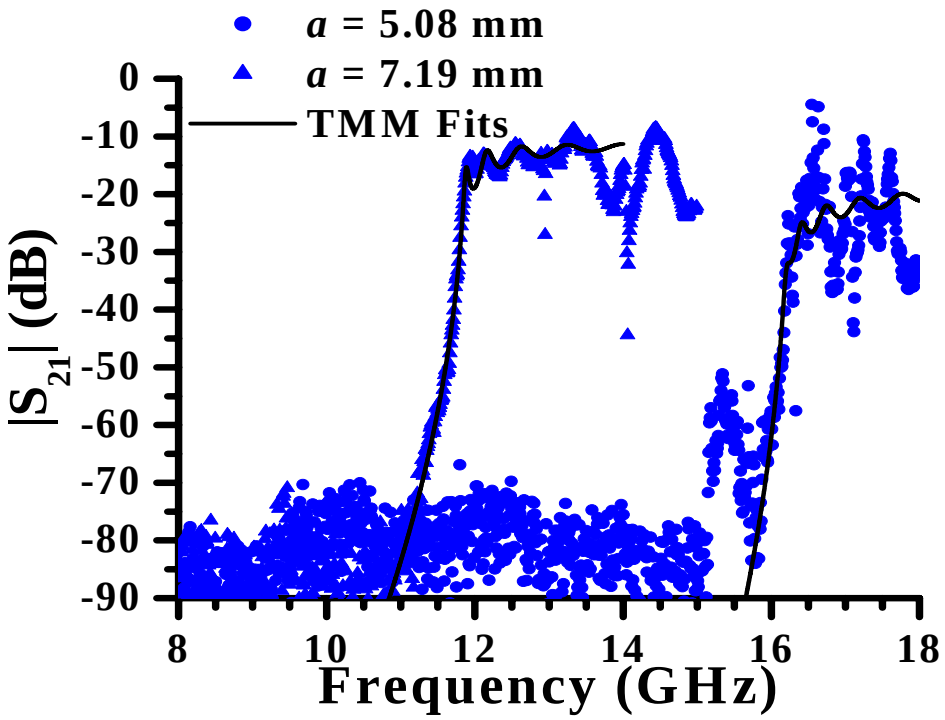

Figure 4.6: A plot of the electromagnetic transmission, $|S_{21}|$, versus frequency for a Nb wire array in the Ag-plated brass X-band waveguide at a temperature of 7 K. The blue circles are the data for the lattice parameter of $a = 5.08$ mm, while the blue triangles are the data for the lattice parameter of $a = 7.19$ mm. The black curves are the fits from the three-layer transfer matrix model.

was believed that all the liquid Helium had boiled off. This resulted in minimal shifts in frequency of the electromagnetic features in $|S_{21}|$ due to the presence of the liquid Helium dielectric. Both arrays of Nb wires increased the lowest mode cutoff frequency of the Ag-plated brass X-band waveguide. In the case of the $a = 7.19$ mm lattice parameter, the new cutoff, or plasma, frequency was within the frequency range of the TE_{10}-only mode at approximately 12.75 GHz. The $a = 5.08$ mm lattice parameter, on the other hand, had a plasma frequency at approximately 16.1 GHz, which is higher than at least two higher order modes, listed in Table (2.1).

In addition to the data in Figure (4.6), there are fits using a three-layer transfer matrix model, shown as black curves. This three-layer transfer matrix model used a plasmalike permittivity, as given in Equation (2.22), and had fit parameters of plasma frequency, ω_p, loss, γ, material length, l, and an overall constant, C, to adjust the insertion loss. The fit parameters are listed in Table (4.2). The plasma frequencies for the $a = 5.08$ mm and $a = 7.19$ mm lattice parameters were found to be, respectively, $2\pi \times 16.1$ GHz and $2\pi \times 11.8$ GHz, and the loss parameters, γ, were found to be $2\pi \times 72.0$ MHz and $2\pi \times 23.7$ MHz, respectively. The ideal frequency of operation is the frequency, ω_{-1}, such that $\Re[\epsilon(\omega = \omega_{-1})] = -1$, and the imaginary part of the permittivities at $\omega = \omega_{-1}$ were 1.26×10^{-2} and 5.70×10^{-3} for the $a = 5.08$ mm and $a = 7.19$ mm lattice parameters, respectively. The length parameters, l, were 10.1 cm and 9.92 cm for the $a = 5.08$ mm and $a = 7.19$ mm lattice parameters, respectively, which are close to the expected value of 10.16 cm.

4.3.1.2 Room temperature measurements

The Nb wire arrays in the Ag-plated brass X-band waveguide measured in Figure (4.6) were allowed to warm up to room temperature. A plot of the electromagnetic transmission, $|S_{21}|$, versus frequency for the lattice parameters of $a = 5.08$ mm and $a = 7.19$ mm at room temperature is shown in Figure (4.7). The circles are the data for the $a = 5.08$ mm lattice parameter, and the triangles are the data for the $a = 7.19$ mm lattice parameter. The most noticeable difference between Figure (4.7) and Figure (4.6) is the insertion loss. As expected, the insertion loss

Table 4.2: Fit parameter results for the Nb wire array in the Ag-plated brass X-band waveguide.

	$a = 5.08$ mm		$a = 7.19$ mm	
Temperature	7 K	RT[a]	7 K	RT[a]
$\omega_p/2\pi$ (GHz)	16.1	16.2	11.8	11.7
$\gamma/2\pi$ (MHz)	72.0	51.2	23.7	146
C (dB)	-18	-28	-11	-24
l (cm)	10.1	9.88	9.92	10.6
$\omega_{-1}/2\pi$ (GHz)	11.4	11.3	8.3	8.3
ϵ_i $(\times 10^{-2})^b$	1.26	0.903	0.570	3.53

[a]The abbreviation RT stands for room temperature.

[b]See Equation (2.24), at $\omega = \omega_{-1}$.

increased in the Nb wire arrays above $T_c \approx 9.25$ K, due to an increase in the resistivity of Nb. For the $a = 7.19$ mm lattice parameter, the three-layer transfer matrix model fit parameter γ was $2\pi \times 146$ MHz, however for the $a = 5.08$ mm lattice parameter, the result was less clear. The three-layer transfer matrix model returned $\gamma = 2\pi \times 51.2$ MHz, which is less than the γ from the three-layer transfer matrix model fit to the Nb wire array at 7 K. One possible reason is that the data did not have a smooth passband above the cutoff frequency for the $a = 5.08$ mm lattice parameter due to higher order modes, making it difficult to fit the data. The imaginary parts to the permittivities of the $a = 5.08$ mm and the $a = 7.19$ mm lattice parameters were 9.03×10^{-3} and 3.53×10^{-2} at frequencies of $\omega_{-1} = 2\pi \times 11.7$ GHz and $2\pi \times 8.3$ GHz, respectively, while the plasma frequencies were 16.2 GHz and 11.7 GHz, respectively. The fit parameters are tabulated in Table (4.2).

4.3.1.3 Comparison of two theories to the data

There were two competing theories discussed in Chapter 2 that predict the plasma frequency for a given lattice parameter and wire radius of an array of metallic wires. The first theory was derived by Pendry, and others, in CE 1996 [34]. The other theory was derived by Pokrovski and Efros in CE 2003 [55]. These theories were described in Chapter 2 in detail. For the Nb wire arrays in the Ag-plated brass X-band waveguide, the filling, or volume, fractions defined through Equation (2.94), with a wire radius, $r = 0.127$ mm, and a lattice parameter, a, were approximately 1×10^{-3} and 2×10^{-3} for the $a = 7.19$ mm and $a = 5.08$ mm lattice parame-

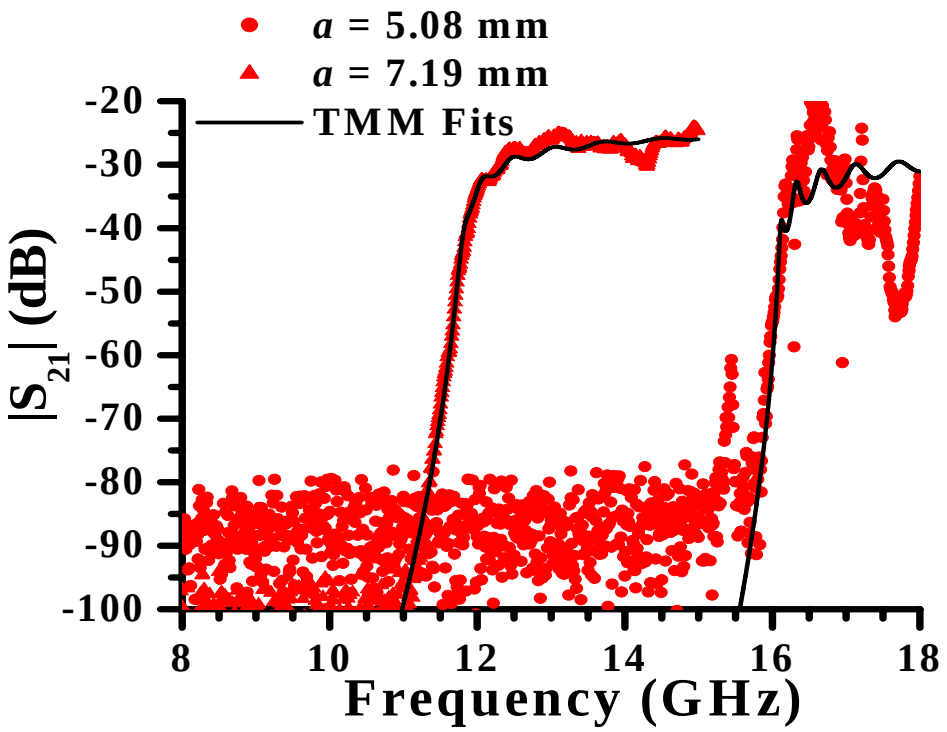

Figure 4.7: A plot of the electromagnetic transmission, $|S_{21}|$, versus frequency for a Nb wire array in the Ag-plated brass X-band waveguide at room temperature. The red circles are the data for the lattice parameter of $a = 5.08$ mm, while the red triangles are the data for the lattice parameter of $a = 7.19$ mm. The black curves are the fits from the three-layer transfer matrix model.

Table 4.3: Comparison of theories to the three-layer transfer matrix model.

	$\omega_p/2\pi$ (GHz)		
lattice parameter	Fit[a]	Pendry[b]	Pokrovsky[c]
$a = 7.19$ mm	11.8	9.7 (11.7)[d]	10.0 (11.9)
$a = 5.08$ mm	16.1	14.6 (16.0)	16.9 (18.1)

[a]The superconducting value at 7 K is used. See Table (4.2).

[b]From Equation (2.95) with the minus sign correction as discussed in Appendix A. See also Reference [34].

[c]From Equation (8) of Reference [55].

[d]Values in parentheses are from Equation (4.2).

ters, respectively. The values of χ_0, used in the theory of Pokrovsky and Efros, in Equation (8) of Reference [55], were read off of Figure (1) of Reference [55], and the plasma frequencies were estimated to be [45] 10.0 GHz and 16.9 GHz for the $a = 7.19$ mm and $a = 5.08$ mm lattice parameters, respectively. The theory of the Pendry group used Equation (2.95) with the minus sign correction as discussed in Appendix A, with $r = 0.127$ mm as the wire radius and a as the lattice parameter, and predicted plasma frequencies of 9.7 GHz and 14.6 GHz for the $a = 7.19$ mm and $a = 5.08$ mm lattice parameters, respectively. The results are shown in Table (4.3).

One issue with the theories used to predict the observed plasma frequencies is that the theories were not derived for a waveguide geometry. A solution to this problem is to add the waveguide cutoff frequency to the predicted values, in quadra-

ture. A better prediction of the plasma frequency of a metallic wire array inside a waveguide is then given by Equation (2.62),

$$\omega_p = \sqrt{\omega_T^2 + \omega_c^2}, \tag{4.2}$$

where ω_T is the plasma frequency predicted by the theories of the Pendry and Pokrovsky groups, and ω_c is the waveguide cutoff frequency. This equation was discussed in Chapter 2, in Equation (2.62). The new predictions are shown in Table (4.3) in parentheses.

4.3.2 Nb X-band waveguide

Although the empty Nb X-band waveguide had approximately the same insertion loss as the Ag-plated brass X-band waveguide, as shown in Figure (4.3), the Nb X-band waveguide has the ability to screen any stray magnetic fields that pass through the mu-metal shield surrounding the base of the cryogenic Dewar. Another advantage of the Nb X-band waveguide is the lattice parameter of the holes drilled in the broadsides. The chosen parameter was $a = 4.57$ mm, because this would allow the image of the wires in the wall of the waveguide to be at the same lattice parameter*. The lattice parameter of the drilled holes in the Nb X-band waveguide was smaller than the lattice parameter of the drilled holes in the Ag-plated brass X-band waveguide by 0.51 mm, and made wiring the Nb X-band waveguide much more difficult. The shorter lattice parameter meant that the Nb wire had a smaller

*The Ag-plated brass X-band waveguide had an image with a lattice parameter of $a = 2.54$ mm for the wires closest to the wall.

turning radius between the holes, and this caused the wires to have a very noticeable curve inside the Nb X-band waveguide. Thus, the wires were no longer parallel to the applied transverse electric field, as shown in Figure (3.9). The electromagnetic transmission through the Nb wire array in Figure (3.9) is shown in Figure (4.8) for two lattice parameters.

The green curve in Figure (4.8) is data for the lattice parameter of $a = 4.57$ mm, while the blue curve is data for a lattice parameter of $a = 6.47$ mm. Both sets of data were taken while the waveguides were immersed in liquid Helium. The data making up the blue curve was taken using a Nb X-band waveguide with Nb waveguide-to-coaxial cable couplers, however the waveguide-to-coaxial cable couplers used for the data of the green curve are unknown, but where either the Nb or Cu waveguide-to-coaxial cable couplers. This is significant because the flanges of the Nb X-band waveguide had curvature due to the tightening of the nuts that held the Nb X-band waveguide and Nb waveguide-to-coaxial cable couplers together. When the Cu waveguide-to-coaxial cable couplers were used rather than the Nb waveguide-to-coaxial cable couplers with the Nb X-band waveguide, the curvature in the flange prohibited a tight seal between the waveguide and the waveguide-to-coaxial cable coupler. Thus, there was a gap between the Cu waveguide-to-coaxial cable couplers and the Nb X-band waveguide. An electromagnetic wave can leak through a gap, creating a surface wave on the outside of the Nb X-band waveguide that travels to the other gap and produces a substantial amount of transmission for a metallic wire array when there should be just the noise floor, such as the frequency bandwidth of approximately 6.5 GHz to approximately 12 GHz for the blue curve,

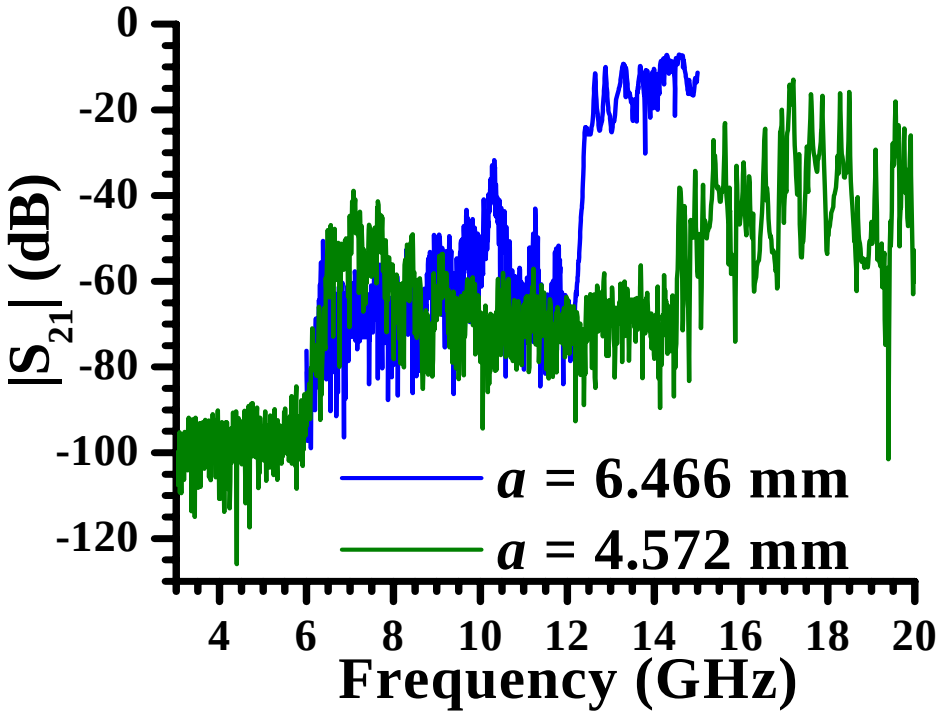

Figure 4.8: A plot of the electromagnetic transmission, $|S_{21}|$, versus frequency for a Nb wire array in a Nb X-band waveguide immersed in liquid Helium. The green curve is for a lattice parameter of $a = 4.57$ mm, while the blue curve is for a lattice parameter of $a = 6.47$ mm. The Nb wires inside the Nb X-band waveguide were not straight, and therefore not parallel to the applied transverse electric field. See Figure (3.9). Note that the waveguide-to-coaxial cable couplers for the $a = 6.47$ mm lattice parameter were made of Nb, however the waveguide-to-coaxial cable couplers for the $a = 4.57$ mm lattice parameter were either the Nb or the Cu waveguide-to-coaxial cable couplers.

or approximately 14 GHz for the green curve, in Figure (4.8).

4.4 Comparison of $|S_{21}|$ between a Cu wire array and a Nb wire array in the Ag-plated brass X-band waveguide

Since many of the wire arrays used in experiments by other groups were made of Cu wires, for instance, Reference [41], it is necessary to compare the electromagnetic transmission of a superconducting Nb wire array to the electromagnetic transmission of a Cu wire array at the same temperature, as well as observe how the electromagnetic transmission of a Cu wire array changes with temperature. Figure (4.9) shows the result of metallic wire arrays in the Ag-plated brass X-band waveguide. The black curve is a Nb wire array, and the blue curve is a Cu wire array. Both sets of data were taken while the Ag-plated brass X-band waveguide was immersed in liquid Helium, and the lattice parameter was $a = 5.08$ mm for both sets of data. The data suggests that in this geometry, both Cu and Nb wire arrays produce the same plasma edge, and have similar insertion losses above the plasma edge, despite the superconducting nature of the Nb metal. The inset shows the same Cu wire array measured in the main figure at two temperatures. The low temperature measurement is the same data as the main figure, and the high temperature data was taken at room temperature. Note that both sets of data are very similar in terms of the plasma frequency, and passband insertion loss. All these data imply that a room temperature Cu wire array performs as well as a Nb wire array, in terms of the plasma frequency and passband insertion loss. While this may be true for

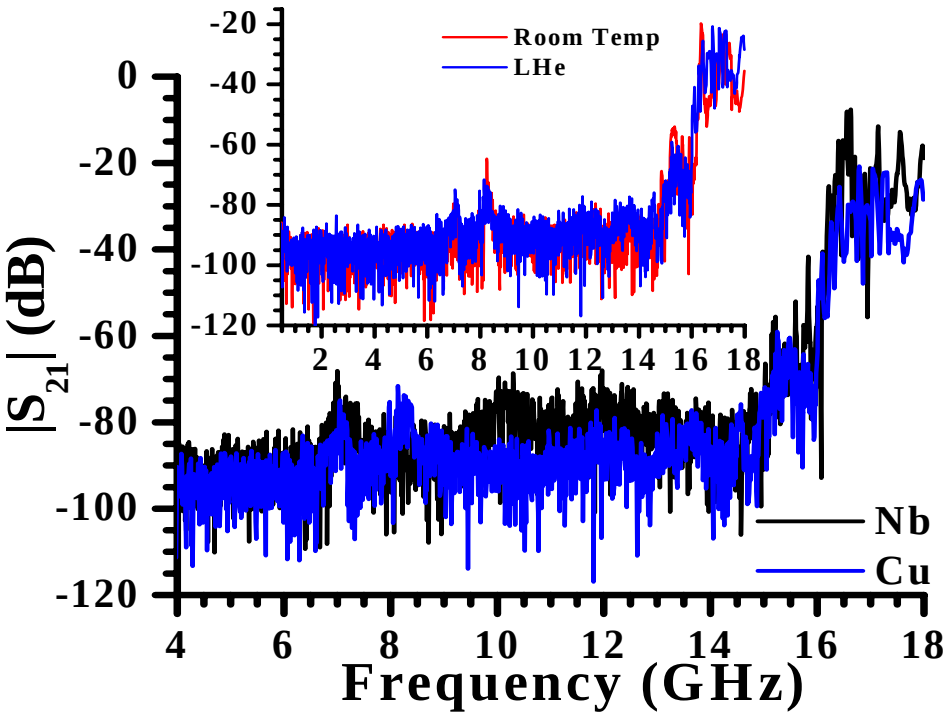

Figure 4.9: A plot of the electromagnetic transmission, $|S_{21}|$, versus frequency for the Ag-plated brass X-band waveguide immersed in liquid Helium, with a Nb wire array (black curve) and a Cu wire array (blue curve). In all cases, the lattice parameter was $a = 5.08$ mm. *Inset*: The Cu wire array data at room temperature (red curve) and immersed in liquid Helium (blue curve), abbreviated as LHe.

the wire arrays, this is not true for single split-ring resonators, as will be shown in Chapter 6.

4.5 Nb wire arrays in the Ag-plated brass X-band waveguide – short arrays

The theory that an array of metallic wires will produce a plasmalike permittivity assumes that the wire array is infinite in three dimensions. However,

experimentally the extent of the metallic wire array is finite. The electromagnetic transmission of two arrays of Nb wires with different lengths was measured in the Ag-plated brass X-band waveguide while immersed in liquid Helium. The red curve is data taken from a Nb wire array with five wires transverse, and seven wires deep, with a lattice parameter of $a = 5.08$ mm, for a total length of 3.05 cm. The blue curve is data taken from a Nb wire array with five wires transverse, and five wires deep, with a lattice parameter of $a = 5.08$ mm, and a total length of 2.03 cm. Each Nb wire array was centered in the waveguide, so that the distance from an antenna to a face of the Nb wire array was equal for both antennas. Even though, for this lattice parameter, the cutoff frequency is approximately 16 GHz, there was significant electromagnetic transmission in the five-by-five Nb wire array for frequencies less than 16 GHz. The five-by-seven Nb wire array had a similar electromagnetic transmission spectrum, although the amount of transmission was less than the five-by-five Nb wire array.

Both Nb wire arrays in Figure (4.10) have increasing electromagnetic transmission as the plasma frequency is approached from values of frequency less than the plasma frequency. The explanation for the increase in electromagnetic transmission is the tunneling of the non-propagating electromagnetic waves through the Nb wire array. For regions outside the metallic wire array, the applied electromagnetic field is a propagating wave. Once inside the metallic wire array, the wave is non-propagating if the frequency is less than the plasma frequency. However, if the metallic wire array is short enough, the wave can tunnel through to the opposite side. This is an analog to tunneling in quantum mechanics [107], and is also observed

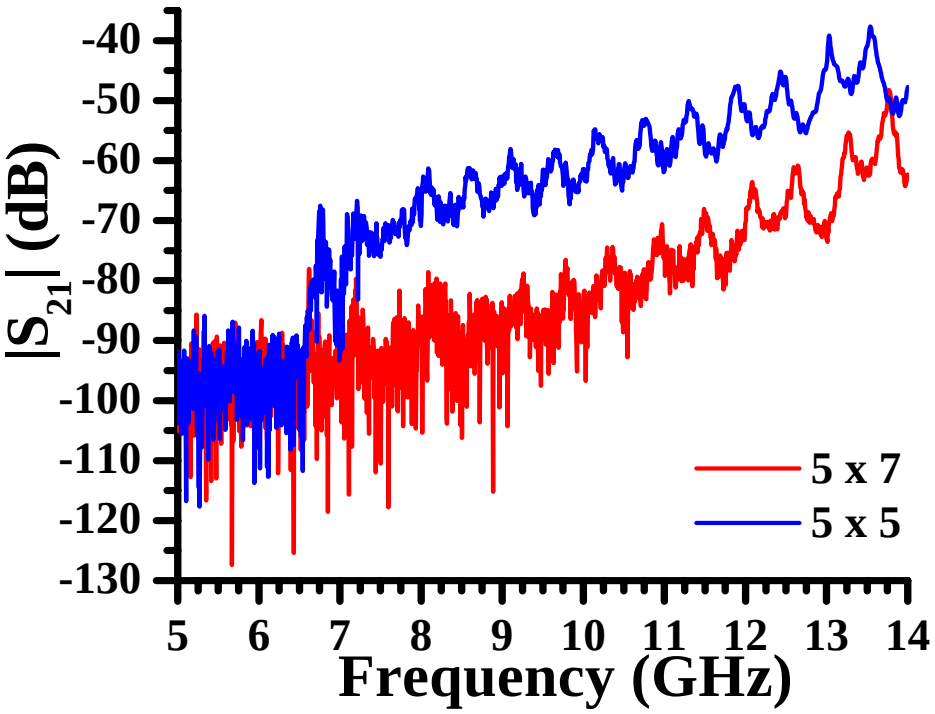

Figure 4.10: A plot of the electromagnetic transmission, $|S_{21}|$, versus frequency for a Nb wire array in the Ag-plated brass X-band waveguide. The red curve corresponds to an array of five wires transverse and seven wires deep, while the blue curve is data taken for a Nb wire array with five wires transverse and five wires deep. In both cases, the wires were symmetric with respect to the center of the Ag-plated brass X-band waveguide, and the waveguide was immersed in liquid Helium.

in total internal reflection in a prism [108] where an evanescent wave forms on the prism-dielectric boundary, and can tunnel through space and become a propagating wave if another prism brought close to the original prism.

The results in Figure (4.10) can be modeled with the three-layer transfer matrix model. Figure (4.11) shows three curves, black, red, and blue, that correspond to medium lengths of 10 cm, 1 cm, and 1 mm, respectively. The permittivity used for these curves was Equation (2.22), with $\omega_p = 2\pi \times 16$ GHz, and $\gamma = 2\pi \times 100$ MHz. The plots show that the plasma edge is very sharp for long media, but has a more gentle slope for shorter media, as the electromagnetic signals can tunnel through the shorter media and appear as propagating signals on the opposite side of the shorter media.

4.6 Summary

The electromagnetic transmission, $|S_{21}|$, of empty waveguides of types X-band and Ka-band was measured. The Ka-band waveguide was made of Cu, while the X-band waveguides were made of either brass with the interior coated in Ag, or Nb. Data showed a cutoff frequency, ω_c, of approximately $2\pi \times 6.5$ GHz for the X-band waveguides, and $2\pi \times 21$ GHz for the K-band waveguide, in agreement with theory. A three-layer transfer matrix model was used to model the empty Ag-plated brass X-band waveguide, using a constant complex permittivity, and with a plasmalike permittivity. Both results were in agreement with each other. The electromagnetic transmission of metallic wire arrays made of Cu and Nb was

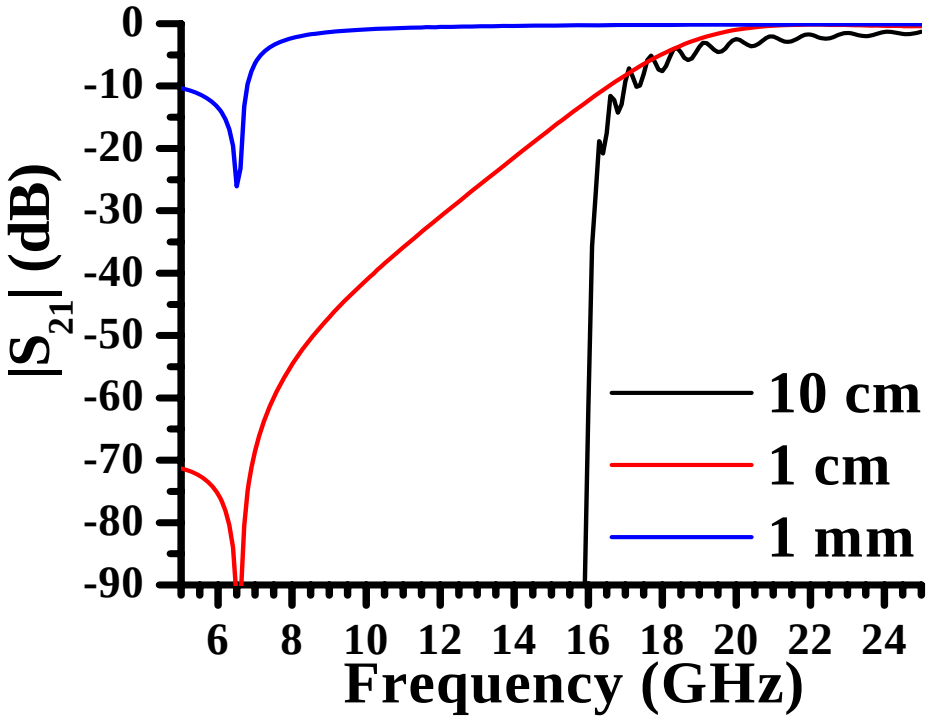

Figure 4.11: A plot of the electromagnetic transmission, $|S_{21}|$, calculated from the three-layer transfer matrix model with a plasmalike permittivity, versus frequency for various medium lengths. The black curve is a medium 10 cm in length, the red line a medium 1 cm in length, and the blue curve a medium 10 mm in length. The parameters used to calculate these curves were $\omega_p = 2\pi \times 16$ GHz, and $\gamma = 2\pi \times 100$ MHz.

measured in the Ag-plated brass X-band waveguide and the Nb X-band waveguide. The electromagnetic transmission results of the Nb wire array in the Ag-plated brass X-band waveguide measurement were fit with the three-layer transfer matrix model for 7 K and room temperature, for lattice parameters of $a = 5.08$ mm, and $a = 7.19$ mm. Results showed an increase in losses above the T_c of the Nb wires for the $a = 7.19$ mm lattice parameter, however for the $a = 5.08$ mm lattice parameter the results were less clear since the plasma frequency was greater than at least two higher order modes of the X-band waveguide. Comparison of the fitted plasma frequency from the three-layer transfer matrix model to theories by the Pendry group, and Pokrovsky and Efros, showed that the predicted plasma frequencies were less than the observed frequencies. The explanation for this result was that the theories were derived for an infinite plane wave rather than inside a waveguide, and for infinite media. Adding the waveguide cutoff frequency in quadrature to the predicted values was in better agreement with the results from the three-layer transfer matrix model fits. The electromagnetic transmission of a Nb wire array in the Nb X-band waveguide showed the importance of having the wires parallel to the applied transverse electric field. A comparison of the electromagnetic transmission results of a Nb wire array to that of a Cu wire array showed that both types of metal give very similar $|S_{21}|$ spectra. Finally, the electromagnetic transmission results of a Nb wire array with various longitudinal lengths showed a sloping edge for short arrays, and a sharper, step-function-like edge for longer arrays.

Chapter 5

Experiments and simulations of arrays of split-ring resonators

5.1 Overview

The last chapter tested the theory of an array of wires producing a frequency region where the real part of the permittivity is negative. The electromagnetic transmission was measured as a function of frequency, and the result was the increase of the cutoff frequency of the empty waveguide when a wire array was introduced. In keeping with the theory described in Chapter 2, it is now necessary to design a material that can not only produce a frequency-dependent permeability, such that the real part of the permeability is negative over a limited frequency bandwidth, but also a material that may eventually be combined with the wire arrays in Chapter 4.

In Chapter 2, the theory of creating a frequency-dependent permeability, such that the real part of the permeability is negative over a limited frequency bandwidth, from an array of split-cylinders was described. Unfortunately, inserting an entire split-cylinder of Nb into an X-band waveguide would be impractical, and would disrupt a wire array. However, it was mentioned that rather than an entire split-cylinder, cross sectional slices may be used, such that for a long enough wavelength of incident radiation, the structure would appear as a whole split-cylinder. These split-ring resonators, as they are called, were introduced in Chapter 3, and their electromagnetic transmission spectra are now discussed.

First, the electromagnetic transmission of an array of Cu-Ni-Au split-ring resonators is shown, and has a single dip at the resonant frequency of the split-ring resonators, while similar arrays of Nb split-ring resonators produced multiple dips in electromagnetic transmission, presumably due to the low-loss nature of the Nb films. The electromagnetic transmission results of the large arrays of Nb split-ring resonators are qualitatively modeled by an average permeability, summed over each split-ring resonator in the larger array. Smaller arrays are then shown to have as many dips as Nb split-ring resonators in the array, and the electromagnetic transmission of a single Nb split-ring resonator is measured. The change in resonant frequency and quality factor with temperature is measured and modeled. The change with applied dc H field, and with applied power are measured. Magneto-optical imaging of a single Nb split-ring resonator is presented in order to explain the data from the applied dc H field experiment by showing the film quality and locations where magnetic vortices can enter and leave the Nb film. Photoresponse imaging of a $YBa_2Cu_3O_{7-\delta}$ split-ring resonator is presented in order to explain the data from the applied power experiment by showing the current buildup in the inside corners of the split-rings, which leads to thermal runaway, destroying superconductivity in the split-ring resonators. Experiments investigating the electromagnetic transmission spectra of single split-ring resonators, made of $YBa_2Cu_3O_{7-\delta}$, and Cu-Ni-Au, and an experiment using a closed-ring resonator, show that these resonators do not produce a frequency bandwidth where the real part of the permeability is negative, like the single Nb split-ring resonator. Finally, experimental data investigating perturbations of a single Nb split-ring resonator by a wall of the waveguide, and wires,

are shown, and the bianisotropy of the split-ring resonators is presented with electromagnetic transmission spectra of various orientations with respect to the applied electromagnetic field.

5.2 Array of 216 Cu-Ni-Au split-ring resonators

Previous experiments, as discussed in Chapter 1, used normal metal split-ring resonators at room temperature in order to create an artificial medium with an effective permeability. An array of 216 Cu-Ni-Au split-ring resonators, as described in Chapter 3, were measured at room temperature in the Ag-plated brass X-band waveguide. The results of the electromagnetic transmission, $|S_{21}|$, versus frequency are shown in Figure (5.1). Rohacell® HF was used to keep the Cu-Ni-Au split-ring resonators in the proper orientation, that is, with the rings coupling to the applied transverse magnetic field, such as that shown in Figure (3.8.d). The frequency regions of interest are as follows. The region of little transmission, that is, $|S_{21}| \approx -90$ dB, from 4 GHz to approximately 6.5 GHz, was due to the cutoff frequency of the Ag-plated brass X-band waveguide.

The second frequency region of interest in Figure (5.1) is approximately 9 GHz to approximately 10.5 GHz. Within this frequency region, the real part of the permeability is assumed to be less than zero, according to the model discussed in Chapter 2. The actual limits of frequency where the real part of the permeability is less than zero is not clear from these plots of electromagnetic transmission, $|S_{21}|$, versus frequency, the only way to determine the exact frequency range where the

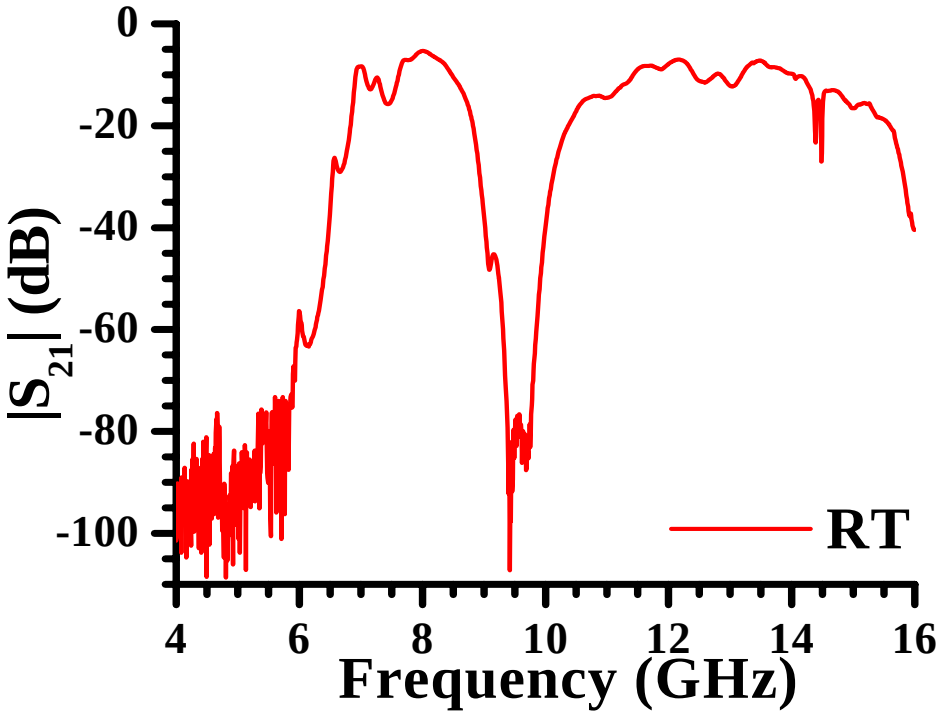

Figure 5.1: A plot of the electromagnetic transmission, $|S_{21}|$, versus frequency for an array of 216 Cu-Ni-Au split-ring resonators, measured at room temperature, abbreviated as RT in the figure, in the Ag-plated brass X-band waveguide. Rohacell® HF was used to orient the Cu-Ni-Au split-ring resonators.

real part of the permeability is negative is to calibrate the experiment up to the edges of the Cu-Ni-Au split-ring resonator array, and extract the permittivity and permeability from the electromagnetic transmission, and electromagnetic reflection data. However, for all further discussion of the matter, it is assumed that deep, or sharp, dips in the TE_{10} mode, where there should otherwise be approximately full transmission, are due to a negative real part of the permeability, as discussed in the description of the transfer matrix model. Thus, the two sharp dips at approximately 14.5 GHz may be due to a higher order resonance of the Cu-Ni-Au split-ring resonators, or may be due to higher order waveguide modes. Higher order modes of the split-ring resonators will not be discussed in this chapter, except for the $YBa_2Cu_3O_{7-\delta}$ photoresponse measurement. Higher order modes are discussed in Chapter 6. Finally, the third frequency region of interest is where there is nearly full transmission, that is, $|S_{21}| \approx 0$ dB. In this case, both real parts of the permittivity and permeability are positive, and any deviations from $|S_{21}| = 0$ dB are due to losses.

5.3 Arrays of 216 and 108 Nb split-ring resonators

From the preceding section, it was originally thought that an array of 216 Nb split-ring resonators would produce an electromagnetic transmission spectrum similar to the Cu-Ni-Au split-ring resonators, as shown in Figure (5.1), except the metallic and substrate losses would be less in the case of the Nb split-ring resonators. However, this was not the case. Figure (5.2) shows a plot of the electromagnetic

transmission, $|S_{21}|$, versus frequency for an array of 216 Nb split-ring resonators, measured in liquid Helium, denoted by the blue curve, and at 10.0 K, denoted by the red curve, in the Ag-plated brass X-band waveguide [109]. Note how the data taken in liquid Helium do not form a single, large dip in transmission, as in Figure (5.1). Rather, there are shallow, but very sharp, that is, high quality factor, dips in transmission between approximately 10 GHz, and 11 GHz. It is believed that these sharp dips in transmission are individual resonances of the split-ring resonators. In other words, rather than acting as a single, homogeneous medium, the individual Nb split-ring resonators are interacting with their environment, for instance, with the waveguide walls, and thus perturbing the resonance frequency so that the Nb split-ring resonators are not all resonating at the same frequency. It also appears, in the data taken at 10.0 K, that above the critical temperature of the Nb split-ring resonators, the large losses in the normal-state Nb reduce the quality factor of the Nb split-ring resonators, and force them to resonate at the same frequency. This is in fact not the case, and it will be shown in Chapter 6 that the dip at approximately 10.5 GHz is not a frequency region where the real part of the permeability is negative, but rather just a resonance of the normal-metal Nb split-ring resonators, producing large losses, and thus reducing the electromagnetic transmission.

The electromagnetic transmission through an array of 108 Nb split-ring resonators is shown in Figure (5.3). This array is similar to the larger, 216 Nb split-ring resonator array with the shallow, sharp dips in electromagnetic transmission. However, the distribution of resonances appeared to be within a larger bandwidth. It

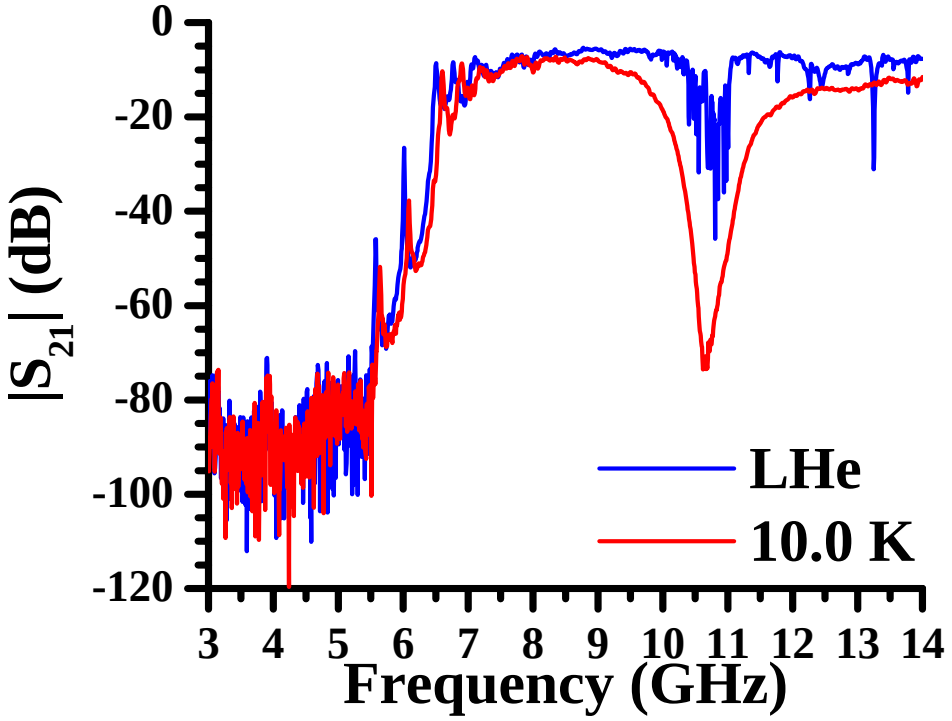

Figure 5.2: A plot of the electromagnetic transmission, $|S_{21}|$, versus frequency for an array of 216 Nb split-ring resonators, measured in liquid Helium, denoted by the blue curve, and at 10.00 K, denoted by the red curve, in the Ag-plated brass X-band waveguide. Rohacell® HF was used to orient the Cu-Ni-Au split-ring resonators.

is believed that the Nb split-ring resonators resonated within a frequency region of 9.50 GHz to 11.25 GHz. This seems contradictory, since the larger 216 Nb split-ring resonator array should be expected to have more dips in electromagnetic transmission and a larger frequency spread of negative permeability compared to the 108 Nb split-ring resonator array because there are twice as many Nb split-ring resonators in the 216 Nb split-ring resonator array than the 108 Nb split-ring resonator array. There may be more overlapping of resonant frequencies in the 216 Nb split-ring resonator array, however, the difference in the appearances of Figures (5.2) and (5.3) is not given here.

Fitting the electromagnetic transmission in Figure (5.2) or Figure (5.3) with the three-layer transfer matrix model was too difficult to provide reasonable fit parameters, since the number of fit parameters necessary is too large, and so rather than attempt to fit the data in Figures (5.2) and (5.3), the main features of the data were modeled [109]. Assuming that there are 108 dips between approximately 9.75 GHz and approximately 11.50 GHz in Figure (5.3), it stands to reason that there are 108 individual resonances from the 108 Nb split-ring resonators. However, rather than write all of these individual relative permeabilities, an average relative permeability is taken,

$$\mu_{\text{avg}} \stackrel{def}{=} \frac{1}{108}\sum_{j=1}^{108}\left(1-\frac{f\omega^2}{\omega^2-\omega_{0,j}^2+i\Gamma\omega}\right), \tag{5.1}$$

where $\omega_{0,j}$ is given by,

$$\omega_{0,j} = \omega_0 + \eta_j, \tag{5.2}$$

where η_j is a normal distribution. For a distribution centered at $x = X$, with a

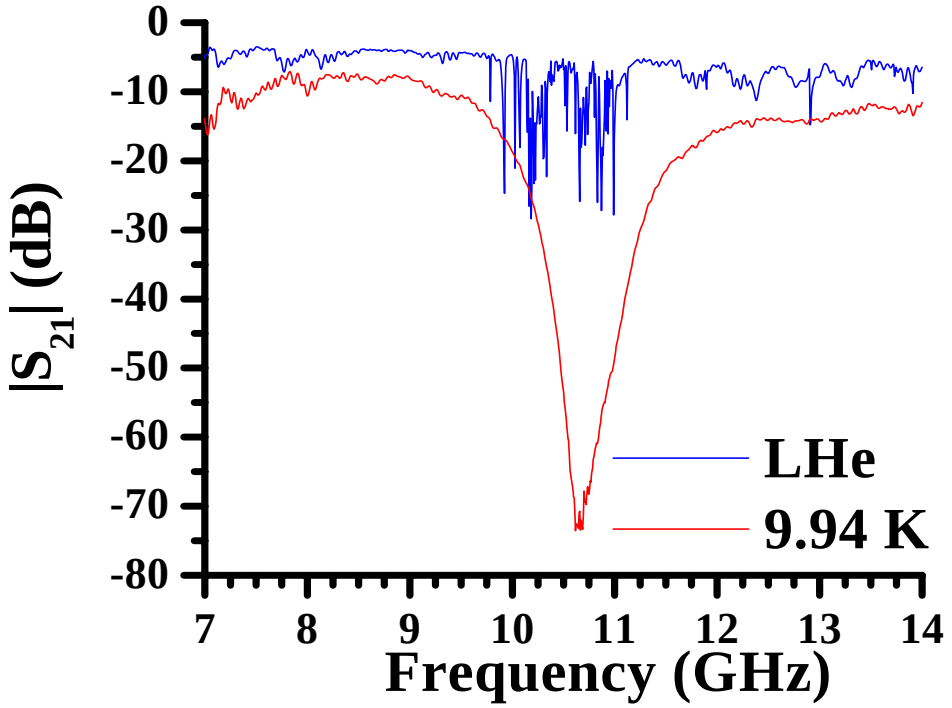

Figure 5.3: A plot of the electromagnetic transmission, $|S_{21}|$, versus frequency for an array of 108 Nb split-ring resonators, measured in liquid Helium, denoted by the blue curve and labeled LHe, and at 9.94 K, denoted by the red curve, in the Ag-plated brass X-band waveguide. Rohacell® HF was used to orient the Cu-Ni-Au split-ring resonators.

full-width at half-maximum of σ, the normal distribution is a Gaussian distribution, $N_{X,\sigma}(x)$, defined as [110, p. 133, Eq. (5.25)],

$$N_{X,\sigma}(x) = \frac{1}{\sigma\sqrt{2\pi}} e^{(x-X)^2/2\sigma^2}. \tag{5.3}$$

In the case here, $X = 0$, and $\sigma = 1$, and the actual value of η used was scaled in order to replicate the resonant frequency distribution in the data,

$$\eta_j = 0.126 * N_{0,1}(x_j) \tag{5.4}$$

The rest of the terms in Equation (5.1) were discussed in Chapter 2*.

Using Equation (5.1), the qualitative features of Figures (5.2) and (5.3) were reproduced in Figure (5.4) [109]. The three curves were generated with the three-layer transfer matrix model, with parameters of loss, Γ, filling fraction, f, a center resonant frequency, ω_0, and an overall insertion loss constant, C. The center resonant frequency was held constant in all three plots, $\omega_0 = 2\pi \times 10.7$ GHz, and the insertion loss constant for the red and green curves was $C = -4$ dB, while $C = -1$ dB for the blue curve. The filling fraction and loss, however, were changed for each curve in a manner believed to be experimentally accurate, that is, both parameters were decreased with decreasing temperature, where here temperature was not an actual parameter, however it is clear that the red curve is modeling a Nb split-ring resonator array above the critical temperature, while the blue curve is modeling a Nb split-ring resonator array below the critical temperature. The green

*Note that an attempt at a distribution of Γ was attempted, however this proved to be very difficult due to the sensitivity of the individual values, and so a single average value of Γ was assumed.

curve is modeling a Nb split-ring resonator array near, but less than, the critical temperature. The values of the filling fraction and loss were as follows, $f = 0.05$ and $\Gamma = 2\pi \times 637$ MHz for the red curve, $f = 0.01$ and $\Gamma = 2\pi \times 48$ MHz for the green curve, and $f = 0.006$ and $\Gamma = 2\pi \times 13$ MHz for the blue curve.

The model results in Figure (5.4) qualitatively describe the experimental results of Figures (5.2) and (5.3). Below the critical temperature of the Nb split-ring resonators, the losses should be very small and increase as the temperature approaches the critical temperature, due to an increasing surface impedance of the Nb film. It was necessary to reduce the filling fraction, f in Equation (5.1), as the losses were decreased in order to obtain an accurate insertion loss for the frequency region where the real part of the permeability is negative. It will be shown in this chapter that an individual Nb split-ring resonator has a much larger insertion loss at resonance than indicated in, for instance, Figure (5.3), and that interactions with various objects, such as the wall of the X-band waveguide, reduce the insertion loss.

While the model in Figure (5.4) qualitatively describes the electromagnetic transmission spectra in Figures (5.2) and (5.3), plotting the real part of the average permeability versus frequency reveals that in fact there are no regions of frequency where the real part of the permeability is negative, for the values used for Figure (5.4). Figure (5.5) shows the real part of the average permeability, that is, the real part of Equation (5.1), versus frequency for the parameters of the curves in Figure (5.4). The colors in both figures correspond to the same parameters, mentioned earlier. Note that even in the lowest loss case, the real part of the average permeability is never negative. The reason for this is that the actual model of an array of

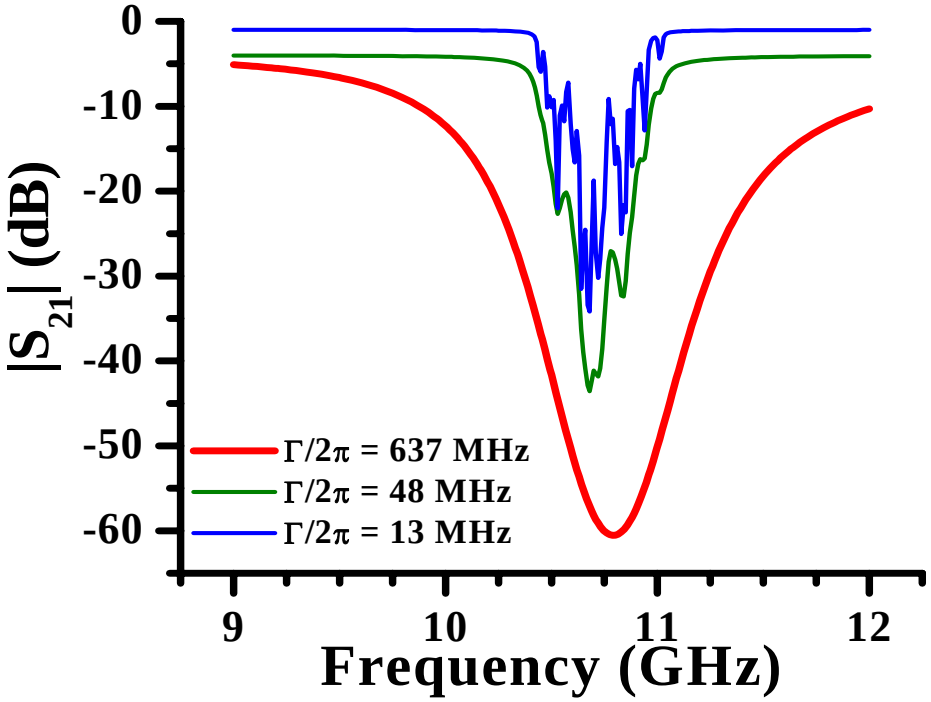

Figure 5.4: A plot of the electromagnetic transmission, $|S_{21}|$, versus frequency for a model of an array of 108 Nb split-ring resonators. Equation (5.1) was used with the three-layer transfer matrix model. Each curve had a resonant frequency of $\omega_0 = 2\pi \times 10.7$ GHz, and the following filling fraction and loss parameters: $f = 0.05$ and $\Gamma = 2\pi \times 637$ MHz for the red curve, $f = 0.01$ and $\Gamma = 2\pi \times 48$ MHz for the green curve, and $f = 0.006$ and $\Gamma = 2\pi \times 13$ MHz for the blue curve. The overall insertion loss for the blue curve was -1 dB, while the other two curves had an overall insertion loss of -4 dB.

Nb split-ring resonators is more complicated than Equation (5.1). For instance, as stated in the footnote earlier, a distribution of Γ should be used, but increased the complexity of the plots. Figure (5.4) motivates the need to test the hypothesis that each dip in Figures (5.2) and (5.3) is a result of a single Nb split-ring resonator in the array, or multiple Nb split-ring resonators with a degenerate resonance frequency. In other words, as the number of Nb split-ring resonators in the array is decreased, the number of dips, as seen in in Figures (5.2) and (5.3), should also decrease, until a single dip is observed with a single Nb split-ring resonator*.

5.4 Three-Nb split-ring resonator array

According to the preceding discussion, inserting a chip with only three Nb split-ring resonators should produce three dips in electromagnetic transmission, each dip due to the functional form of the permeability of a split-ring resonator. Figure (5.6) shows a plot of the electromagnetic transmission, $|S_{21}|$, versus frequency for an array of 3 Nb split-ring resonators, inside the Ag-plated brass X-band waveguide [45]. The Nb split-ring resonators on this smaller chip were longitudinal in orientation. In other words, there was no transverse lattice parameter inside the waveguide between each single Nb split-ring resonator on the chip, and the longitudinal lattice para-

*It is also pointed out that the ultimate test of whether or not the electromagnetic transmission in Figures (5.2) and (5.3) was due to a negative real part of the permeability is to insert the Nb split-ring resonator arrays into arrays of metallic wires. The combined negative real parts of the permeability and permittivity would then, over a limited frequency band, produce a transmission peak, as discussed in Chapter 2.

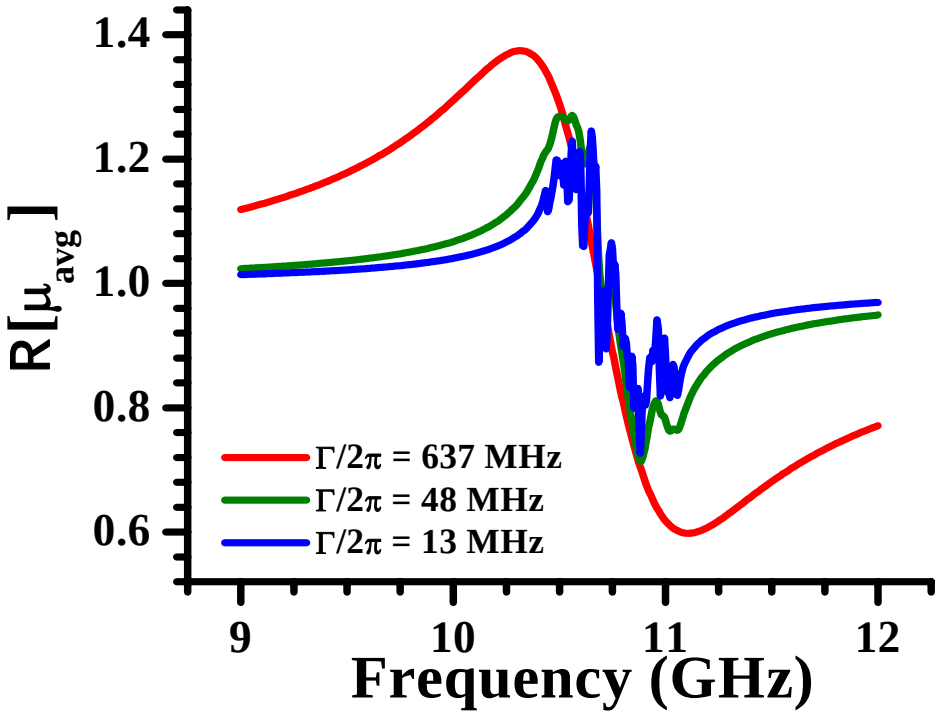

Figure 5.5: A plot of the real part of the real part of the average permeability, $\Re[\mu_{\text{avg}}]$, versus frequency for a model of an array of 108 Nb split-ring resonators. Equation (5.1) was used with the three-layer transfer matrix model. Each curve had a resonant frequency of $\omega_0 = 2\pi \times 10.7$ GHz, and the following filling fraction and loss parameters: $f = 0.05$ and $\Gamma = 2\pi \times 637$ MHz for the red curve, $f = 0.01$ and $\Gamma = 2\pi \times 48$ MHz for the green curve, and $f = 0.006$ and $\Gamma = 2\pi \times 13$ MHz for the blue curve.

meter was the same as that shown in Figure (3.2.c). The blue curve in Figure (5.6) is data taken while the Ag-plated brass X-band waveguide and Nb split-ring resonators were immersed in liquid Helium, while the red curve is data that was taken above the critical temperature of the Nb film, at 10.05 K. Below the critical temperature of the Nb film, there are three dips in electromagnetic transmission. The dips are much deeper, that is, they have a greater insertion loss, compared to the 108 and 216 Nb split-ring resonator array, presumably due to less interactions. Note that the dips in electromagnetic transmission in Figure (5.6) also do not fall at the same frequency. This was presumably due to the interactions of each Nb split-ring resonator with each other, was well as with the Ag-plated brass X-band waveguide.

Above the critical temperature of the Nb film, Figure (5.6) shows no deep dips in electromagnetic transmission. There is a slight dip at roughly the frequency where the three individual dips were located below the critical temperature, which may be due to the resonant losses of the three Nb split-ring resonators, similar to, for instance, the 10 K data shown in Figure (5.2). The sets of data, that is, Figures (5.2), (5.3), and (5.6), all seem to point to the following conclusion above the critical temperature of the Nb film: that the dips in electromagnetic transmission were not due to a region where the real part of the permeability is negative, but rather the dips in electromagnetic transmission were due to the large normal metal losses in the film. The greater the number of Nb split-ring resonators above the critical temperature, the more loss there is, and the less applied electromagnetic field reaches the receiving antenna inside the waveguide. With these assumptions as to the origins of the dips in electromagnetic transmission above and below the critical temperature of the Nb

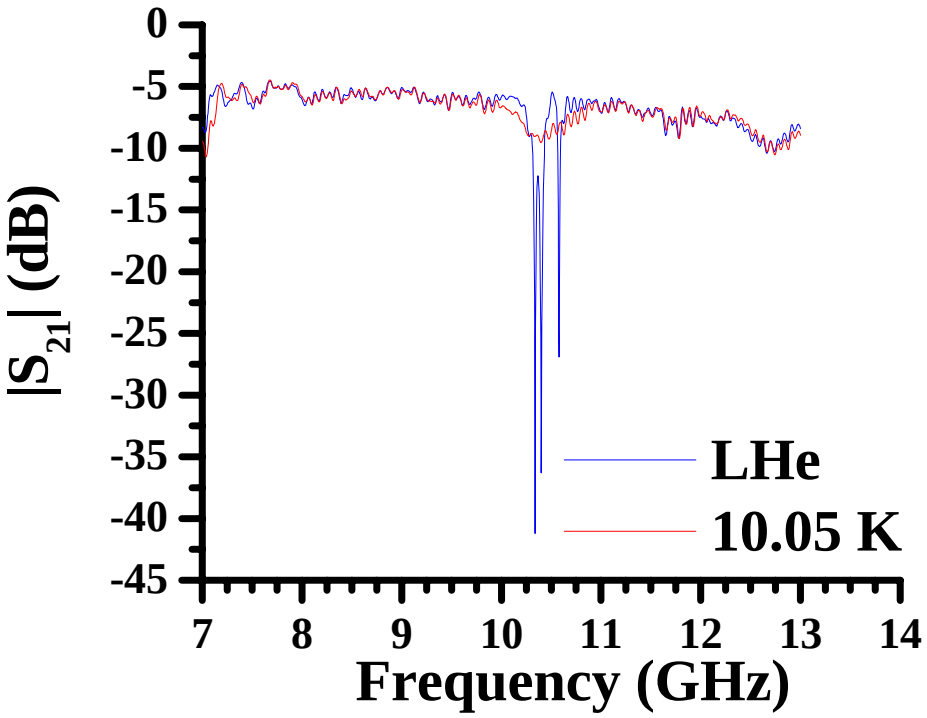

Figure 5.6: A plot of the electromagnetic transmission, $|S_{21}|$, versus frequency for an array of 3 Nb split-ring resonators, inside the Ag-plated brass X-band waveguide. The blue curve is data taken while the Ag-plated brass X-band waveguide and Nb split-ring resonators were immersed in liquid Helium, denoted LHe, while the red curve is data that was taken at 10.05 K.

film, it was hypothesized that a single Nb split-ring resonator would produce a single dip in electromagnetic transmission below the critical temperature of the Nb film, and no dip, or a very shallow dip, in electromagnetic transmission above the critical temperature of the Nb film.

5.5 Single Nb split-ring resonator in an empty Nb X-band waveguide

As stated in the last section, it was believed that the spikes in the transmission data, such as Figure (5.3), were the result of individual resonances of the Nb split-ring resonators in the larger array. The array of one hundred eight Nb split-ring resonators was reduced to three Nb split-ring resonators, Figure (5.6), and it was believed that this reduction could be continued to a single Nb split-ring resonator in the otherwise empty Nb X-band waveguide. The ability to observed a single dip in transmission would allow for the resonant frequency of a single Nb split-ring resonator, that is, the frequency of minimum electromagnetic transmission in the dip in transmission, to be tracked as a function of the temperature, an applied dc H field, or the power of the incident applied electromagnetic field. In addition to tracking the resonant frequency, the quality factor, or Q, of the single Nb split-ring resonator can also be tracked as a function of the aforementioned quantities.

The following sections detail experiments on a single Nb split-ring resonator in an otherwise empty X-band waveguide. First the electromagnetic transmission and three-layer transfer matrix model fit of a single Nb split-ring resonator is shown, followed by the temperature dependence of the single Nb split-ring resonator is

shown, and the changes in resonant frequency and quality factor with respect to the temperature are fit using a two-fluid model, and an LC resonator model of the single Nb split-ring resonator. Next, the changes in resonant frequency and quality factor with respect to an applied dc H field are presented, along with magneto-optical imaging of a single Nb split-ring resonator. Finally, the changes in resonant frequency and quality factor with respect to the applied power of the incident applied electromagnetic field are presented, with photoresponse imaging of the currents in a $YBa_2Cu_3O_{7-\delta}$ split-ring resonator in a microstrip geometry.

It is noted that several single Nb split-ring resonators were used throughout these experiments. Repeated cooling and warming, in addition to general handling, seemed to degrade the quality of the Nb split-ring resonators. For instance, when changing the power of the applied electromagnetic field, it was noticed that the maximum quality factor between successive experiments was decreasing. The labeling of the Nb split-ring resonators by the author of this dissertation was to use the Greek alphabet for each Nb split-ring resonator. This will be followed in this dissertation for two reasons. It informs the reader as to which sets of data used the same Nb split-ring resonator, and it helps future experiments replicate the data as best as possible.

5.5.1 Single Nb split-ring resonator–α electromagnetic transmission

In order to test the hypothesis that a single Nb split-ring resonator would produce a single dip in electromagnetic transmission below the critical temperature of

the Nb film, and no dip, or a very shallow dip, in electromagnetic transmission above the critical temperature of the Nb film, a single Nb split-ring resonator was harvested from a larger array, and its electromagnetic transmission was measured as a function of frequency inside the Nb X-band waveguide. This single Nb split-ring resonator was labeled α. The results are shown in Figure (5.7), where the blue circles are the data, and the black curve is a fit [45]. The fit was performed with the three-layer transfer matrix model, using a constant permittivity, $\epsilon = 1$, and a permeability given by Equation (2.97), with fit parameters of resonant frequency, ω_0, loss, Γ, filling fraction, f, material length, l, and an overall insertion loss, C. As expected, a single Nb split-ring resonator produced a single dip in electromagnetic transmission below the critical temperature of the Nb film. While it is not shown, above the critical temperature of the Nb film, there was no obvious dip in electromagnetic transmission, which is expected, since the dip in electromagnetic transmission above the critical temperature of the Nb film in Figure (5.6) is already very shallow for three Nb split-ring resonators. For a single Nb split-ring resonator, then, any dip in electromagnetic transmission above the critical temperature of the Nb film would be even more shallow, that is, smaller in insertion loss at the resonant frequency of the single Nb split-ring resonator, compared to the three Nb split-ring resonator case. The electromagnetic losses in the Nb film of a single Nb split-ring resonator above the critical temperature of the Nb film may not be large enough to produce any dip in electromagnetic transmission at temperatures above the critical temperature of the Nb film. From the previous figures in this chapter, it is clear that multiple Nb split-ring resonators make the interpretations of the data, and any fit

Table 5.1: Fit parameter results of Figure (5.7) for the single Nb split-ring resonator–α in the Nb X-band waveguide.

$\omega_0/2\pi$ (GHz)	$\Gamma/2\pi$ (kHz)	f	l (mm)	C (dB)
10.786	366	0.14	0.19	-15

to the data, very difficult. However, a single dip in electromagnetic transmission allows for an easier fit in order to determine the nature of the dip in electromagnetic transmission at temperatures below the critical temperature of the Nb film.

The black curve in Figure (5.7) was calculated using a three-layer transfer matrix model, with $\epsilon = 1$, and a permeability given by Equation (2.97), with fit parameters of resonant frequency, ω_0, a loss parameter, Γ, a filling fraction, f, a material length, l, and an overall insertion loss, C. The fit parameter values are listed in Table (5.1) [45]. The nonlinear least squares fit returned values of a resonant frequency of $\omega_0 = 2\pi \times 10.786$ GHz, a loss parameter of $\Gamma = 2\pi \times 366$ kHz, a filling fraction of $f = 0.14$, a material length of $l = 0.19$ mm, and an overall insertion loss of $C = -15$ dB. While the material length is less than the actual length by an order of magnitude*, the loss parameter indicates the very low losses achieved by using Nb films, and the filling fraction agrees with the qualitative analysis presented earlier in this chapter, although it is difficult to define a filling fraction for a single split-ring resonator. The question still remains, however, as to what exactly causes the dip in electromagnetic transmission in Figure (5.7). It is the belief of the author of this

*The single Nb split-ring resonator length should be roughly 2.36 mm. See Chapter 3.

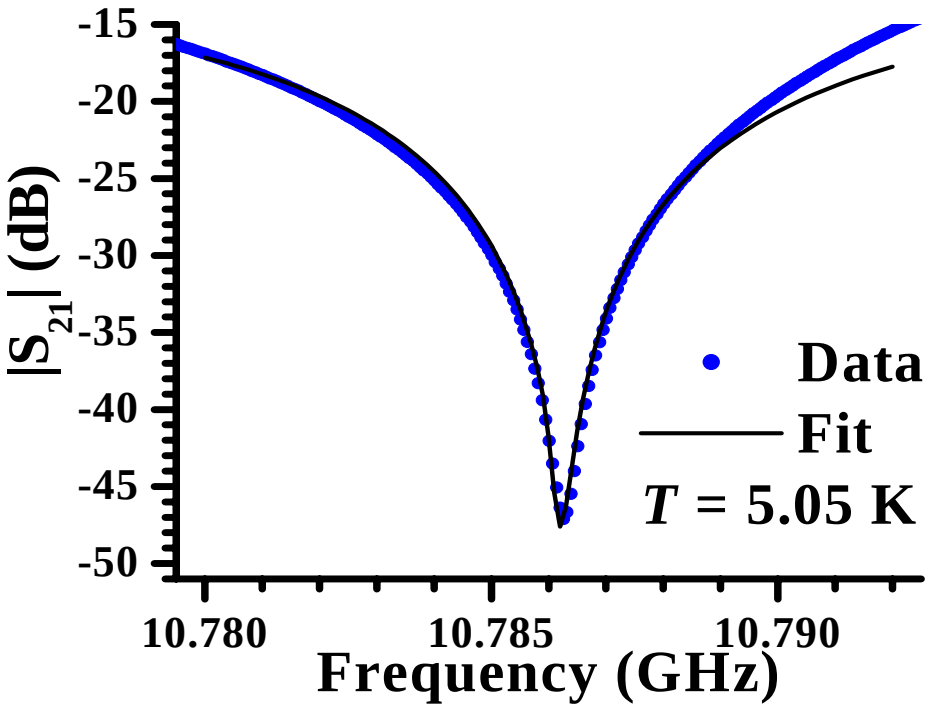

Figure 5.7: A plot of the electromagnetic transmission, $|S_{21}|$, versus frequency for the single Nb split-ring resonator–α inside a Nb X-band waveguide, at 5.05 K. The blue circles are the data, while the black curve is a fit using a three-layer transfer matrix model, using a constant permittivity, $\epsilon = 1$, and a permeability given by Equation (2.97), with fit parameters of resonant frequency, ω_0, loss, Γ, filling fraction, f, material length, l, and an overall insertion loss, C

dissertation that the dip in electromagnetic transmission in Figure (5.7) was due to the aforementioned functional form of the permeability, where there is a region where the real part of the permeability is negative, for the single Nb split-ring resonator. Not only does the model fit the data, with reasonable parameters, but plotting the real part of the permeability while using the fit parameters in Table (5.1) produces a curve where $\Re[\mu] < 0$ over a finite frequency range, as shown in Figure (5.8). This is not an exact replication of the actual permeability of the system. In order to recreate the actual permeability, the waveguide should be calibrated up to the longitudinal edges of the Nb split-ring resonator and substrate, and the permeability extracted from the S-parameters as discussed in Chapter 2. The ultimate test of whether or not the dip in electromagnetic transmission in Figure (5.7) was due to a frequency range where the real part of the permeability is negative is to insert the single Nb split-ring resonator into an array of wires, and observe a peak in electromagnetic transmission. This is done in Chapter 6.

5.5.2 Temperature dependence of a single Nb split-ring resonator

As stated in Chapter 2, the kinetic inductance of a superconductor can be comparable, and even greater, than the geometric inductance. Close to the critical temperature of a superconductor, the kinetic inductance contribution will be greatest. The single Nb split-ring resonator is modeled as an LC resonator, and so changes in the resonant frequency are expected for changes in temperature, with the largest changes near the critical temperature of the single Nb split-ring resonator.

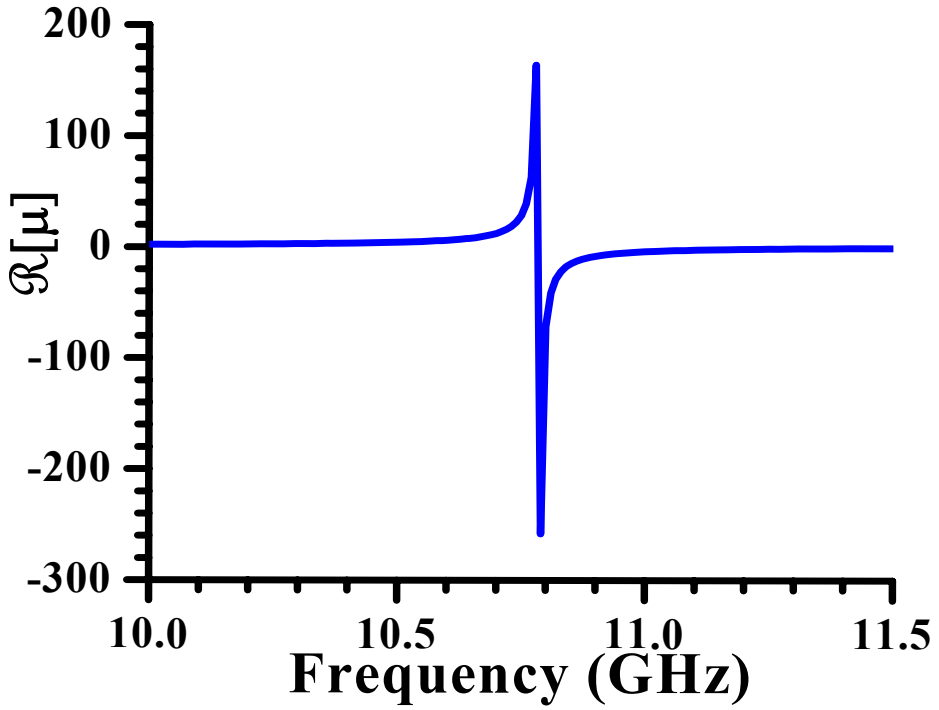

Figure 5.8: A plot of the real part of the permeability, $\Re[\mu]$, versus frequency, for Equation (2.97), using the fit parameter values in Table (5.1).

Figure (5.9) shows the electromagnetic transmission versus frequency results of the single Nb split-ring resonator–α in an otherwise empty Nb X-band waveguide [45]. The experiment was performed in vacuum, as described in Chapter 3. The temperature of each curve is, moving right to left, 5.05 K (blue), 7.70 K (green), 7.80 K (red), and 8.10 K (maroon). The inset of Figure (5.9) shows a schematic of the definition of the resonant frequency, f_0, and quality factor, Q, used in this dissertation. While the quality factor is typically defined as the resonant frequency divided by the bandwidth measured at the frequencies that correspond to values in, for instance, the electromagnetic transmission that are 3 dB *less* than the *maximum* electromagnetic transmission, the definition used in the case of a single split-ring resonator in an otherwise empty waveguide uses the bandwidth measured at the frequencies that correspond to values that are 3 dB *greater* than the *minimum* electromagnetic transmission. The frequency of minimum transmission is referred to as the resonant frequency. It is understood that the minimum transmission value is measured within the limits of the TE_{10}-only mode. This removes the frequency ranges that correspond to the noise floor, and higher order modes, where electromagnetic transmission values may be less than those observed in Figure (5.9).

Even from the four temperature curves in Figure (5.9), it is apparent that the resonant frequency, labeled in the inset, is decreasing, with larger changes in resonant frequency as the temperature approaches the critical temperature of the Nb split-ring resonator. The resonant frequency of the single Nb split-ring resonator–α, labeled as f_0, as a function of temperature is shown in Figure (5.10) [45]. The blue dots are the data, while the black curve is a fit, using Equation (2.151). This data is

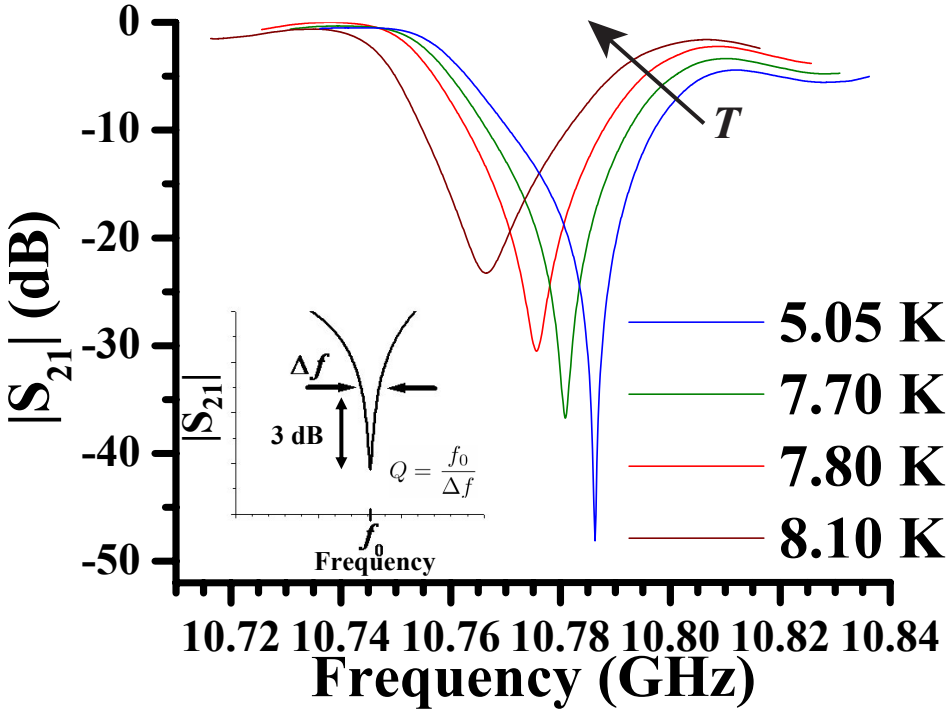

Figure 5.9: A plot of the temperature dependence of the electromagnetic transmission, $|S_{21}|$, versus frequency for the single Nb split-ring resonator–α in an otherwise empty Nb X-band waveguide. The temperature of each curve is, moving right to left, 5.05 K (blue), 7.70 K (green), 7.80 K (red), and 8.10 K (maroon). The increase in temperature is shown by the black arrow, where T stands for temperature. *Inset*: Schematic of a dip in the electromagnetic transmission versus frequency for the purpose of defining the resonant frequency, f_0, and the quality factor, Q, used in the models in this dissertation.

Table 5.2: Fit parameter results of the resonant frequency shift in Figure (5.10) for the single Nb split-ring resonator–α in the Nb X-band waveguide.

	T_c (K)	χ	β	$\omega_{0,g}/2\pi$ (GHz)
Estimate	8.65[a]	4	5×10^{-4}	—
Fit Value	8.47	2.63	1.3×10^{-3}	10.80

[a]From ac magnetic susceptibility measurements.

not taken from Figure (5.9), but was taken from a different data set that was taken at a later time.

The fit in Figure (5.10) had fit parameters of $\omega_{0,g}$, T_c, χ, and β, where each fit parameter is defined in Equation (2.151). Table (5.2) lists the values of these fit parameters, along with the expected values. From the ac magnetic susceptibility measurements discussed in Chapter 3, the critical temperature is approximately 8.65 K, while the temperature fit parameter in Equation (2.151) was 8.47 K, with respect to the data in Figure (5.10). The ratio of the film thickness, d, to the zero-temperature penetration depth, $\lambda(0)$, is roughly $\chi \stackrel{def}{=} d/\lambda(0) \approx 200 \text{ nm}/50 \text{ nm} = 4$, where a value of $\lambda(0) = 50$ nm was used rather than the bulk value of $\lambda(0) = 39$ nm [94, inside back cover] to account for the lowered critical temperature due to impurities in the film. The fit value was $\chi = 2.63$. The fit parameter $\beta \stackrel{def}{=} 2\pi\lambda(0)/(\kappa w) \approx 5 \times 10^{-4}$ was found to be $\beta = 1.3 \times 10^{-3}$. Since the capacitance of the actual Nb split-ring resonator is not easily calculated, $\omega_{0,g}$ is not estimated, but the fit parameter was $\omega_{0,g} = 2\pi \times 10.80$ GHz.

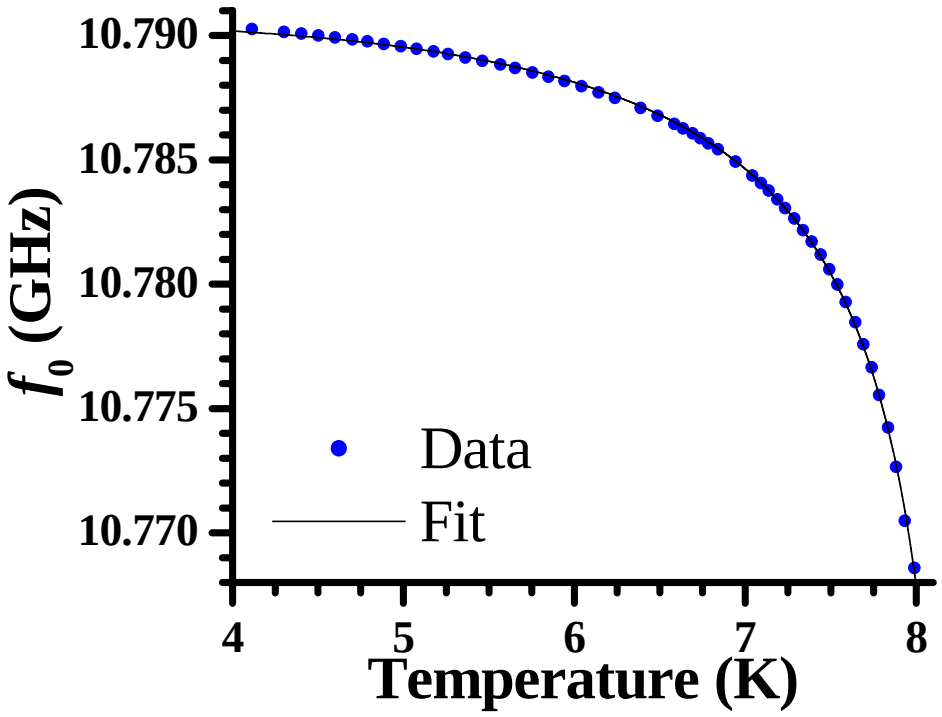

Figure 5.10: A plot of the resonant frequency, f_0, defined earlier in Figure (5.9), versus temperature for the single Nb split-ring resonator–α. Note that this data is not taken from the data in Figure (5.9), but rather taken at a later time. The blue dots are the data, while the black curve is a fit using Equation (2.151).

It is apparent from Figure (5.9) that in addition to a shift in resonant frequency, the width of the dip in transmission widens as the temperature approaches the critical temperature. The quality factor should decrease then, with increasing temperature, however this behavior is not as obvious as the resonant frequency shift, since $Q \sim \omega L/R_{\text{eff}}$, as shown in Equation(2.152), and L is increasing rapidly as the temperature approaches the critical temperature. However, R_{eff} is increasing faster, implying that resistive losses increase faster than the energy stored in the magnetic and kinetic inductance.

If the assumption that near the critical temperature,

$$\frac{T}{T_c} \approx 1, \tag{5.5}$$

$$\lambda \gg d, \tag{5.6}$$

where λ is the penetration depth, and d the film thickness, then the following assumptions can be made [81, p. 137, Eqs. (22.33) and (22.34)],

$$\coth\left(\frac{d}{\lambda}\right) \approx 1 + \frac{1}{2}\left(\frac{d}{\lambda}\right)^2, \tag{5.7}$$

$$\tag{5.8}$$

$$\sinh\left(\frac{d}{\lambda}\right) \approx \frac{d}{\lambda}, \tag{5.9}$$

where terms of order $(d/\lambda)^3$ and smaller are dropped. Thus, an approximation to Equation (2.153) is,

$$R_{\text{eff}} = R_s G\left[\coth\left(\frac{d}{\lambda}\right) + \frac{d}{\lambda}\frac{1}{\sinh^2\left(\frac{d}{\lambda}\right)}\right] \tag{5.10}$$

$$\approx R_s\left[1 + \frac{1}{2}\left(\frac{d}{\lambda}\right)^2 + \frac{\lambda}{d}\right] \tag{5.11}$$

$$\approx R_s\frac{\lambda}{d}. \tag{5.12}$$

Keeping only terms involving frequency and a temperature dependence, inEquations (2.147) and (2.154),

$$R_s \approx \omega_0^2 \lambda^3, \tag{5.13}$$

$$L \approx \lambda \left[1 + \frac{1}{2} \left(\frac{d}{\lambda} \right)^2 \right]. \tag{5.14}$$

Putting Equations (5.12) – (5.14) together,

$$Q = \frac{\omega_0 L}{R_{\text{eff}}} \tag{5.15}$$

$$\approx \frac{\omega_0 \lambda \left[1 + \frac{1}{2} \left(\frac{d}{\lambda} \right)^2 \right]}{\omega_0^2 \lambda^3 (\lambda/d)} \tag{5.16}$$

$$\approx \frac{d}{\omega_0 \lambda^2} + \frac{1}{2} \left(\frac{d}{\lambda} \right)^3 \frac{1}{\omega_0 \lambda} \tag{5.17}$$

$$\approx \frac{d}{\omega_0 \lambda^2}. \tag{5.18}$$

Thus, as $T \to T_c$, $\lambda \to \infty$, and so $Q \to 0$.

Figure (5.11) shows the results of fitting the quality factor of the single Nb split-ring resonator–α, as a function of temperature [45]. The blue dots are the data, while the black line is a fit using Equation (2.161). Unfortunately, due to the geometric factor of the quality factor in Equation (2.161), an estimate of the fit parameters cannot be given. This was explained in Chapter 2. In fact, the fit of the quality factor was so sensitive to initial values, that the fit parameters of β, χ, and T_c obtained from the fit of the resonant frequency, listed in Table (5.2), were directly inserted into the expression, Equation (2.161). Otherwise, the fitting algorithm returned unreasonable parameters, for instance, a very large or very small T_c. In order to determine whether or not the other fit parameters are reasonable, these values will be compared to those obtained from fitting the quality factor of a single

Table 5.3: Fit parameter results of the quality factor shift in Figure (5.11) for the single Nb split-ring resonator–α in the Nb X-band waveguide.

T_c (K)[a]	χ^a	β^a	ζ	Q_b
8.47	2.63	1.3×10^{-3}	1.13×10^{-5}	6.48×10^4

[a]Obtained from Table (5.2), and inserted directly into Equation (2.161).

Nb split-ring resonator in a wire array. For the single Nb split-ring resonator in the otherwise empty waveguide, the fit parameters were $\zeta = 1.13 \times 10^{-5}$ and $Q_b = 6.48 \times 10^4$. The fit parameters are summarized in Table (5.3).

5.5.3 dc H field dependence of a single Nb split-ring resonator

When in the presence of a sufficiently large dc magnetic field, a thin-film of Nb will experience the formation of vortices, that is, regions of circulating current, within the film. These vortices enter and leave the film at edges, corners, and defects in general. Since they add an inductive and resistive component to any current flowing in the rings of a Nb split-ring resonator, the resonant frequency and quality factor of a single Nb split-ring resonator should change as a function of the applied dc H field.

Figure (5.12) shows the resonant frequency of a single Nb split-ring resonator–β after placing the Nb split-ring resonator–β in a dc H field applied parallel to the x-axis in Figure (2.3) [111]. The applied dc H field was generated with a solenoid, as described in Chapter 3, and the waveguide used was the Ag-plated brass X-band

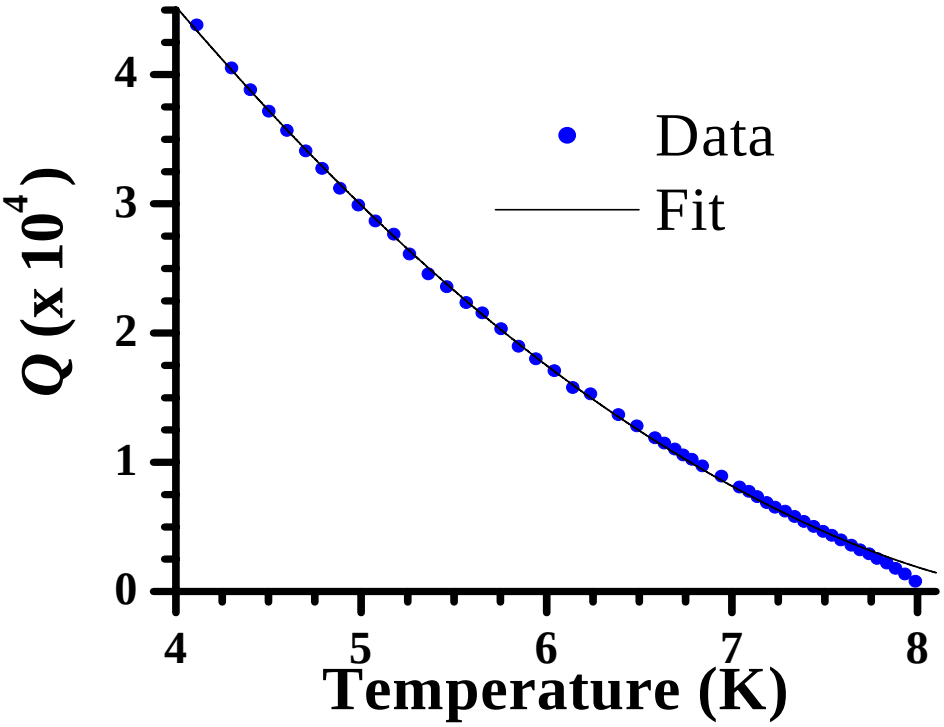

Figure 5.11: A plot of the quality factor, Q, versus temperature for the single Nb split-ring resonator–α. Note that this data is not taken from the data in Figure (5.9), but rather taken at a later time. The blue dots are the data, while the black curve is a fit using Equation (2.160).

waveguide, in order to have the applied dc H field penetrate the waveguide. If the Nb X-band waveguide was used, the applied dc H field would have been screened from the inside of the Nb X-band waveguide due to Meißner screening. The values of the applied dc H field quoted in Figure (5.12) come from Equation (3.1), where the current was known, and the field was calculated.

The features of Figure (5.12) are explained in the picture of the vortices. As the applied dc H field is increased, vortices will enter the Nb film of the single Nb split-ring resonator [112]. Thus, there is no superconductivity inside the core of the vortices, and the applied dc H field can penetrate the Nb film along the axis of rotation of the vortices. These vortices can become pinned at defects and impurities in the Nb film. In fact, once pinned, a vortex can be thought of as being in the bottom of a potential well [113], assuming that there is a linear restoring force. For some applied H field, $\mathbf{H} = H\hat{\mathbf{h}}$, define the flux as,

$$\mathbf{\Phi} \stackrel{def}{=} \int \mu \mathbf{H} \cdot d\mathbf{A} \quad \hat{\mathbf{h}}, \tag{5.19}$$

and so a Lorentz force, $\mathbf{F}$, acts on the vortex, given by [113],

$$\mathbf{F} = \mathbf{J} \times \mathbf{\Phi}, \tag{5.20}$$

where $\mathbf{J}$ is the current density flowing in the film, also called the transport current [114]. For small displacements away from the pinning site, the vortex has the equation of motion,

$$m\ddot{x} + \eta\dot{x} + kx = J\Phi, \tag{5.21}$$

where m is an effective vortex mass, $\eta\dot{x}$ is a dissipation term, coming from the normal-fluid core [113], and the viscous drag associated with the boundary between

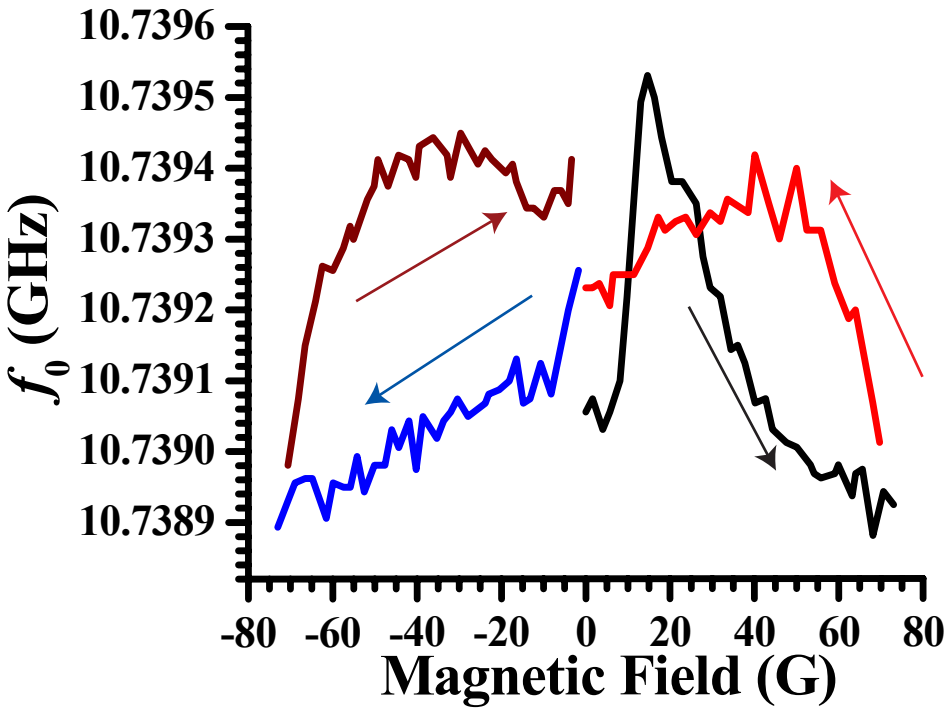

Figure 5.12: A plot of the resonant frequency, f_0, versus an applied dc H field for the single Nb split-ring resonator–β in an otherwise empty Ag-plated brass X-band waveguide, immersed in liquid Helium. The arrows indicate the direction of the change of the applied dc H field.

the normal-fluid core and the transport current made up of the Cooper pairs [114]. The term k in Equation (5.21) is an effective spring constant, and is a measure of the restoring force on the vortex. Equation (5.21) shows that the transport current displaces the vortices from the pinning sites, and acts as an oscillating driving force, at least in the situation presented in this dissertation. Thus, in addition to the inductance of the superconducting electrons, that is, the kinetic inductance, there is an inductance associated with moving these vortices. Thus, the total inductance, L_T of the single Nb split-ring resonator in an applied dc H field becomes,

$$L_T = L_k + L_g + L_v, \tag{5.22}$$

where L_v is the inductance associated with the vortices, and L_k and L_g were defined in Equation (2.147). This inductance is larger than the inductance in the absence of an applied dc H field, and so the resonant frequency of the single Nb split-ring resonator is expected to decrease as more vortices enter the film. This is in fact generally observed in Figure (5.12).

The hysteresis in Figure (5.12) can be explained in terms of the Bean critical state model [115]. As the applied dc H field enters the Nb film of the single Nb split-ring resonator, the field profile is expected to be approximately linear from both film edges, where the point of view is the thickness-width plane. The minimum field is at the center of the width of the Nb strip making up the perimeter of the single Nb split-ring resonator. This is shown in References [92, p. 179, Fig. (5.8)] and [115, Fig. (1)]. While initially the applied dc H field only penetrates a small lateral distance from the edges of the film, eventually, for a large enough applied dc H field,

there will be a non-zero value of H in the center of the film. As the applied dc H field is then decreased, the field in the center of the film is the last to exit the film, and thus even if the applied dc H field is reduced to zero from its maximum, there will be a non-zero field in the center of the film, and thus vortices. This is called trapped flux [92, p. 179]. In fact, in order to completely remove vortices in the single Nb split-ring resonator after applying a dc H field, the Nb split-ring resonator must be warmed to above the critical temperature in the absence of any dc H field. Note that Figure (5.12) is similar to data seen in Reference [96, Fig. (8)]*.

The quality factor of the single Nb split-ring resonator–β in an applied dc H field, versus the strength of the field, is shown in Figure (5.13), where the arrows refer to the direction of change of the applied dc H field [111]. Note that the data fits our picture of the vortices, described earlier. From the Bean critical state argument, it is expected that there was some residual H field in the Nb film after the applied dc H field was reduced to zero. This residual field implies the existence of vortices in the Nb film. The resistive losses from vortices were discussed earlier. Thus, the picture of Figure (5.13) is that as the applied dc H field was increased, vortices entered the Nb film, increasing resistive losses and reducing the quality factor. As the field was reduced to zero, vortices in the center of the film remained, and thus the quality factor never returned to its original value.

*It is noted that in Reference [96], the authors state that the hysteresis and field dependence of the resonant frequency are due to boundary currents and an "increase [in] the energy of the transport current," respectively. It is believed by the author of this dissertation that these statements are equivalent to the preceding discussion.

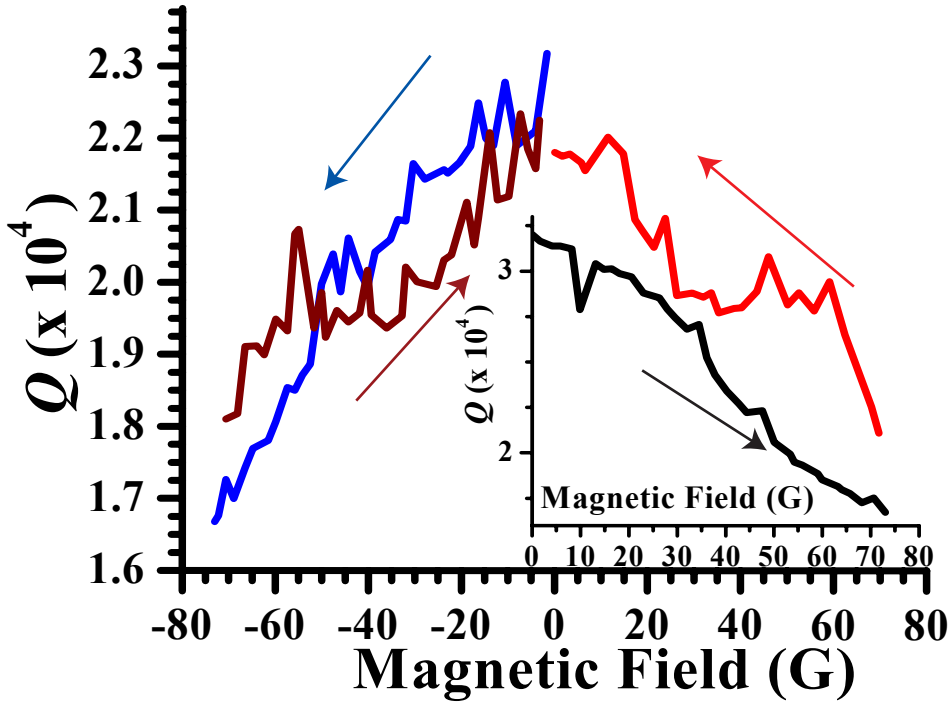

Figure 5.13: A plot of the quality factor, Q, versus an applied dc H field for the single Nb split-ring resonator–β in an otherwise empty Ag-plated brass X-band waveguide, immersed in liquid Helium. The arrows indicate the direction of the change of the applied dc H field.

While vortices will enter the film at the edges and corners of the single Nb split-ring resonator, defects in the Nb film, such as a scratch, can serve as a location where vortices may enter and exit the film, at low applied fields. A method of imaging vortex flow in Nb thin film samples is magneto-optical imaging, which takes advantage of the Meißner screening of a superconducting film. If a single Nb split-ring resonator is placed under a magneto-optical material and polarized light is incident on the single Nb split-ring resonator while a dc H field is applied orthogonal to the single Nb split-ring resonator, then the Faraday rotation of the incident light can be measured for any penetrating H field. Since defects in the Nb film of the single Nb split-ring resonator will allow the applied dc H field to penetrate the film, and thus cause the Faraday rotation within the magneto-optical material, the defects will appear different than regions of no defects where the H field is completely screened. This was discussed in Chapter 3, and Figure (3.15) shows a setup of the measurement.

Figure (5.14) shows an optical image of the single Nb split-ring resonator–β [111]. The background rings come from the machining lines on the cold-finger that the single Nb split-ring resonator–β was placed upon for the experiment. Note the surface defects on the Nb film, for instance the scratch on the outer ring on the left, and some scratches on the inner ring, opposite the gap. It is expected that the applied dc H field will penetrate at these Nb film defects, and create vortices in the Nb film.

Figure (5.15) shows the results of magneto-optical imaging of the single Nb split-ring resonator–β [111]. In both parts of the figure, lighter regions of the film

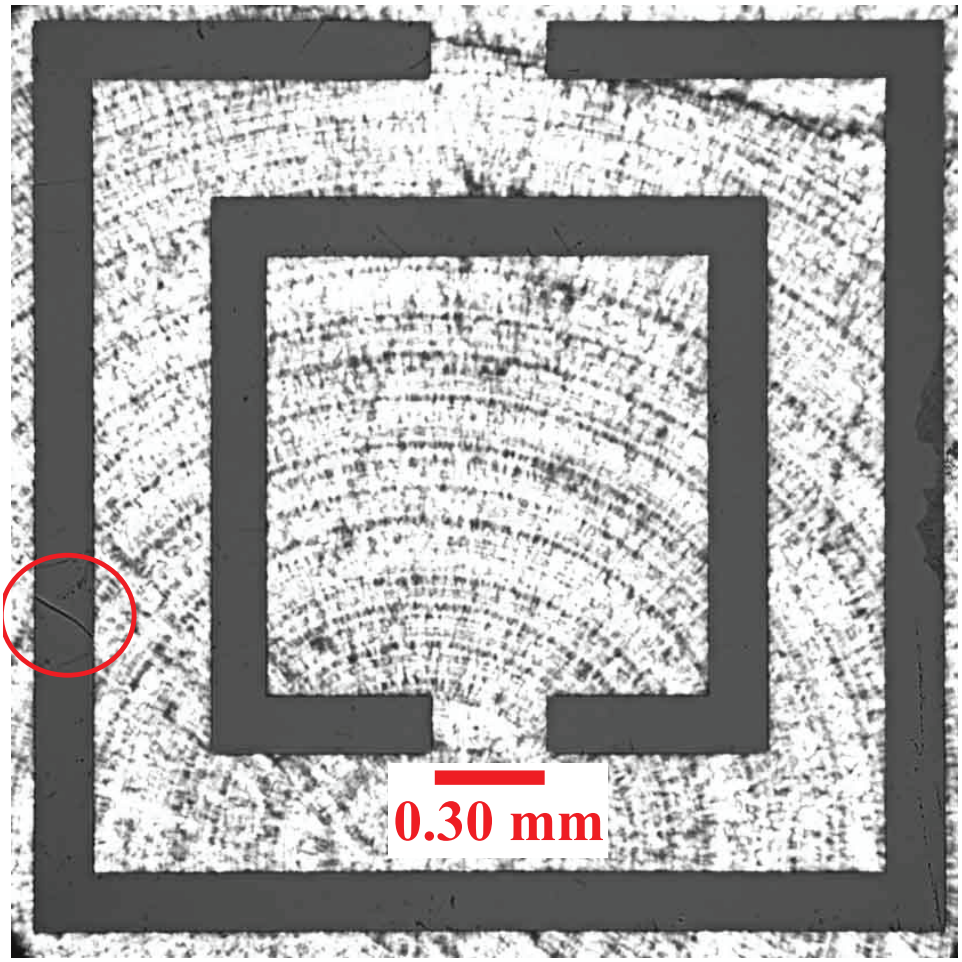

Figure 5.14: An optical image of the single Nb split-ring resonator–β. Note surface defects on the Nb film. The rings in the background were from the cold-finger that the single Nb split-ring resonator–β was placed upon. A scratch on the left side on the outer ring is circled in red.

indicate where magnetic flux is penetrating, while darker regions indicate where no flux is penetrating. In the top figure, the lack of magnetic flux penetration is due to the Meißner screening of the Nb film. Figure (5.15.a) was taken after the applied dc H field was ramped up to a value of 75 Oe. The Nb film was mostly in the Meißner state, indicating a good quality film, however there was magnetic flux penetration at several defects. Figure (5.15.b) is an image of trapped flux, where the applied dc H field was increased to a value of 1 kOe, and then decreased to zero field. The figure shows the magnetic flux still trapped in the Nb film, as discussed earlier with regards to the Bean critical state. The trapped magnetic flux image shows that even when the applied dc H field was removed, magnetic flux, and therefore vortices, still remains in the film. At defects, the flux is not trapped, and these are regions where vortices may leave the film. Figure (5.15.b) shows why the quality factor never returns to its maximum value in Figure (5.13) at zero applied H field.

5.5.4 rf B field dependence of a single Nb split-ring resonator

In addition to applying a dc H field, the power of the applied electromagnetic field can be increased. Increasing the power of the applied electromagnetic field has nonlinear effects on superconductors, as shown in Reference [116], for instance. In the case of the single Nb split-ring resonator–β, the change in the resonant frequency, f_0, defined as the minimum of electromagnetic transmission in the frequency region that is believed to be the frequency region where the real part of the permeability is negative, with the applied power is shown in Figure (5.16). The power is measured

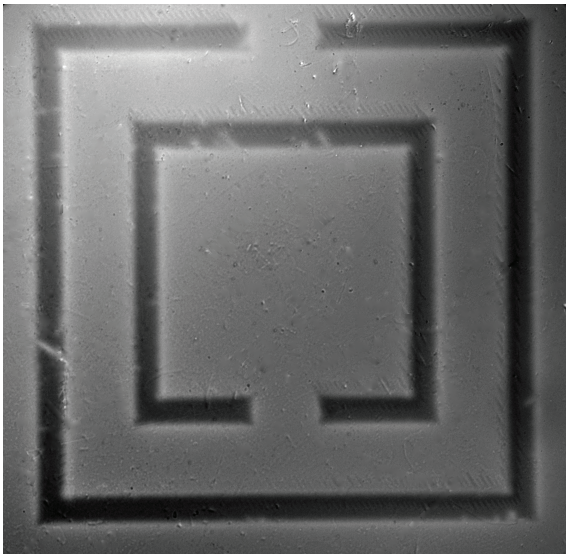

***a*) Penetrating flux at 5 K and 75 Oe**

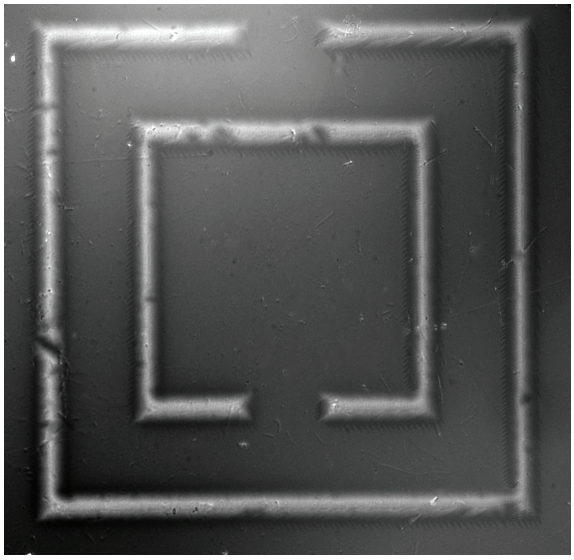

***b*) Trapped flux at 4.8 K after a 1 kOe field ramp**

Figure 5.15: A magneto-optical image of the single Nb split-ring resonator–β. In both figures, darker regions of the Nb film are where no magnetic flux was penetrating, while lighter regions have penetrating magnetic flux. Figure (a) shows a penetrating magnetic flux of 75 Oe at 5.0 K. Figure (b) shows trapped magnetic flux at 4.8 K after ramping the applied dc H field to 1 kOe, and then back to 0 Oe.

after the amplifier, but before entering the waveguide, as shown in Figure (3.14). The blue curve is increasing power, and the red curve is decreasing power.

The plot of the resonant frequency, f_0 with applied power in Figure (5.16) shows a mostly constant resonant frequency up to approximately +15 dBm*, at which point there is an almost step-functionlike increase in the resonant frequency. After this increase, the resonant frequency is, again, mostly constant, up to the maximum output of the amplifier, as discussed in Chapter 3. Decreasing the applied power is similar, in that the resonant frequency is rather constant to about +15 dBm, at which point there is an almost step-functionlike decrease in the resonant frequency. After this decrease, the resonant frequency is, again, mostly constant.

The quality factor, defined by the 3 dB point above the minimum in electromagnetic transmission as discussed in Chapter 5.4, almost follows a similar trend of a step-functionlike change in values at +15 dB. Figure (5.17) shows a plot of the quality factor, Q, versus applied power for the single Nb split-ring resonator–β in the Ag-plated brass X-band waveguide [111]. The blue curve is increasing power, and the red curve is decreasing power. The quality factor decreases steadily with increasing applied power up to approximately +15 dBm, at which point there is a large suppression of the quality factor. Decreasing the power shows a similar change, where the quality factor had a sharp increase at slightly less than +15 dBm. After this sharp increase, the quality factor increases steadily to the original quality

*Clearly the resonant frequency, f_0, in Figure (5.16) is not strictly constant up to +15 dBm, in that it is the same exact value at each level of power. By constant, then, it is meant that the measured values of the resonant frequency seem to center about a constant value.

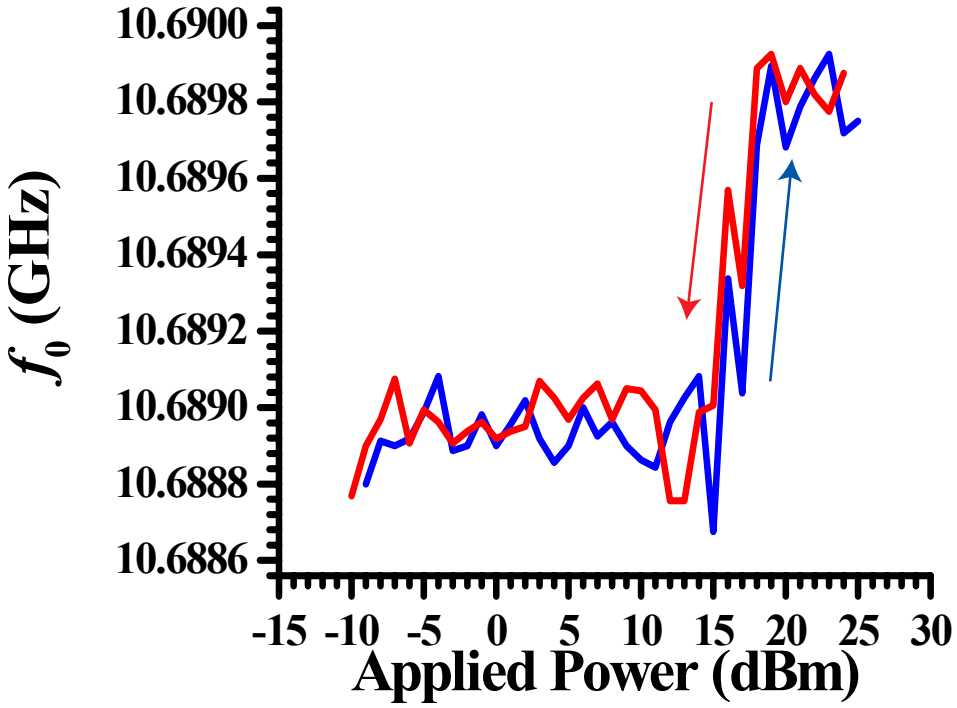

Figure 5.16: A plot of the resonant frequency, f_0, versus applied power for the single Nb split-ring resonator–β, inside the Ag-plated brass X-band waveguide, immersed in liquid Helium. The power is measured after the amplifier, but before entering the waveguide, as shown in Figure (3.14). The blue curve is increasing power, and the red curve is decreasing power.

factor, before the experiment began.

A possible explanation of the sudden shifts in both resonant frequency and quality factor at approximately +15 dBm begins with the currents flowing in the rings. In order to measure these currents, a scanning laser photoresponse measurement was performed on a single $YBa_2Cu_3O_{7-\delta}$ split-ring resonator in a microstrip geometry*. The setup was discussed in Chapter 3, and in Reference [117].

The photoresponse imaging results are shown in Figure (5.18) [111]. The figure shows four photoresponse plots of two resonances, at 5.146 GHz, and at 10.838 GHz. The left photoresponse plots are the two-dimensional photoresponse plots at the two resonant frequencies, while the photoresponse plots on the right are the three-dimensional photoresponse plots at the two resonant frequencies. As observed in the color scale, the blue regions have very little current density, while the green, and especially the red, regions have high current densities. In both cases, there was very little current activity in the inner ring, compared to the outer ring. In the outer ring, the currents appear appeared to be maximum in the inner corners, and on the edges of the $YBa_2Cu_3O_{7-\delta}$ film. Thus, is it believed that in the experiment involving the increase of the power of the applied electromagnetic field incident on the single Nb split-ring resonator, that the currents in the single Nb split-ring resonator increased as the applied power increased until superconductivity was destroyed by locally strong rf current flows. The resulting ohmic heating increased the temperature of the Nb film at the corners of the Nb split-ring resonator to a temperature above

*Due to time constraints, and difficulty with the plasma etcher, a Nb split-ring resonator was not used for the photoresponse measurement.

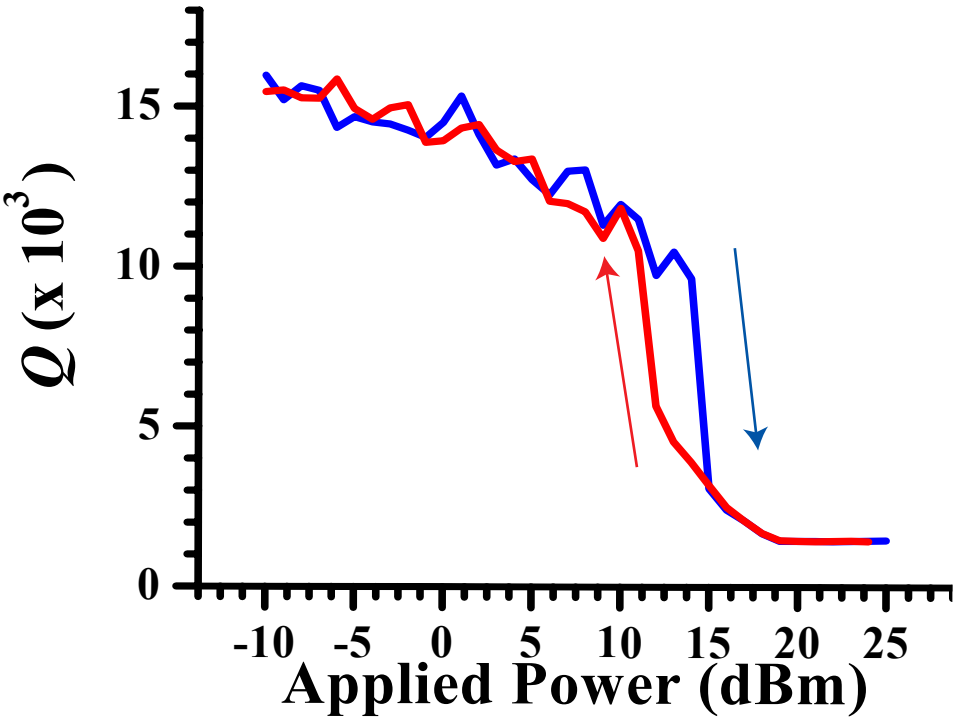

Figure 5.17: A plot of the quality factor, Q, versus applied power for the single Nb split-ring resonator–β in the Ag-plated brass X-band waveguide, immersed in liquid Helium. The blue curve is increasing power, and the red curve is decreasing power.

the critical temperature of the Nb film. This then caused thermal runaway, and the region of normal metal once confined to the edges and corners of the Nb film spread out, and large regions of Nb film became normal, rather than superconducting, and the resonant frequency of the single Nb split-ring resonator increased sharply. Likewise, the sudden increase in normal metal regions of film caused the losses to increase, and this lead to a sudden suppression of the quality factor. Decreasing the power had the opposite effect, as the currents decreasing allowed the Nb film to cool below the critical temperature, and become entirely superconducting.

5.6 The electromagnetic transmission spectra of other single split-ring resonators in an empty X-band waveguide

One unexpected result of using a superconducting metal for the construction of the split-ring resonators was the ability to reduce the number of split-ring resonators needed in an array to produce a bandwidth of negative permeability from a large number, for instance 216, to just a single Nb split-ring resonator. This ability is a result of the low loss nature of the superconductor, and in a rough analogy to scattering of particles, appears to increase the scattering cross-section of the split-ring resonator with respect to the applied electromagnetic field. However, this may not be unique to superconductors, and so the electromagnetic transmission spectra of single split-ring resonators made of Cu-Ni-Au, and $YBa_2Cu_3O_{7-\delta}$, were measured inside the Nb X-band waveguide and Ag-plated brass X-band waveguide, respectively. Also, this section will deal with another test of the nature of the dip

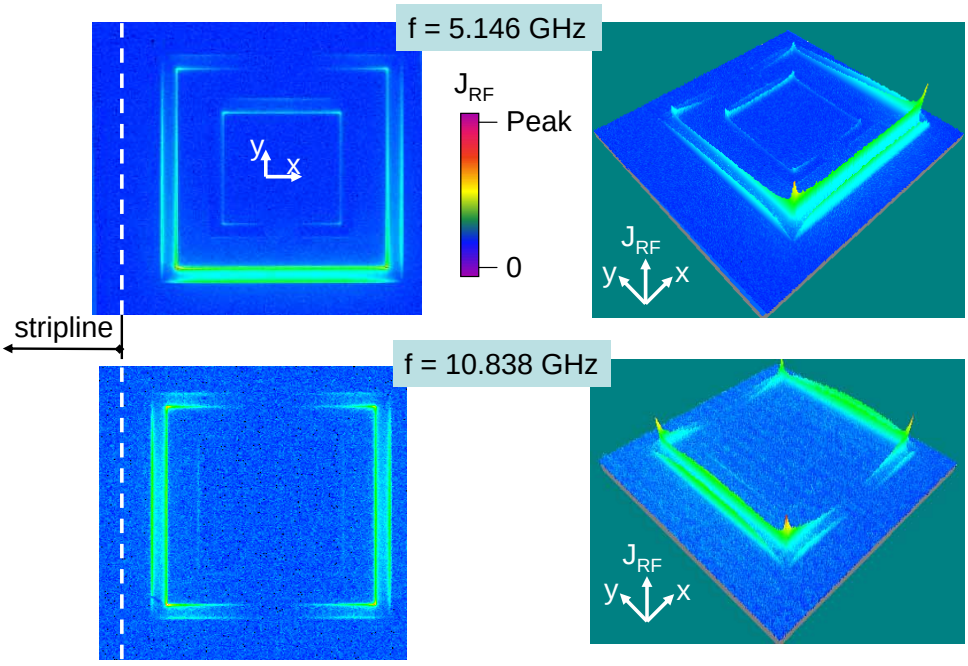

Figure 5.18: A plot of the photoresponse of a $YBa_2Cu_3O_{7-\delta}$ split-ring resonator. (a): Outer ring resonance at 5.146 GHz; (b): Outer ring resonance at 10.838 GHz. (c) and (d): Three dimensional plots of (a) and (b), respectively.

in electromagnetic transmission in Figure(5.7). Defects in photonic crystals, for instance, can introduce a spike of electromagnetic transmission in a region where there otherwise should be no electromagnetic transmission [118, p. 125]. Thus, it may be possible that the Nb split-ring resonator acts as a defect in the waveguide, contributing to the dip in electromagnetic transmission.

Figure (5.19) shows the electromagnetic transmission spectra for three single resonator experiments. First, a single $YBa_2Cu_3O_{7-\delta}$ split-ring resonator is shown in blue*. However, no dip in electromagnetic transmission is noticeable in the electromagnetic transmission of the $YBa_2Cu_3O_{7-\delta}$ split-ring resonator, at least none larger than the ringing passband noise. Although not shown, a simulation with a single perfect electric conductor split-ring resonator, on a substrate with a relative permittivity of $\epsilon \approx 22$, which is approximately the relative permittivity of the $NdGaO_3$ substrate of the $YBa_2Cu_3O_{7-\delta}$ split-ring resonator, did not produce a dip in electromagnetic transmission. Thus it appears that a large permittivity of the split-ring resonator substrate can affect the electromagnetic properties of the split-ring resonator, and in this case, remove the dip in electromagnetic transmission due to the negative real part of the permeability over a limited bandwidth. Whether the actual permeability changes with the permittivity of the substrate is not pursued here, and the reader is directed to Reference [119]

The electromagnetic transmission spectrum of a single Cu-Ni-Au split-ring

*Note that the $YBa_2Cu_3O_{7-\delta}$ split-ring resonator data was measured in liquid Nitrogen, and thus all frequencies are shifted down in frequency by approximately 1.5 GHz, compared to a vacuum measurement at the same temperature.

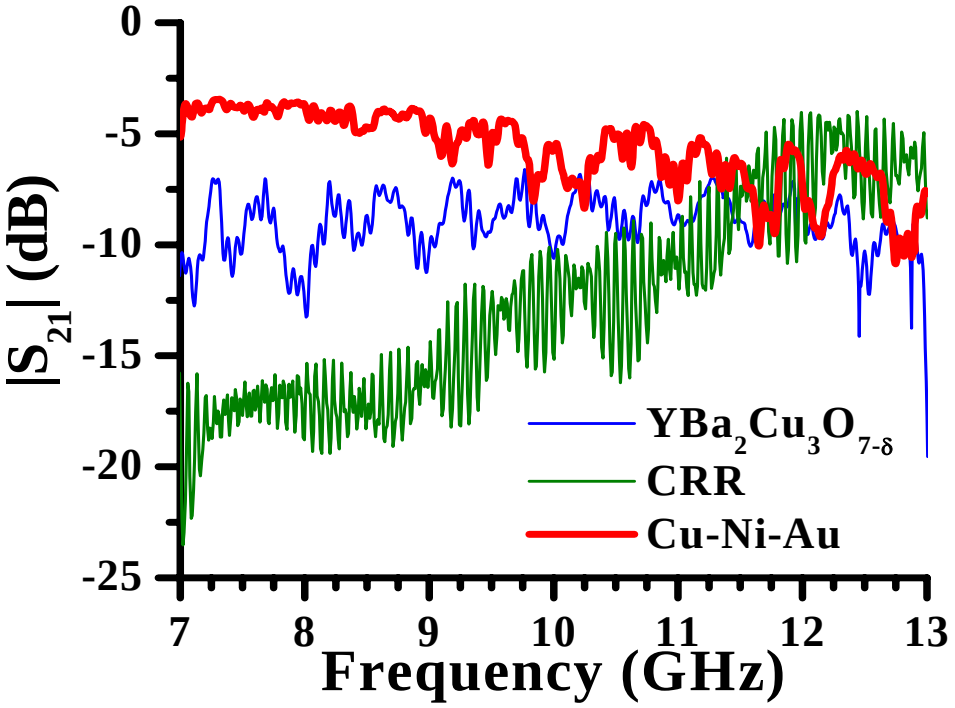

Figure 5.19: A plot of the electromagnetic transmission, $|S_{21}|$, versus frequency for a single $YBa_2Cu_3O_{7-\delta}$ split-ring resonator, shown in blue, a single Cu-Ni-Au split-ring resonator, shown in red, and a single Nb closed-ring resonator, shown in green. The closed-ring resonator was measured in the all-Nb X-band waveguide, the Cu-Ni-Au split-ring resonator was measured in the Ag-plated brass X-band waveguide with the Nb waveguide-to-coaxial cable couplers, and the $YBa_2Cu_3O_{7-\delta}$ split-ring resonator was measured in the Ag-plated brass X-band waveguide with the Cu waveguide-to-coaxial cable couplers. The ringing in the data were due to standing waves in the coaxial cables, due to impedance mismatches in the entire circuit. Also, note that the $YBa_2Cu_3O_{7-\delta}$ split-ring resonator data was measured in liquid Nitrogen, and thus all frequencies are shifted down in frequency by approximately 1.5 GHz, compared to a vacuum measurement at the same temperature.

resonator is shown in red in Figure (5.19). Note that there is no noticeable dip in electromagnetic transmission, at least larger than the noise of the passband. Since an array of Cu-Ni-Au split-ring resonators did appear to produce a bandwidth where the real part of the permeability is negative, as shown in Figure (5.1), the results of the single Cu-Ni-Au split-ring resonator seem to imply that the scattering cross-section is much smaller than the single Nb split-ring resonator. This assumes that the dip in electromagnetic transmission in Figure (5.1) was in fact due to the functional form of the permeability that includes a frequency bandwidth where the real part of the permeability is negative. Instead, if it were due to large ohmic losses, then the absence of a dip in electromagnetic transmission in Figure (5.19) is in agreement with the arguments earlier in this chapter with regard to the normal-metal losses of an array of Nb split-ring resonators. In order to determine the cause of the dip in electromagnetic transmission of Figure (5.1), and the absence of a dip in electromagnetic transmission in Figure (5.19), the array of Cu-Ni-Au split-ring resonators should be inserted into an array of metallic wires, although this was not measured for this dissertation.

For the case of the single Cu-Ni-Au split-ring resonator, there was no dip in electromagnetic transmission. However, what about an array of three Cu-Ni-Au split-ring resonators? This experiment is shown in Figure (5.20), with the single Cu-Ni-Au split-ring resonator data in blue, and the data for the three Cu-Ni-Au split-ring resonators shown in green. The three Cu-Ni-Au split-ring resonators have a similar geometry to the three Nb split-ring resonators discussed earlier. Note the dip in electromagnetic transmission for the three-split-ring res-

onators case, occurring at roughly the average resonant frequency observed in Figure (5.1). If this dip in electromagnetic transmission is truly from the functional form of the permeability that includes a frequency bandwidth where the real part of the permeability is negative, then increasing the number of Cu-Ni-Au split-ring resonators increases the scattering cross-section, or there in fact is a dip in electromagnetic transmission from the single Cu-Ni-Au split-ring resonator, however this dip in electromagnetic transmission is not strong enough to overcome the standing wave background in the measurement.

To close this section, the closed-ring resonator is discussed. It is apparent that the magnetic properties of the split-ring resonators are enhanced by the gaps in the loops. Closing this gap removes this low-order magnetic effect [120, 121]. In fact, the Pendry group showed that an infinite array of infinitely long metallic cylinder shells has no resonance frequency, and merely reduces the real part of the permeability by an amount equal to the filling fraction, assuming no losses. The square closed-ring resonators do have a resonance, as will be shown in Chapter 6, however, this resonance is greater than the lowest-order resonance of the split-ring resonators used in this dissertation, and the nature of the closed-ring resonator resonance is also not clear [91].

Suppose that the dip in electromagnetic transmission from the single Nb split-ring resonator was not due to a permeability that includes a frequency bandwidth where the real part of the permeability is negative, but rather some electric defect effect in the waveguide. In that case, the magnetic resonance of the split-ring resonator should not matter, and a closed-ring resonator of similar dimensions should

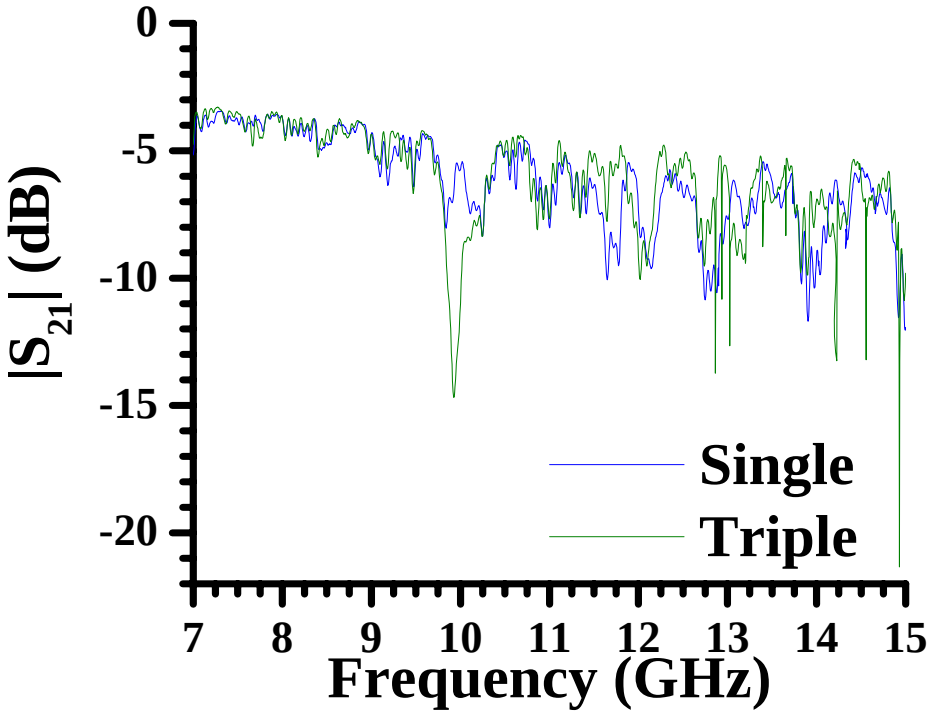

Figure 5.20: A plot of the electromagnetic transmission, $|S_{21}|$, versus frequency for an array of a single Cu-Ni-Au split-ring resonator, shown in blue, and three Cu-Ni-Au split-ring resonators, shown in green. The data were measured in the Ag-plated brass X-band waveguide with the Nb waveguide-to-coaxial cable couplers. The ringing in the data were due to standing waves in the coaxial cables, due to impedance mismatches in the entire circuit.

act as a similar electric defect. This was shown in Reference [121], where replacing split-ring resonators with closed-ring resonators did not remove peaks in electromagnetic transmission thought to be due to a negative real part of the index of refraction. While the discussion of a negative real part of the index of refraction is reserved for Chapter 6, the motivation is applied here, and is simply that the closed-ring resonator should remove any bandwidths where the real part of the permeability is negative, and any remaining dips in electromagnetic transmission are most likely due to an electric defect effect.

The electromagnetic transmission spectrum of a Nb closed-ring resonator was shown in Figure (5.19), as the green curve. The rapidly oscillating values of $|S_{21}|$ in the passband was due to standing waves in the coaxial cables of the circuit, due to impedance mismatches. There is no dip in electromagnetic transmission apparent in the figure, at least none larger than the oscillation. This implies that the dip in electromagnetic transmission from the single Nb split-ring resonator shown in Figure (5.7) was due to a magnetic resonance, and most likely due to a functional form of the permeability that includes a frequency bandwidth where the real part of the permeability is negative. While this test furthers the claim of a negative real part of the permeability, Chapter 6 provides even more evidence of the nature of the dip in electromagnetic transmission of Figure (5.7).

5.7 Bianisotropy

In Chapter 2, it was stated that the split-ring resonator geometry used for this dissertation shows bianisotropy, such that the resonant frequency due to the applied transverse magnetic field is equal to the resonant frequency due to the applied electric field [85, 122]. The physical implication of this was shown in Equations (2.122)–(2.124), where the magnetic field induced an electric dipole moment, and the electric field induced a magnetic dipole moment, in certain orientations with respect to the applied electromagnetic field. The orientations were shown in Figure (2.10), and the Nb split-ring resonator was placed in the center, transversely, of the waveguide, where the applied transverse electric field, and applied transverse magnetic field are at their maximum value. Figure (5.21) shows the experimental results, using the single Nb split-ring resonator–π. These results are now compared to the equations written in Chapter 2 for each orientation in Figure (2.10).

For the plane-parallel gap-orthogonal case, the blue curve in Figure (5.21), Equations (2.128)–(2.130) show that the magnetic dipole moment is due solely to the applied transverse magnetic field. While there is an electric dipole due to the applied transverse magnetic field, its orientation, along the waveguide axis, is believed to not contribute to the electromagnetic transmission spectrum. Finally, the electric dipole due to the applied transverse electric field is believed to be at a higher resonance than the lowest order magnetic resonance. Thus, despite the bianisotropy, it is believed that in the TE_{10} mode of the waveguide, the electric field contributions to the magnetic dipole moments, and the magnetic field contributions to the electric

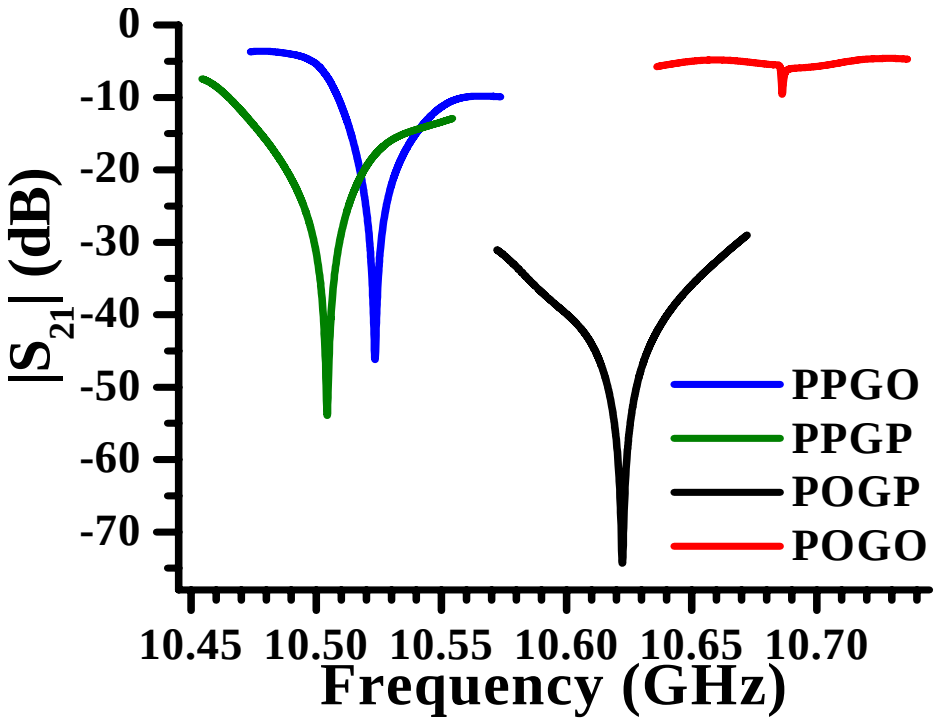

Figure 5.21: A plot of the electromagnetic transmission, $|S_{21}|$, versus frequency for the single Nb split-ring resonator–π, inside the Nb X-band waveguide immersed in liquid Helium. The curves are labeled as follows: PPGO (blue): plane-parallel gap-orthogonal; PPGP (green): plane-parallel gap-parallel; POGP (black): plane-orthogonal gap-parallel; POGO (red): plane-orthogonal gap-orthogonal. The orientations were described in Figure (2.10).

dipole moments, were nonexistent, or at best, minimal.

For the plane-parallel gap-parallel case, the green curve in Figure (5.21), Equations (2.125)–(2.127) show that the magnetic dipole moment is due to the applied transverse magnetic field and the applied transverse electric field. In fact, since there is no symmetry of the split-ring resonator about a plane parallel to the cross-section of the waveguide, the electric field should drive a resonance of the split-ring resonator at the same frequency as the magnetic dipole resonance. This perhaps causes the electromagnetic transmission spectrum seen in Figure (5.21). The electric dipole moment along the waveguide axis is nonexistent, however, the electric dipole moment parallel to the applied transverse electric field may have some effect on the data, and was due to both the applied transverse electric field and the applied transverse magnetic field.

For the next two orientations, it will be assumed that the applied longitudinal magnetic field was zero since the experiments were measured with the Nb split-ring resonator in the center of the Nb X-band waveguide. For the first case, the plane-orthogonal gap-parallel orientation, shown as the black curve in Figure (5.21), has a magnetic dipole moment due to the applied transverse electric field, as shown in Equations (2.131)–(2.133). There is no electric dipole moment in the plane of the waveguide cross-section, but orthogonal to the applied transverse electric field, however there is an electric dipole moment parallel to the applied transverse electric field. Thus, assuming that the applied longitudinal magnetic field is negligible, the dip in electromagnetic transmission in the plane-orthogonal gap-parallel orientation is ambiguous as to whether it was due to an electric or magnetic dipole moment.

The solution to this is continued in the bianisotropy section of Chapter 6. The shape of the dip in electromagnetic transmission for this orientation does not appear to be much like the other orientations. The insertion loss was much larger, and the dip itself seemed much wider that the other orientations. It is noted that upon removing the sample, the Nb split-ring resonator had slipped out of its orientation. It was unsure at what moment this slipping occurred, and so the black curve may not represent the actual response of the plane-orthogonal gap-parallel orientation to an applied electromagnetic field.

Finally, in the plane-orthogonal gap-orthogonal orientation, shown as the red curve in Figure (5.21), Equations (2.134)–(2.136) show that there should only be an electric dipole moment parallel to the applied transverse electric field. The other dipole moments are due entirely to the applied longitudinal magnetic field, and the assumption is that the amount of applied longitudinal magnetic field was negligible. This data is in disagreement with that in Figure (8) in Reference [91], and are several possibilities for the discrepancy. First, the data for the plane-orthogonal gap-orthogonal orientation in Figure (5.21) may be be a result of the low losses of superconductivity. This should be testable by simulations, using a perfect electric conductor split-ring resonator. A second possibility is that the orientation of the Nb split-ring resonator was slightly off-center, allowing for a small amount of flux from the applied longitudinal magnetic field. It is believed by the author of this dissertation that the electric dipole parallel to the applied transverse electric field is at a higher resonance than the lowest order magnetic dipole resonance in this orientation, and that the Nb split-ring resonator was indeed off-center slightly during

the experiment.

The simulations of the experimental data in Figure (5.21) are shown in Figure (5.22). A split-ring resonator made of perfect electric conductor material was used since superconductivity could not be simulated. All the resonant frequencies in the simulation are nearly equal, and have resonant frequencies less than the observed resonant frequencies in Figure (5.21). The relation of the resonant frequencies for each orientation also do not match. For instance, the lowest resonant frequency in the measured data occurred for the plane-parallel gap-parallel orientation, while for the simulations, the the lowest resonant frequency occurred for the plane-parallel gap-orthogonal orientation. The insertion losses for the plane-parallel gap-parallel and plane-parallel gap-orthogonal orientations appear to agree with the experimental results in Figure (5.21). Also, note that the plane-orthogonal gap-orthogonal case has no dip in electromagnetic transmission in the frequency region shown. This implies that the dip in electromagnetic transmission for the plane-orthogonal gap-orthogonal orientation in Figure (5.22) was most likely due to the Nb split-ring resonator begin off-center, and a small amount of flux from the applied longitudinal magnetic field coupled to the Nb split-ring resonator.

In order to couple the plane-orthogonal orientations to the applied longitudinal magnetic field, the simulated perfect electric conductor split-ring resonator was simulated next to the narrow-side wall of the waveguide. The results are shown in Figure (5.23). For the plane-orthogonal gap-orthogonal orientation, moving the split-ring resonator to either narrow-side waveguide wall should produce the same electromagnetic transmission spectrum, since the split-ring resonator is symmet-

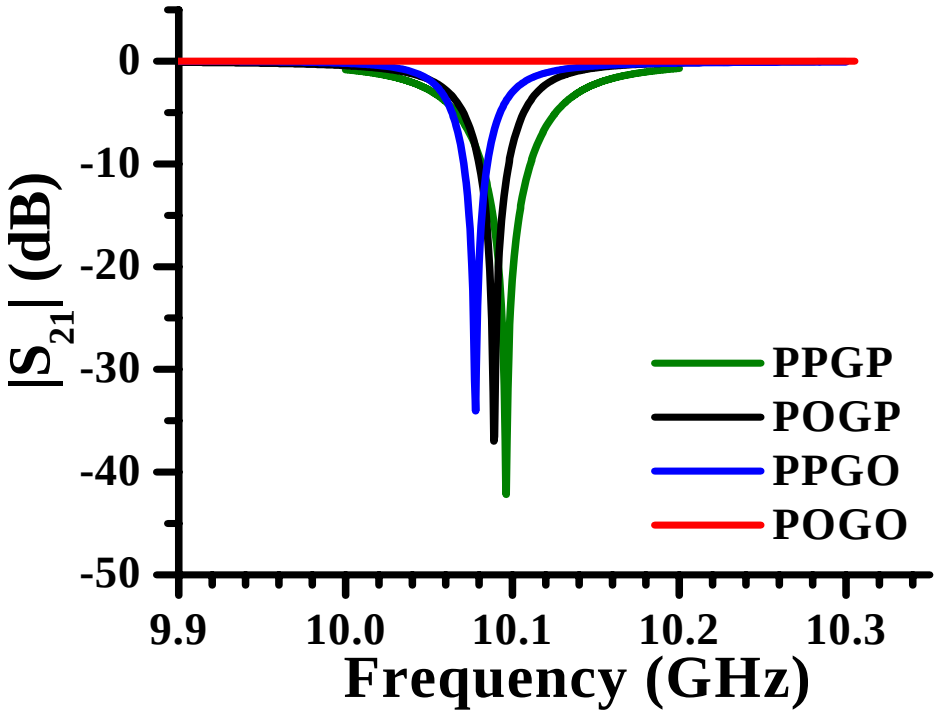

Figure 5.22: A plot of the electromagnetic transmission, $|S_{21}|$, versus frequency for a simulation of a single split-ring resonator made of a perfect electric conductor. The curves are labeled as follows: PPGO (blue): plane-parallel gap-orthogonal; PPGP (green): plane-parallel gap-parallel; POGP (black): plane-orthogonal gap-parallel; POGO (red): plane-orthogonal gap-orthogonal. The orientations were described in Figure (2.10).

ric about a plane parallel to the narrow-side walls. The simulated electromagnetic transmission for the plane-orthogonal gap-orthogonal orientation in the center of the waveguide, transversally, is shown in maroon. Note that there is no dip in electromagnetic transmission, as discussed earlier. However, after shifting the split-ring resonator next to the narrow-side waveguide wall, the green curve emerges. This is entirely due to the applied longitudinal magnetic field, as the applied transverse electric field is nearly zero at this location. Thus, from Equations (2.134)–(2.136), the electric dipole moment parallel to the applied transverse electric field is nearly zero, while the electric dipole moment parallel to the applied transverse magnetic field, and the magnetic dipole moment, parallel to the applied longitudinal magnetic field, are both non-zero.

Since the plane-orthogonal gap-parallel orientation is not symmetric about a plane parallel to the narrow-side walls, the electromagnetic transmission spectrum for each wall should be different. That is, since the capacitive gap of the outer loop of the split-ring resonator will have a different distance from the narrow-side waveguide wall, depending on which wall the split-ring resonator is placed next to, the electromagnetic transmission spectra will not necessarily be equal. The simulations in Figure (5.23) confirm this. The black curve is the plane-orthogonal gap-parallel orientation in the center of the waveguide. When placed next to the narrow-side waveguide wall, with the capacitive gap of the outer loop of the split-ring resonator farthest from the wall, the resonant frequency increases, as shown in red. However, when placed next to the narrow-side waveguide wall, with the capacitive gap of the outer loop of the split-ring resonator closest to the wall, the resonant

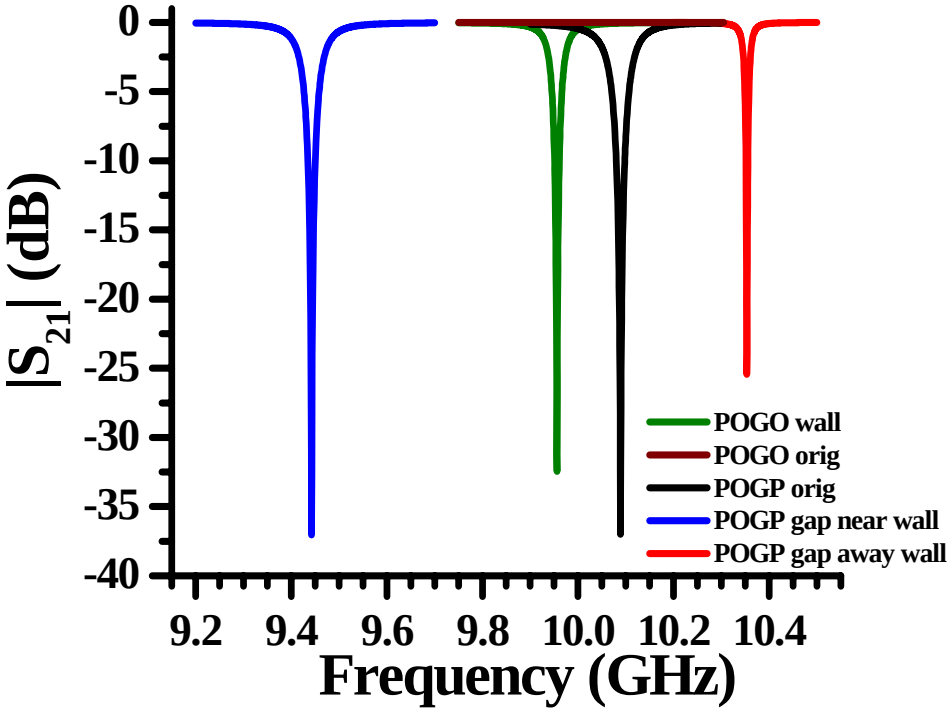

Figure 5.23: A plot of the electromagnetic transmission, $|S_{21}|$, versus frequency for a simulation of a single split-ring resonator made of a perfect electric conductor. The position of the split-ring resonator is next to the short-side wall of the X-band waveguide. The curves are labeled as follows: POGO wall (green): plane-orthogonal gap-orthogonal next to the short-side waveguide wall; POGO orig (maroon): plane-orthogonal gap-orthogonal in the center of the waveguide; POGP orig (black): plane-orthogonal gap-parallel in the center of the waveguide; POGP gap near wall (blue): plane-orthogonal gap-parallel next to the wall, with the side of the outer loop with the capacitive gap closest to the short-side waveguide wall, POGP gap away wall (red): plane-orthogonal gap-parallel next to the wall, with the side of the outer loop with the capacitive gap farthest from the short-side waveguide wall. The orientations were described in Figure (2.10).

frequency decreases, as shown in blue. This behavior may be roughly explained in terms of Equation (5.23). With the capacitive gap of the outer loop of the split-ring resonator farthest from the wall, the perturbation is largely magnetic, and thus a positive frequency shift, while the orientation the capacitive gap of the outer loop of the split-ring resonator closest to the wall, the perturbation is largely electric, giving a negative frequency shift.

However, the actual amount of frequency shifts, and insertion loss changes, is questionable. For instance, in the plane-orthogonal gap-parallel orientation next to the short-side waveguide wall, the applied transverse electric field should be nearly zero, while the applied longitudinal magnetic field is nearly maximum. Thus the main force driving the currents around the split-ring resonator rings should come from the applied longitudinal magnetic field, and the insertion loss for both positions, that is, outer loop capacitive gap closest and farthest from the short-side waveguide wall, should be nearly equal. Figure (5.23) shows that the difference in insertion loss, however, is more than 10 dB. It is interesting to note that the plane-orthogonal gap-orthogonal orientation next the short-side waveguide wall has an insertion loss roughly equal to the average of the plane-orthogonal gap-parallel orientation insertion losses for the two wall positions. The plane-orthogonal gap-orthogonal orientation has an essentially neutral orientation of the outer loop capacitive gap of the split-ring resonator, as described earlier. The resonant frequency of the plane-orthogonal gap-orthogonal orientation next to the short-side waveguide wall is also roughly the average of the plane-orthogonal gap-parallel orientation resonant frequencies for the two wall positions. However, without more careful analysis, and

actual experimental data, this is mere coincidence.

5.8 Perturbations

It is apparent that the Nb split-ring resonators used in this experiment were very sensitive to their environment. For instance, the resonant frequency of a Nb split-ring resonator appears to be dependent on its temperature, the power of the applied electromagnetic field, and the presence of any dc magnetic field. In order to attempt to explain some of the features observed in the multiple Nb split-ring resonator array, such as Figure (5.3), a single Nb split-ring resonator was placed approximately 1.27 mm from a short-side wall of the Ag-plated brass X-band waveguide. This is shown in Figure (5.24) as a maroon curve. For comparison, the black curve is the same Nb split-ring resonator in the center of the Ag-plated brass X-band waveguide. The shift in frequency is explained in terms of a perturbation in the volume integral of the magnetic field density.

For a resonant structure, such as a cavity, a perturbation will shift the resonant frequency of the structure depending on how the perturbation couples to the applied electromagnetic field. For a resonant frequency, ω_0, a perturbation will cause a new resonant frequency, ω_n, to shift by [123, Eq. 1],

$$\Delta\omega_0 \stackrel{def}{=} \omega_n - \omega_0 = \left[\int \left(|H|^2 - |E|^2 \right) dV \right], \tag{5.23}$$

where H is the magnitude of the normalized unperturbed magnetic field, E is the magnitude of the normalized unperturbed electric field, and the integral is performed over the volume of the perturbation. Thus, a perturbation in the magnetic field

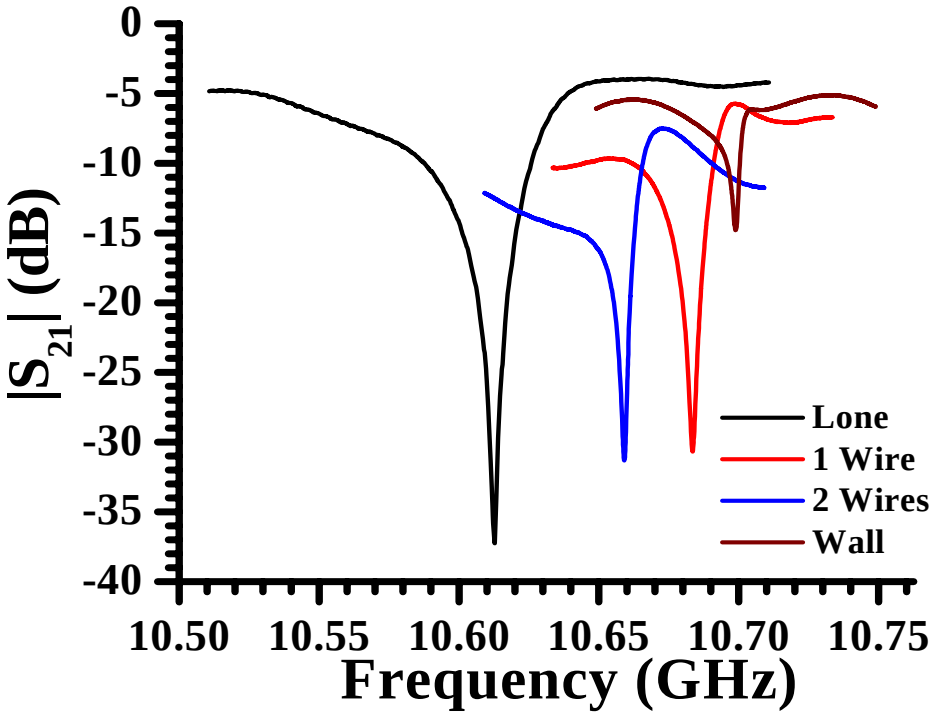

Figure 5.24: A plot of the electromagnetic transmission, $|S_{21}|$, versus frequency for the single Nb split-ring resonator–β in an otherwise empty Nb X-band waveguide, with various perturbations. All Nb split-ring resonator orientations were plane-parallel gap-orthogonal.

density will cause a positive shift in the resonant frequency, while a perturbation in the electric field density will cause a negative shift in the resonant frequency. In the case of the single Nb split-ring resonator against the wall of a waveguide, the magnetic field generated by the Nb split-ring resonator had a smaller volume due to the boundary conditions on the magnetic field at the waveguide wall. Since the normal component of the magnetic field must vanish at a wall of a waveguide, the extent of the magnetic field structure of a single Nb split-ring resonator near a waveguide wall is smaller than in the center, transversally, of the waveguide, and so this magnetic perturbation increases the resonant frequency of the centered Nb split-ring resonator. The decrease in the insertion loss was most likely due to the fact that the applied transverse magnetic field is nearly zero near the short-side wall that the Nb split-ring resonator was placed near for the data in Figure (5.24). The field strength was discussed in Chapter 2, and a plot is shown in Appendix A.

Figure (5.24) also shows data of the single Nb split-ring resonator–β placed a distance of 1.27 mm from a single Nb wire, shown as the red curve, and placed between two Nb wires, shown as the blue curve, with a separation distance of 2.54 mm between a Nb wire and the single Nb split-ring resonator. All data were measured in the Ag-plated brass X-band waveguide with the Cu waveguide-to-coaxial cable couplers. This experiment is useful for Chapter 6, since in that chapter, arrays of Nb split-ring resonators are placed in between rows of wires, in order to achieve a negative index of refraction over a limited range of frequencies. Note that while both wire perturbations cause an increase in the lone split-ring resonator case, shown as the black curve, the one wire perturbation causes a much larger increase

in the resonant frequency of the single Nb split-ring resonator, while the two wire perturbation is shifted down in frequency compared to the one wire perturbation. It is believed by the author of this dissertation that the interaction between the wires and the single Nb split-ring resonator is more complicated than Equation (5.23), however the results were confirmed by simulations.

Except for the antennas, the simulation was an accurate portrayal of the actual experimental setup, although since superconductivity was not modeled, a perfect electrical conductor was used for the single split-ring resonator, rather than Nb metal. Figure (5.25) shows the results. Ignoring the actual values, the shifts in frequency and, in some cases, the electromagnetic transmission, $|S_{21}|$, are similar to the experimental data in Figure (5.24). The case of the single split-ring resonator next to the wall of the waveguide, shown as the green curve, the insertion loss decreased, and the resonant frequency increased. For the single split-ring resonator next to a single wire, made of perfect electrical conductor material, the resonant frequency increased. Adding a second wire in a similar fashion to the real setup caused the resonant frequency to decrease to a value less than the lone split-ring resonator case.

5.9 Summary

The electromagnetic transmission, $|S_{21}|$, of arrays of split-ring resonators was measured and presented in this chapter. An array of Cu-Ni-Au split-ring resonators was shown to have a single dip in electromagnetic transmission at the resonant frequency of the split-ring resonators, while similar arrays of Nb split-ring

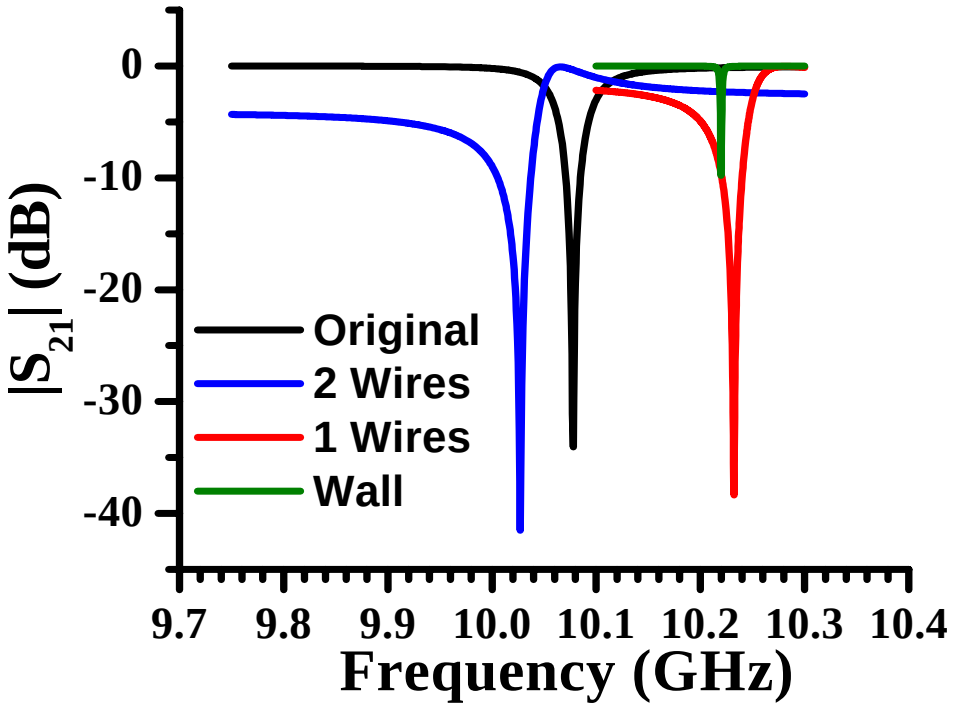

Figure 5.25: A plot of the electromagnetic transmission, $|S_{21}|$, versus frequency for a simulation of a single perfect electric conductor split-ring resonator in an otherwise empty X-band waveguide, with various perturbations.

resonators produced multiple dips in electromagnetic transmission, presumably due to the low-loss nature of the Nb films. The results were qualitatively modeled by an average permeability, summed over each split-ring resonator in the larger array. Smaller arrays were shown to have as many dips as Nb split-ring resonators in the array, and the electromagnetic transmission of a single Nb split-ring resonator was measured. The change in resonant frequency and quality factor with temperature, an applied dc H field, and applied power was measured, and modeled in the case of temperature changes. Magneto-optical imaging of a single Nb split-ring resonator revealed an imperfect film quality and locations where magnetic vortices can enter and leave the Nb film. Photoresponse imaging of a $YBa_2Cu_3O_{7-\delta}$ split-ring resonator showed current buildup in the inside corners of the split-rings. This lead to thermal runaway at large values of the applied power, destroying superconductivity in the split-ring resonators, and offers an explanation for the data presented in the applied power experiment. Finally, experimental data, and simulations, investigating perturbations of a single Nb split-ring resonator, and its bianisotropy, were presented.

Chapter 6

Combination of arrays of split-ring resonators and arrays of metallic wires

6.1 Overview

This chapter details the experimental results of combining an array of metallic wires, discussed in Chapter 4, with an array of split-ring resonators, discussed in Chapter 5. The theory, explained in Chapter 2, showed that combining a medium that has a negative real part of the permittivity over a bandwidth of frequencies with a medium with a negative real part of the permeability over a bandwidth of frequencies, will produce a medium that has a negative real part of the index of refraction over the intersection of the aforementioned bandwidths of frequency.

Due to the similarities in the setup, the experiments in this chapter closely parallel the experiments in Chapter 5. First, the electromagnetic transmission of an array of Nb wires with various lattice parameters, combined with an array of Nb split-ring resonators, is shown, and this electromagnetic transmission spectrum is shown to produce multiple peaks in electromagnetic transmission on top of a larger peak in electromagnetic transmission, presumably due to the individual Nb split-ring resonators that make up the larger array. The distance separating the Nb wires and Nb split-ring resonators is changed, and it is shown that the peak in elec-

tromagnetic transmission decreases with decreasing distance. It is also shown that the peak in electromagnetic transmission reduces in magnitude as the temperature increases, and above the critical temperature of the Nb film, the peak in electromagnetic transmission disappears. The electromagnetic transmission of a single Nb split-ring resonator in a Nb wire array of various lengths is measured, and shows a single peak in electromagnetic transmission. This single peak in electromagnetic transmission is fit with a five-layer transfer matrix model for one specific Nb wire array length, assuming that the medium has a permittivity given by Equation (2.22), and a permeability given by Equation (2.97). The change in the resonant frequency and the quality factor with temperature of the single peak in electromagnetic transmission is measured and fit as a function of temperature. Measurements of the electromagnetic transmission spectra of a single Cu-Ni-Au split-ring resonator, and a closed-ring resonator, show that these resonators do not produce a peak in electromagnetic transmission, presumably due to the Ohmic losses in the former case, and the lack of a half-wave resonance of the current density in the latter case. The bianisotropy of a single Nb split-ring resonator in a Nb wire array is investigated and the electromagnetic transmission spectra of various orientations with respect to the applied electromagnetic field are presented*. Finally, the electromagnetic transmission spectra of measurements of a single Nb split-ring resonator and a single closed-ring resonator inside of a Ka-band waveguide are shown, and a peak in electromagnetic transmission is observed in both cases, and exhibit properties unlike

*It is noted that unless otherwise specified, the orientation of the split-ring resonators are plane-parallel gap-orthogonal.

other peaks in electromagnetic transmission measured in this chapter.

6.2 Array of 216 Nb split-ring resonators in a Nb wire array

6.2.1 Nb wire lattice parameter of $a = 5.08$ mm

From the experiments in Chapter 5, it seems reasonable to predict that an array of 216 Nb split-ring resonators, as described in Chapter 3, would produce an electromagnetic transmission spectrum with multiple spikes, that is, sharp peaks in electromagnetic transmission, due to the individual Nb split-ring resonators in the larger array, and that perhaps these peaks in electromagnetic transmission merge into a single, smooth, peak in electromagnetic transmission, much like the multiple Nb split-ring resonator data shown in Figure (5.2). All peaks in electromagnetic transmission are presumably due to a negative real part of the index of refraction, as described in Chapter 2. The setup of the experiment was described in Chapter 3, and the electromagnetic transmission results are shown in Figure (6.1) [109]. The electromagnetic transmission, $|S_{21}|$, versus frequency for an array of 216 Nb split-ring resonators in a Nb wire array measuring five wires transversely and eighteen wires longitudinally, with a lattice parameter of $a = 5.08$ mm is shown, where the blue curve was measured at 5.05 K and the green curve was measured at 10.94 K [109], both measured in the Ag-plated brass X-band waveguide. The distance separating the Nb wires and the Nb split-ring resonators was $d = 2.54$ mm. The bandwidth of frequency from roughly 9.75 GHz to approximately 11 GHz for the 5.05 K data shows a large peak in electromagnetic transmission, with smaller sharp

peaks in electromagnetic transmission near the maximum value. These smaller peaks in electromagnetic transmission were presumably due to the individual Nb split-ring resonators. The frequency bandwidth of the larger peak in electromagnetic transmission of the 5.05 K data is very similar to the frequency bandwidth of the dips in electromagnetic transmission of the blue curve in Figure (5.3). For the data measured at 10.94 K, Figure (6.1), there is no longer a peak in electromagnetic transmission, at least above the noise floor. Thus, it is believed that the single, smooth dip in electromagnetic transmission of the red curves in Figures (5.2) and (5.3) was due to the metallic losses of normal-state Nb, rather than a negative real part of the permeability.

Note also that the plasma edge, or cutoff edge, of the Nb wire array and Nb split-ring resonator combination is at approximately 12 GHz, rather than roughly 16 GHz, as was the case in Chapter 4 with the Nb wires–only array. This reduction of the cutoff frequency of the Nb wire array is complicated, and a possible explanation is that the quartz substrates of the Nb split-ring resonators reduced the cutoff frequency, as explained through Equation (2.59). However, comparing differences in the distance separating the Nb wires and Nb split-ring resonators will be shown to also change the cutoff frequency of the Nb wire array.

The temperature dependence of the larger peak in electromagnetic transmission in the blue curve in Figure (6.1) is investigated further in Figure (6.2) [109]. The electromagnetic transmission, $|S_{21}|$, is plotted versus frequency, and the temperature is increasing from the top curve to the bottom curve. The temperatures shown are, starting with the top curve, 5.05 K, shown as a blue curve, 8.07 K,

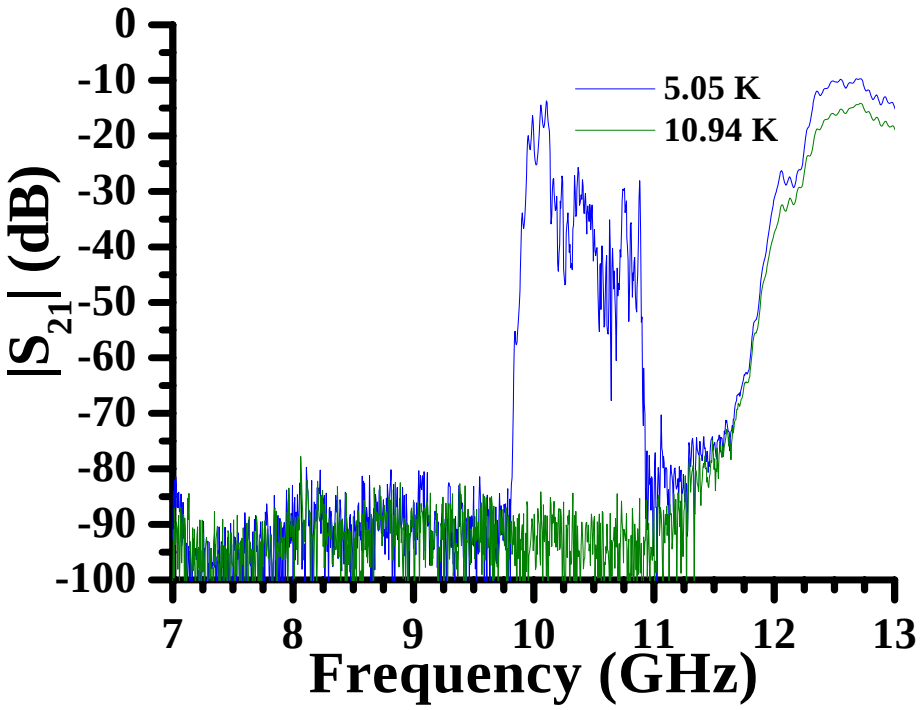

Figure 6.1: A plot of the electromagnetic transmission, $|S_{21}|$, versus frequency for an array of 216 Nb split-ring resonators in a Nb wire array measuring five wires transversely and eighteen wires longitudinally, with a lattice parameter of $a = 5.08$ mm. The blue curve was measured at 5.05 K and the green curve was measured at 10.94 K. The distance separating the wires and Nb split-ring resonator was approximately $d = 2.54$ mm.

shown as a green curve, 8.39 K, shown as a black curve, and 8.58 K, shown as a red curve. Figure (6.2) shows that by at least 8.58 K, there is no longer any peak in electromagnetic transmission above the noise floor, even though the critical temperature of the Nb film of the Nb split-ring resonators is approximately 8.65 K. This is consistent with Figure (5.11), where the quality factor was shown to be very low, approximately 500, or about 1% of the maximum quality factor, at approximately 8 K. Thus losses appear to destroy the negative real part of the permeability of the Nb split-ring resonators, and thus the negative real part of the index of refraction of the combination of Nb wires and Nb split-ring resonators, before the critical temperature of the Nb film of the Nb split-ring resonators is reached.

Based on the results of Figure (5.24), it is expected that there will be some effect of the distance, d, separating the wires and Nb split-ring resonators, on the electromagnetic transmission spectrum. Two electromagnetic transmission spectra, $|S_{21}|$, were measured for distances of approximately $d = 2.54$ mm, and approximately $d = 350$ μm, which is the thickness of the quartz substrate. The measurements at 5.05 K are plotted in Figure (6.3). Note the reduction in peak magnitude for the case where the Nb split-ring resonator arrays were placed immediately next to the wire in the Nb wire array. This was done by placing the quartz substrate in direct contact with the wires, but on the back of the substrate so that the Nb split-ring resonators did not short-circuit with the wires. In Figure (5.24), it was observed that placing a single Nb split-ring resonator near a wire reduced the insertion loss, and Figure (6.3) confirms this for a large array of Nb wires and Nb split-ring resonators. Presumably, the Nb wires and the Nb split-ring resonators perturb the

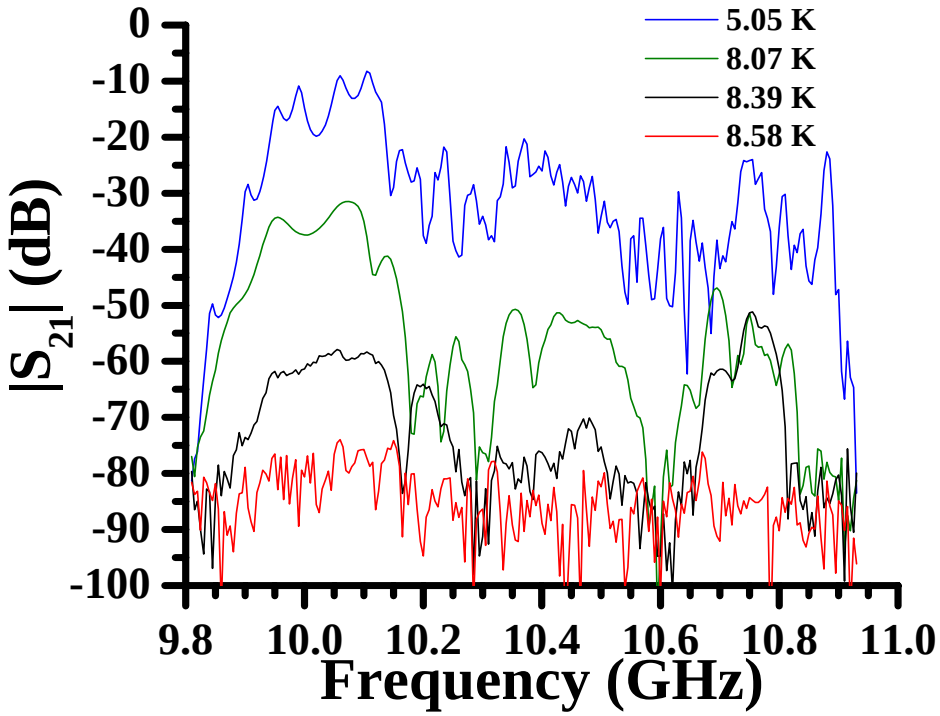

Figure 6.2: A plot of the electromagnetic transmission, $|S_{21}|$, versus frequency for an array of 216 Nb split-ring resonators in a Nb wire array measuring five wires transversely and eighteen wires longitudinally, with a lattice parameter of $a = 5.08$ mm, as a function of temperature. The blue curve was measured at 5.05 K, the green curve was measured at 8.07 K, the black curve was measured at 8.39 K, and the red curve was measured at 8.58 K. The distance separating the wires and Nb split-ring resonator was approximately $d = 2.54$ mm.

electromagnetic field structures of each other, and reduce the currents flowing in the Nb wires and Nb split-ring resonators, thereby reducing the magnitude of the peak in electromagnetic transmission, $|S_{21}|$, and changing the location of the cutoff frequency of the wire array.

6.2.2 Nb wire lattice parameter of $a = 7.19$ mm

Recalling that the Nb wire array with a lattice parameter of $a = 7.19$ mm had a cutoff edge at approximately 12 GHz, it would be interesting to observe the Nb split-ring resonator array inserted into a Nb wire array with a lattice parameter of $a = 7.19$ mm, since the cutoff edge of the Nb wire array with this lattice parameter is close to the resonant frequency of the Nb split-ring resonators. This is shown in Figure (6.4), where the blue curve is data measured at 5.10 K, and the red curve is data measured at 10.42 K [109]. Note that the cutoff edge begins at approximately 9 GHz, and the frequency bandwidth of approximately 9.75 GHz to roughly 11 GHz has sharp dips in electromagnetic transmission below the critical temperature of the Nb film of the Nb split-ring resonators, while above the critical temperature of the Nb film of the Nb split-ring resonators, the bandwidth has a smoother dip in electromagnetic transmission. It is believed that this medium did not exhibit a negative real part of the index of refraction, but rather, the cutoff edge was reduced to less than the resonant frequencies of the Nb split-ring resonators, and so the dips in electromagnetic transmission between approximately 9.75 GHz to approximately 11 GHz were due to a negative real part of the permeability. This plot is interesting

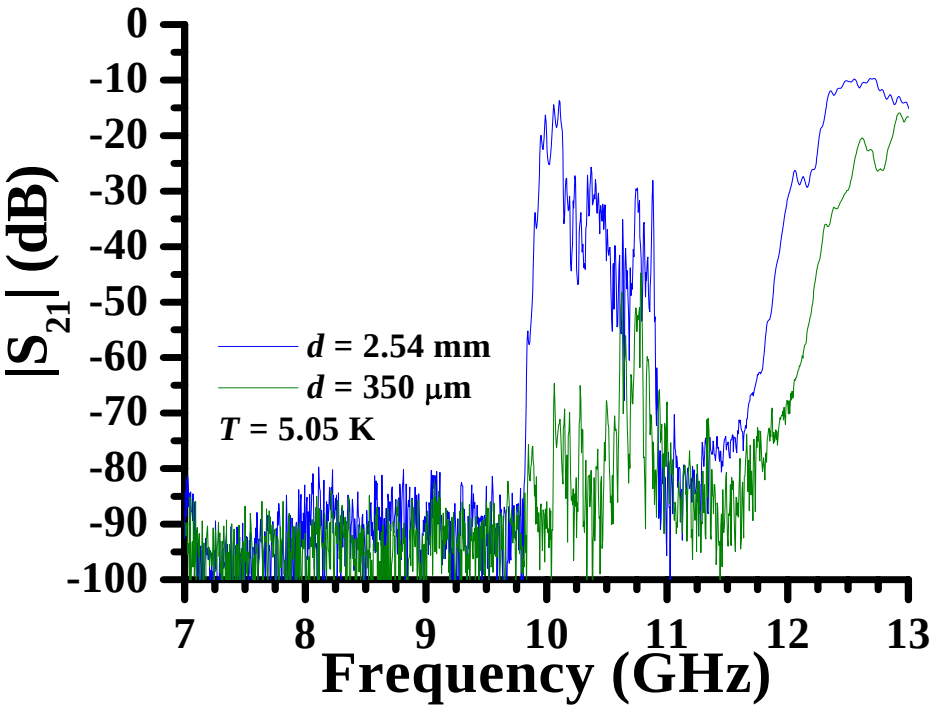

Figure 6.3: A plot of the electromagnetic transmission versus frequency for an array of 216 Nb split-ring resonators in a Nb wire array measuring five wires transversely and eighteen wires longitudinally, with a lattice parameter of $a = 5.08$ mm. The data were measured at 5.05 K. The distance separating the wires and Nb split-ring resonator was approximately $d = 2.54$ mm for the blue curve, and approximately $d = 350$ μm for the green curve.

as it is a combination of wires and split-ring resonators that produces frequency bandwidths of negative real parts of the permittivity and permeability that do not intersect.

6.3 Single Nb split-ring resonator in a Nb wire array

Building on the experience from Chapter 5, the ability to observe an electromagnetic response from a single Nb split-ring resonator in a Nb wire array would greatly simplify the problem of multiple interactions. If a single peak in electromagnetic transmission could be observed and measured, it could be fit with a transfer matrix model much easier than, for instance, Figure (6.1), and the changes in the resonant frequency and quality factor with temperature could be measured and fit with the simple model from Chapter 2. A question that arises is how long should the Nb wire array be? It is clear from Figure (6.4) that the lattice parameter should be $a = 5.08$ mm, or smaller, however, a full length of eighteen longitudinal rows would most likely wash out any electromagnetic response to the applied electromagnetic field by the single Nb split-ring resonator, while from Figure (4.11), Nb wire arrays that are too short may not exhibit clearly the feature of a negative real part of the index of refraction.

The first subsection will investigate various longitudinal lengths of the Nb wire array. The next sections will show a single peak in electromagnetic transmission due to a single Nb split-ring resonator in a Nb wire array of what was believed to be the optimal longitudinal length. The peak in electromagnetic transmission is fit with

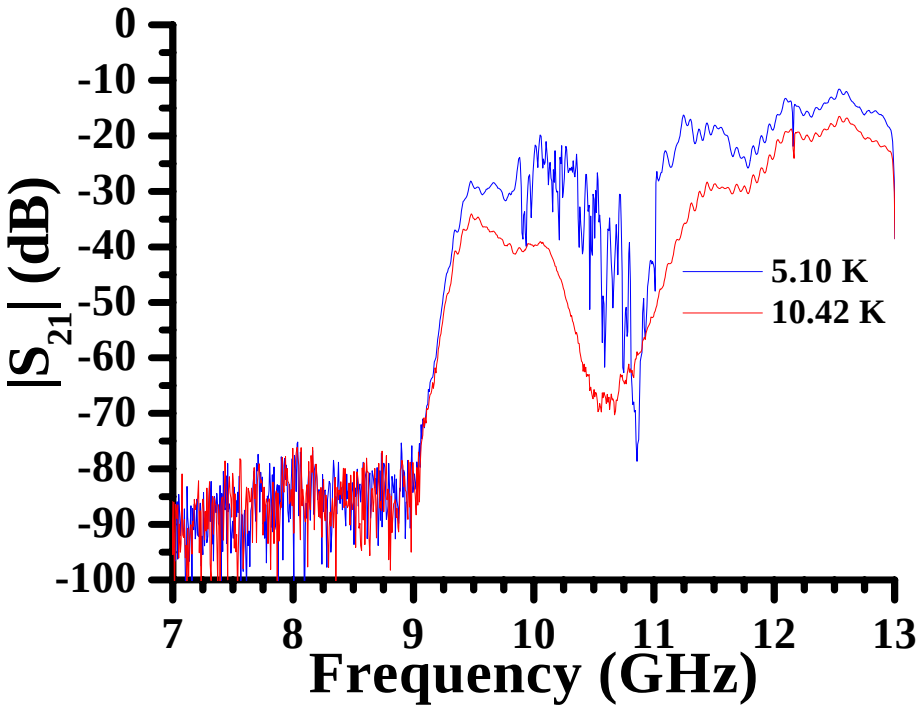

Figure 6.4: A plot of the electromagnetic transmission, $|S_{21}|$, versus frequency for an array of 216 Nb split-ring resonators in a Nb wire array measuring five wires transversely and eighteen wires longitudinally, with a lattice parameter of $a = 7.19$ mm. The blue curve was measured at 5.10 K and the green curve was measured at 10.42 K. The distance separating the wires and Nb split-ring resonator was approximately $d = 2.54$ mm.

a five-layer transfer matrix model, and the change in the resonant frequency and quality factor with temperature is measured and fit. All fits are compared to similar fits for the single Nb split-ring resonator in Chapter 5.

6.3.1 Various Nb wire array lengths

The first test was inserting a single Nb split-ring resonator into a Nb wire array with a lattice parameter of $a = 5.08$ mm, measuring five wires transversely and eighteen wires longitudinally. This is shown as the blue curve in Figure (6.5). No observable peak in electromagnetic transmission above the noise floor was present, and this is attributed to the combination of the evanescent electromagnetic modes as a result of the negative permittivity, and the length of the Nb wire array. Thus, either the evanescent electromagnetic modes cannot reach the single Nb split-ring resonator, or these modes do reach the single Nb split-ring resonator, but decay before reaching the receiving antenna in the waveguide.

The electromagnetic transmission after reducing the length of the Nb wire array of Figure (6.1) by one-half is shown as the green curve in Figure (6.5). A single Nb split-ring resonator was inserted into a Nb wire array with a lattice parameter of $a = 5.08$ mm, measuring five wires transversely and nine wires longitudinally. It is with this length of the Nb wire array that a peak in electromagnetic transmission emerges at roughly 10.83 GHz. However, this peak is 20 dB above the noise floor, and it was believed that the peak could be larger, for instance, 30 dB, above the noise floor for a smaller length of the Nb wire array. An odd number

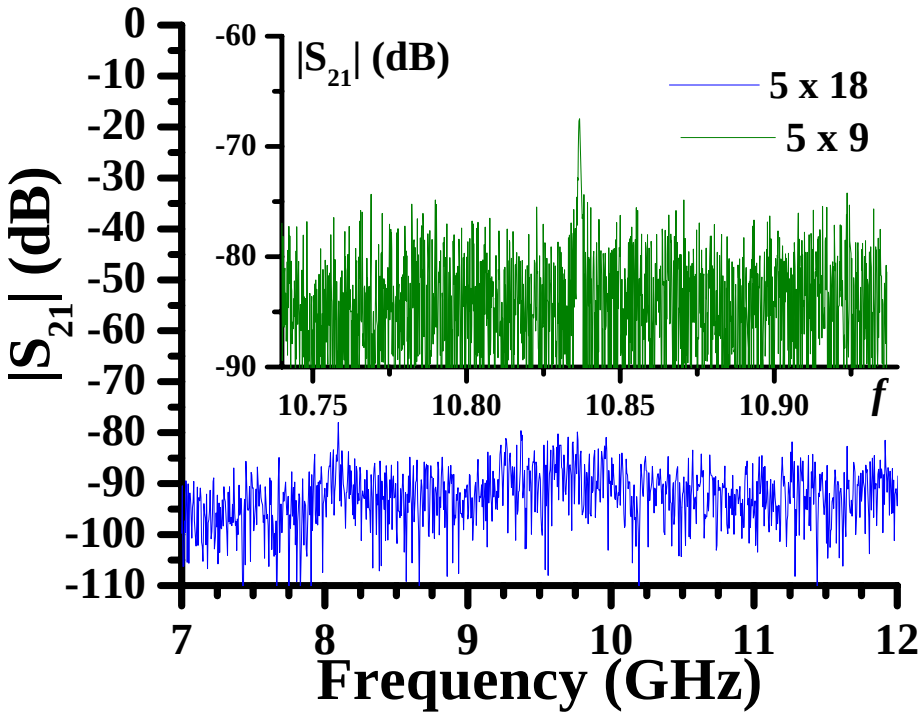

Figure 6.5: A plot of the electromagnetic transmission, $|S_{21}|$, versus frequency for a single Nb split-ring resonator in a Nb wire array with a lattice parameter of $a = 5.08$ mm, and various longitudinal lengths. The blue curve is a single Nb split-ring resonator in a Nb wire array with eighteen rows longitudinally, and the green curve is a single Nb split-ring resonator in a Nb wire array with nine rows longitudinally. The single Nb split-ring resonator was approximately $d = 2.54$ mm from the Nb wires.

of longitudinal rows was desired to make the array symmetric with respect to the waveguide-flange planes, however, based on Figure (4.10), five longitudinal rows was believed to be too short to produce a reliable, understandable result of electromagnetic transmission. Thus, it was settled that seven longitudinal rows would suffice for the experiments of a single Nb split-ring resonator [45].

Another interesting experiment is a single Nb split-ring resonator in a Nb wire array with a lattice parameter of $a = 7.19$ mm. The Ag-plated brass X-band waveguide was used, with a Nb wire array measuring five wires transversely and thirteen wires longitudinally, with a lattice parameter of $a = 7.19$ mm, and the single Nb split-ring resonator–γ was inserted into the middle of the Nb wire array. The results are shown in Figure (6.6), where the blue curve is data measured in liquid Helium, and the red curve is data taken at 9.37 K. Note the resonant feature on the blue curve near 10.75 GHz that disappears above the critical temperature of the Nb film of the Nb split-ring resonator. This feature is presumably due to the Nb split-ring resonator, and a result of a medium with a negative real part of the index of refraction. This plot looks very similar to the green curve in Figure (2.9).

6.3.2 Fit of the electromagnetic transmission

The single Nb split-ring resonator–α was inserted into a Nb wire array with a lattice parameter of $a = 4.57$ mm, with five wires transversely and seven wires longitudinally, in the Nb X-band waveguide [45]. A peak in electromagnetic transmission presumably due to a frequency bandwidth where the wire-split-ring res-

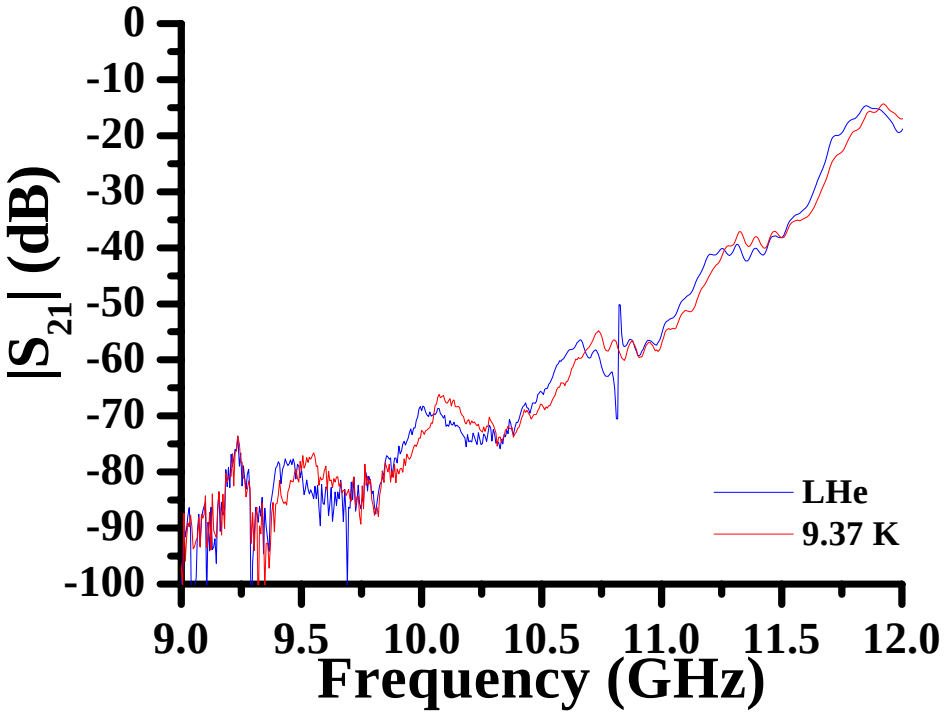

Figure 6.6: A plot of the electromagnetic transmission, $|S_{21}|$, versus frequency for the single Nb split-ring resonator–γ in a Nb wire array measuring five wires transversely, and thirteen wires longitudinally, with a lattice parameter of $a = 7.19$ mm, in the Ag-plated brass X-band waveguide. The blue curve was measured in liquid Helium, denoted as LHe, and the red curve was measured at 9.37 K.

onator medium had a negative real part of the index of refraction, is shown in Figure (6.7) at 5.05 K. The data are the blue circles, a fit is the black curve. The single peak in electromagnetic transmission was fit with a five-layer transfer matrix model, consisting of two sections of infinite waveguide, sandwiching two sections of a medium with a permittivity like that of Equation (2.22), sandwiching a section of a medium with a permittivity like that of Equation (2.22) and a permeability like that of Equation (2.97).

The five-layer transfer matrix model for the fit in Figure (6.7) used a permittivity given by Equation (2.22), and a permeability given by Equation (2.97), while fixing the lengths of the layers to values determined by measuring geometry of the experiment [45]. The fit parameters were a metallic wire plasma frequency, $\omega_p = 2\pi \times 18.0$ GHz, a permittivity loss parameter, $\gamma = 2\pi \times 500$ kHz, a filling fraction, $f = 0.032$, a split-ring resonator resonant frequency, $\omega_0 = 2\pi \times 10.72$ GHz, a permeability loss parameter of $\Gamma = 2\pi \times 600$ kHz, and an overall insertion loss constant, C, although the value of the insertion loss constant is not known*. These parameters are tabulated in Table (6.1). The theoretical plasma frequency, found by using Equation (2.62) with Equation (2.95), is predicted to be at $\omega_p = 2\pi \times 17.7$ GHz for this Nb wire array geometry, close to the fit value of $\omega_p = 2\pi \times 18.0$ GHz. The single Nb split-ring resonator in an otherwise empty Nb X-band waveguide had

*The reason for not knowing the value of the fit constant is that this fit was performed on a computer that had a catastrophic hard disc failure, in which all the data was lost. The value of the fit constant, unlike the other values, was not published, and therefore, the value of the fit constant is unknown.

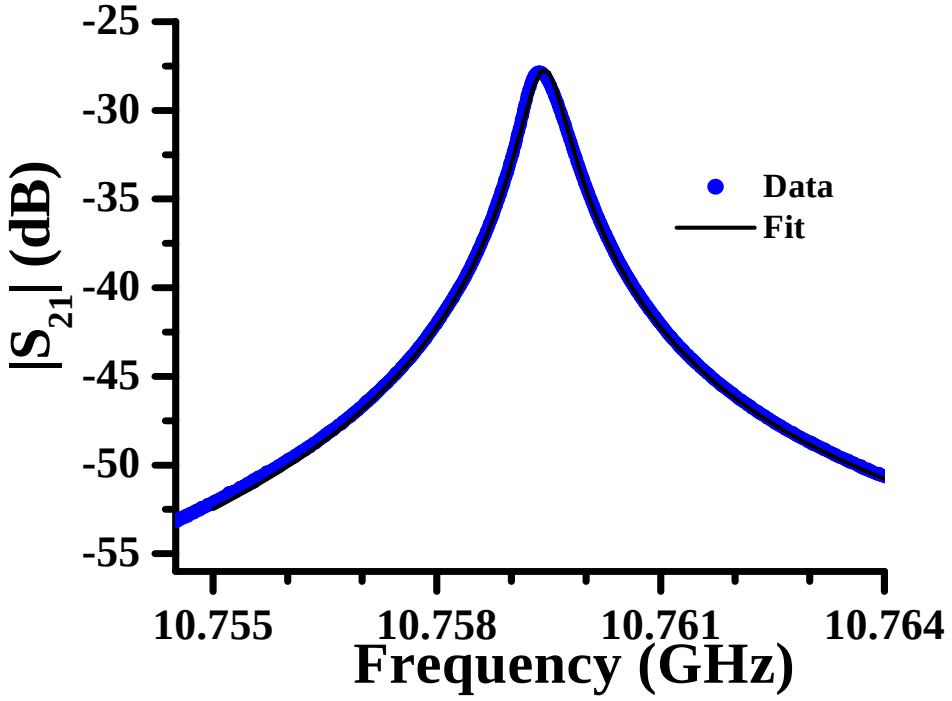

Figure 6.7: A plot of the electromagnetic transmission, $|S_{21}|$, versus frequency for the single Nb split-ring resonator–α in a Nb wire array measuring five rows transversely and seven rows longitudinally with a lattice parameter of $a = 4.57$ mm, inside the Nb X-band waveguide, at 5.09 K. The distance separating the singe Nb split-ring resonator, and the Nb wires, is approximately $d = 2.29$ mm. The blue circles are the data, while the black curve is a fit using a five-layer transfer matrix model, using a permittivity given by Equation (2.22) with fit parameters of plasma frequency ω_p, and loss, γ, and a permeability given by Equation (2.97), with fit parameters of resonant frequency, ω_0, loss, Γ, filling fraction, f, material length, l, and an overall insertion loss, C.

Table 6.1: Fit parameter results of Figure (6.7) for the single Nb split-ring resonator–α in a Nb wire array.

$\omega_p/2\pi$ (GHz)	$\gamma/2\pi$ (kHz)	$\omega_0/2\pi$ (GHz)	$\Gamma/2\pi$ (kHz)	f
18.0	500	10.72	600	0.032

a resonant frequency of $\omega_0 = 2\pi \times 10.79$ GHz, while in the reduced Nb wire array, the resonant frequency of the peak in electromagnetic transmission due to the negative index of refraction was $\omega_0 = 2\pi \times 10.72$ GHz. The permeability loss parameters for the lone Nb split-ring resonator and the negative index of refraction medium were similar, $\Gamma = 2\pi \times 366$ kHz and $\Gamma = 2\pi \times 600$ kHz, respectively. The filling fractions, f, between the lone Nb split-ring resonator and the single Nb split-ring resonator in the Nb wire array differed by an order of magnitude, $f = 0.14$ and $f = 0.032$, respectively. Also, the loss parameter of the wire array was much less in the case of the single Nb split-ring resonator in the Nb wire array medium versus the Nb wire-only array, $\gamma = 2\pi \times 500$ kHz, and $\gamma = 2\pi \times 72$ MHz, respectively.

6.3.3 Temperature dependence of the resonant frequency and quality factor

Similar to the case of the lone Nb split-ring resonator in the Nb X-band waveguide, the peak in electromagnetic transmission due to the single Nb split-ring resonator in the reduced Nb wire array may be tracked as a function of temperature,

with regards to the resonant frequency and quality factor. The single Nb split-ring resonator–α in the plane-parallel gap-orthogonal orientation was inserted into the center of a Nb wire array measuring five rows transversely and seven rows longitudinally, with a lattice parameter of $a = 4.57$ mm. The distance separating the single Nb split-ring resonator and the Nb wires was approximately $d = 2.29$ mm, and the experiment was performed using the Nb X-band waveguide, Nb waveguide-to-coaxial cable couplers, and in vacuum. As the temperature was increased, the electromagnetic transmission was measured versus frequency. The results are shown in Figure (6.8), where the temperature of each curve is, moving right to left, 5.09 K for the blue curve, 7.70 K for the green curve, 7.80 K for the red curve, and 8.10 K for the maroon curve [45]. The peak in electromagnetic transmission decreases in frequency and magnitude, and widens as the temperature increases, a result of the increasing kinetic inductance and surface resistance, similar to the lone Nb split-ring resonator data presented in Chapter 5.

The resonant frequency of the peak in electromagnetic transmission in Figure (6.8) was tracked as a function of temperature, and is shown in Figure (6.9) as the blue dots, along with a fit, shown as the black curve, using Equation (2.151). The fit parameters were very similar to the results in Table (5.2), and are summarized in Table (6.2). The value of χ that was fit in the lone Nb split-ring resonator case was fixed for the fit of the frequency shift of the single Nb split-ring resonator in the Nb wire array. The critical temperature was fit with 8.67 K, close to the measured value of 8.65 K. The value of β was fit with 1.5×10^{-3}, which is similar to the value of β obtained for the lone split-ring resonator fit, 1.3×10^{-3}, and close to the predicted

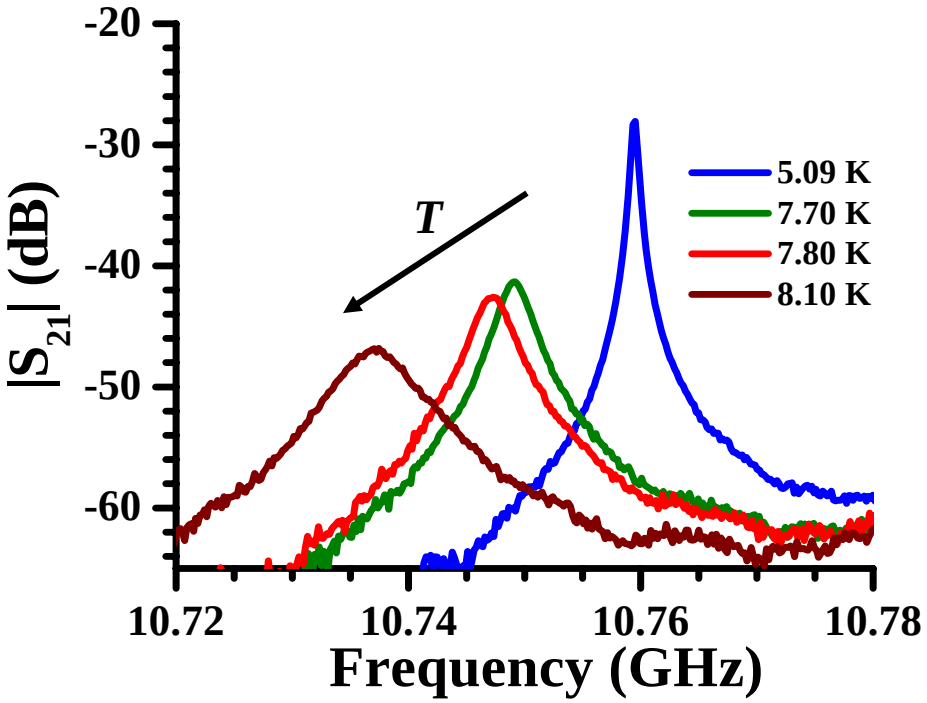

Figure 6.8: A plot of the electromagnetic transmission, $|S_{21}|$, versus frequency for a single Nb split-ring resonator in a Nb wire array measuring five rows transversely and seven rows longitudinally, measured at various temperatures in the Nb X-band waveguide. The temperature of each curve is, moving right to left, 5.09 K (blue), 7.70 K (green), 7.80 K (red), and 8.10 K (maroon). The increase in temperature is shown by the black arrow, where T stands for temperature. The setup is similar to that of Figure (6.7).

Table 6.2: Fit parameter results of the resonant frequency shift in Figure (6.9) for the single Nb split-ring resonator–α in the Nb X-band waveguide.

	T_c (K)	χ	β	$\omega_{0,g}/2\pi$ (GHz)
Estimate	8.65[a]	4	5×10^{-4}	—
Fit Value	8.67	2.63[b]	1.5×10^{-3}	10.77

[a]From ac magnetic susceptibility measurements.

[b]This value was fixed at $\chi = 2.63$ for the fit.

value of 5×10^{-4}.

If the maximum value of the peak in electromagnetic transmission occurs at a resonant frequency, ω_0, and has a magnitude of M dB at the resonant frequency, then the quality factor is defined, in this case, as [124, p. 130, Eq. (3.65)],

$$Q = \frac{\omega_0}{\Delta\omega}, \tag{6.1}$$

where [124, p. 130],

$$\Delta\omega \stackrel{def}{=} \omega_R(M-3) - \omega_L(M-3), \tag{6.2}$$

and $\omega_R(M-3)$ is the frequency located to the right of the peak in electromagnetic transmission, at the electromagnetic transmission value that is 3 dB less than M, and $\omega_L(M-3)$ is the frequency located to the left of the peak in electromagnetic transmission, at the electromagnetic transmission value that is 3 dB less than M. The change in the quality factor with temperature is fit with the same model as the lone Nb split-ring resonator in the Nb X-band waveguide, presented in Chapter 5. A plot of the quality factor versus temperature is shown in Figure (6.10), where the

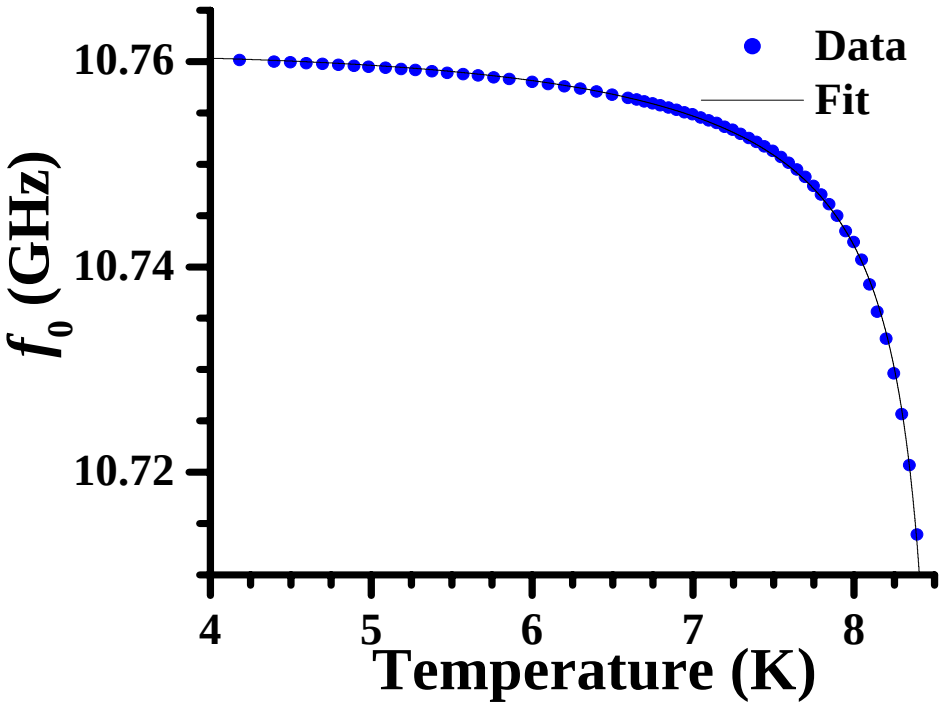

Figure 6.9: A plot of the resonant frequency, f_0, versus temperature for the single Nb split-ring resonator–α in a Nb wire array measuring five rows transversely and seven rows longitudinally, as in Figure (6.8). The blue dots are the data, while the black curve is a fit using Equation (2.151).

Table 6.3: Fit parameter results of the quality factor shift in Figure (6.10) for the single Nb split-ring resonator–α in a Nb wire array in the Nb X-band waveguide.

T_c (K)[a]	χ^a	β^a	ζ	Q_b
8.67	2.63	1.5×10^{-3}	1.21×10^{-5}	2.7×10^4

[a]Obtained from Table (6.2), and inserted directly into Equation (2.161).

blue dots are the data, and the black curve is a fit using Equation (2.161) [45]. As with the lone Nb split-ring resonator fit in Chapter 5, the fit parameters cannot, at this moment, be predicted without knowledge of the current density profile in the Nb rings that make up the Nb split-ring resonator. However, the fit parameter values for the single Nb split-ring resonator in the Nb wire array can be compared to the lone Nb split-ring resonator data, and may be similar since the only difference in thte setup is the addition of a medium with a negative permittivity, which may effect the parameter ζ in Equation (2.161), through the geometric factor, G, and there may be an effect on the background quality factor, Q_b. The parameters are listed in Table (6.3), where the T_c and β were fixed based on the results in Table (6.2), and χ was held constant, based on the value from the lone Nb split-ring resonator case, detailed in Table (5.2). The fit value of $\zeta = 1.21 \times 10^{-5}$ agrees with the lone Nb split-ring resonator case of $\zeta = 1.13 \times 10^{-5}$, while the background quality factor, $Q = 2.7 \times 10^4$, is less that the lone Nb split-ring resonator case, $Q = 6.5 \times 10^4$, and a result of adding slightly lossy wires into the system.

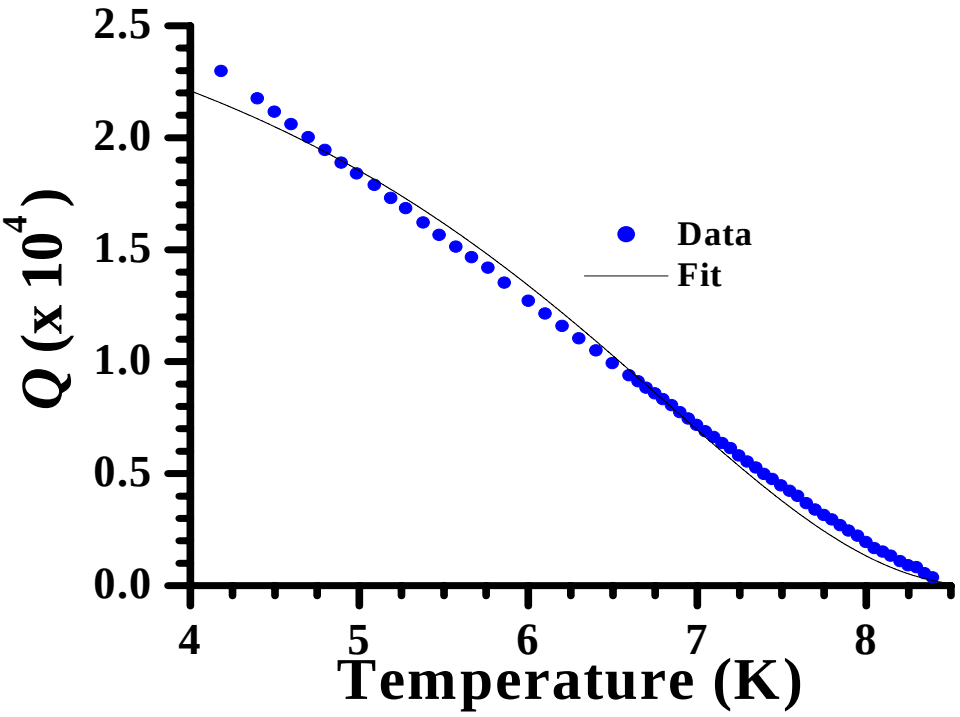

Figure 6.10: A plot of the quality factor, Q, versus temperature for the single Nb split-ring resonator–α in a Nb wire array measuring five rows transversely and seven rows longitudinally, as in Figure (6.8), inside the Nb X-band waveguide. The blue dots are the data, while the black curve is a fit using Equation (2.161).

6.4 Single Cu-Ni-Au split-ring resonator and single Nb closed-ring resonator in a Nb wire array

Despite the absence of any special feature in the electromagnetic transmission spectra of a single Cu-Ni-Au split-ring resonator, and a single Nb closed-ring resonator, in an otherwise empty waveguide, each resonator was inserted into the Nb wire array measuring five rows transversely and seven rows longitudinally. Both measurements were in liquid Helium, but the Cu-Ni-Au split-ring resonator was measured in the Ag-plated brass X-band waveguide, with a lattice parameter of $a = 5.08$ mm, and the Nb closed-ring resonator was measured in the Nb X-band waveguide, with a lattice parameter of $a = 4.57$ mm. The results are shown in Figure (6.11), where the green curve is the closed-ring resonator data, and the blue curve is the Cu-Ni-Au split-ring resonator data. The frequency bandwidths in both sets of data are wide enough that the resonator was expected to have some feature, if any, within the limits. However, similar to the otherwise empty waveguide data, there was no noticeable feature above the noise floor due to either resonator. Thus, the single Cu-Ni-Au split-ring resonator is thought to be too lossy for its array size, and the Nb closed-ring resonator appears to have no resonance near 10 GHz like the single Nb split-ring resonator.

6.5 Bianisotropy of a single Nb split-ring resonator in a Nb wire array

A unique ability of the superconducting artificial materials used in this research is the ability to reduce the number of individual devices in an array, while still

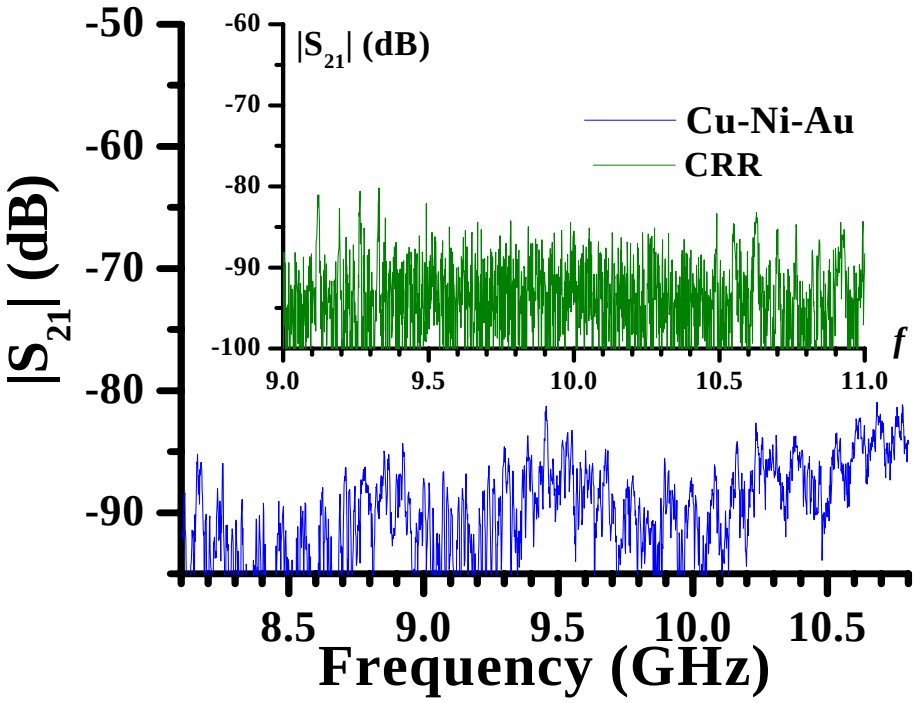

Figure 6.11: A plot of the electromagnetic transmission versus frequency for a single Cu-Ni-Au and a single Nb closed-ring resonator in a Nb wire array measuring five rows transversely and seven rows longitudinally, immersed in liquid Helium. The single Cu-Ni-Au split-ring resonator, shown as the blue curve, was measured inside the Ag-plated brass X-band waveguide with a lattice parameter of $a = 5.08$ mm, and the single Nb closed-ring resonator, shown as the green curve, was measured inside the Nb X-band waveguide with a lattice parameter of $a = 4.57$ mm. In both case, the distance separating the single ring-resonator and the wires was approximately one-half the lattice parameter.

maintaining the desired frequency response of the effective parameters. For instance, an array of Nb split-ring resonators was reduced to a single Nb split-ring resonator, which appeared to have the same permeability as a larger array, unlike the single Cu-Ni-Au split-ring resonator. One subject where this property of reducibility is immediately applicable is the study of the bianisotropy of the split-ring resonators. This was studied in Chapter 5 in an otherwise empty waveguide, however, the materials used in this dissertation allow for the single Nb split-ring resonator to be inserted into a reduced wire array, and perhaps determine how the single Nb split-ring resonator is coupling to the applied electromagnetic field.

The labels for the different orientations of the single Nb split-ring resonator with respect to the applied electromagnetic field were discussed in Chapter 5. As a summary, the plane-parallel gap-orthogonal orientation had a magnetic dipole moment due to only the applied transverse magnetic field, however there was also an electric dipole moment due to the applied transverse magnetic field. The plane-parallel gap-parallel orientation, on the other hand, had a magnetic dipole moment due to the applied transverse magnetic field, and the applied transverse electric field, as well as an electric dipole moment due to those two field components. For the other two orientations, recall that the applied electromagnetic field strengths are a function of position. The applied longitudinal magnetic field has a maximum at the walls, and a minimum in the center, of the waveguide, while the applied transverse electric field is the opposite. Since the measurements to be presented were measured in the center of the waveguide, only this position is considered. The plane-orthogonal gap-parallel orientation thus had a magnetic dipole, and an

electric dipole moment, due to the applied transverse electric field. Finally, the plane-orthogonal gap-orthogonal orientation had no magnetic dipole moment, but did have an electric dipole moment due to the applied transverse electric field.

The various orientations were measured with the single Nb split-ring resonator–π inserted in the center of a Nb wire array measuring five rows transversely and seven rows longitudinally, with a lattice parameter of $a = 4.57$ mm, in the Nb X-band waveguide, with a separation distance of $d = 2.29$ mm. All data were measured immersed in liquid Helium. The electromagnetic transmission spectra are plotted in Figure (6.12). The plane-parallel gap-orthogonal, shown as a blue curve, plane-parallel gap-parallel, shown as a red curve, and plane-orthogonal gap-parallel, shown as the black curve, orientations all exhibit a peak in electromagnetic transmission, while the plane-orthogonal gap-orthogonal orientation has no noticeable peak in electromagnetic transmission above the noise floor. The plane-orthogonal gap-orthogonal orientation is not expected to have any peak in electromagnetic transmission since the coupling to the applied electromagnetic field is very weak; recall from Figure (5.22) that the simulated electromagnetic transmission of the plane-orthogonal gap-orthogonal orientation in the otherwise empty waveguide was featureless, that is, $|S_{21}| = 0$ dB. The other orientations in Figure (6.12), however, are very complicated, in fact, they do not correlate with their empty waveguide counterparts in Figure (5.21).

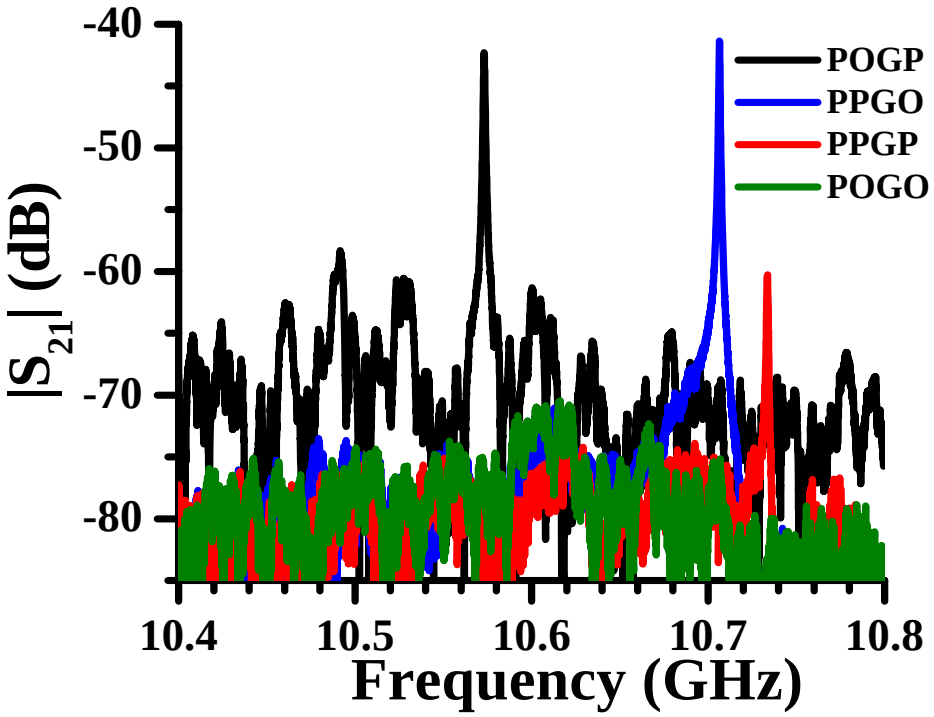

Figure 6.12: A plot of the electromagnetic transmission, $|S_{21}|$, versus frequency for a single Nb split-ring resonator in a Nb wire array measuring five rows transversely and seven rows longitudinally, with a lattice parameter of $a = 4.57$ mm, for various orientations with respect to the applied electromagnetic field. The orientations are plane-parallel gap-orthogonal, shown as the PPGO blue curve, plane-parallel gap-parallel, shown as the PPGP red curve, plane-orthogonal gap-parallel, shown as the POGP black curve, and plane-orthogonal gap-orthogonal, shown as the POGO green curve. See Figure (2.10).

6.6 Ka-band waveguide

6.6.1 Single Nb split-ring resonator

To finish this chapter, the suggestion that a waveguide below cutoff can be thought of as a plasma with a negative real part of the permeability is investigated. The Nb split-ring resonators had a resonant frequency of approximately 11 GHz, and the waveguide was of type Ka-band, with a TE_{10} cutoff frequency of approximately 21 GHz. Since the resonant frequencies of the Nb split-ring resonators are much less than the waveguide cutoff frequency of the lowest mode, the electromagnetic modes that couple to the Nb split-ring resonator are highly evanescent, which means that the decay length, that is, the length at which the signal has decayed by a factor of $\exp(-1)$, is very short, and so the total length of the waveguide must be minimized in order for these modes to couple to the single Nb split-ring resonator. Thus, only the waveguide-to-coaxial cable couplers of the Ka-band waveguide were used, as described in Chapter 3.

The electromagnetic transmission of a single Nb split-ring resonator in the Ka-band waveguide is shown in Figure (6.13), measured in liquid Helium, shown as the blue curve, and at 11.06 K, shown as the red curve. The figure shows several interesting features. The first is the apparent absence of a split-ring resonator resonance near 11 GHz. While it appears that there is no low-order resonance of the Nb split-ring resonator in Figure (6.13), there is in fact such a resonance, hidden in the figure due to the step size of the frequency. Narrowing the frequency bandwidth to 10.75 GHz to 10.80 GHz reveals a peak in electromagnetic transmission, shown

in Figure (6.14). There, the single Nb split-ring resonator–π was inserted into the Ka-band waveguide-to-coaxial cable couplers, and the data shown were measured in liquid Helium, shown as the blue curve, and at 10.95 K, shown as the red curve. Note the absence of the peak in electromagnetic transmission above the critical temperature of the Nb film of the Nb split-ring resonator.

A second interesting feature of Figure (6.13) is the change in the cutoff edge, compared to the empty Ka-band waveguide as shown in Figure (4.4) as the blue curve. This change in the appearance of the cutoff edge was likely due to the "broken-wire" effect, since the height, b, of the waveguide, as defined in Figure (2.3), is almost equal to the length of an edge of the Nb split-ring resonator.

6.6.2 Single Nb closed-ring resonator

The third interesting feature of Figure (6.13) is the prominent peak in electromagnetic transmission at approximately 17.5 GHz. What makes this peak in electromagnetic transmission especially interesting is that it remains, even above the critical temperature of the Nb film of the Nb split-ring resonator, despite most electromagnetic transmission features discussed in this dissertation vanishing above the critical temperature of the Nb film of the Nb split-ring resonator. This motivates inserting other resonators, in particular a single Nb closed-ring resonator, into the Ka-band waveguide-to-coaxial cable couplers. The fact that a peak in electromagnetic transmission remains above the critical temperature of the single Nb split-ring resonator means that these other resonators may also produce a peak in

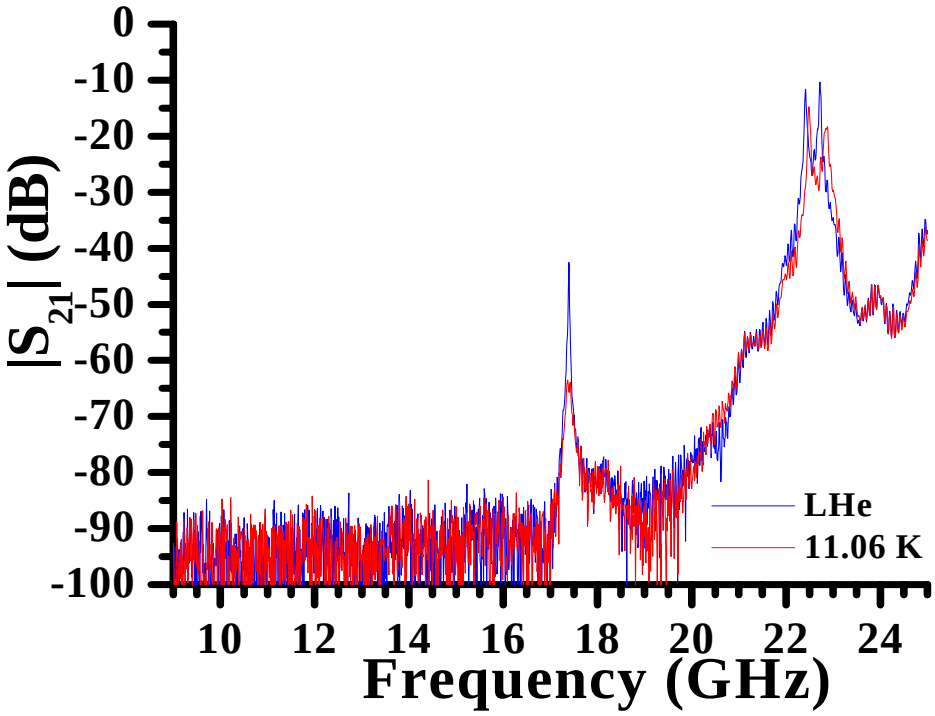

Figure 6.13: A plot of the electromagnetic transmission, $|S_{21}|$, versus frequency for a single Nb split-ring resonator in the Ka-band waveguide, measured in liquid Helium, shown as the blue curve, and 11.06 K, shown as the red curve.

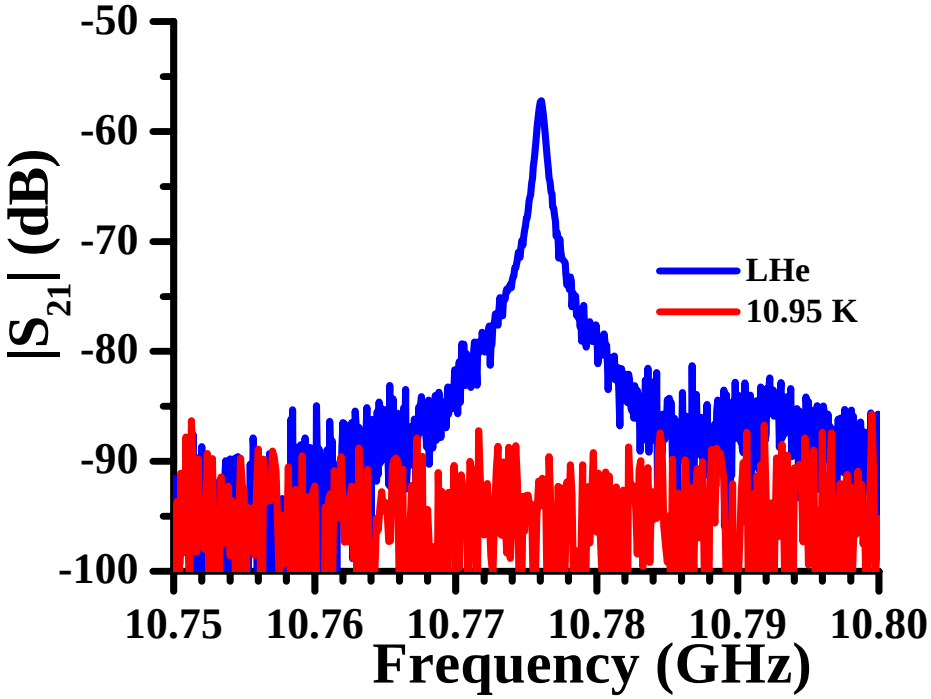

Figure 6.14: A plot of the electromagnetic transmission, $|S_{21}|$, versus frequency for the single Nb split-ring resonator–π in the Ka-band waveguide-to-coaxial cable couplers, measured in liquid Helium, denoted LHe, shown as the blue curve, and 10.95 K, shown as the red curve.

electromagnetic transmission. The results are shown in Figure (6.15), where there is a peak in electromagnetic transmission from the single Nb closed-ring resonator at approximately 17 GHz, and no peak in electromagnetic transmission at approximately 11 GHz. The reason for this is the current density resonant structure in the resonator rings. While a plot is not shown here, a Microwave Studio CST simulation revealed that the peak in electromagnetic transmission at approximately 17 GHz is a higher order mode, and in fact the standing waves in the rings have a full wavelength resonance; that is, there are two nodes in the simulated current density profile. Since one node is at the capacitive gap, and the other node is 180° from the capacitive gap, the capacitive gap is almost meaningless, and thus the single Nb closed-ring resonator was able to resonate and produce a peak in electromagnetic transmission at the higher frequency, approximately 17 GHz. At the lower frequency, approximately 11 GHz, the capacitive gap serves as a node for the lower half-wave resonance, and since the closed-ring resonator lacks a capacitive gap, it could not resonate at the lower frequency, approximately 11 GHz.

6.7 Summary

Arrays of split-ring resonators were placed inside Nb wire arrays of various lattice parameters, and the electromagnetic transmission spectra were measured. The 216-Nb split-ring resonator array showed a large frequency bandwidth of transmission as a result of a negative real part of the index of refraction, in the Nb wire array with a lattice parameter of $a = 5.08$ mm, while the same array in the Nb

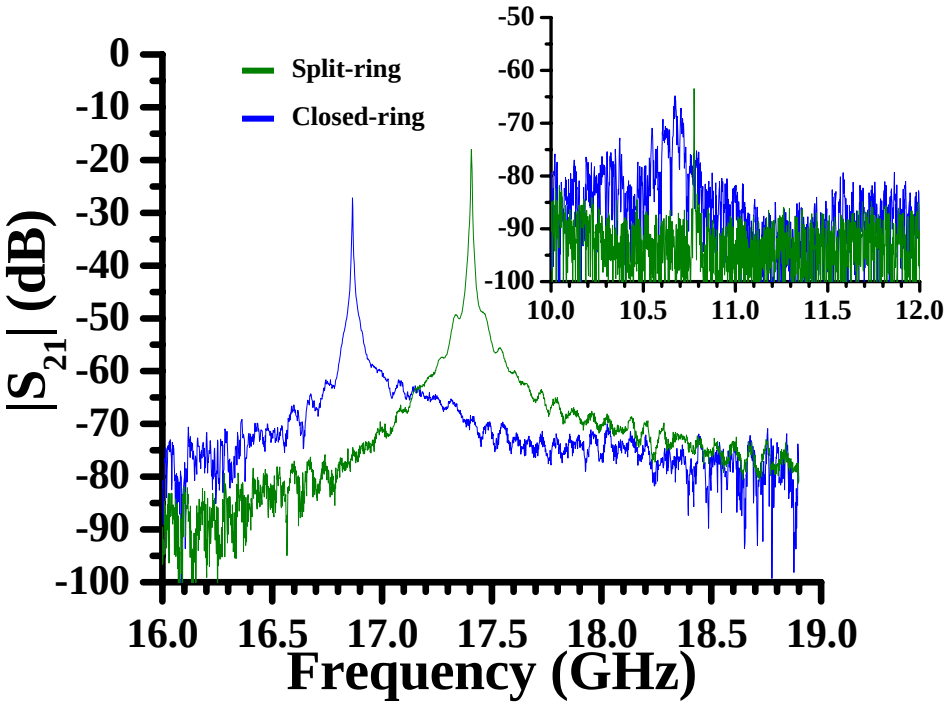

Figure 6.15: A plot of the electromagnetic transmission, $|S_{21}|$, versus frequency for the single Nb split-ring resonator–π, shown as the green curve, and a single Nb closed-ring resonator, shown as blue curve, in the Ka-band waveguide-to-coaxial cable couplers, measured in liquid Helium. The main figure is the second harmonic of the current density, and the inset is the fundamental mode of the current density.

wire array with a lattice parameter of $a = 7.19$ mm showed a large reduction in the plasma edge of the wire array. As a result, the data showed a dip in electromagnetic transmission due to a negative real part of the permeability, rather than a peak in electromagnetic transmission due to a negative real part of the index of refraction. When a single Nb split-ring resonator was placed inside a Nb wire array with a lattice parameter of $a = 5.08$ mm, a single peak in electromagnetic transmission was observed, with a height above the noise floor depending on the length of the Nb wire medium. For the Nb wire array measuring eighteen rows longitudinally, the peak in electromagnetic transmission, if present, was below the noise floor, and a length of seven rows of Nb wires was chosen as ideal. When the single Nb split-ring resonator was placed into a Nb wire array with a lattice parameter of $a = 7.19$ mm, the single peak in electromagnetic transmission was on the cutoff edge of the Nb wire array, and the functional form produced by the three-layer transfer matrix model was observed; that is, there was a sharp dip in electromagnetic transmission followed by a sharp peak in electromagnetic transmission, both due to the single Nb split-ring resonator. The bianisotropy of a single Nb split-ring resonator was measured and simulated.

The peak in electromagnetic transmission of the single Nb split-ring resonator inside a Nb wire array measuring five rows transversely and seven rows longitudinally, with a lattice parameter of $a = 5.08$ mm, was fit with a five-layer transfer matrix model, and the values compare well with the single Nb split-ring resonator inside an otherwise empty waveguide fit from Chapter 5. The parameter values corresponding to the Nb wire array agreed with the fits and theories of Chapter 2. The peak in

electromagnetic transmission of the single Nb split-ring resonator was also tracked as a function of temperature, and the resonant frequency and quality factor shifts were measured and fit. The fit parameters for these two fits agree with that of the single Nb split-ring resonator inside an otherwise empty waveguide fit from Chapter 5. Finally, the electromagnetic transmission of a single Nb split-ring resonator inside an otherwise empty Ka-band waveguide-to-coaxial cable couplers was measured, and a low frequency mode resonance was observed, along with a higher frequency mode resonance. The lower resonance was attributed to the fundamental mode of the current density in the Nb split-ring resonator rings, while the higher resonance was attributed with the second harmonic mode of the current density. While the peak in electromagnetic transmission due to the fundamental mode of the current density disappeared above the critical temperature of the film of the single Nb split-ring resonator, the peak in electromagnetic transmission due to the second harmonic mode of the current density remained above the critical temperature of the film of the single Nb split-ring resonator. This motivated inserting a single Nb closed-ring resonator into the Ka-band waveguide-to-coaxial cable couplers, where it was observed that there was a peak in electromagnetic transmission due to the second harmonic mode of the current density, while no peak in electromagnetic transmission existed at a lower frequency resonant mode.

Chapter 7

Conclusions

7.1 Overview

This chapter is broken up into two parts. The first part details the conclusions from each preceding chapter, and the second part consists of future work of this thesis project.

7.2 Chapter summaries

7.2.1 Chapter 2

Basic principles of electromagnetic theory were written. The basic ideas of linear media, and in particular the permittivity and permeability of media, were shown. These ideas were used as a basis for more complicated theories involving negative values of the permittivity and permeability, along with non-linear, bian-isotropic media. Since the experiments in this dissertation were performed inside a waveguide, the basic theories of waveguides were written, and showed how field structures may be exploited by the geometry of the split-ring resonators. The theory of refraction was also shown, and this was used, along with the waveguide theories, to derive a transfer matrix model in order to model the experiments in this dissertation. Basic principles of superconductivity were shown, and a temperature

dependent resonant frequency and quality factor of the split-ring resonators was derived using the London model.

The chapter also discussed the theory of obtaining a negative real part of the permittivity, a negative real part of the permeability, and a negative real part of the index of refraction, at microwave frequencies. First, an infinite array of metallic wires, with their infinite lengths parallel to the polarization of an applied electromagnetic field, were shown to act as a solid slab of metal for incident radiation with a wavelength much larger than the lattice parameter and metallic wire thickness. A plasma frequency was derived as a function of the lattice parameter and metallic wire radius, and for frequencies below this plasma frequency, the real part of the permittivity was shown to be negative. Next, an infinite array of metallic split-cylinders, with the cylindrical axes aligned with an applied ac H field, were shown to have a resonant response to the applied ac H field. This resonant response produced a large diamagnetic response, and produced a frequency bandwidth where the real part of the permeability was negative. Finally, the physical implementation of these theories was discussed, where two-dimensional slices of the infinite metallic split-cylinders, called split-ring resonators, were inserted between rows of metallic wires, and an applied electromagnetic field was incident such that the applied transverse electric field coupled to the metallic wires, while the applied transverse magnetic field coupled to the split-ring resonators. The result was a medium with a frequency bandwidth where the real part of the index of refraction was negative, located near the frequency overlap where the permittivity and permeability were both negative.

7.2.2 Chapter 3

The Nb wires were aquired from Advent Research Materials LTD, and the manufacture of the Cu-Ni-Au split-ring resonators was also outsourced. All Nb split-ring resonators were made in-house by rf sputtering Nb film, performing lithography, and plasma etching excess Nb. The wire and split-ring resonator properties were measured inside $X-$ and Ka-band waveguides made of either Nb or brass. These waveguides were used with two probes. One probe was immersed in liquid Helium, while the other was in vacuum, which itself was immersed in liquid Helium. A Lakeshore 340 was used to control any heaters and monitor the temperature, while an HP 8722Du vector network analyzer measured the S-parameters of the experiment. A dc solenoid was used for the applied dc H field experiment, and a magneto-optical experiment setup was also shown. A Windows-based PC controlled the entire experiment through Matlab. All analysis was performed with Matlab and Mathematica, and simulations were performed with Microwave Studio CST.

7.2.3 Chapter 4

The electromagnetic transmission, $|S_{21}|$, of empty waveguides of types X-band and Ka-band was measured. The Ka-band waveguide was made of Cu, while the X-band waveguides were made of either brass with the interior coated in Ag, or Nb. Data showed a cutoff frequency, ω_c, of approximately $2\pi \times 6.5$ GHz for the X-band waveguides, and $2\pi \times 21$ GHz for the K-band waveguide, in agreement with theory. A three-layer transfer matrix model was used to model the empty

Ag-plated brass X-band waveguide, using a constant complex permittivity, and with a plasmalike permittivity. Both results were in agreement with each other. The electromagnetic transmission of metallic wire arrays made of Cu and Nb was measured in the Ag-plated brass X-band waveguide and the Nb X-band waveguide. The electromagnetic transmission results of the Nb wire array in the Ag-plated brass X-band waveguide measurement were fit with the three-layer transfer matrix model for 7 K and room temperature, for lattice parameters of $a = 5.08$ mm, and $a = 7.19$ mm. Results showed an increase in losses above the T_c of the Nb wires for the $a = 7.19$ mm lattice parameter, however for the $a = 5.08$ mm lattice parameter the results were less clear since the plasma frequency was greater than at least two higher order modes of the X-band waveguide. Comparison of the fitted plasma frequency from the three-layer transfer matrix model to theories by the Pendry group, and Pokrovsky and Efros, showed that the predicted plasma frequencies were less than the observed frequencies. The explanation for this result was that the theories were derived for an infinite plane wave rather than inside a waveguide, and for infinite media. Adding the waveguide cutoff frequency in quadrature to the predicted values was in better agreement with the results from the three-layer transfer matrix model fits. The electromagnetic transmission of a Nb wire array in the Nb X-band waveguide showed the importance of having the wires parallel to the applied transverse electric field. A comparison of the electromagnetic transmission results of a Nb wire array to that of a Cu wire array showed that both types of metal give very similar $|S_{21}|$ spectra. Finally, the electromagnetic transmission results of a Nb wire array with various longitudinal lengths showed

a sloping edge for short arrays, and a sharper, step-function-like edge for longer arrays.

7.2.4 Chapter 5

The electromagnetic transmission, $|S_{21}|$, of arrays of split-ring resonators was measured and presented in this chapter. An array of Cu-Ni-Au split-ring resonators was shown to have a single dip in electromagnetic transmission at the resonant frequency of the split-ring resonators, while similar arrays of Nb split-ring resonators produced multiple dips in electromagnetic transmission, presumably due to the low-loss nature of the Nb films. The results were qualitatively modeled by an average permeability, summed over each split-ring resonator in the larger array. Smaller arrays were shown to have as many dips as Nb split-ring resonators in the array, and the electromagnetic transmission of a single Nb split-ring resonator was measured. The change in resonant frequency and quality factor with temperature, an applied dc H field, and applied power was measured, and modeled in the case of temperature changes. Magneto-optical imaging of a single Nb split-ring resonator revealed an imperfect film quality and locations where magnetic vortices can enter and leave the Nb film. Photoresponse imaging of a $YBa_2Cu_3O_{7-\delta}$ split-ring resonator showed current buildup in the inside corners of the split-rings. This lead to thermal runaway at large values of the applied power, destroying superconductivity in the split-ring resonators, and offers an explanation for the data presented in the applied power experiment. Finally, experimental data, and simulations, in-

vestigating perturbations of a single Nb split-ring resonator, and its bianisotropy, were presented.

7.2.5 Chapter 6

Arrays of split-ring resonators were placed inside Nb wire arrays of various lattice parameters, and the electromagnetic transmission spectra were measured. The 216-Nb split-ring resonator array showed a large frequency bandwidth of transmission as a result of a negative real part of the index of refraction, in the Nb wire array with a lattice parameter of $a = 5.08$ mm, while the same array in the Nb wire array with a lattice parameter of $a = 7.19$ mm showed a large reduction in the plasma edge of the wire array. As a result, the data showed a dip in electromagnetic transmission due to a negative real part of the permeability, rather than a peak in electromagnetic transmission due to a negative real part of the index of refraction. When a single Nb split-ring resonator was placed inside a Nb wire array with a lattice parameter of $a = 5.08$ mm, a single peak in electromagnetic transmission was observed, with a height above the noise floor depending on the length of the Nb wire medium. For the Nb wire array measuring eighteen rows longitudinally, the peak in electromagnetic transmission, if present, was below the noise floor, and a length of seven rows of Nb wires was chosen as ideal. When the single Nb split-ring resonator was placed into a Nb wire array with a lattice parameter of $a = 7.19$ mm, the single peak in electromagnetic transmission was on the cutoff edge of the Nb wire array, and the functional form produced by the three-layer transfer matrix model was

observed; that is, there was a sharp dip in electromagnetic transmission followed by a sharp peak in electromagnetic transmission, both due to the single Nb split-ring resonator. The bianisotropy of a single Nb split-ring resonator was measured and simulated.

The peak in electromagnetic transmission of the single Nb split-ring resonator inside a Nb wire array measuring five rows transversely and seven rows longitudinally, with a lattice parameter of $a = 5.08$ mm, was fit with a five-layer transfer matrix model, and the values compare well with the single Nb split-ring resonator inside an otherwise empty waveguide fit from Chapter 5. The parameter values corresponding to the Nb wire array agreed with the fits and theories of Chapter 2. The peak in electromagnetic transmission of the single Nb split-ring resonator was also tracked as a function of temperature, and the resonant frequency and quality factor shifts were measured and fit. The fit parameters for these two fits agree with that of the single Nb split-ring resonator inside an otherwise empty waveguide fit from Chapter 5. Finally, the electromagnetic transmission of a single Nb split-ring resonator inside an otherwise empty Ka-band waveguide-to-coaxial cable couplers was measured, and a low frequency mode resonance was observed, along with a higher frequency mode resonance. The lower resonance was attributed to the fundamental mode of the current density in the Nb split-ring resonator rings, while the higher resonance was attributed with the second harmonic mode of the current density. While the peak in electromagnetic transmission due to the fundamental mode of the current density disappeared above the critical temperature of the film of the single Nb split-ring resonator, the peak in electromagnetic transmission due to the second harmonic mode

of the current density remained above the critical temperature of the film of the single Nb split-ring resonator. This motivated inserting a single Nb closed-ring resonator into the Ka-band waveguide-to-coaxial cable couplers, where it was observed that there was a peak in electromagnetic transmission due to the second harmonic mode of the current density, while no peak in electromagnetic transmission existed at a lower frequency resonant mode.

7.2.6 Final summary

This dissertation presented data of a variety of experiments with arrays of metallic wires, split-ring resonators, and the combination of metallic wires and split-ring resonators. The metallic wire arrays were fit with a three-layer transfer matrix model, and with a plasmalike permittivity. The fitted plasma frequency was in agreement with two theories.

The Nb split-ring resonators were shown to be very sensitive to their environment, and as a result had non-degenerate resonant frequencies when arranged in an array. A single Nb split-ring resonator was shown to exhibit a single dip in electromagnetic transmission that was fit with a three-layer transfer matrix model with a resonant model of the permeability. Extracted fit parameters showed a frequency bandwidth where the real part of the permeability is negative. The single dip in electromagnetic transmission was tracked with changing temperature, and the resonant frequency and quality factor were fit with a two-fluid model of the temperature dependent resonant frequency and quality factor. The dip in electromagnetic trans-

mission was also shown to be a function of an applied dc H field, and the applied incident power. The single Nb split-ring resonator was shown to be very sensitive to its environment, and metallic wires and metallic walls perturbed the resonant frequency and insertion loss of the dip in electromagnetic transmission. Bianisotropic measurements of the single Nb split-ring resonator were taken, and agreed qualitatively with simulations.

The combination of metallic wires and Nb split-ring resonators exhibited a low-insertion loss, and wide peak in electromagnetic transmission, although there were many smaller peaks in electromagnetic transmission on top of the larger peak in electromagnetic transmission. A single Nb split-ring resonator in a reduced Nb wire array was shown to exhibit a single peak in electromagnetic transmission that was fit with a three-layer transfer matrix model with a resonant model of the permeability. Extracted fit parameters showed a frequency bandwidth where the real parts of the permittivity and permeability are negative. The single peak in electromagnetic transmission was tracked with changing temperature, and the resonant frequency and quality factor was fit with a two-fluid model of the resonant frequency and quality factor. Bianisotropic measurements of the single Nb split-ring resonator were taken.

7.3 Future work

This final section of this dissertation features what the author of this dissertation believes to be experiments that should be considered in continuing research

of the field.

7.3.1 dc magnetic cloak

In Reference [125], B. Wood and J. B. Pendry describe how to extend the electromagnetic cloak of Reference [75] to dc signals using superconducting artificial materials. They require [125] "anisotropic magnetic permeability with both paramagnetic and diamagnetic components[,]" and achieve this by using ferrites and superconducting plates. The plates should be very easy to construct, as they are very similar to the Nb split-ring resonators discussed in this dissertation, except that the entire loop would be filled in with Nb metal.

7.3.2 Degenerate resonant frequencies of the Nb split-ring resonators

One issue with the current experiment is that the Nb split-ring resonators are very sensitive to their environment. This appears to cause a large spread in the resonant frequencies of the Nb split-ring resonators. This was observed in Figure (5.3), for instance, and was the reason for switching to a single Nb split-ring resonator for the experiments. The problem with a single Nb split-ring resonator is that it is ambiguous as to if a true medium is obtained. In other words, what is considered to be the lattice parameter? The observations seemed to imply that there was most likely a region of frequency of negative permeability, much like a bulk medium. Comparing Figure (6.1) to Figure (6.8), it appeared that even without a degenerate resonant frequency, the Nb split-ring resonator array had an insertion loss less than

the single Nb split-ring resonator data.

7.3.3 Negative refraction

One experiment to perform once the resonant frequency degeneracy problem has been solved is a real negative refraction experiment. While these have been done with split-ring resonators and wires made of normal metals, as described in Chapter 1, this experiment has not been done yet with split-ring resonators and wires made of superconducting metals. This would need to be performed on a cold plate, although a proof-of-principle experiment could be done immersed in liquid Helium. A benefit to using superconducting metals for the split-ring resonators and wires is that they are tunable with a variety of methods, especially temperature. Thus, the angle of refraction for one frequency could be changed with temperature, and this could happen for positive and negative refraction. In fact, one can imagine a situation where at some temperature, T, there is a positive angle of refraction, and upon decreasing, or increasing the temperature, by some small amount to $T + \delta T$, the angle changes to a negative angle of refraction. Such a scheme has already been proposed for photonic crystals [126].

7.3.4 Plasmon model

It is the opinion of the author of this dissertation that the plasmon model that the Pendry group presents for the metallic wire array has not been settled. The objections to the Pendry group's work have never been that a wire array has

a permittivity like that of a plasma, but rather whether or not there is a true plasmon resonance, or if the wire response is due to currents flowing through very thin wires, giving rise to a large inductance. This should be experimentally provable by more than just measuring a plasma frequency. Superconducting wires are the best materials for any tests. For instance, the Walser group's objection with the plasmon model was the very short collision time, τ in a normal metal, such as copper [53]. However, for a pure superfluid, $\tau \rightarrow \infty$. In addition to this, the Pendry group suggests the interaction of a "Higgs boson" in the array of superconducting thin wires, however this subject was not dealt with in depth [34]. A review paper, Reference [127], by van der Marel discusses the role of the boson mechanism in superconductivity.

7.3.5 High-T_c superconductors

While the experiment involving a single Nb split-ring resonator in an otherwise empty Nb X-band waveguide showed a dip in electromagnetic transmission, the experiment involving a single split-ring resonator made of $YBa_2Cu_3O_{7-\delta}$ in an otherwise empty Nb X-band waveguide did not show a dip in electromagnetic transmission. The likely reason for this, as shown on computer simulations, is the high dielectric constant of the substrate. High-T_c split-ring resonators and wires would be very worthy to pursue since any application of superconducting metamaterials will be with high-T_c metamaterials before lower critical temperature metamaterials. While high-T_c left-handed transmission lines have been fabricated and

tested [128, 129], as of 17 April 2007, the author of this dissertation is unaware of any published work concerning split-ring resonators or a combination of wires and split-ring resonators, made of a high-T_c material. These may show interesting properties, as the high-T_c superconductors, for instance the cuprates, are not isotropic, and therefore may have different couplings to the electromagnetic fields depending on how the films were fabricated.

7.3.6 The extraction method

While some groups have used an extraction model that extracts the permeability and permittivity from the S-parameters with claimed success, see for instance Reference [75], a successful extraction model has not been created for the Anlage group, as of 17 April 2007. First, while the method has successfully extracted the correct parameters for "data" generated by the three-layer transfer matrix model, the method has not extracted the correct parameters for a simulation of the real experimental setup on Microwave Studio CST. The reason appears to be in the difference between the S-parameters that Microwave Studio CST produces, and the S-parameters that the three-layer transfer matrix model produces. Thus, it is necessary to determine how Microwave Studio CST calculates the S-parameters, however this is most likely proprietary. In order to estimate the permeability and permittivity from real data, the planes of calibration should be right on the boundary between the media and vacuum, where vacuum is understood to mean the empty regions of the waveguide.

7.3.7 Do the real parts of the permeability and permittivity need to be simultaneously negative for a negative index of refraction?

One recent calculation showed that while the dip in electromagnetic transmission in Figure (5.2) may or may not be due to a frequency bandwidth where the real part of the permeability is less than zero, the absence of a peak in electromagnetic transmission above the critical temperature of the Nb film in Figure (6.1) may not necessarily mean the absence of a negative index of refraction. In fact, the peaks in electromagnetic transmission in Figure (6.8) might not all be due to a frequency bandwidth of simultaneously negative real parts of the permittivity and permeability.

Figure (7.1) shows a plot of the index of refraction for $\Re[\epsilon] < 0$ and $\Re[\mu] < 0$. The blue curve is the real part of the index of refraction and the green curve is the imaginary part of the index of refraction. The inset shows a plot of the relative permeability used in the main figure. The black curve is the real part of the relative permeability and the red curve is the imaginary part of the relative permeability. The parameters in Equation (2.97) used were $f = 0.1$, $\omega_0 = 2\pi \times 10$ GHz, and $\Gamma = 2\pi \times 0.1$ GHz. The relative permittivity is from Equation (2.22) with parameters $\omega_p = 2\pi \times 18$ GHz, and $\gamma = 2\pi \times 0.1$ GHz. The index of refraction was calculated using two equations, Equation (2.14) and Equation (2.18), where the k_z in Equation (2.18) was obtained from Equation (2.56) and from Equation (2.106). The requirement on the index of refraction was that if the imaginary part of the index of refraction was negative, then a factor of π was added to the argument.

In all cases, the same plot was produced. Note how the real part of the index of refraction is negative between approximately 10 GHz, and approximately 10.5 GHz, which corresponds to the frequency bandwidth where the real part of the relative permeability is negative.

Now consider Figure (7.2), where a similar plot to Figure (7.1) is shown, however the real part to the permeability in Figure (7.2) is never less than zero, shown as the black curve in the inset. However, there is clearly a frequency bandwidth where the real part of the index of refraction is less than zero. It is conjectured that combining a lossy medium of split-ring resonators with a low-loss medium of metallic wires can push the square of the index of refraction over the branch cut in the complex plane, and as a result, the $j = 1$ solution to Equation (2.69) must be taken in order to have the imaginary part of the index of refraction greater than zero. While the author of this dissertation believes that all the peaks in electromagnetic transmission in Figure (6.8) were due to a negative real part of the index of refraction, there may actually be a small peak due to a negative real part of the index of refraction in Figure (6.1) at temperatures above the critical temperature of the Nb film. This peak may be below the noise floor of the vector network analyzer, however, and so more precise measurements should be taken in order to determine if a peak in electromagnetic transmission does exist.

Note that this also makes less clear the extraction code discussed in this dissertation. Since a negative real part of the index of refraction can be obtained for a negative real part of the permittivity and a positive real part of a lossy permeability, the extraction code may produce a permeability with a negative real part,

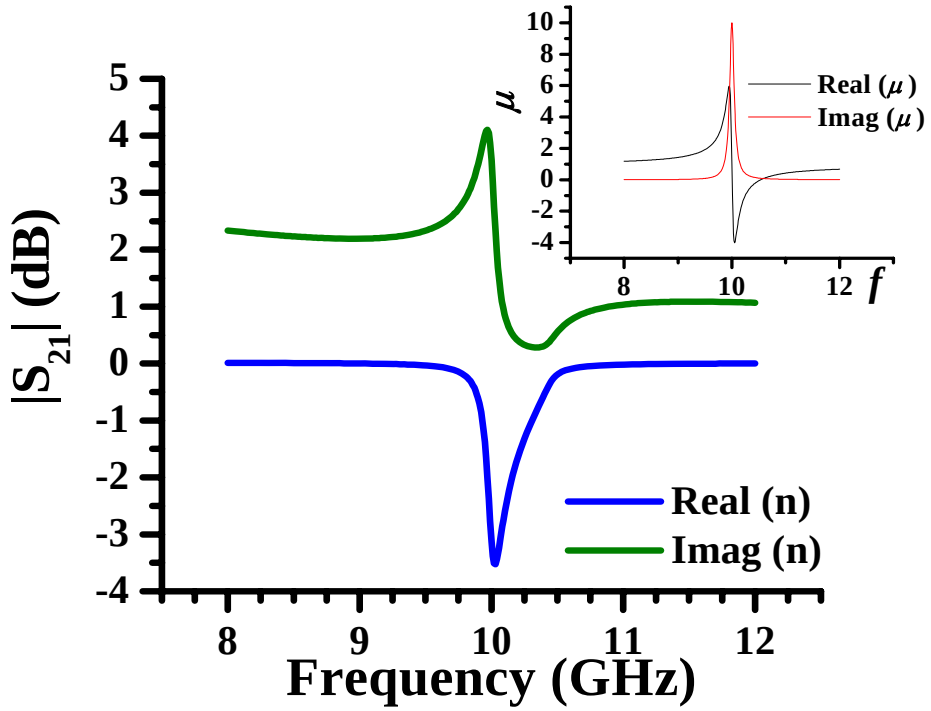

Figure 7.1: A plot of the index of refraction for $\Re[\epsilon] < 0$ and $\Re[\mu] < 0$. The blue curve is the real part of the index of refraction and the green curve is the imaginary part of the index of refraction. *Inset*: A plot of the relative permeability used in the main figure. The black curve is the real part of the relative permeability and the red curve is the imaginary part of the relative permeability. The parameters in Equation (2.97) used were $f = 0.1$, $\omega_0 = 2\pi \times 10$ GHz, and $\Gamma = 2\pi \times 0.1$ GHz. The relative permittivity is from Equation (2.22) with parameters $\omega_p = 2\pi \times 18$ GHz, and $\gamma = 2\pi \times 0.1$ GHz.

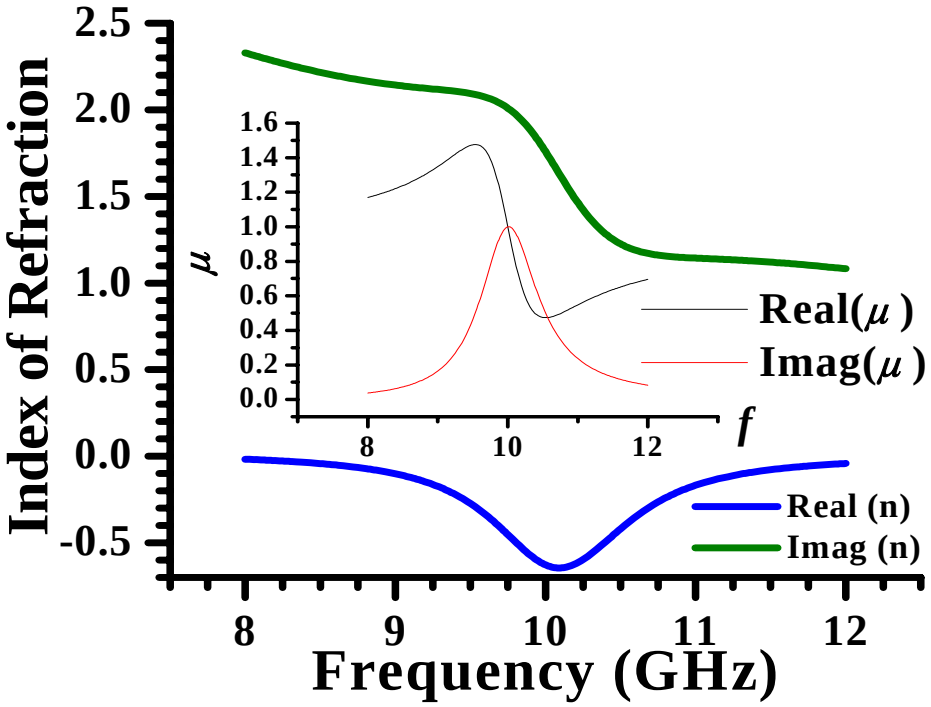

Figure 7.2: A plot of the index of refraction for $\Re[\epsilon] < 0$ and $\Re[\mu] > 0$. The blue curve is the real part of the index of refraction and the green curve is the imaginary part of the index of refraction. *Inset*: A plot of the relative permeability used in the main figure. The black curve is the real part of the relative permeability and the red curve is the imaginary part of the relative permeability. The parameters in Equation (2.97) used were $f = 0.1$, $\omega_0 = 2\pi \times 10$ GHz, and $\Gamma = 2\pi \times 1$ GHz. The relative permittivity is from Equation (2.22) with parameters $\omega_p = 2\pi \times 18$ GHz, and $\gamma = 2\pi \times 0.1$ GHz.

when a positive real part was actually used. Figure (7.3) shows the result of starting with a given permittivity, given by Equation (2.22) with $\omega_p = 2\pi \times 18$ GHz, and $\gamma = 2\pi \times 0.1$ GHz, and a given permeability, given by Equation (2.97) with $f = 0.1$, $\omega_0 = 2\pi \times 10$ GHz, and $\Gamma = 2\pi \times 0.1$ GHz, and calculating the S-parameters, Equations (2.101) and (2.102). The permittivity are then extracted using the description in Chapter 2. The blue curve is the real part of the generating permeability and the green curve is the imaginary part of the generating permeability. The maroon curve is the real part of the extracted permeability, labeled EX, and the red curve is the imaginary part of the extracted permeability, labeled EX. Note how the extraction code is able to reproduce the permeability, and although not all the data points are shown, the extracted values are in very good agreement over the entire frequency range.

Figure (7.4) shows a similar plot as Figure (7.3), however $\Gamma = 2\pi \times 1$ GHz in Equation (2.97). The blue curve is the real part of the generating permeability and the green curve is the imaginary part of the generating permeability. The black curve is the real part of the extracted permeability, labeled EX, and the red curve is the imaginary part of the extracted permeability, labeled EX. Note how, at the resonance, the generating real part of the permeability in Figure (7.4) is never less than zero, however the extracted value is very similar to the previous Figure (7.3). Thus, the cases where the real part of the index of refraction is negative, but not due to simultaneously negative real parts of the permittivity and permeability, may require extra care in extracting the permittivity and the permeability from S-parameter data. This requires special care for experimental data. As a final note, similar re-

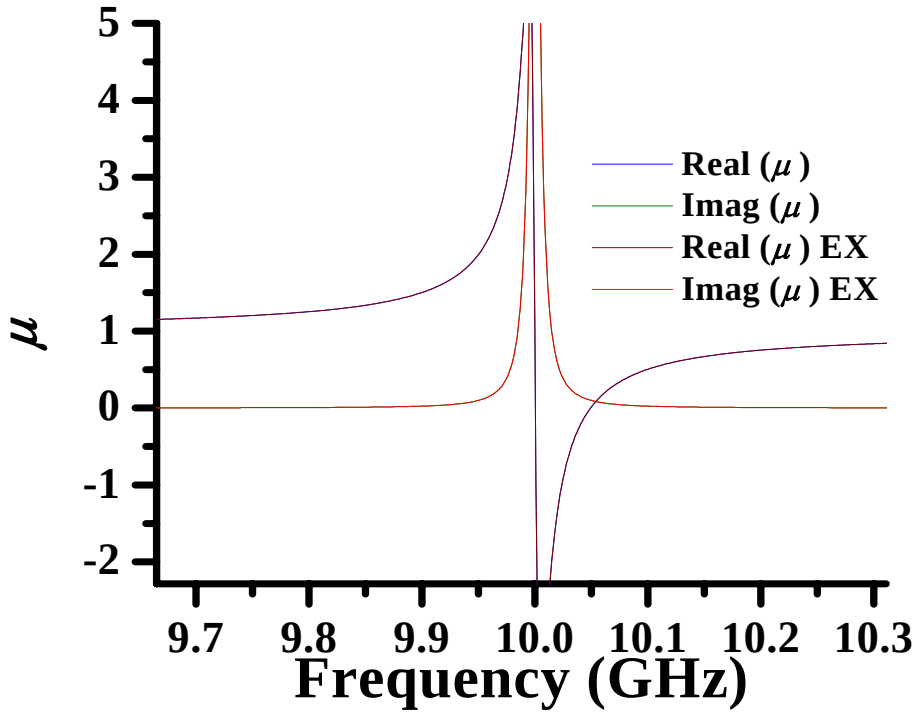

Figure 7.3: A plot of the extracted permeability for $\Re[\mu] < 0$. The blue curve is the real part of the generating permeability and the green curve is the imaginary part of the generating permeability. The maroon curve is the real part of the extracted permeability, labeled EX, and the red curve is the imaginary part of the extracted permeability, labeled EX. The parameters in Equation (2.97) for the generating permeability were $f = 0.1$, $\omega_0 = 2\pi \times 10$ GHz, and $\Gamma = 2\pi \times 0.1$ GHz.

sults are produced if the permittivity and permeability are reversed, that is, a very low loss permeability is used with a higher loss permittivity.

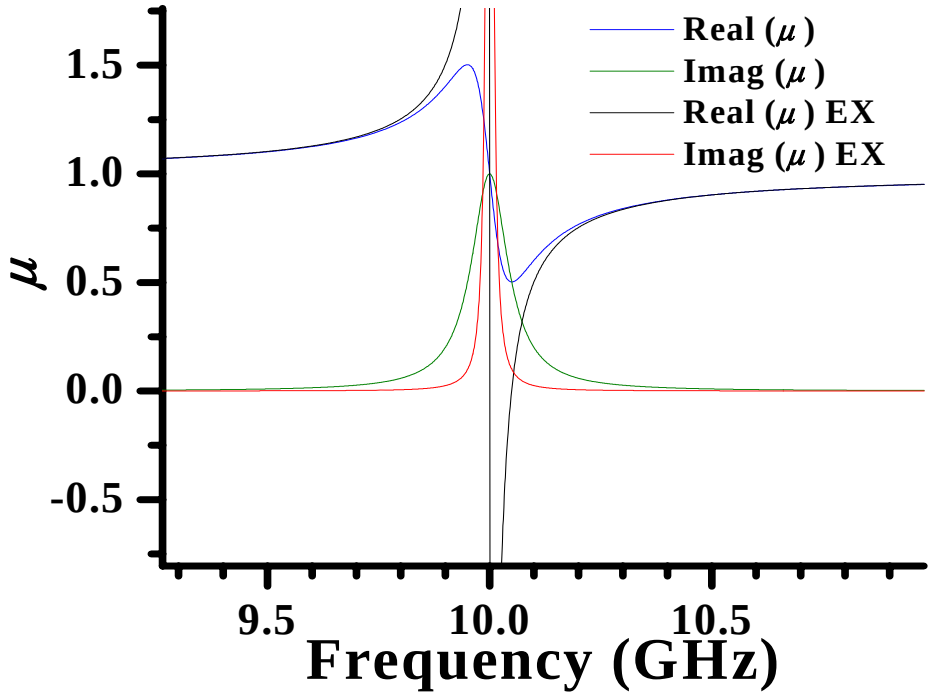

Figure 7.4: A plot of the extracted permeability for $\Re[\mu] > 0$. The blue curve is the real part of the generating permeability and the green curve is the imaginary part of the generating permeability. The black curve is the real part of the extracted permeability, labeled EX, and the red curve is the imaginary part of the extracted permeability, labeled EX. The parameters in Equation (2.97) for the generating permeability were $f = 0.1$, $\omega_0 = 2\pi \times 10$ GHz, and $\Gamma = 2\pi \times 1$ GHz.

Chapter A

Appendix

A.1 Overview

This Appendix details calculations in the main text that were not otherwise detailed.

A.2 Vector Identities

Below are useful vector identities used in this dissertation. For any vector $\mathbf{A}$ [130, p. 52, Eq. (1.86)],

$$\nabla \times \nabla \times \mathbf{A} = \nabla(\nabla \cdot \mathbf{A}) - \nabla^2 \mathbf{A}. \tag{A.1}$$

The last term in Equation (A.1) is the vector Laplacian. In cylindrical coordinates, the term along the ϕ-direction of the vector Laplacian is [130, p. 116, Eq. (2.35)],

$$\begin{aligned} \nabla^2 \mathbf{A}|_\phi &= \frac{1}{r}\frac{\partial}{\partial r}\left(r\frac{\partial A_\phi}{\partial r}\right) + \frac{1}{r^2}\frac{\partial^2 A_\phi}{\partial \phi^2} + \frac{\partial^2 A_\phi}{\partial z^2} && \text{(A.2)} \\ &- \frac{A_\phi}{r^2} + \frac{2}{r^2}\frac{\partial A_r}{\partial \phi}. && \text{(A.3)} \end{aligned}$$

The divergence in cylindrical coordinates is given by [130, p. 116, Eq. (2.32)],

$$\nabla \cdot \mathbf{A} = \frac{1}{r}\frac{\partial}{\partial r}(rA_r) + \frac{1}{r}\frac{\partial A_\phi}{\partial \phi} + \frac{\partial A_z}{\partial z}. \tag{A.4}$$

A.3 Derivation of the wave structure inside a metallic waveguide

Starting with Maxwell's Equations (2.1)–(2.4), the curl of $\mathbf{E}$ is given by,

$$\nabla \times \mathbf{E} = \begin{vmatrix} \hat{\mathbf{x}} & \hat{\mathbf{y}} & \hat{\mathbf{z}} \\ \frac{\partial}{\partial x} & \frac{\partial}{\partial y} & \frac{\partial}{\partial z} \\ E_x & E_y & E_z \end{vmatrix} \tag{A.5}$$

$$= \left(\frac{\partial E_z}{\partial y} - \frac{\partial E_y}{\partial z}\right)\hat{\mathbf{x}} - \left(\frac{\partial E_z}{\partial x} - \frac{\partial E_x}{\partial z}\right)\hat{\mathbf{y}} + \left(\frac{\partial E_y}{\partial x} - \frac{\partial E_x}{\partial y}\right)\hat{\mathbf{z}} \tag{A.6}$$

$$= -\frac{\partial \mathbf{B}}{\partial t} = -(-i\omega)\mathbf{B} \tag{A.7}$$

$$= i\omega B_x\hat{\mathbf{x}} + i\omega B_y\hat{\mathbf{y}} + i\omega B_z\hat{\mathbf{z}}, \tag{A.8}$$

where $\partial/\partial t \rightarrow -i\omega$ was used in Equation (A.7). Equations (A.6) and (A.8) lead to three equations, obtained after dotting with $\hat{\mathbf{x}}$, $\hat{\mathbf{y}}$, and $\hat{\mathbf{z}}$ [54, p. 406, Eq. (9.179)],

$$\frac{\partial E_z}{\partial y} - ikE_y = i\omega B_x, \tag{A.9}$$

$$-\frac{\partial E_z}{\partial x} + ikE_x = i\omega B_y, \tag{A.10}$$

$$\frac{\partial E_y}{\partial x} - \frac{\partial E_x}{\partial y} = i\omega B_z. \tag{A.11}$$

Equation (2.4) becomes,

$$\nabla \times \mathbf{B} = \begin{vmatrix} \hat{\mathbf{x}} & \hat{\mathbf{y}} & \hat{\mathbf{z}} \\ \frac{\partial}{\partial x} & \frac{\partial}{\partial y} & \frac{\partial}{\partial z} \\ B_x & B_y & B_z \end{vmatrix} \tag{A.12}$$

$$= \left(\frac{\partial B_z}{\partial y} - \frac{\partial B_y}{\partial z}\right)\hat{\mathbf{x}} - \left(\frac{\partial B_z}{\partial x} - \frac{\partial B_x}{\partial z}\right)\hat{\mathbf{y}} + \left(\frac{\partial B_y}{\partial x} - \frac{\partial B_x}{\partial y}\right)\hat{\mathbf{x}} \tag{A.13}$$

$$= \frac{1}{c^2}\frac{\partial \mathbf{E}}{\partial t} = -i\frac{1}{c^2}\omega\mathbf{E} \tag{A.14}$$

$$= -i\tilde{\epsilon}\tilde{\mu}\omega E_x\hat{\mathbf{x}} - i\tilde{\epsilon}\tilde{\mu}\omega E_y\hat{\mathbf{y}} - i\tilde{\epsilon}\tilde{\mu}\omega E_z\hat{\mathbf{z}}. \tag{A.15}$$

Equations (A.12)–(A.15) lead to the following equations [54, p. 406, Eq. (9.179)],

$$\frac{\partial B_z}{\partial y} - ikB_y = -i\frac{\mu\epsilon\omega}{c}E_x, \tag{A.16}$$

$$-\frac{\partial B_z}{\partial x} + ikB_x = -i\frac{\mu\epsilon\omega}{c}E_y, \tag{A.17}$$

$$\frac{\partial B_y}{\partial x} - \frac{\partial B_x}{\partial y} = -i\frac{\mu\epsilon\omega}{c}E_z, \tag{A.18}$$

where $c = 1/\sqrt{\epsilon_0\mu_0}$ is the speed of light in vacuum.

While assuming that the waveguide longitudinal axis is aligned with the z-axis, and the transverse plane of the waveguide is the $x-y$ plane, as in Figure (2.3), then Equations (A.9)–(A.11), and Equations (A.16)–(A.18) can be solved for the transverse components in terms of the longitudinal components. Multiplying Equa-

tion (A.17) by $i\omega$ and then plugging Equation (A.9) into Equation (A.17) gives [54, p. 407, Eq. (9.180)],

$$ik\left(\frac{\partial E_z}{\partial y} - ikE_y\right) - i\omega\frac{\partial B_z}{\partial x} = \epsilon\mu\frac{-(i\omega)^2}{c^2}E_y = \epsilon\mu\left(\frac{\omega}{c}\right)^2 E_y \tag{A.19}$$

$$i\left(k\frac{\partial E_z}{\partial y} - \omega\frac{\partial B_z}{\partial x}\right) = \left[\epsilon\mu\left(\frac{\omega}{c}\right)^2 - k^2\right]E_y \tag{A.20}$$

$$E_y = \frac{i}{\epsilon\mu\left(\frac{\omega}{c}\right)^2 - k^2}\left(k\frac{\partial E_z}{\partial y} - \omega\frac{\partial B_z}{\partial x}\right). \tag{A.21}$$

Similarly, plugging Equation (A.10) into Equation (A.16) after multiplying Equation (A.16) by $i\omega$ yields [54, p. 407, Eq. (9.180)],

$$-ik\left(-\frac{\partial E_z}{\partial x} + ikE_x\right) + i\omega\frac{\partial B_z}{\partial y} = \epsilon\mu\frac{-(i\omega)^2}{c^2}E_x = \epsilon\mu\left(\frac{\omega}{c}\right)^2 E_x \tag{A.22}$$

$$E_y = \frac{i}{\epsilon\mu\left(\frac{\omega}{c}\right)^2 - k^2}\left(k\frac{\partial E_z}{\partial x} + \omega\frac{\partial B_z}{\partial x}\right). \tag{A.23}$$

To obtain the transverse magnetic field components, plug Equation (A.10) into Equation (A.16) after multiplying Equation (A.16) by ik, and plug Equation (A.9) into Equation (A.17) after multiplying Equation (A.17) by ik. These processes yield, respectively [54, p. 407, Eq. (9.180)],

$$B_y = \frac{i}{\epsilon\mu\left(\frac{\omega}{c}\right)^2 - k^2}\left(k\frac{\partial B_z}{\partial y} + \epsilon\mu\frac{\omega}{c^2}\frac{\partial E_z}{\partial x}\right), \tag{A.24}$$

$$B_x = \frac{i}{\epsilon\mu\left(\frac{\omega}{c}\right)^2 - k^2}\left(k\frac{\partial B_z}{\partial x} - \epsilon\mu\frac{\omega}{c^2}\frac{\partial E_z}{\partial y}\right). \tag{A.25}$$

The two remaining Maxwell equations are Equations (2.1) and (2.3). Plugging

Equations (A.24) and (A.25) into Equation (2.3) [54, p. 407, Eq. (9.181)],

$$\begin{aligned}
\nabla \cdot \mathbf{B} &= \frac{i}{\epsilon\mu\left(\frac{\omega}{c}\right)^2 - k^2}\left(k\frac{\partial^2 B_z}{\partial x^2} - \epsilon\mu\frac{\omega}{c^2}\frac{\partial^2 E_z}{\partial x \partial y}\right) && \text{(A.26)}\\
&+ \frac{i}{\epsilon\mu\left(\frac{\omega}{c}\right)^2 - k^2}\left(k\frac{\partial^2 B_z}{\partial y^2} + \epsilon\mu\frac{\omega}{c^2}\frac{\partial^2 E_z}{\partial y \partial x}\right) + ik\frac{\partial B_z}{\partial z} && \text{(A.27)}\\
&= \frac{i}{\epsilon\mu\left(\frac{\omega}{c}\right)^2 - k^2}k\left(\frac{\partial^2 B_z}{\partial x^2} + \frac{\partial^2 B_z}{\partial y^2}\right) + ikB_z && \text{(A.28)}\\
&= \left[\frac{\partial^2}{\partial x^2} + \frac{\partial^2}{\partial y^2} + \epsilon\mu\left(\frac{\omega}{c}\right)^2 - k^2\right]B_z = 0. && \text{(A.29)}
\end{aligned}$$

Similarly, for E_z, plug Equations (A.21) and (A.23) into Equation (2.1) [54, p. 407, Eq. (9.181)],

$$\nabla \cdot \mathbf{E} = \left[\frac{\partial^2}{\partial x^2} + \frac{\partial^2}{\partial y^2} + \epsilon\mu\left(\frac{\omega}{c}\right)^2 - k^2\right]E_z = 0. \qquad \text{(A.30)}$$

The solutions to Equations (A.29) and (A.30), with the appropriate boundary conditions given by Equations (2.40)–(2.43), give the wave structure inside of a waveguide. For $B_z = 0$, the waves are called transverse magnetic, or TM, and for $E_z = 0$, the waves are called transverse electric, or TE [1, p. 358]. If E_z and B_z are both zero, the waves are transverse electromagnetic waves, or TEM waves [1, p. 359]; however in the case of a hollow rectangular waveguide, these cannot exist. If such a wave were to exist inside a hollow rectangular waveguide, then Equations (2.1) and (2.2) would yield, respectively [54, p. 407],

$$\begin{aligned}
\frac{\partial E_x}{\partial x} &= -\frac{\partial E_y}{\partial y}, && \text{(A.31)}\\
\frac{\partial E_x}{\partial x} &= \frac{\partial E_y}{\partial y}. && \text{(A.32)}
\end{aligned}$$

The only solution to Equations (A.31) and (A.32) is a constant electric field, and using the boundary condition of Equation (2.40), this means that this constant is zero.

However, if a conducting rod was to be inserted down the center of the waveguide, and the rod was allowed to hold a voltage, then a transverse electromagnetic wave would be supported. This is, in fact, the principle of a coaxial cable [1, p. 411].

For the waveguide used in this dissertation, the transverse electric mode was excited. Solving Equation (A.29) requires the separation of variables. Letting $B_z(x,y) = X(x)Y(y)$, and defining $X'' \stackrel{def}{=} d^2X/dx^2$ and $Y'' \stackrel{def}{=} d^2Y/dy^2$, Equation (A.29) reduces to [54, p. 408],

$$0 = YX'' + XY'' + \left[\left(\frac{\omega}{c}\right)^2 - k^2\right] XY \tag{A.33}$$

$$= \frac{X''}{X} + \frac{Y''}{Y} + \left[\left(\frac{\omega}{c}\right)^2 - k^2\right]. \tag{A.34}$$

Since X and Y are independent of each other, then [54, p. 408, Eq. (9.182)],

$$\frac{X''}{X} = -k_x^2, \tag{A.35}$$

$$\frac{Y''}{Y} = -k_y^2. \tag{A.36}$$

This gives exactly Equation (2.46) [54, p. 408, Eq. (9.183)],

$$k^2 = \epsilon\mu\left(\frac{\omega}{c}\right)^2 - k_x^2 - k_y^2. \tag{A.37}$$

In order to determine k_x and k_y, Equations (A.35) and (A.36) are solved with boundary conditions. From Equation (2.41), components of the magnetic field that are orthogonal to the waveguide walls must vanish [54, p. 405, Eq. (9.175)], and therefore Equations (A.24) and (A.25) must also vanish at the waveguide walls. Since $E_z = 0$ by assumption, this places a condition on the spatial derivatives of B_z.

For instance [54, p. 409],

$$\frac{X''}{X} = -k_x^2 \tag{A.38}$$

$$X'' = -k_x^2 X \tag{A.39}$$

$$X(x) = A_1 \sin(k_x x) + A_2 \cos(k_x x). \tag{A.40}$$

From Equation (2.41), normal components of the magnetic field vanish at the waveguide walls. This means that Equation (A.25) vanishes at the waveguide walls. Since this was written in terms of B_z and E_z, and $E_z = 0$, the boundary condition is,

$$\left.\frac{dB_z}{dx}\right|_{0,a} = 0. \tag{A.41}$$

Applying this to Equation (A.40) [54, p. 409, Eq. (9.184)],

$$\frac{d}{dx}X(x) = -k_x A_1 \cos(k_x x) + k_x A_1 \sin(k_x x) \tag{A.42}$$

$$X'(0) = -k_x A_1 \cos(0) + k_x A_1 \sin(0) = -k_x A_1 = 0 \tag{A.43}$$

$$\rightarrow A_1 = 0 \tag{A.44}$$

$$X'(a) = k_x A_2 \sin(k_x a) = 0 \tag{A.45}$$

$$\rightarrow k_x a = n\pi, \quad n \in \mathbb{Z} \tag{A.46}$$

$$\rightarrow k_x = \frac{n\pi}{a}, \quad n \in \mathbb{Z}, \tag{A.47}$$

$$\tag{A.48}$$

where n is an integer, and a is the width of the waveguide shown in Figure (2.3). Note that $A_2 = 0$ was a possible solution to Equation (A.45). However, this implies that there is no wave at all inside the waveguide. A similar process for $Y(y)$ yields [54,

p. 409, Eq. (9.185)],

$$Y(y) = A_4 \cos(k_y y) \tag{A.49}$$

$$k_y = \frac{m\pi}{b}, \quad m \in \mathbb{Z}, \tag{A.50}$$

where A_4 is a constant, and b is the height of the waveguide, shown in Figure (2.3). Equations (A.40) and (A.49) yield for the longitudinal magnetic field, ignoring the time and z-dependencies,

$$B_z(x, y) = B_0 \cos\left(\frac{n\pi}{a}x\right) \cos\left(\frac{n\pi}{b}y\right), \tag{A.51}$$

where $B_0 = B_z(0, 0) = A_2 A_4$.

For the TE_{10} mode, discussed in Chapter 2.2.4, and implying a multiplicative factor of $\exp(i\mathbf{k} \cdot \mathbf{x} - i\omega t)$,

$$B_z(x, y) = B_0 \cos\left(\frac{\pi x}{a}\right). \tag{A.52}$$

Plugging this in Equation (A.25) [1, p. 362, Eq. (8.46)],

$$B_x = \frac{ik}{\epsilon\mu\omega^2/c^2 - k^2} \frac{\partial}{\partial x} B_z \tag{A.53}$$

$$= \frac{-ik\pi}{a(\epsilon\mu\omega^2/c^2 - k^2)} B_0 \sin\left(\frac{\pi x}{a}\right) \tag{A.54}$$

$$= \frac{-ika}{\pi} B_0 \sin\left(\frac{\pi x}{a}\right), \tag{A.55}$$

where the following were used, and hold for the TE_{10} mode,

$$k_{10}^2 = \epsilon\mu(\omega^2 - \omega_{10}^2)/c^2, \tag{A.56}$$

$$\epsilon\mu\omega_{10}^2 = c^2\frac{\pi^2}{a^2}, \tag{A.57}$$

$$\frac{-ik\pi}{a(\epsilon\mu\omega^2/c^2 - k_{10}^2)} = \frac{-ik\pi}{a\epsilon\mu[\omega^2/c^2 - (\omega^2 - \omega_{10}^2)/c^2]} \tag{A.58}$$

$$= \frac{-ik\pi}{a\epsilon\mu\omega_{10}^2/c^2} \tag{A.59}$$

$$= \frac{-ik\pi}{a[(c^2)(\pi/a)^2/c^2]} \tag{A.60}$$

$$= \frac{-ika}{\pi}. \tag{A.61}$$

The y-component of the magnetic field for the TE_{10} mode vanishes [1, p. 362, Eq. (8.46)],

$$B_y = \frac{ik}{\mu\epsilon\omega^2/c^2 - k^2}\frac{\partial}{\partial y}B_z = 0, \tag{A.62}$$

since $B_z = B_z(x)$ for the TE_{10} mode.

The electric fields for the TE_{10} mode are found in a similar manner. First, $E_z = 0$ by assumption. Next [1, p. 362, Eq. (8.46)],

$$E_x = \frac{-i\omega}{\mu\epsilon\omega^2/c^2 - k^2}\hat{\mathbf{z}} \times \left(\frac{\partial}{\partial y}B_z\right) = 0. \tag{A.63}$$

However, there is a y-component to the electric field [1, p. 362, Eq. (8.46)],

$$E_y = \frac{-i\omega}{\mu\epsilon\omega^2/c^2 - k^2}\hat{\mathbf{z}} \times \left(\frac{\partial}{\partial x}B_z\right) \tag{A.64}$$

$$= \frac{i\omega\pi}{a(\mu\epsilon\omega^2/c^2 - k^2)}B_0 \sin\left(\frac{\pi x}{a}\right) \tag{A.65}$$

$$= \frac{i\omega a}{\pi}B_0 \sin\left(\frac{\pi x}{a}\right). \tag{A.66}$$

To summarize, the field equations for the TE_{10} mode are, with all spatial and time dependencies [1, p. 362, Eq. (8.46)],

$$B_z(x) = B_0 \cos\left(\frac{\pi x}{a}\right) e^{i(k_z z - \omega t)}, \tag{A.67}$$

$$B_x(x) = \frac{-ika}{\pi}B_0 \sin\left(\frac{\pi x}{a}\right) e^{i(k_z z - \omega t)}, \tag{A.68}$$

$$E_y(x) = \frac{i\omega a}{\pi}B_0 \sin\left(\frac{\pi x}{a}\right) e^{i(k_z z - \omega t)}. \tag{A.69}$$

The normalized magnitudes of Equations (A.67)–(A.69) are plotted for an arbitrary time and z-position, at $\omega = 2\pi \times 10$ GHz, and assuming a waveguide with X-band dimensions with vacuum inside the waveguide. The blue, red, and green curves are, respectively, $|B_z|_0^2$, $|B_x|_0^2$, and $|E_y|_0^2$. Note that $|E_y|_0^2$ and $|B_x|_0^2$ are maximum in the center, and zero along the sides of the waveguide, while $|B_z|_0^2$ is maximum along the sides and zero in the center of the waveguide. This field structure was exploited in the bianisotropy measurements and simulations presented in Chapter 5.

A.4 Superconducting current density

The superconducting current density is found by assuming quasistationary fields, and solving [93, p. 32, Eq. (3″)],

$$\nabla^2 \mathbf{J} = \frac{1}{\lambda^2}\mathbf{J}, \tag{A.70}$$

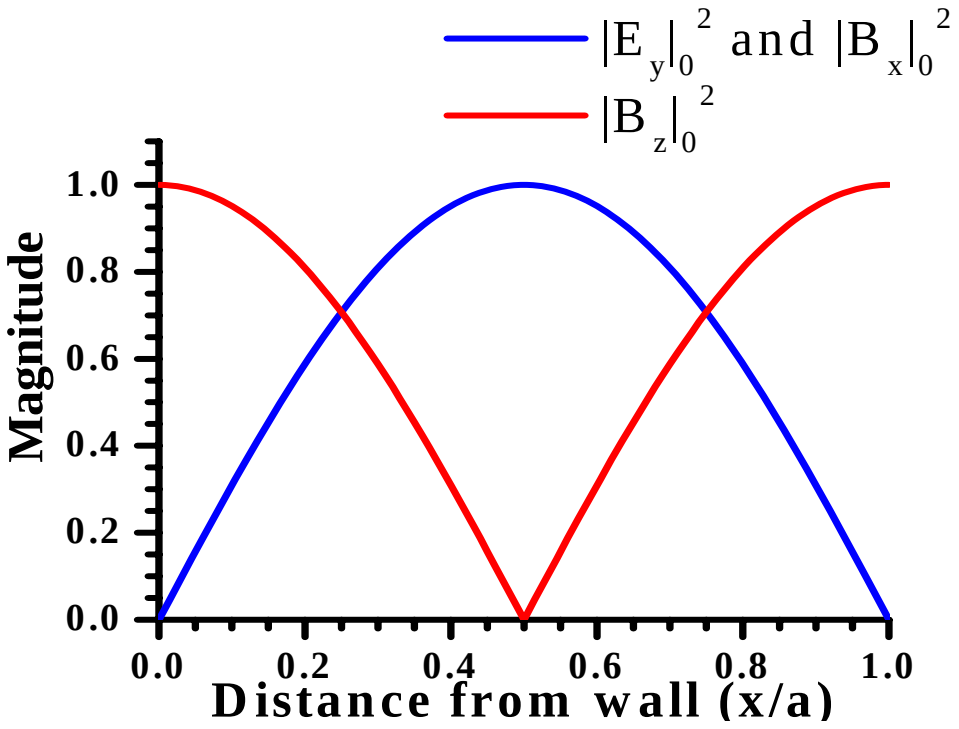

Figure A.1: A plot of the field structure of the TE_{10} mode of a waveguide in the transverse plane. Each field is normalized to its maximum value. The blue curve shows $|E_y|_0^2$ and $|B_x|_0^2$, and the red curve shows $|B_z|_0^2$.

where **J** is used here, rather than **j** in Chapter 2, in order to be similar to references.

A.4.1 J_ϕ constant along r

For the first problem, the simplification that $\mathbf{J} = J_\phi(z)\hat{\phi}$ is made. Using Equation (for j),

$$\frac{\partial^2 J_\phi}{\partial z^2} = \frac{1}{\lambda^2} J_\phi, \tag{A.71}$$

$$J_\phi = A_1 \cosh\left(\frac{z}{\lambda}\right) + A_2 \sinh\left(\frac{z}{\lambda}\right), \tag{A.72}$$

where A_1 and A_2 are determined from the boundary conditions, and other physical properties of the ring. The first boundary condition used comes from Reference [97], Equation (2), and is the condition that J_ϕ is even in z, $J_\phi(z) = J_\phi(-z)$. This implies that $A_2 = 0$. To solve for A_1, the definition of the current, I, is used,

$$I = \int \mathbf{J} \cdot d\mathbf{A}, \tag{A.73}$$

$$= \int_{r_i}^{r_o} dr \int_{-d/2}^{d/2} dz A_1 \cosh\left(\frac{z}{\lambda}\right), \tag{A.74}$$

$$= A_1(r_o - r_i)\lambda \sinh\left(\frac{z}{\lambda}\right)\Big|_{-d/2}^{d/2}, \tag{A.75}$$

$$= A_1 w\lambda \left[\sinh\left(\frac{d}{2\lambda}\right) - \sinh\left(-\frac{d}{2\lambda}\right)\right], \tag{A.76}$$

$$= 2A_1 w\lambda \sinh\left(\frac{d}{2\lambda}\right), \tag{A.77}$$

$$A_1 = \frac{I}{2w\lambda \sinh\left(\frac{d}{2\lambda}\right)}, \tag{A.78}$$

where $d\mathbf{A} = drdz\ \hat{\mathbf{n}}$ is an area element with unit vector $\hat{\mathbf{n}}$ pointing parallel to **J**, and $w = r_o - r_i$ is the ring width. Thus,

$$\mathbf{J} = \frac{I}{2w\lambda \sinh\left(\frac{d}{2\lambda}\right)} \cosh\left(\frac{z}{\lambda}\right) \hat{\phi}. \tag{A.79}$$

The kinetic inductance is found by [97, Eq. (11)],

$$L_k = \frac{\mu_0}{I^2}\int \lambda^2 J^2 dV, \tag{A.80}$$

$$= \frac{\mu_0}{I^2}\lambda^2 \frac{I^2}{4w^2\lambda^2 \sinh^2\left(\frac{d}{2\lambda}\right)} \int_{r_i}^{r_o}\int_0^{2\pi}\int_{-d/2}^{d/2} \cosh^2\left(\frac{z}{\lambda}\right) r dr d\theta dz, \tag{A.81}$$

$$= \frac{\mu_0}{4w^2}\frac{1}{\sinh^2\left(\frac{d}{2\lambda}\right)}\frac{1}{2}(r_0^2 - r_i^2)2\pi\left[\frac{z}{2} + \frac{\sinh z/\lambda \cosh z/\lambda}{2/\lambda}\right], \tag{A.82}$$

where the z-integral was solved using Equation (17.28.8) of Reference ([81, p. 99]. Using the definitions in Chapter 2,

$$L_k = \frac{2\pi\mu_0}{4w^2}\frac{Rw}{\sinh^2\left(\frac{d}{2\lambda}\right)}\left[\frac{d}{4} + \frac{\sinh d/2\lambda \cosh d/2\lambda}{2/\lambda} - \left(-\frac{d}{4} + \frac{\sinh -d/2\lambda \cosh -d/2\lambda}{2/\lambda}\right)\right], \tag{A.83}$$

$$= \frac{\pi\mu_0}{2w}\frac{R}{\sinh^2\left(\frac{d}{2\lambda}\right)}\left[\frac{d}{2} + \lambda \sinh\frac{d}{2\lambda}\cosh\frac{d}{2\lambda}\right], \tag{A.84}$$

$$= \frac{\pi\mu_0}{2w}\frac{R}{\sinh^2\left(\frac{d}{2\lambda}\right)}\left[\frac{d + \lambda\sinh d/\lambda}{2}\right], \tag{A.85}$$

$$= \frac{\pi R\mu_0}{2w}\frac{d + \lambda\sinh d/\lambda}{\sinh^2\left(\frac{d}{2\lambda}\right)}. \tag{A.86}$$

A.4.2 J_ϕ a function of r and z

For this problem, $\mathbf{J} = J_\phi(r,z)\hat{\phi}$. This involves the separation of variables technique. First, start by reducing Equation (2.142) to,

$$\frac{\partial^2 J_\phi}{\partial r^2} + \frac{1}{r}\frac{\partial J_\phi}{\partial r} - \left(\frac{1}{\lambda^2} + \frac{1}{r^2}\right)J_\phi + \frac{\partial^2 J_\phi}{\partial z^2} = 0. \tag{A.87}$$

The separation of variables solution for this problem begins by assuming that $J_\phi(r,z) = R(r)Z(z)$. Plugging this into Equation (A.87),

$$ZR'' + \frac{1}{r}ZR' + \left(\frac{1}{\lambda^2} - \frac{1}{r^2}\right)ZR + RZ'' = 0, \tag{A.88}$$

where,

$$R'' \stackrel{def}{=} \frac{\partial^2 R}{\partial r^2}, \tag{A.89}$$

$$R' \stackrel{def}{=} \frac{\partial R}{\partial r}, \tag{A.90}$$

$$Z'' \stackrel{def}{=} \frac{\partial^2 Z}{\partial z^2}. \tag{A.91}$$

The standard technique for separation of variables is to now divide by J_ϕ. This results in one part of Equation (A.88) being a function of only r, and the other part of Equation (A.88) being a function of only z. These parts must cancel, and therefore equal the absolute value of the same constant,

$$\frac{R'' + \frac{1}{r}R' + (\frac{1}{\lambda^2} - \frac{1}{r^2})R}{R} = -\frac{Z''}{Z} = \kappa^2, \tag{A.92}$$

where κ is some constant. The solution to this is very complicated, but with the appropriate boundary conditions will give the current density, from which the kinetic inductance can be found.

A.5 Transmission and reflection for an electromagnetic plane wave

A.5.1 Two media

Suppose an infinite electromagnetic plane wave is traveling at a frequency ω in one medium with wave number k_1, into another medium with wave number k_2,

and at some angle, θ_I, measured from the normal to boundary, such as is the case in Figure 2.2. The incoming electric field can be written as [1, p. 303, Eq. (7.30)],

$$\mathbf{E}_I = \mathbf{E}_{0I} e^{i(\mathbf{k}_I \cdot \mathbf{x} - \omega t)}, \tag{A.93}$$

where I means incident, and $\mathbf{E}_{0I}$ is the amplitude vector, and $\mathbf{k}_I$ is the incident wave vector. For the geometry assumed, the magnetic field must be transverse, and given by, assuming no sources [1, p. 295, Eq. (7.1)],

$$\nabla \times \mathbf{E} = -\frac{\partial \mathbf{B}}{\partial t}. \tag{A.94}$$

Taking the curl of Equation (A.93),

$$\nabla \times \mathbf{E}_I = i k_I e^{i(\mathbf{k}_I \cdot \mathbf{x} - \omega t)} \hat{\mathbf{k}}_I \times \mathbf{E}_{0I}, \tag{A.95}$$

whereupon plugging Equation (A.95) into Equation (A.94) and integrating with time, produces the magnetic field [1, p. 303, Eq. (7.30)],

$$\mathbf{B}_I = \frac{k_I}{\omega} e^{i(\mathbf{k}_I \cdot \mathbf{x} - \omega t)} \hat{\mathbf{k}}_I \times \mathbf{E}_{0I}. \tag{A.96}$$

Similarly, the equations for the reflected waves denoted by R, are [1, p. 304, Eq. (7.32)],

$$\mathbf{E}_R = \mathbf{E}_{0R} e^{i(\mathbf{k}_R \cdot \mathbf{x} - \omega t)}, \tag{A.97}$$

$$\mathbf{B}_R = \frac{k_R}{\omega} e^{i(\mathbf{k}_R \cdot \mathbf{x} - \omega t)} \hat{\mathbf{k}}_R \times \mathbf{E}_{0R}, \tag{A.98}$$

and the transmitted waves, denoted by T, are [1, p. 303, Eq. (7.31)],

$$\mathbf{E}_T = \mathbf{E}_{0T} e^{i(\mathbf{k}_T \cdot \mathbf{x} - \omega t)}, \tag{A.99}$$

$$\mathbf{B}_T = \frac{k_T}{\omega} e^{i(\mathbf{k}_R \cdot \mathbf{x} - \omega t)} \hat{\mathbf{k}}_T \times \mathbf{E}_{0T}. \tag{A.100}$$

Note that $\mathbf{k}_I \neq \mathbf{k}_R$, but, $k_I = k_R = k_1$, and likewise, $k_T = k_2$. The phase of each field must be the same at the interface, regardless of the boundary conditions [1, p. 304]. As the incident wave travels towards the boundary, its phase winds. Upon striking the boundary, the reflected and transmitted waves are created, and must begin with the same phase that the incident wave had upon striking the boundary. All fields have the same time component, $\exp(-i\omega t)$, and so these cancel, and what is left is a condition on the spatial component of the fields at the boundary,

$$\mathbf{k}_I \cdot \mathbf{x} = \mathbf{k}_R \cdot \mathbf{x} = \mathbf{k}_T \cdot \mathbf{x}. \tag{A.101}$$

This condition also implies that the wave vectors all lie in the same plane, called the plane of incidence [1, p. 304].

If the angle of reflection and the angle of transmission are labeled θ_R and θ_T, respectively, as in Figure (2.2), then Equation (A.101) implies that [1, p. 304, Eq. (7.35)],

$$k_I \sin\theta_I = k_R \sin\theta_R = k_T \sin\theta_T, \tag{A.102}$$

and since, as stated earlier, $k_I = k_R = k_1$, it follows that [1, p. 304],

$$\theta_I = \theta_R. \tag{A.103}$$

Another equation that follows is known as Snell's Law [1, p. 304, Eq. (7.36)],

$$k_1 \sin\theta_I = k_2 \sin\theta_T, \tag{A.104}$$

$$\frac{\sin\theta_I}{\sin\theta_T} = \frac{k_2}{k_1} = \frac{n_2}{n_1}, \tag{A.105}$$

where n is the index of refraction, and the following was used, $k = \omega\sqrt{\tilde{\epsilon}\tilde{\mu}} = \omega n/c$, where $c = 1/\sqrt{\epsilon_0\mu_0}$ is the speed of light. Note that the angle of transmission is more

commonly referred to as the angle of refraction. Also note here that if $n_2 < 0$, then the angle of refraction is measured on the same side of the normal as the angle of incidence, as shown in Figure (1.1).

The boundary conditions are given in Equations (2.40)–(2.43) [1, p. 304, Eq. (7.37)],

$$[\epsilon_1(\mathbf{E}_{0I} + \mathbf{E}_{0R}) - \epsilon_2(\mathbf{E}_{0T})] \cdot \hat{\mathbf{n}} = 0, \tag{A.106}$$

$$(\mathbf{E}_{0I} + \mathbf{E}_{0R} - \mathbf{E}_{0T}) \times \hat{\mathbf{n}} = 0, \tag{A.107}$$

$$(\mathbf{B}_{0I} + \mathbf{B}_{0R} - \mathbf{B}_{0T}) \cdot \hat{\mathbf{n}} = 0, \tag{A.108}$$

$$\left[\frac{1}{\mu_1}(\mathbf{B}_{0I} + \mathbf{B}_{0R}) - \frac{1}{\mu_2}(\mathbf{B}_{0T})\right] \times \hat{\mathbf{n}} = 0, \tag{A.109}$$

where [54, p. 389],

$$\mathbf{B}_{0x} = (k_x/\omega)\hat{\mathbf{k}} \times \mathbf{E}_{0x}, \tag{A.110}$$

for $x = I$, R, and T. Solving these boundary conditions for S-polarization, as shown in Figure (2.2), Equation (A.106) gives $0 = 0$, since $\mathbf{E} \cdot \hat{\mathbf{n}} = 0$. Equation (A.107) is really two equations, one for the x-components, and one for the y-components. The equation for the x-components is $0 = 0$, since there is no component of $\mathbf{E}$ along the x-axis. The equation for the y-component simply states,

$$E_{0I} + E_{0R} = E_{0T}. \tag{A.111}$$

Equation (A.108) deals with the components of $\mathbf{B}$ along the z-axis. Since the magnetic field makes an angle with the normal, Equation (A.108) reduces to,

$$B_{0I} \sin\theta_I + B_{0R} \sin\theta_R = B_{0T} \sin\theta_T. \tag{A.112}$$

Using Equation (A.110) and Equation (A.103), Equation (A.112) can be rewritten as,

$$\frac{1}{v_1}\left(E_{0I}+E_{0R}\right)\sin\theta_I=\frac{1}{v_2}E_{0T}\sin\theta_T, \tag{A.113}$$

where $v=\omega/k=c/n$. Note that,

$$\begin{aligned}\frac{1}{v_1}\left(E_{0I}+E_{0R}\right) &= \frac{1}{v_2}E_{0T}\frac{\sin\theta_T}{\sin\theta_I} &\text{(A.114)}\\ &= \frac{1}{v_2}E_{0T}\frac{n_1}{n_2} &\text{(A.115)}\\ &= \frac{1}{v_2}E_{0T}\frac{v_2}{v_1} &\text{(A.116)}\\ &= \frac{1}{v_1}E_{0T}. &\text{(A.117)}\end{aligned}$$

Thus, Equation (A.113) reproduces Equation (A.111). Finally, Equation (A.109) is really two equations, however the y-component gives nothing since there is no component of $\mathbf{B}$ along the y-axis. For the x-component,

$$\frac{1}{\mu_1}\left(B_{0I}-B_{0R}\right)\cos\theta_I=\frac{1}{\mu_2}B_{0T}\cos\theta_T, \tag{A.118}$$

or rewriting in terms of the electric fields, using Equation (A.110),

$$\frac{1}{\mu_1 v_1}\left(E_{0I}-E_{0R}\right)\cos\theta_I=\frac{1}{\mu_2 v_2}E_{0T}\cos\theta_T. \tag{A.119}$$

At this point, it is useful to group terms together, and following the notation of

Griffiths, define [54, p. 390, Eqs. (9.106) and (9.108)],

$$\alpha \stackrel{def}{=} \frac{\cos\theta_T}{\cos\theta_I}, \tag{A.120}$$

$$\beta \stackrel{def}{=} \frac{\mu_1 v_1}{\mu_2 v_2}. \tag{A.121}$$

Equation (A.119) can be rewritten as,

$$E_{0I} - E_{0R} = \frac{\mu_1 v}{\mu_2 v_2}\frac{\cos\theta_T}{\cos\theta_I}E_{0T} = \beta\alpha E_{0T}. \tag{A.122}$$

At this point, there are two equations, but three unknowns. However, it is assumed that the amplitude of the incident electromagnetic field is known, and so the solution obtained will be the ratio of the transmitted amplitude to the incident amplitude, and the ratio of the reflected amplitude to the incident amplitude. The two equations to be solved are,

$$E_{0I} + E_{0R} = E_{0T}, \tag{A.123}$$

$$E_{0I} - E_{0R} = \beta\alpha E_{0T}. \tag{A.124}$$

The solutions as stated above are,

$$t \stackrel{def}{=} \frac{E_{0T}}{E_{0I}} = \frac{2}{1+\alpha\beta}, \tag{A.125}$$

$$r \stackrel{def}{=} \frac{E_{0R}}{E_{0I}} = \frac{1-\alpha\beta}{1+\alpha\beta}, \tag{A.126}$$

where t and r are the Fresnel coefficients of transmission and reflection, respec-

tively [54, p. 390]. For normal incidence, $\alpha = 1$, and,

$$t = \frac{2}{1+\beta} = \frac{2\mu_2 n_1}{\mu_2 n_1 + \mu_1 n_2}, \tag{A.127}$$

$$r = \frac{1-\alpha\beta}{1+\alpha\beta} = \frac{\mu_2 n_1 - \mu_1 n_2}{\mu_2 n_1 + \mu_1 n_2}. \tag{A.128}$$

Rewriting in terms of $k_i = n_i\omega/c$, for $i = 1, 2$,

$$t = \frac{2\mu_2 k_1}{\mu_2 k_1 + \mu_1 k_2}, \tag{A.129}$$

$$r = \frac{\mu_2 k_1 - \mu_1 k_2}{\mu_2 k_1 + \mu_1 k_2}. \tag{A.130}$$

Note that if $\mu_i = \mu_0$ and $n_i^2 = \epsilon_i$ for $i = 1, 2$, then the intensity, defined as [54, p. 391, Eq. (9.113)],

$$I \stackrel{def}{=} \frac{1}{2}\epsilon v E_0^2, \tag{A.131}$$

can be used to find the transmissivity, $\mathcal{T}$, and the reflectivity, $\mathcal{R}$. Using $v = c/n$ [54,

p. 391, Eq. (9.116)],

$$\mathcal{T} \stackrel{def}{=} \frac{I_T}{I_I} \tag{A.132}$$

$$= \frac{\epsilon_2 n_1}{\epsilon_1 n_2}\left(\frac{E_{0T}}{E_{0I}}\right)^2 \tag{A.133}$$

$$= \frac{\epsilon_2 n_1}{\epsilon_1 n_2}\frac{4n_1^2}{(n_1+n_2)^2} \tag{A.134}$$

$$= \frac{n_2}{n_1}\frac{4n_1^2}{(n_1+n_2)^2} \tag{A.135}$$

$$= \frac{4n_1 n_2}{(n_1+n_2)^2}, \tag{A.136}$$

where I_I is the intensity of the incident electric field. For R [54, p. 391, Eq. (9.116)],

$$\mathcal{R} \stackrel{def}{=} \frac{I_R}{I_I} \tag{A.137}$$

$$= \left(\frac{E_{0R}}{E_{0I}}\right)^2 \tag{A.138}$$

$$= \frac{(n_1-n_2)^2}{(n_1+n_2)^2} \tag{A.139}$$

$$= \frac{n_1^2 - 2n_1 n_2 + n_2^2}{(n_1+n_2)^2}. \tag{A.140}$$

Using Equation (A.136) and Equation (A.140),

$$\mathcal{T} + \mathcal{R} = 1, \tag{A.141}$$

while from Equations (A.129) and (A.130),

$$t = r + 1. \tag{A.142}$$

The above derivation of t and r used S-polarization. For P-polarization, Griffiths provides a complete solution [54, p. 386]. However, below is a slight variation on the solution presented in Reference [54]. Starting with Equation (9.102) in Reference [54], γ is defined as,

$$\gamma \stackrel{def}{=} \frac{\epsilon_2 n_1}{\epsilon_1 n_2}. \tag{A.143}$$

The equations to solve for t and r are then [54, p. 390, Eqs. (9.105) and (9.107)],

$$E_{0I} - E_{0R} = \gamma E_{0T}, \tag{A.144}$$

$$E_{0I} + E_{0R} = \alpha E_{0T}, \tag{A.145}$$

with α defined in Equation (A.120). The solutions are then,

$$t = \frac{E_{0I}}{E_{0T}} = \frac{2}{\alpha + \gamma}, \tag{A.146}$$

$$r = \frac{E_{0I}}{E_{0R}} = \frac{\alpha - \gamma}{\alpha + \gamma}, \tag{A.147}$$

which, for normal incidence, that is, $\alpha = 1$, and substituting for γ, reduce to,

$$t = \frac{2\epsilon_1 n_1}{\epsilon_1 n_1 + \epsilon_2 n_2}, \tag{A.148}$$

$$r = \frac{\epsilon_1 n_1 - \epsilon_2 n_2}{\epsilon_1 n_1 + \epsilon_2 n_2}, \tag{A.149}$$

or in terms of the wave number,

$$t = = \frac{2\epsilon_1 k_1}{\epsilon_1 k_1 + \epsilon_2 k_2}, \tag{A.150}$$

$$r = \frac{\epsilon_1 k_1 - \epsilon_2 k_2}{\epsilon_1 k_1 + \epsilon_2 k_2}. \tag{A.151}$$

Note, again that $t - r = 1$. Assuming $\mu_i = \mu_0$ and $n_i^2 = \epsilon_i$ for $i = 1, 2$, it can be shown that P-polarized waves obey Equation (A.141), while from Equations (A.150) and (A.151), it is readily observed that they also obey Equation (A.142).

A.5.2 Three media

The transmission and reflection through a single boundary separating two semi-infinite media was solved in Appendix A.4. Extending the problem to three media, with three boundaries, is a simple extension of the two media problem. Figure (A.2) contains the setup of the problem. After the calculation, medium 1 and medium 3 will be set equal to vacuum, and the angle of incidence, θ_I will be set equal to zero radians. The j^{th} medium has a wave number $k_j = |\mathbf{k}_j|$, index of refraction n_j, permittivity ϵ_j, and permeability μ_j. The solution of the Fresnel coefficients build upon the solution for the two media problem, from Equations (A.129) and (A.130), which state, for any two layers j and $j + 1$,

$$t_{j,j+1} = \frac{2\mu_{j+1} k_j \cos\theta_j}{\cos\theta_j \mu_{j+1} k_j + \cos\theta_{j+1} \mu_j k_{j+1}} \tag{A.152}$$

$$r_{j,j+1} = \frac{\cos\theta_j \mu_{j+1} k_j - \cos\theta_{j+1} \mu_j k_{j+1}}{\cos\theta_j \mu_{j+1} k_j + \cos\theta_{j+1} \mu_j k_{j+1}}, \tag{A.153}$$

where θ_j is the angle of incidence at the boundary between the j and $j+1$ media, and θ_{j+1} is the angle of transmission at the boundary between the j and $j+1$ media.

Following Figure (A.2) with $\theta_{T1} = \theta_T$, it follows that the Fresnel coefficient for reflection is the sum of each reflecting ray, that is,

$$\begin{aligned} r &= r_{12} + t_{12}r_{23}t_{21}e^{i2k_2d\cos\theta_T} + t_{12}r_{23}r_{21}r_{23}t_{21}e^{i4k_2d\cos\theta_T} \\ &+ t_{12}r_{23}r_{21}r_{23}r_{21}r_{23}t_{21}e^{i6k_2d\cos\theta_T} + ... \qquad \text{(A.154)} \\ &= r_{12} + t_{12}r_{23}t_{21}e^{i2k_2d\cos\theta_T}(1 + r_{21}r23e^{i2k_2d\cos\theta_T} \\ &+ r_{21}^2r_{23}^2e^{i4k_2d\cos\theta_T} + ...). \qquad \text{(A.155)} \end{aligned}$$

At this point, define $x \stackrel{def}{=} r_{21}r_{23}\exp(i2k_2d\cos\theta_T)$. Then Equation (A.155) follows a geometric series,

$$r = r_{12} + t_{12}r_{23}t_{21}e^{i2k_2d\cos\theta_T}(1 + x + x^2 + x^3 + ...). \qquad \text{(A.156)}$$

The solution for a geometric series is given by [81, p. 131, Eq. (21.5)],

$$\sum_{j=0}^{j=N} x^j = \frac{1}{1-x}, \qquad \text{(A.157)}$$

provided that $|x| < 1$. Equation (A.157) also holds when x is complex [77, p. 1086, Prob. 9]. Since $r_{j,j+1} \stackrel{def}{=} E_{0R}/E_{0I}$, where E_{0R} is the amplitude of the wave reflecting off the boundary, and E_{0I} is the wave incident on the boundary, it follows that the maximum value of r is $r = 1$, if there is total reflection at a boundary. Since $|\exp i\phi| \leq 1$ for any real ϕ, it follows that in Equation (A.156), $|x| < 1$ in the very least. Using Equation (A.157), Equation (A.156) reduces to,

$$r = r_{12} + \frac{t_{12}t_{21}r_{23}e^{i2k_2d\cos\theta_T}}{1 - r_{21}r_{23}e^{i2k_2d\cos\theta_T}}. \qquad \text{(A.158)}$$

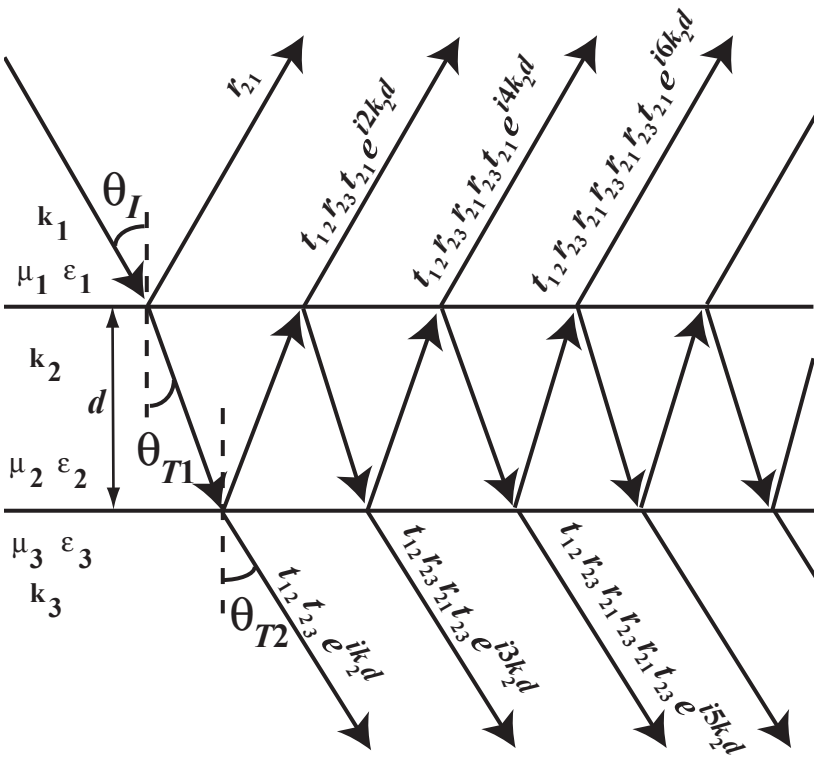

Figure A.2: A plot of the reflection and transmission through a dielectric film. The arrows are the rays of the applied electromagnetic field, and the incident ray makes an angle θ_I at the first boundary, and the first transmitted ray makes an angle θ_{T1} at the first and second boundary, and the second transmitted ray makes an angle θ_{T2} at the second boundary. The film thickness is d, while the other two layers are semi-infinite. Each layer has its own permittivity, and permeability.

It is sometimes useful to rewrite Equation (A.158) with a common denominator. In that case, Equation (A.158) becomes,

$$r = r_{12} + \frac{t_{12}t_{21}r_{23}e^{i2k_2d\cos\theta_T}}{1 - r_{21}r_{23}e^{i2k_2d\cos\theta_T}} \tag{A.159}$$

$$= \frac{r_{12} + (-r_{12}r_{21} + t_{12}t_{21})r_{23}e^{i2k_2d\cos\theta_T}}{1 - r_{21}r_{23}e^{i2k_2d\cos\theta_T}}. \tag{A.160}$$

However, the following property holds,

$$r_{12} = \frac{\cos\theta_1\mu_2k_1 - \cos\theta_2\mu_1k_2}{\cos\theta_1\mu_2k_1 + \cos\theta_2\mu_1k_2} = -\frac{\cos\theta_2\mu_1k_2 - \cos\theta_1\mu_2k_1}{\cos\theta_1\mu_2k_1 + \cos\theta_2\mu_1k_2} = -r_{21}, \tag{A.161}$$

and so, with Equations (A.152) and (A.161),

$$\begin{aligned} -r_{12}r_{21} + t_{12}t_{21} &= \frac{(\mu_2k_1\cos\theta_1)^2 - 2\mu_1\mu_2k_1k_2\cos\theta_1\cos\theta_2 + (\mu_1k_2\cos\theta_2)^2}{(\mu_2k_1\cos\theta_1 + \mu_1k_2\cos\theta_2)^2} \\ &+ \frac{4\mu_1\mu_2k_1k_2\cos\theta_1\cos\theta_2}{(\mu_2k_1\cos\theta_1 + \mu_1k_2\cos\theta_2)^2} \end{aligned} \tag{A.162}$$

$$= \frac{(\mu_2k_1\cos\theta_1)^2 + 2\mu_1\mu_2k_1k_2\cos\theta_1\cos\theta_2 + (\mu_1k_2\cos\theta_2)^2}{(\mu_2k_1\cos\theta_1 + \mu_1k_2\cos\theta_2)^2} \tag{A.163}$$

$$= \frac{(\mu_2k_1\cos\theta_1 + \mu_1k_2\cos\theta_2)^2}{(\mu_2k_1\cos\theta_1 + \mu_1k_2\cos\theta_2)^2} \tag{A.164}$$

$$= 1. \tag{A.165}$$

Thus, Equation (A.160) reduces to [131, p. 61, Eq. (57)],

$$r = \frac{r_{12} + r_{23}e^{i2k_2d\cos\theta_T}}{1 - r_{21}r_{23}e^{i2k_2d\cos\theta_T}}. \tag{A.166}$$

For the Fresnel coefficient of transmission [131, p. 61, Eq. (58)],

$$\begin{aligned} t &= t_{12}t_{23}e^{ik_2 d\cos\theta_T} + t_{12}r_{23}r_{21}t_{23}e^{i3k_2 d\cos\theta_T} \\ &+ t_{12}r_{23}r_{21}r_{23}r_{21}t_{23}e^{i5k_2 d\cos\theta_T} + ... \qquad \text{(A.167)} \\ &= t_{12}t_{23}e^{ik_2 d\cos\theta_T}(1 + r_{23}r_{21}e^{i2k_2 d\cos\theta_T} + r_{23}^2 r_{21}^2 e^{i4k_2 d\cos\theta_T} + ...) \qquad \text{(A.168)} \\ &= \frac{t_{12}t_{23}e^{ik_2 d\cos\theta_T}}{1 - r_{21}r_{23}e^{i2k_2 d\cos\theta_T}}, \qquad \text{(A.169)} \end{aligned}$$

where the term in the parentheses in Equation (A.168) is a geometric series, with the solution given by Equation (A.157) by letting $x = r_{21}r_{23}e^{i2k_2 d\cos\theta_T}$. Note that $t_{j,j+1} \stackrel{def}{=} E_{0T}/E_{0I}$, where E_{0T} is the amplitude of the wave transmitting through a boundary, and E_{0I} is the wave incident on the boundary, it follows that the maximum value of t is $t = 1$, if there is total transmission through a boundary. Since $|\exp i\phi| \leq 1$ for any ϕ, it follows that in Equation (A.168), $|x| < 1$ in the very least.

A.6 The metallic wire arrays and the magnetic vector potential

The Pendry group's derivation of the plasma frequency, Equation (2.95), presented in Reference [35] has a missing minus sign. Starting with the equation of the H field, Equation (2.84), the magnetic vector potential outside of the metallic wire, and assuming the wire is embedded in vacuum, is given by,

$$\begin{aligned} \mathbf{B} &= \nabla \times \mathbf{A} \qquad \text{(A.170)} \\ &= \left(\frac{\partial A_\rho}{\partial z} - \frac{\partial A_z}{\partial \rho}\right)\hat{\theta}, \qquad \text{(A.171)} \end{aligned}$$

where only the θ-component is considered since the magnetic field is azimuthal about the wire. Since the wires extend to infinity, there cannot be a dependence on z for the magnetic vector potential, and so $\partial/\partial z = 0$. Thus the equation to solve is,

$$B_\theta = -\frac{\partial A_z}{\partial \rho}, \tag{A.172}$$

which leads to, using I for the current,

$$-\frac{\partial A_z}{\partial \rho} = \frac{\mu_0 I}{2\pi\rho} - \frac{\mu_0 I \rho}{2\pi R_c^2}, \tag{A.173}$$

$$A_z(\rho) = \frac{\mu_0 I}{2\pi}\left[-\ln\rho + \frac{\rho^2}{2R_c^2} + C\right], \tag{A.174}$$

where C is a constant of integration. In order to find this constant of integration, the boundary condition is used that $B_\theta = A_z = 0$ at $\rho = R_c$,

$$A_z(\rho = R_c) = 0 = -\ln R_c + \frac{R_c^2}{2R_c^2} + C, \tag{A.175}$$

$$C = \ln R_c - \frac{1}{2}. \tag{A.176}$$

Plugging Equation (A.176) into Equation (A.174), the solution for the magnetic vector potential is,

$$\mathbf{A}(\rho) = \frac{\mu_0 I}{2\pi}\left[-\ln\rho + \frac{\rho^2}{2R_c^2} + \ln R_c - \frac{1}{2}\right]\hat{\mathbf{z}}, \quad 0 < \rho < R_c \tag{A.177}$$

$$= \frac{\mu_0 I}{2\pi}\left[\ln\left(\frac{R_c}{\rho}\right) + \frac{\rho^2 - R_c^2}{2R_c^2}\right]\hat{\mathbf{z}}, \quad 0 < \rho < R_c, \tag{A.178}$$

and $\mathbf{A} = 0$ for $\rho \geq R_c$. Equation (A.178) was the equation for the magnetic vector potential used throughout this dissertation in all fits to the plasma frequency of the arrays of metallic wires.

In Reference [53], Walser, Valanju, and Valanju objected to the Pendry group's use of the magnetic vector potential in the derivation of he plasma frequency. Specifically, the plasma frequency, in terms of $\mathbf{A}$, is,

$$\omega_p = \frac{nve^2}{\epsilon_0|\mathbf{A}|}, \tag{A.179}$$

and their argument is the ambiguity of the magnetic vector potential. Since the magnetic vector potential is related to the magnetic field through Equation (A.170), and the magnetic field is the physically observable quantity, any term added to $\mathbf{A}$ such that the term is equal to the gradient of some scalar will yield the same magnetic field. For instance, for,

$$\tilde{\mathbf{A}} = \mathbf{A} + \nabla\zeta, \tag{A.180}$$

then it follows that,

$$\mathbf{B} = \nabla \times \tilde{\mathbf{A}} = \nabla \times (\mathbf{A} + \nabla\zeta) \tag{A.181}$$

$$= \nabla \times \mathbf{A} + \nabla \times \nabla\zeta = \nabla \times \mathbf{A}, \tag{A.182}$$

where ζ is some scalar field. This is because the curl of any gradient of a scalar is equal to zero [81, p. 120, Eq. (20.43)]. Thus, the magnetic field is said to be gauge invariant, while the magnetic vector potential is the gauge [54, p. 419]. The Walser group's argument is clear now: if any term can be added to Equation (A.178) such that it not effect the magnetic field, then the plasma frequency given by Equation (A.179) will change too, even though the actual fields have not changed. As of the writing of this dissertation*, the Pendry group has not responded to this comment of the Walser group. It is noted that the gauge chosen by the Pendry group is

*17 April 2007.

the Coulomb gauge, since $\nabla \cdot \mathbf{A} = 0$, where $\mathbf{A}$ is given by Equation (A.178), which implies that $\nabla^2 \zeta = 0$. However, for the geometry here, it is not necessarily true that $\zeta = 0$.

A.7 Derivation of the effective permeability for an infinite array of two concentric metallic split-cylinders

This derivation attempts to duplicate the frequency dependent permeability derivation made by the Pendry group in Reference [37]. First, the Pendry group decides to use Maxwell's equations in integral form in order to average the fields over unit cells. A unit cell is a square mesh in the $x - y$ plane that contains a single metallic split-cylinder element, as shown in Figure (2.5). Suppose an external ac H field, H_0, is applied parallel to the cylindrical axis, that is, parallel to the z-axis in Figure (2.5). Then the total H field, H, inside the metallic cylinders is given by [37, Eq. (20)],

$$H = H_0 + (1 - f)j, \tag{A.183}$$

where f is the filling fraction, defined in Equation (2.94), and $j \stackrel{def}{=} J2\pi r$, where J is the current density. The total electromotive force, $\mathcal{E}$, is still given by [37, Eq. (9)],

$$\mathcal{E} = -\pi r^2 \mu_0 \frac{\partial}{\partial t}[H_0 + (1 - f)j] - 2\pi r \sigma j, \tag{A.184}$$

however, this time the electromotive force is not equal to zero, due to the gap in the circumference of the metallic cylinders. Using Equation (2.28) for vacuum, and

using* $\partial/\partial t \rightarrow -i\omega$,

$$D = \epsilon_0 E \tag{A.185}$$

$$\frac{\partial D}{\partial t} = J_D = -i\omega\epsilon_0 E, \tag{A.186}$$

where J_D is the displacement current density. The voltage, V, and the electromotive force, are given by [54, p. 293, Eq. (7.10)],

$$\mathcal{E}_D = V = -\int \mathbf{E} \cdot d\mathbf{l} = -Ed, \tag{A.187}$$

where the line integral of $\mathbf{E}$ is just given by the magnitude of $\mathbf{E}$ times the distance between the metallic cylinders, d. Equation (A.187) can be plugged into Equation (A.186) to obtain,

$$J_D = -i\omega\epsilon_0 E \tag{A.188}$$

$$= i\omega\frac{\epsilon_0}{d}\mathcal{E}_D = i\omega C\mathcal{E}_D, \tag{A.189}$$

where C is the capacitance. Using the definition of j,

$$\mathcal{E}_D = \frac{ij}{2\pi r\omega C}, \tag{A.190}$$

and so Equation (A.184) becomes,

$$\mathcal{E} - \mathcal{E}_D = 0 \tag{A.191}$$

$$= i\omega\pi r^2\mu_0(H_0 + (1-f)j) - 2\pi r\sigma j - \frac{ij}{2\pi r\omega C}, \tag{A.192}$$

*This comes from letting the functions vary with time like $\exp(-i\omega t)$.

and solving for j,

$$j = \frac{i\omega\pi r^2\mu_0 H_0}{\frac{i}{2\pi r\omega C} - i\omega\pi r^2\mu_0(1-f) - 2\pi r\sigma} \tag{A.193}$$

$$= \frac{-H_0}{-\frac{1}{2\pi^2 r^3\omega^2\mu_0 C} + (1-f) - \frac{2\sigma i}{\omega r\mu_0}}. \tag{A.194}$$

The average magnetic field is given by [37, Eq. (6)],

$$B_{\text{avg}} \stackrel{def}{=} \frac{1}{a^2}\int \mathbf{B}\cdot d\mathbf{S}, \tag{A.195}$$

where $d\mathbf{S}$ is an area element with its direction perpendicular to the $x-y$ plane, and a is the lattice parameter. This average magnetic field, Equation(A.195), is found by integrating over the surface of a unit cell, and dividing this integral by the area of a face of a unit cell. The average magnetic field is also given by [37, Eq. (11)],

$$B_{\text{avg}} = \mu_0 H_0, \tag{A.196}$$

It also still holds that [37, Eq. (12)],

$$H_{\text{avg}} = H_0 - fj, \tag{A.197}$$

where H_{avg} is the average H field defined along the z-axis, defined by [37, Eq. (5)],

$$H_{\text{avg}} \stackrel{def}{=} \frac{1}{a}\int_{r_1=(0,0,0)}^{r_2=(0,0,a)} \mathbf{H}\cdot d\mathbf{r}, \tag{A.198}$$

where $d\mathbf{r}$ is the line element pointing in the $+z$-direction, and the limits of r are written explicitly on the integral. Note that this line lies [37] "entirely outside of

the [metallic] cylinders." Using Equation (A.194), the average H field becomes,

$$H_{\text{avg}} = H_0 - fj \tag{A.199}$$

$$= H_0 - \frac{-fH_0}{-\frac{1}{2\pi^2 r^3 \omega^2 \mu_0 C} + (1-f) - \frac{2\sigma i}{\omega r \mu_0}} \tag{A.200}$$

$$= H_0 \left[\frac{-\frac{1}{2\pi^2 r^3 \omega^2 \mu_0 C} + 1 - \frac{2\sigma i}{\omega r \mu_0}}{-\frac{1}{2\pi^2 r^3 \omega^2 \mu_0 C} + (1-f) - \frac{2\sigma i}{\omega r \mu_0}} \right], \tag{A.201}$$

and so the effective permeability, μ is [37, Eq. (7)],

$$\mu = \frac{B_{\text{avg}}}{\mu_0 H_{\text{avg}}} = \frac{\mu_0 H_0}{\mu_0 H_{\text{avg}}} \tag{A.202}$$

$$= \left[\frac{-\frac{1}{2\pi^2 r^3 \omega^2 \mu_0 C} + 1 - \frac{2\sigma i}{\omega r \mu_0}}{-\frac{1}{2\pi^2 r^3 \omega^2 \mu_0 C} + (1-f) - \frac{2\sigma i}{\omega r \mu_0}} \right]^{-1} \tag{A.203}$$

$$= \frac{-\frac{1}{2\pi^2 r^3 \omega^2 \mu_0 C} + 1 - \frac{2\sigma i}{\omega r \mu_0}}{-\frac{1}{2\pi^2 r^3 \omega^2 \mu_0 C} + 1 - \frac{2\sigma i}{\omega r \mu_0}} - \frac{f}{-\frac{1}{2\pi^2 r^3 \omega^2 \mu_0 C} + 1 - \frac{2\sigma i}{\omega r \mu_0}} \tag{A.204}$$

$$= 1 - \frac{f}{-\frac{1}{2\pi^2 r^3 \omega^2 \mu_0 C} + (1-f) - \frac{2\sigma i}{\omega r \mu_0}}, \tag{A.205}$$

where Equation (A.205) is *almost* Equation (17) of Reference [37]. The difference lies in the term,

$$\frac{1}{2\pi^2 r^3 \omega^2 \mu_0 C}, \tag{A.206}$$

in Equation (A.205). Whereas Equation (A.206) contains a factor of 1/2, Equation (17) of Reference [37] contains a factor of 3. It is the belief of the author of this dissertation that this difference in factors arises from the definition of the electric displacement in Equation (A.185). While a definition of zero polarization vector was used, that is, Equation (2.28 with $\mathbf{P} = 0$, the polarization of the metallic

cylinders can be determined, or even roughly approximated. For instance, a dipole or quadrupole moment could be assumed. These moments could be averaged over several unit cells. However, these expressions are very cumbersome [1, p. 146], and it is the belief of the author of this dissertation that the most important result from Reference [37] is that the effective permeability of an array of metallic split-cylinders, and ultimately split-ring resonators, has the functional form given in Equation (2.97),

$$\mu(\omega) = \frac{f\omega^2}{\omega^2 - \omega_0^2 + i\Gamma\omega}. \tag{A.207}$$

A.8 Amplification of evanescent waves

In the year CE 2000, Sir John Pendry showed how evanescent waves can be amplified in a medium with simultaneous negative permittivity and permeability at some frequency $\omega = \omega_0$, as well as a medium with only a negative permittivity in the electrostatic limit [38]. The property of amplifying an evanescent wave is an added benefit to the flat-lens imaging mentioned in Chapter 1, Figure (1.2). First, Pendry considers a flat slab with $n(\omega_0) = -1$, and thickness d, and surrounded by vacuum. The assumption concerning the value of the index of refraction is important, because this derivation does not work for $n \neq -1$, and it will only work for the single frequency, ω_0, where $n(\omega_0) = -1$. This index of refraction was generated by a medium that had the properties $\epsilon(\omega_0) = -1$ and $\mu(\omega_0) = -1$. See Figure (1.2). Assuming S-polarization, the incident, reflected, and transmitted evanescent electric fields through the slab, with permittivity ϵ and permeability μ,

can be written, respectively, as [38, Eqs. (13), (15), and (16)],

$$\mathbf{E}_{0+} = e^{i(k_z z + k_x x - \omega t)}\hat{\mathbf{y}}, \tag{A.208}$$

$$\mathbf{E}_{0-} = re^{i(-k_z z + k_x x - \omega t)}\hat{\mathbf{y}}, \tag{A.209}$$

$$\mathbf{E}_{1+} = te^{i(k'_z z + k_x x - \omega t)}\hat{\mathbf{y}}, \tag{A.210}$$

where r and t were shown to be the following, for normal incidence [38, Eq. (18)]*

$$t = \frac{2\mu k_z}{\mu k_z + k'_z}, \tag{A.211}$$

$$r = \frac{\mu k_z - k'_z}{\mu k_z + k'_z}, \tag{A.212}$$

and [38, Eqs. (14) and (17)],

$$k_z = i\sqrt{k_x^2 + k_y^2 - \omega^2 c^{-2}} \quad \text{with} \quad k_x^2 + k_y^2 > \omega^2 c^{-2}, \tag{A.213}$$

$$k'_z = i\sqrt{k_x^2 + k_y^2 - \epsilon\mu\omega^2 c^{-2}} \quad \text{with} \quad k_x^2 + k_y^2 > \epsilon\mu\omega^2 c^{-2}, \tag{A.214}$$

where the primes denote values inside the slab, and unprimed values denote values that are outside the slab. Note that the reflected and transmitted waves decay exponentially away from the interface in the $-z$ and $+z$-directions, respectively. The incident wave decays as it travels along the z-direction towards the slab. Inside the slab, t and r are, for normal incidence on the other boundary [38, Eq. (19)]†

$$t' = \frac{2k'_z}{\mu k_z + k'_z}, \tag{A.215}$$

$$r' = \frac{-\mu k_z + k'_z}{\mu k_z + k'_z}. \tag{A.216}$$

*Let $\mu_1 = 1$, $\mu_2 = \mu$, $k_1 = k_z$, $k_2 = k'_z$ in Equations (2.36) and (2.37).

†Let $\mu_1 = \mu$, $\mu_2 = 1$, $k_1 = k'_z$, $k_2 = k_z$ in Equations (2.36) and (2.37).

Multiple reflections from both interfaces are accounted for, so the transmission through both interfaces is given by [38, Eq. (20)][‡],

$$T = \frac{\mu k_z}{\mu k_z + k'_z} \frac{2k'_z}{\mu k_z + k'_z} \frac{\exp(ik_z d)}{1 - [(k' - \mu k_z)/(k'_z + \mu k_z)]^2 \exp(i2k_z d)}, \tag{A.217}$$

where the limits of $\epsilon = -1$ and $\mu = -1$ have not been taken yet. Equation (A.217) can be rewritten to [38],

$$T = \frac{4\mu k_z k'_z}{(k'_z + \mu k_z)^2} \frac{(k'_z + \mu k_z)^2 \exp(ik_z d)}{(k'_z + \mu k_z)^2 - (k'_z - \mu k_z)^2 \exp(i2k_z d)} \tag{A.218}$$

$$= \frac{4\mu k_z k'_z \exp(ik_z d)}{(k'_z + \mu k_z)^2 - (k'_z - \mu k_z)^2 \exp(i2k_z d)}. \tag{A.219}$$

The limits take the form,

$$\lim_{\substack{\epsilon \to -1 \\ \mu \to -1}} (k'_z + \mu k_z)^2 = (k_z - k_z)^2 = 0, \tag{A.220}$$

$$\lim_{\substack{\epsilon \to -1 \\ \mu \to -1}} (k'_z - \mu k_z)^2 = (k_z + k_z)^2 = 4k_z^2, \tag{A.221}$$

and so Equation (A.219) becomes [38, Eq. (21)],

$$\lim_{\substack{\epsilon \to -1 \\ \mu \to -1}} T = \frac{-4k_z^2 \exp(ik_z d)}{0 - 4k_z^2 \exp(i2k_z d)} = e^{-ik_z d} = e^{-ik'_z d}. \tag{A.222}$$

Since k_z and k'_z are both purely imaginary, let $k_z = k'_z = i\kappa$, where κ is purely real. Then Equation (A.222) becomes [38],

$$\lim_{\substack{\epsilon \to -1 \\ \mu \to -1}} T = e^{\kappa d}, \tag{A.223}$$

[‡]See Equation (A.169). Let $t_{12} = t$, $t_{23} = t'$, $r_{23} = r_{21} = r'$.

which is a non-propagating wave that is increasing exponentially. This property comes from the electromagnetic properties of the slab, and the interference from the multiple reflections inside the slab.

The Fresnel coefficient for reflection becomes [38, Eq. (22)],

$$\begin{aligned} R &= \frac{-k'+\mu k}{k'+\mu k} \\ &+ \frac{4\mu k k'}{(k'+\mu k)^2}\frac{(k'+\mu k)^2\exp(i2kd)}{(k'+\mu k)^2-(k'-\mu k)^2\exp(i2kd)}\frac{k'-\mu k}{k'+\mu k} \qquad \text{(A.224)} \\ &= \frac{-k'+\mu k}{k'+\mu k}+\frac{4\mu k k'(k'-\mu k)\exp(i2kd)}{(k'+\mu k)[(k'+\mu k)^2-(k'-\mu k)^2\exp(i2kd)]}. \qquad \text{(A.225)} \end{aligned}$$

The last expression, Equation (A.225), can be factored into the following,

$$\frac{(-k'+\mu k)[(k'+\mu k)^2-(k'-\mu k)^2\exp(i2kd)]-4\mu k k'(-k'+\mu k)\exp(i2kd)}{(k'+\mu k)[(k'+\mu k)^2-(k'-\mu k)^2\exp(i2kd)]} \qquad \text{(A.226)}$$

$$\frac{(-k'+\mu k)[(k'+\mu k)^2-(k'-\mu k)^2\exp(i2kd)-4\mu k k'(-k'+\mu k)\exp(i2kd)]}{(k'+\mu k)[(k'+\mu k)^2-(k'-\mu k)^2\exp(i2kd)]} \qquad \text{(A.227)}$$

$$\frac{(-k'+\mu k)[(k'+\mu k)^2-(k'+\mu k)^2\exp(i2kd)]}{(k'+\mu k)[(k'+\mu k)^2-(k'-\mu k)^2\exp(i2kd)]} \qquad \text{(A.228)}$$

$$\frac{(-k'+\mu k)(k'+\mu k)^2[1-\exp(i2kd)]}{(k'+\mu k)[(k'+\mu k)^2-(k'-\mu k)^2\exp(i2kd)]} \qquad \text{(A.229)}$$

$$\frac{(-k'+\mu k)(k'+\mu k)[1-\exp(i2kd)]}{[(k'+\mu k)^2-(k'-\mu k)^2\exp(i2kd)]} \quad . \qquad \text{(A.230)}$$

Plugging Equation (A.230) into Equation (A.225), the Fresnel coefficient for reflection becomes [38, Eq. (22)],

$$\begin{aligned} R &= \frac{(-k'+\mu k)(k'+\mu k)[1-\exp(i2kd)]}{[(k'+\mu k)^2-(k'-\mu k)^2\exp(i2kd)]} \qquad \text{(A.231)} \\ \lim_{\substack{\epsilon\to-1\\ \mu\to-1}} R &= \frac{(-2k)(0)[1-\exp(i2kd)]}{[(0)^2-(4k)^2\exp(i2kd)]} \qquad \text{(A.232)} \\ &= 0. \qquad \text{(A.233)} \end{aligned}$$

Note that the reflectivity and transmissivity, defined in Equations (A.132) and (A.137) give, using the Equations (A.223) and (A.233) [131, p. 61, Eqs. (59) and (60)],

$$\mathcal{R} + \mathcal{T} = |R|^2 + \frac{n_3}{n_1}|T|^2 = 0^2 + |e^{\kappa d}|^2 = e^{2\kappa d} > 1, \tag{A.234}$$

where $n_1 = n_3 = 1$. The case for P-polarized waves is exactly the same, except Equations (A.150) and (A.151) are used [38, Eq. (23)].

Chapter B

Review of the fits

B.1 Three-layer transfer matrix model fits to the electromagnetic transmission

Table (B.1) combines Tables (4.2), (5.1), and (6.1), in order to compare the fit parameters of the fits to the Nb wire array, the single Nb split-ring resonator, and the single Nb split-ring resonator in the Nb wire array. The fit parameters are an overall insertion loss, C, a Nb wire array plasma frequency, ω_p, a permittivity loss parameter, γ, a filling fraction, f, a split-ring resonator resonant frequency, ω_0, and a permeability loss parameter, Γ. The combination medium used all of those parameters. Note that since the Nb wire array and Nb split-ring resonator did not use all of those parameters, the missing parameters are not listed in Table (B.1). Also note that the fit for the combination medium was performed on a computer that had a catastrophic failure of the hard disc, and therefore the fit constant was lost, although the other parameters were not since they were already published in Reference [45]. The lattice parameter of the Nb wire array listed was $a = 5.08$ mm, while the Nb wire array lattice parameter for the combination medium was $a = 4.57$ mm. A fit to the Nb wire array-only measurement with a lattice parameter of $a = 4.57$ was not performed.

Table B.1: Combination of Tables (4.2), (5.1), and (6.1)

	Wires	SRR[a]	NIR[b]
C (dB)	-18	-15	—
$\omega_p/2\pi$ (GHz)	16.1	—	18.0 (17.7)
$\gamma/2\pi$ (MHz)	72.0	—	0.500
f	—	0.14	0.032
$\omega_0/2\pi$ (GHz)	—	10.786	10.72
$\Gamma/2\pi$ (kHz)	—	366	600

[a]SRR stands for split-ring resonator.

[b]NIR stands for negative index of refraction (medium).

B.2 Temperature dependent resonant frequency fits

Table (B.2) combines Tables (5.2) and (6.2). Note that $\chi = 2.63$ was fixed for the combination medium, in order to obtain a fit with reasonable values.

B.3 Temperature dependent quality factor fits

Table (B.3) combines Tables (5.3) and (6.3). Note that χ, β, T_c were fixed from Table (**??**) for the quality factor fits of both the lone-split-ring resonator, and the split-ring resonator in the wire array, in order to obtain a fit with reasonable values.

Table B.2: Combination of Tables (5.2) and (6.2)

	Estimate	SRR[a]	NIR[b]
χ	4	2.63	2.63[c]
β	5×10^{-4}	1.3×10^{-3}	1.5×10^{-5}
T_c (K)	8.65	8.47	8.67
$\omega_{0,g}/2\pi$ (GHz)	—	10.80	10.77

[a]SRR stands for split-ring resonator.

[b]NIR stands for negative index of refraction (medium).

[c]This value was fixed.

Table B.3: Combination of Tables (5.3) and (6.3)

	Estimate	SRR[a]	NIR[b]
χ	4	2.63[c]	2.63[c]
β	5×10^{-4}	$(1.3 \times 10^{-3})^c$	$(1.5 \times 10^{-5})^c$
T_c (K)	8.65	$(8.47)^c$	$(8.67)^c$
ζ	–	1.13×10^{-5}	1.21×10^{-5}
Q_b	—	6.48×10^4	2.7×10^4

[a]SRR stands for split-ring resonator.

[b]NIR stands for negative index of refraction (medium).

[c]Fixed from Table (B.2).

Bibliography

[1] J. D. Jackson, *Classical Electrodynamics*, 3rd ed. John Wiley and Sons, Inc., 1999.

[2] Sir Edmund Whittaker, *A History of the Theories of Aether and Electricity.* Harper & Brothers, 1960, vol. one.

[3] A. Moroz, "Some negative refractive index material headlines long before veselago work and going back as far as to 1905..." last accessed 10 April 2007. [Online]. Available: http://www.wave-scattering.com/negative.html

[4] H. Lamb, "On group-velocity," *Proceedings of the London Mathematical Society*, vol. 1, p. 473, 1904.

[5] Sir Horace Lamb, *Hydrodynamics*, 6th ed. Cambridge University Press, 1932.

[6] Sir Arthur Schuster and John William Nicholson, *An Introduction to the Theory of Optics*, 3rd ed. Edward Arnold & Co., 1928.

[7] L. I. Mandelshtam, "Lectures on some problems of the theory of oscillations (1984)," in *Complete Collection of Works.* Moscow: Academy of Sciences, 1950, vol. five, pp. 428–467.

[8] ——, "Group velocity in a crystal lattice," *Zhurnal Éksperimental'noĭ i Teoreticheskoĭ Fiziki*, vol. 15, no. 9, pp. 476–478, 1945, in Russian.

[9] G. D. Malyuzhinets, "A note on the radiation principle," *Zhurnal Technicheskoi Fiziki*, vol. 21, pp. 940–942, 1951, in Russian.

[10] S. A. Tretyakov, "Research on negative refraction and backward-wave media: A historical perspective," in *Negative refraction: revisiting electromagnetics from microwaves to optics*, 2005.

[11] D. V. Sivukhin, "The energy of electromagnetic waves in dispersive media," *Optika i spektroskopiya*, vol. 3, pp. 308–312, 1957, in Russian.

[12] V. E. Pafomov, "Transition radiation and cerenkov radiation," *Journal of Experimental and Theoretical Physics*, vol. 9, p. 1321, 1959.

[13] ——, "Transition radiation and cerenkov radiation," *Zhurnal Éksperimental'noĭ i Teoreticheskoĭ Fiziki*, vol. 36, p. 1853, 1959, in Russian.

[14] V. G. Veselago, "Properties of materials having simultaneously negative values of the dielectric (ϵ) and the magnetic (μ) susceptibilities," *Soviet Physics – Solid State*, vol. 8, p. 2854, 1967.

[15] ——, "Properties of materials having simultaneously negative values of the dielectric (ϵ) and the magnetic (μ) susceptibilities," *Fizika Tverdogo Tela*, vol. 8, p. 3571, 1966, in Russian. Original journal: Физика Твердого Тела.

[16] ——, "The electrodynamic properties of a mixture of electric and magnetic charges," *Journal of Experimental and Theoretical Physics*, vol. 25, p. 680, 1967.

[17] ——, "The electrodynamic properties of a mixture of electric and magnetic charges," *Zhurnal Éksperimental'noĭ i Teoreticheskoĭ Fiziki*, vol. 52, p. 1025, 1967, in Russian. Original journal:.

[18] V. G. Veselago, "The electrodynamics of substances with simultaneously negative values of ϵ and μ," *Soviet Physics Uspekhi*, vol. 10, p. 509, 1968.

[19] ——, "The electrodynamics of substances with simultaneously negative values of ϵ and μ," *Uspekhi Fizicheskikh Nauk*, vol. 92, p. 517, 1967, in Russian. Original journal: Успехки Физических Наук.

[20] J. Brown, "Artificial dielectrics," in *Progress In Dielectrics*, J. B. Birks and J. H. Schulman, Eds. Heywood & Company, LTD., 1960, vol. two, ch. four, pp. 193–225.

[21] C. J. F. Bottcher, *Theory of Electric Polarisation*, 1st ed. Elsevier, 1952.

[22] J. W. S. Rayleigh, "On the influence of obstacles arranged in rectangular order upon the properties of a medium," *Philosophical magazine*, vol. 34, p. 481, 1892.

[23] ——, "On the incidence of aerial and electric waves upon small obstacles in the form of ellipsoids or elliptic cylinder, and on the passage of electric waves through a circular aperture in a conducting screen," *Philosophical magazine*, vol. 44, p. 28, 1897.

[24] N. M. Rust, "The phase correction of horn radiation," *Journal of the Institution of Electrical Engineers*, vol. 93, p. 50, 1946, part III A.

[25] W. E. Kock, "Metal-lens Antennas," *Proceedings of the Institute of Radio Engineers*, vol. 34, p. 828, 1946.

[26] ——, "Metallic delay lenses," *Bell System Technical Journal*, vol. 27, p. 58, 1948.

[27] J. Brown, "Artificial dielectrics having refractive indices less than unity," *Proceedings of the IEE*, vol. 100, p. 51, 1953, monograph No. 62R, pt. 4.

[28] W. Rotman, "Plasma simulation by artificial dielectrics and parallel-plate media," *IRE Transactions on Antennas and Propagation*, vol. AP-10, p. 82, 1962.

[29] K. E. Golden, "Plasma simulation with an artificial dielectric in a horn geometry," *IEEE Transactions on Antennas and Propagation*, vol. 13, p. 587, 1965.

[30] Sergei A. Schelkunoff and Harald T. Friis, *Antennas: Theory and Practice*. John Wiley & Sons, Inc., 1952.

[31] H. J. Schneider and P. Dullenkopf, "Slotted tube resonator: A new NMR probe head at high observing frequencies," *Review of Scientific Instruments*, vol. 48, no. 1, pp. 68–73, 1977.

[32] W. N. Hardy and L. A. Whitehead, "Split-ring resonator for use in magnetic resonance from 200–2000 MHz," *Review of Scientific Instruments*, vol. 52, no. 2, pp. 213–216, 1981.

[33] S. A. Tretyakov, F. Mariotte, C. R. Simovski, T. G. Kharina, and J.-P. Heliot, "Analytical antenna model for chiral scatterers: Comparison with numerical and experimental data," *IEEE Transactions on Antennas and Propagation*, vol. 44, no. 7, p. 1006, 1996.

[34] J. B. Pendry, A. J. Holden, W. J. Stewart, and I. Youngs, "Extremely low frequency plasmons in metallic mesostructures," *Physical Review Letters*, vol. 76, p. 4773, 1996.

[35] J. B. Pendry, A. J. Holden, D. J. Robbins, and W. J. Stewart, "Low frequency plasmons in thin-wire structures," *Journal of Physics: Condensed Matter*, vol. 10, pp. 4785–4809, 1998.

[36] Charles Kittel, *Introduction to Solid State Physics*, 7th ed. John Wiley & Sons, Inc., 1996.

[37] J. B. Pendry, A. J. Holden, D. J. Robbins, and W. J. Stewart, "Magnetism from conductors and enhanced nonlinear phenomena," *IEEE Transactions on Microwave Theory and Techniques*, vol. 47, p. 2075, 1999.

[38] J. B. Pendry, "Negative refraction makes a perfect lens," *Physical Review Letters*, vol. 85, no. 18, pp. 3966–3969, 2000.

[39] D. R. Smith, W. J. Padilla, D. C. Vier, S. C. Nemat-Nasser, and S. Schultz, "Composite medium with simultaneously negative permeability and permittivity," *Physical Review Letters*, vol. 84, no. 18, pp. 4184–4187, 2000.

[40] R. A. Shelby, D. R. Smith, S. C. Nemat-Nasser, and S. Schultz, "Microwave transmission through a two-dimensional, isotropic, left-handed metamaterial," *Applied Physics Letters*, vol. 78, no. 4, pp. 489–491, 2001.

[41] R. A. Shelby, D. R. Smith, and S. Schultz, "Experimental Verification of a Negative Index of Refraction," *Science*, vol. 292, no. 5514, pp. 77–79, 2001.

[42] A. A. Houck, J. B. Brock, and I. L. Chuang, "Experimental Observations of a Left-Handed Material That Obeys Snell's Law," *Physical Review Letters*, vol. 90, no. 13, p. 137401, 2003.

[43] C. G. Parazzoli, R. B. Greegor, K. Li, B. E. C. Koltenbah, and M. Tanielian, "Experimental verification and simulation of negative index of refraction using snell's law," *Physical Review Letters*, vol. 90, no. 10, p. 107401, Mar 2003.

[44] R. Zengerle, "Light Propagation in Singly and Doubly Periodic Planar Waveguides," *Journal of Modern Optics*, vol. 34, no. 12, pp. 1589–1617, 1987.

[45] M. C. Ricci and S. M. Anlage, "Single superconducting split-ring resonator electrodynamics," *Applied Physics Letters*, vol. 88, no. 26, p. 264102, 2006.

[46] L. D. Landau and E. M. Lifshitz and L. P. Pitaevskiĭ, *Electrodynamics of Continuos Media*, 2nd ed. Pergamon Press, Ltd., 1984.

[47] T. J. Yen, W. J. Padilla, N. Fang, D. C. Vier, D. R. Smith, J. B. Pendry, D. N. Basov, and X. Zhang, "Terahertz Magnetic Response from Artificial Materials," *Science*, vol. 303, no. 5663, pp. 1494–1496, 2004.

[48] S. Linden, C. Enkrich, M. Wegener, J. Zhou, T. Koschny, and C. M. Soukoulis, "Magnetic Response of Metamaterials at 100 Terahertz," *Science*, vol. 306, no. 5700, pp. 1351–1353, 2004.

[49] A. N. Grigorenko, A. K. Geim, H. F. Gleeson, Y. Zhang, A. A. Firsov, I. Y. Khrushchev, and J. Petrovic, "Nanofabricated media with negative permeability at visible frequencies," *Science*, vol. 438, p. 335, 2005.

[50] S. A. Mikhailov, "Comment on "Extremely Low Frequency Plasmons in Metallic Mesostructures"," *Physics Review Letters*, vol. 78, no. 21, p. 4135, May 1997.

[51] M. M. Sigalas, C. T. Chan, K. M. Ho, and C. M. Soukoulis, "Metallic photonic band-gap materials," *Physical Review B*, vol. 52, no. 16, pp. 11 744–11 751, Oct 1995.

[52] J. B. Pendry, A. J. Holden, W. J. Stewart, and I. Youngs, "Pendry et al. reply:," *Physical Review Letters*, vol. 78, no. 21, p. 4136, May 1997.

[53] R. M. Walser, A. P. Valanju, and P. M. Valanju, "Comment on "Extremely Low Frequency Plasmons in Metallic Mesostructures"," *Physical Review Letters*, vol. 87, no. 11, p. 119701, Aug 2001.

[54] D. J. Griffiths, *Introduction to Electrodynamics*, 3rd ed. Prentice-Hall, Inc., 1999.

[55] A. L. Pokrovsky and A. L. Efros, "Electrodynamics of metallic photonic crystals and the problem of left-handed materials," *Physical Review Letters*, vol. 89, no. 9, p. 093901, 2002.

[56] R. Marqués and D. R. Smith, "Comment on "Electrodynamics of Metallic Photonic Crystals and the Problem of Left-Handed Materials"," *Physical Review Letters*, vol. 92, no. 5, p. 059401, 2004.

[57] A. L. Pokrovsky and A. L. Efros, "Pokrovsky and Efros Reply:," *Physical Review Letters*, vol. 92, no. 11, p. 119401, 2004.

[58] P. M. Valanju, R. M. Walser, and A. P. Valanju, "Wave Refraction in Negative-Index Media: Always Positive and Very Inhomogeneous," *Physical Review Letters*, vol. 88, no. 18, p. 187401, 2002.

[59] J. B. Pendry and D. R. Smith, "Comment on "Wave Refraction in Negative-Index Media: Always Positive and Very Inhomogeneous"," *Physical Review Letters*, vol. 90, no. 2, p. 029703, 2003.

[60] D. R. Smith, D. Schurig, and J. B. Pendry, "Negative refraction of modulated electromagnetic waves," *Applied Physics Letters*, vol. 81, no. 15, pp. 2713–2715, 2002.

[61] P. M. Valanju, R. M. Walser, and A. P. Valanju, "Valanju, Walser, and Valanju Reply:," *Physical Review Letters*, vol. 90, no. 2, p. 029704, 2003.

[62] J. M. Williams, "Some problems with negative refraction," *Physical Review Letters*, vol. 87, no. 24, p. 249703, Nov 2001.

[63] G. W. 't Hooft, "Comment on "Negative Refraction Makes a Perfect Lens"," *Physical Review Letters*, vol. 87, no. 24, p. 249701, Nov 2001.

[64] J. Pendry, "Pendry replies:," *Physical Review Letters*, vol. 87, no. 24, p. 249702, Nov 2001.

[65] N. Garcia and M. Nieto-Vesperinas, "Left-handed materials do not make a perfect lens," *Physical Review Letters*, vol. 88, no. 20, p. 207403, 2002.

[66] J. B. Pendry, "Comment on "Left-Handed Materials Do Not Make a Perfect Lens"," *Physical Review Letters*, vol. 91, no. 9, p. 099701, 2003.

[67] N. Garcia and M. Nieto-Vesperinas, "Erratum: Left-Handed Materials Do Not Make a Perfect Lens [Phys. Rev. Lett. **88**, 207403 (2002)]," *Physical Review Letters*, vol. 90, no. 22, p. 229903, Jun 2003.

[68] M. Nieto-Vesperinas and N. Garcia, "Nieto-Vesperinas and Garcia Reply:," *Physical Review Letters*, vol. 91, no. 9, p. 099702, 2003.

[69] J. T. Shen and P. M. Platzman, "Near field imaging with negative dielectric constant lenses," *Applied Physics Letters*, vol. 80, no. 18, pp. 3286–3288, 2002.

[70] G. Gomez-Santos, "Universal features of the time evolution of evanescent modes in a left-handed perfect lens," *Physical Review Letters*, vol. 90, no. 7, p. 077401, 2003.

[71] D. R. Smith, D. Schurig, M. Rosenbluth, S. Schultz, S. A. Ramakrishna, and J. B. Pendry, "Limitations on subdiffraction imaging with a negative refractive index slab," *Applied Physics Letters*, vol. 82, no. 10, pp. 1506–1508, 2003.

[72] N. Fang, H. Lee, C. Sun, and X. Zhang, "Sub-diffraction-limited optical imaging with a silver superlens," *Science*, vol. 308, no. 5721, p. 534, 2005.

[73] R. W. Ziolkowski and A. Erentok, "Metamaterial-based efficient electrically small antennas," *IEEE Transactions on Antennas and Propagation*, vol. 54, no. 7, p. 2113, 2006.

[74] S. Enoch, G. Tayeb, P. Sabouroux, N. Guérin, and P. Vincent, "A metamaterial for directive emission," *Physical Review Letters*, vol. 89, no. 21, p. 213902, Nov 2002.

[75] D. Schurig, J. J. Mock, B. J. Justice, S. A. Cummer, J. B. Pendry, A. F. Starr, and D. R. Smith, "Metamaterial electromagnetic cloak at microwave frequencies," *Science*, vol. 314, no. 5801, p. 977, 2006.

[76] R. P. Feynman, R. B. Leighton, and M. L. Sands, *The Feynman Lectures On Physics: Commemorative Issue*. Addison-Wesley Publishing Co., Inc., 1989, vol. two.

[77] M. D. Greenberg, *Advanced Engineering Mathematics*, 2nd ed. Prentice–Hall, Inc., 1998.

[78] M. Dressel and G. Grüner, *Electrodynamics of Solids: Optical Properties of Electrons in Matter*. Cambridge University Press, 2002.

[79] R. Marqués, J. Martel, F. Mesa, and F. Medina, "Left-handed-media simulation and transmission of em waves in subwavelength split-ring-resonator-loaded metallic waveguides," *Physical Review Letters*, vol. 89, no. 18, p. 183901, 2002.

[80] R. E. Collin, *Field Theory of Guided Waves*. New York, NY: McGraw-Hill, 1960.

[81] M. R. Spiegel and J. Liu, *Mathematical Handbook of Formulas and Tables*, 2nd ed., ser. Schaum's Outlines. McGraw-Hill Companies, Inc., 1999.

[82] A. D. Wunsch, *Complex Variables with Applications*, 2nd ed. Addison-Wesley Publishing Company, 1994.

[83] H. Goldstein, C. Poole, and J. Safko, *Classical Mechanics*, 3rd ed. Addison Wesley, 2002.

[84] J. B. Pendry and S. O'Brien, "Very-low-frequency magnetic plasma," *Journal of Physics: Condensed Matter*, vol. 14, pp. 7409–7416, 2002.

[85] R. Marqués, F. Medina, and R. Rafii-El-Idrissi, "Role of bianisotropy in negative permeability and left-handed metamaterials," *Physical Review B*, vol. 65, no. 14, p. 144440, 2002.

[86] J. D. Baena, L. Jelinek, R. Marqués, and F. Medina, "Near-perfect tunneling and amplification of evanescent electromagnetic waves in a waveguide filled by a metamaterial: Theory and experiments," *Physical Review B (Condensed Matter and Materials Physics)*, vol. 72, no. 7, p. 075116, 2005.

[87] A. M. Nicolson and G. F. Ross, "Measurement of the intrinsic poperties of materials by time-domain techniques," *IEEE Transactions on Instrumentation and Measurement*, vol. IM-19, no. 4, p. 377, 1970.

[88] W. B. Weir, "Automatic measurement of complex dielectric constant and permeability at microwave frequencies," *Proceedings of the IEEE*, vol. 62, no. 1, p. 33, 1974.

[89] J. A. Kong, *Electromagnetic Wave Theory*, 2nd ed. John Wiley & Sons, Inc., 1990.

[90] R. E. Collin, *Foundations for Microwave Engineering*, 2nd ed. Institute of Electrical and Electronics Engineers, Inc., 2001.

[91] J. García-García, F. Martín, J. D. Baena, R. Marqués, and L. Jelinek, "On the resonances and polarizabilities of split ring resonators," *Journal of Applied Physics*, vol. 98, no. 3, p. 033103, 2005.

[92] M. Tinkham, *Introduction to Superconductivity*, 2nd ed. Dover Publications, Inc., 2004.

[93] F. London, *Superfluids: Macroscopic Theory of Superconductivity*, 2nd ed. Dover Publications, Inc., 1961, vol. one.

[94] T. V. Duzer and C. W. Turner, *Principles of Superconductive Devices and Circuits*. Elsevier North Holland, Inc., 1981.

[95] J. D. Baena, R. Marqués, F. Medina, and J. Martel, "Artificial magnetic metamaterial design by using spiral resonators," *Physical Review B (Condensed Matter and Materials Physics)*, vol. 69, no. 1, p. 014402, 2004.

[96] R. Meservey and P. M. Tedrow, "Measurements of the kinetic inductance of superconducting linear structures," *Journal of Applied Physics*, vol. 40, no. 5, pp. 2028–2034, 1969.

[97] N. Bluzer and D. K. Fork, "Inductance of a superconducting corbino ring," *IEEE Transactions on Magnetics*, vol. 28, no. 5, p. 2051, 1992.

[98] W. H. Henkels and C. J. Kircher, "Penetration depth measurements on type II superconducting films," *IEEE Transactions on Magnetics*, vol. 13, no. 1, p. 63, 1977.

[99] R. K. Hoffman, "Microstrip Line Components," in *Handbook of Microwave Technology*, I. Ishii and T. Koryu, Eds. Academic Press, Inc., 1995, vol. one, ch. four, pp. 95–142.

[100] F. E. Terman, *Radio Engineers' Handbook*, 1st ed. McGraw–Hill Book Company, Inc., 1943.

[101] V. V. Talanov, L. V. Mercaldo, S. M. Anlage, and J. H. Claassen, "Measurement of the absolute penetration depth and surface resistance of superconductors and normal metals with the variable spacing parallel plate resonator," *Review of Scientific Instruments*, vol. 71, no. 5, pp. 2136–2146, 2000.

[102] H. Padamsee and J. Knobloch and T. Hays, *RF Superconductivity for Accelerators*. John Wiley & Sons, Inc., 1998.

[103] B. N. Chapman, *Glow Discharge Processes*. John Wiley & Sons, Inc., 1980.

[104] M. C. Sullivan, "The Normal-Superconducting Phase Transition of YBCO In Zero Magnetic Field," Ph.D. dissertation, The University of Maryland at College Park, 2004.

[105] M/A-COM, Inc., *Product Guide*, 1995.

[106] Röhm Degussa–Hüls Group, *Poperties of* ROHACELL® HF.

[107] A. Enders and G. Nimtz, "Evanescent-mode propagation and quantum tunneling," *Physical Review E*, vol. 48, no. 1, pp. 632–634, Jul 1993.

[108] S. Zhu, A. W. Yu, D. Hawley, and R. Roy, "Frustrated total internal reflection: A demonstration and review," *American Journal of Physics*, vol. 54, no. 7, pp. 601–607, 1986.

[109] M. Ricci, N. Orloff, and S. M. Anlage, "Superconducting metamaterials," *Applied Physics Letters*, vol. 87, no. 3, p. 034102, 2005.

[110] John R. Taylor, *An Introduction to Error Analysis: The Study of Uncertainties in Physical Measurements*, 2nd ed. University Science Books, 1997.

[111] M. C. Ricci, H. Xu, R. Prozorov, A. P. Zhuravel, A. V. Ustinov, and S. M. Anlage, "Tunability of superconducting metamaterials," *IEEE Transactions on Superconductivity*, p. 1, 2007, to be published. Available at arXiv:cond-mat/0608737v2.

[112] A. A. Abrikosov, "Nobel lecture: Type-II superconductors and the vortex lattice," *Reviews of Modern Physics*, vol. 76, no. 3, p. 975, 2004.

[113] G. E. Possin and K. W. Shepard, "Complex radio-frequency impedance of type-II superconductors," *Physical Review*, vol. 171, no. 2, pp. 458–460, Jul 1968.

[114] J. Bardeen and M. J. Stephen, "Theory of the motion of vortices in superconductors," *Physical Review*, vol. 140, no. 4A, pp. A1197–A1207, Nov 1965.

[115] L. Ji, R. H. Sohn, G. C. Spalding, C. J. Lobb, and M. Tinkham, "Critical-state model for harmonic generation in high-temperature superconductors," *Physical Review B*, vol. 40, no. 16, pp. 10 936–10 945, Dec 1989.

[116] D. E. Oates, "Nonlinear Behavior of Superconducting Devices," in *Microwave Superconductivity*, H. Weinstock and M. Nisenoff, Eds. Kluwer Academic Publishers, 2001, ch. five, pp. 117–148.

[117] A. P. Zhuravel, A. V. Ustinov, K. S. Harshavardhan, and S. M. Anlage, "Influence of $LaAlO_3$ surface topography on rf current distribution in superconducting microwave devices," *Applied Physics Letters*, vol. 81, no. 26, pp. 4979–4981, 2002.

[118] Kazuaki Sakoda, *Optical Properties of Photonic Crystals*. Springer-Verlag Berlin Hiedelberg, 2001.

[119] Z. Sheng and V. V. Varadan, "Tuning the effective properties of metamaterials by changing the substrate properties," *Journal of Applied Physics*, vol. 101, no. 1, p. 014909, 2007.

[120] T. Koschny, M. Kafesaki, E. N. Economou, and C. M. Soukoulis, "Effective medium theory of left-handed materials," *Physical Review Letters*, vol. 93, no. 10, p. 107402, 2004.

[121] N. Katsarakis, T. Koschny, M. Kafesaki, E. N. Economou, E. Ozbay, and C. M. Soukoulis, "Left- and right-handed transmission peaks near the magnetic resonance frequency in composite metamaterials," *Physical Review B (Condensed Matter and Materials Physics)*, vol. 70, no. 20, p. 201101, 2004.

[122] W. J. Padilla, "Group theoretical description of artificial magnetic metamaterials utilized for negative index of refraction," p. 1, 2005, arXiv:cond-mat/0508307v1.

[123] J. L. C. Maier and J. C. Slater, "Field strength measurements in resonant cavities," *Journal of Applied Physics*, vol. 23, no. 1, pp. 68–77, 1952.

[124] J. B. Marion and S. T. Thornton, *Classical Dynamics of Particles and Systems*, 4th ed. Harcourt Brace & Company, 1995.

[125] B. Wood and J. B. Pendry, "Metamaterials at zero frequency," *Journal of Physics: Condensed Matter*, vol. 19, no. 7, p. 076208, 2007.

[126] L. Feng, X.-P. Liu, J. Ren, Y.-F. Tang, Y.-B. Chen, Y.-F. Chen, and Y.-Y. Zhu, "Tunable negative refractions in two-dimensional photonic crystals with superconductor constituents," *Journal of Applied Physics*, vol. 97, no. 7, p. 073104, 2005.

[127] D. van der Marel, "Optical Spectroscopy of Plasmons and Excitons in Cuprate Superconductors," *Journal of Superconductivity: Incorporating Novel Magnetism*, vol. 17, no. 5, pp. 559–575, 2004.

[128] H. Salehi, A. H. Majedi, and R. R. Mansour, "Analysis and design of superconducting left-handed transmission lines," *IEEE Transactions on Applied Superconductivity*, vol. 15, no. 2, p. 996, 2005.

[129] Y. Wang and M. J. Lancaster, "High-temperature superconducting coplanar left-handed transmission lines and resonators," *IEEE Transactions on Applied Superconductivity*, vol. 16, pp. 1893–1897, 2006.

[130] G. B. Arfken and H. J. Weber, *Mathematical Methods For Physicists*, 5th ed. Harcourt/Academic Press, 2001.

[131] M. Born and E. Wolf, *Principles of Optics: Electromagnetic Theory of Propagation, Interference, and Diffraction of Light.* Pergamon Press, 1959.

Michael Christopher Ricci

Education

Ph.D. Physics, University of Maryland, College Park, August 2007
Thesis Title: Superconducting artificial materials with a negative permittivity, negative permeability, or a negative index of refraction.
Advisor: Professor Steven M. Anlage

M.S. Physics, University of Maryland, College Park, December 2003

B.S. Physics, University of North Carolina, Chapel Hill, May 2001
Minor: Mathematics

Research and Teaching Experience

Graduate Research Assistant 2004–2007
Steven M. Anlage University of Maryland, College Park
Experimental work on the microwave properties of superconducting artificial materials with a negative index of refraction. Designed, built, and executed the experiments. Wrote Matlab code to automate measurements. Fabricated thin-film devices by rf sputtering, photolithography, and plasma etching. Developed theoretical models of the experiments, and wrote code to fit the data using these models. Experience using an HP8722D vector network analyzer to measure electromagnetic transmission, and Microwave Studio to simulate the experiments.

Graduate Research Assistant 2003
Alice Mignerey University of Maryland, College Park
Helped to rewrite code to analyze Gold-Deuterium collision data at the Brookhaven National Laboratory Relativistic Heavy Ion Collider.

Teaching Assistant 2001–2003
Department of Physics University of Maryland, College Park
Taught introductory laboratory courses on electrodynamics and mechanics to over 70 entry level engineering students per semester. Maintained a website with notes and test solutions, and performed lecture demos before certain experiments to reinforce theories.

Undergraduate Research Assistant 2000
Eugene R. Tracy The College of William and Mary
Wrote code to determine the transfer entropy of a colliding pulse mode locked laser to determine the cause of its nonlinear behavior.

Skills

Computer skills include: Auto-CAD, LabView, C, Matlab, Mathematica, HFSS and Microwave Studio, Excel

Electronics and digital signal processing; microwave measurement techniques

Sputtering, lithography, wet and plasma etching techniques; vacuum and low temperature techniques

Metal shop techniques

Refereed Papers

M. C. Ricci and S. M. Anlage, "Tunability of superconducting metamaterials," *IEEE Transactions on Applied Superconductivity*, to be published.

M. C. Ricci and S. M. Anlage, "Single superconducting split-ring resonator electrodynamics," *Applied Physics Letters*, vol. **88**, p. 264102, 2006.

M. Ricci, N. Orloff, and S. M. Anlage, "Superconducting metamaterials," *Applied Physics Letters*, vol. **87**, p. 034102, 2005.

Contributed Talks

American Physical Society March Meeting 2007, "Tunability of Superconducting Split-Ring Resonators With dc And rf Magnetic Fields," session S38.00010

American Physical Society March Meeting 2006, "Single Superconducting Split-Ring Resonator Electrodynamics," session D16.00001

American Physical Society March Meeting 2005, "Microwave Transmission Through A Superconducting Metamaterial," session V39.00008

Service

President, Society of Physics Students, University of North Carolina, Chapel Hill, 2000–2001

Secretary and Treasurer, Society of Physics Students, University of North Carolina, Chapel Hill, 1998–2000

Honors and Awards

The International Summer School on Superconducting Electronics, 2005

The Central Intelligence Agency Directorate of Intelligence Outreach Program, 2005

University of Maryland Excellence in Teaching Award, 2003

Department of Physics Ralph D. Meyers Excellence in Teaching Award Runner-up, 2003

Department of Physics Excellence in Teaching Award, 2002

The National Science Foundation's Research Experience for Undergraduates, 2000

Academic Enhancement Program, University of North Carolina, Chapel Hill, 1997

Summer Ventures in Science and Math, Appalachian State University, 1996

Affiliations

American Physical Society

Institute of Electrical and Electronics Engineers